UAB
Universitat Autònoma de Barcelona

Transient liquid assisted growth of superconducting nanocomposite films

Júlia Jareño Cerulla

PhD thesis

2020

ICMAB
INSTITUT DE CIÈNCIA DE MATERIALS DE BARCELONA

EXCELENCIA SEVERO OCHOA

CSIC
CONSEJO SUPERIOR DE INVESTIGACIONES CIENTÍFICAS

UAB
Universitat Autònoma de Barcelona
Facultat de Ciències
Departament de Física

Transient liquid assisted growth of superconducting nanocomposite films

A dissertation submitted for the degree of

DOCTOR OF PHILOSOPHY IN MATERIALS SCIENCE

by

Júlia Jareño Cerulla

Supervisor:
Prof. Mª Teresa Puig Molina

Superconducting Materials and Large Scale Nanostructures
Institut de Ciència de Materials de Barcelona (ICMAB-CSIC)

Tutor: Dr. Ramon Yáñez
Doctorat en Ciència dels Materials
Departament de Física - Facultat de Ciències
Universitat Autònoma de Barcelona

April 2020

ICMAB
INSTITUT DE CIÈNCIA DE MATERIALS DE BARCELONA
EXCELENCIA SEVERO OCHOA
CSIC
CONSEJO SUPERIOR DE INVESTIGACIONES CIENTÍFICAS

UAB
Universitat Autònoma de Barcelona
Facultat de Ciències
Departament de Física

Memòria que porta per títol **"Transient liquid assisted growth of superconducting nanocomposite films"** i presentada per aspirar al Grau de Doctor en Ciència de Materials per **Júlia Jareño Cerulla**
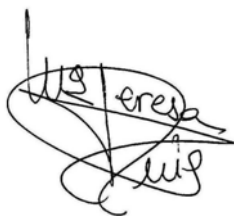
Autor:
Llic. Júlia Jareño Cerulla

amb el vist i plau de: **Prof. Teresa Puig Molina**, Professora d'investigació de l'Institut de Ciències de Materials de Barcelona (ICMAB-CSIC); i **Dr. Ramon Yáñez**, professor del Departament de Química Inorgànica de la Universitat Autònoma de Barcelona (UAB).
I per a que així consti, signen el present certificat.

Directora:
Prof. Teresa Puig Molina

Tutor:
Dr. Ramon Yáñez

Bellaterra, 8 d'abril de 2020

"Distrust everything I say, I am telling the truth."

Ursula K. Le Guin

Abstract

High temperature superconducting materials have unique properties which have been under investigation for many years, mainly involved with their zero resistance properties at high temperatures or at high magnetic fields. Currently, one of the main interest in the superconducting community is to demonstrate the applicability of these materials, in order to achieve the wide-spread use of their applications. As such, there is a big international effort on optimizing performances and developing growth methodologies compatible with big-scale production at low cost. In this context, the results presented in this thesis are an important step forward, reporting for the first time the possibility to use the increased superconducting properties of nanocomposite technology together with a low-cost and high throughput liquid-based methodology based on chemical solution deposition.

The growth of $YBa_2Cu_3O_{7-\delta}$ is performed by the newly reported method of transient liquid assisted growth (TLAG), which combines the inexpensive chemical solution deposition with the presence of a transient liquid that provides ultra-high growth rates. We have been successful in combining this liquid-based growth with the presence of nanoparticles through the understanding of nucleation, microstructure and defect landscape of our films. The key to control the growth process have been the insights on supersaturation and other factors of transient liquid assisted growth, and therefore we devote a chapter to describe this unique methodology.

Pre-formed nanoparticles stabilized in alcoholic media were chosen for these studies. We worked with $BaZrO_3$ of 12 and 4nm of diameter, $BaHfO_3$ of 4nm and LaF_3 of 4nm, the latter nanoparticles being discarded early in the studies due to their reactivity with the liquid.

The results are divided by the different processing routes, presenting the efforts on optimizing the nucleation, growth and superconducting properties of nanocomposites in two chapters. The two different paths consist of the temperature route (heating at constant PO_2), and PO_2-route (heating at very low PO_2 and then increasing PO_2 to reach growth conditions).

In the T-route, several parameters were optimized in order to achieve epitaxial nanocomposite films, such as heating ramp and the thickness of a PLD-YBCO buffer layer. Also different liquid stoichiometries were tested, revealing the importance of supersaturation control to achieve epitaxy. Although J_c self-field at 77K was limited to $1MA/cm^2$ due to reactivity and liquid wetting problems, we demonstrated that introducing pre-formed nanoparticles to TLAG-YBCO creates a defect structure with a lot of potential towards improved vortex pinning.

The growth of YBCO nanocomposites through the PO_2-route with $BaZrO_3$ and $BaHfO_3$ molar percentages ranging from 6% to 32% was studied through XRD techniques which allow the quantification of different YBCO crystalline orientations. Introduction of a seed layer accomplished a better reproducibility and fully c-axis oriented epitaxial films for 6% and 12% nanocomposites. We demonstrated J_c self-field up to 2.2MA/cm^2 at 77K, a very promising result, which led to the evaluation of J_c under applied magnetic fields through dc-SQUID and electrical transport measurements. Thus, we could show the increased performance of nanocomposites with magnetic field in comparison with pristine samples, necessary for high magnetic field applications of coated conductors.

This dissertation also includes a preliminary study on the growth of YBCO thick films ($\sim 1\mu$m) and buffer layer compatibility with TLAG. We demonstrated the successful elimination of barium carbonate in films up to 1μm thick and fully epitaxial YBCO layers could be processed by the PO_2 route. CSD methodologies were used to grow thin films of $Ba_2Cu_3O_4Cl_2$, Nd_2CuO_4, $LaMnO_3$ and $La_{0.8}Sr_{0.2}MnO_3$, in order to evaluate the reactivity of the transient liquid with these materials as well as the nucleation of YBCO on top. $LaMnO_3$ (LMO) was found to be a very promising material and was further investigated by using PLD-grown LMO and SuNAM commercial tape with LMO as the last layer of their architecture. We achieved epitaxial YBCO films with good T_c on top of these buffers layers, demonstrating that TLAG is compatible with commercial coated conductors architecture.

Resum

Els materials superconductors d'alta temperatura tenen propietats úniques les quals són objecte d'investigació des de fa molts anys, especialment les propietats relacionades amb la conductivitat sense resistència a temperatures relativament altes o sota camps magnètics alts. Actualment, l'enfoc de la comunitat de recerca en superconductivitat es centra en intentar demostrar l'aplicabilitat d'aquests materials, per aconseguir l'ús estès de totes les seves possibles aplicacions. Per tant, existeix un gran esforç a nivell internacional per optimitzar les propietats d'aquests materials i desenvolupar metodologies pel seu creixement que siguin compatibles amb la producció a gran escala i baix cost. En aquest context, els resultats inclosos en aquesta tesi són un important pas endavant, ja que demostren per primera vegada la possibilitat d'utilitzar la millora de propietats superconductores aconseguida amb tecnologia de nanocompòsits combinada amb una metodologia de creixement basada en la deposició de solucions químiques i intermedis líquids que presenta un baix cost i alt rendiment.

El creixement de l'YBa$_2$Cu$_3$O$_{7-\delta}$ s'ha dut a terme mitjançant una nova metodologia anomenada "creixement assistit per líquid transitori" (TLAG per les seves sigles en anglès), la qual combina el baix cost de la deposició de solucions químiques amb la presència d'un líquid transitori que proveeix velocitats de creixement ultra-ràpides. Hem aconseguit combinar aquest creixement a través de fases líquides amb la presència de nanopartícules a través de l'estudi de la nucleació, la micro-estructura i la disposició de defectes en les nostres capes primes. Hem descobert que les claus per controlar el procés de creixement són la sobresaturació i altres factors involucrats en el mètode TLAG, i per tant hem dedicat un capítol a descriure aquesta peculiar metodologia.

Pels estudis de capes nanocompòsites vam triar nanopartícules estabilitzades en medis alcohòlics. Hem treballat amb BaZrO$_3$ de 12nm i 4nm de diàmetre, BaHfO$_3$ de 4nm i LaF$_3$ de 4nm, tot i que les nanopartícules de LaF$_3$ han estat descartades degut a la seva reactivitat amb la fase líquida.

Els resultats presentats estan dividits segons les diferents rutes de creixement, amb dos capítols descrivint els esforços realitzats per optimitzar la nucleació, el creixement i les propietats superconductores de les capes primes nanocompòsites. La primera ruta de creixement s'anomena ruta de temperatura, en la qual s'escalfen les capes a pressió parcial d'oxigen (PO$_2$) constant. La segona ruta és la ruta de PO$_2$, on s'escalfa la mostra a pressions parcials d'oxigen molt baixes i posteriorment es realitza un salt cap a PO$_2$ més alta per arribar a les condicions desitjades de creixement.

En la ruta de temperatura, varis paràmetres han estat optimitzats amb l'objectiu d'aconseguir capes nanocompòsites epitaxials, tals com la rampa d'escalfament i el gruix de capes tampó d'YBCO sintetitzades a través de PLD. També presentem resultats amb diferents estequiometries de la fase líquida, elucidant la importància de controlar la sobresaturació per aconseguir capes epitaxials. La densitat de corrent crítica a 77K està limitada a $1MA/cm^2$ degut a la reactivitat del líquid amb el substrat i a problemes de mullat del líquid. Tot i això, hem demostrat que introduir nanopartícules al creixement d'YBCO per TLAG crea una estructura de defectes amb un gran potencial per millorar la fixació de vòrtexs sota camps magnètics.

Hem investigat el creixement de capes nanocompòsites d'YBCO a través de la ruta de PO_2 amb quantitats de $BaZrO_3$ o $BaHfO_3$ entre el 6% i el 32%. Diferents tècniques de difracció de raigs X han permès la quantificació de les diverses orientacions cristal·lines de l'YBCO. Hem descrit l'ús d'una capa prima precursora sense nanopartícules per tal d'aconseguir una bona reproductibilitat i capes nanocompòsites epitaxials completament orientades en l'eix c en el cas de nanocompòsits amb 6% i 12% de nanopartícules. Hem demostrat una densitat de corrent crítica (J_c) de fins a $2.2MA/cm^2$ a 77K, el qual és un resultat molt prometedor que ens ha portat a avaluar la J_c respecte camps magnètics aplicats, a través de magnetometria SQUID i mesures de transport elèctric. D'aquesta manera hem pogut demostrar com les propietats dels nanocompòsits sota camp magnètic són millors que en les mostres estàndard, cosa que és una característica necessària per aplicacions de les cintes recobertes superconductores sota alts camps magnètics.

Aquesta dissertació també inclou un estudi preliminar sobre el creixement de capes gruixudes d'YBCO ($\sim 1\mu m$) i sobre la compatibilitat de capes tampó amb TLAG. Hem pogut demostrar la completa eliminació del carbonat de bari en capes de $1\mu m$ de gruix, alhora que hem aconseguit capes gruixudes completament epitaxials a través de la ruta de PO_2. Hem fet servir el mètode de deposició de solucions químiques per créixer capes de $Ba_2Cu_3O_4Cl_2$, Nd_2CuO_4, $LaMnO_3$ i $La_{0.8}Sr_{0.2}MnO_3$, la reactivitat de les quals ha estat avaluada durant el creixement amb fases líquides. També s'ha estudiat la nucleació de YBCO a sobre d'aquestes capes tampó. El material més prometedor ha estat $LaMnO_3$ (LMO), sobre el qual s'han dut a terme més experiments, utilitzant capes tampó de LMO sintetitzades a través de PLD i substrats metàl·lics comercials amb LMO com a l'última de les capes tampó de la seva arquitectura. Hem aconseguit el creixement epitaxial de capes d'YBCO amb bona temperatura crítica a sobre d'aquestes capes, cosa que demostra que la metodologia TLAG és compatible amb arquitectures comercial de capes recobertes superconductores.

Acknowledgements

I would like to acknowledge, first of all, my supervisor and head of SUMAN group Prof. Teresa Puig, who has guided me through this tortuous journey that is a PhD project. Her knowledge and optimism have shown the way.

This thesis would not be possible without the collaboration of my colleagues Dr. Laia Soler and Juri Banchewski which whom I've shared most of the headaches from trying to understand TLAG; Natalia Chamorro and Jordi Martinez-Esain who provided the nanoparticles; Bernat Mundet and Roger Guzmán responsible for the TEM images and discussion, Silvia Rasi, Adrià Pacheco, Diana Garcia and Lavinia Saltarelli for Soleil days and other discussions, and Max Sieger and Albert Queraltó for their valuable input in the research for buffer layers. Very important is as well the contribution of technicians like Joshua Bailo and Mariona de Palau who make sure our labs run smoothly, Mar Tristany for so much help with managing paperwork that we don't understand, Bernat Bozzo for the SQUID measurements, Raul Solanas for the PLD films and Neus Romà for managing the clean room. The discussions with Anna Crespi and the other crew from XRD ICMAB service were always fruitful, and in general all the services from ICMAB, including technicians, maintenance, administrative personnel, etc. have provided with an excellent work environment. The knowledge provided by Cristian Mocuta from Soleil synchrotron was also very essential to this thesis.

Many thanks to all the other members of SUMAN for the meetings and the insights, specially Xavier Obradors and Susagna Ricart who are a source of knowledge, as well as Jordi Farjas and Pere Roura from Universitat de Girona.

Arigato to Prof. Jun-ichi Shimoyama, Takanori Motoki and other members of Shimoyama's lab who welcomed me with open arms during my short stay in Japan. They provided the opportunity to learn about a new material, new techniques but also a window into their interesting culture.

I acknowledge the financial support that made this thesis possible. The FPU grant by MECD which gave me a salary to live on (and not much more), the ERC Advanced grant ULTRASUPERTAPE which provided the funding for everything TLAG needed, to COACHSUPENERGY MAT2014-51778-C2-1-R from MINECO, to the award Center of Excellence Severo Ochoa and to Soleil synchrotron for the provided beamtime.

And how to thank Dr.Laia Soler and Dr.Palito, I mean, Dr. Alexander Stangl. Laia you have been always here, from the first days in the lab, through our countless weekends and trips, until Sandwichez writing and videocalls on these last days. Except in the improvised parties, nowhere to be found then. I follow your steps one year later and I'm happy to do so. Alex we have so many things in common that I cannot name them all, from being neighbours

x

to the music, the vermuts, the skiing, the mountains, and canine activities in general. My thesis time would have certainly been more dull without a friend like you, you are a catalyst of new things and happiness. I hope to keep a bit of the craziness and all of the friendship while we continue on getting older, thank you Laia and Alex.

Juan Carlos you are one of the nicest people I know. Que tu hi siguis fa que tot sembli fàcil i assumible, un tè, una abraçada, una mica de commmèdia, una mica de relax herbal, i palante. Guardo tots els moments compartits. Vish, everything is fun when shared with you. From hours in a sofa, to night-long pub crawls, weekends... Few people know me so well and I know we will keep on sharing. Ana me alegro tanto (mazo!) de tener una amiga que siempre escucha y siempre sabe qué decir. Si tienes un problema, cuéntaselo a Ana. Y, Ortigueira, y cosas ácidas, y todas las demás risas.

And thanks to my officemates thorough these years, Ziliang, Pablo, Artur, Juri (which whom I never really shared an office but it feels like we did, thanks for all the talks man), a en Ferran (vallès) i companyes i companys de pis que m'han aguantat. And merci to Antoine, for the craziness and happiness and for the friendship. I hope we'll meet again.

Carlos, el meu primer amic a l'ICMAB, gràcies pels cafès a la terrassa, i per tota la música, i perquè sabem que no importa quan de temps estiguem sense veure'ns, sempre serà com si ens haguessim vist el dia anterior.

I gràcies a en Ferran i a tots els nostres dimarts, que ja en són moltíssims i en queden molts més. Ets una estabilitat en el meu camí.

Y un brindis para la gente de desgraciades y las Tordera talks. Por las birras y las discusiones y los debates y los vermuts. Buena gente.

Filipaos! Sou sens dubte el millor d'aquell viatge a Filipines. Tots i cadascun de nosaltres, tan diferents, formem un grup inigualable. Amb ningú més faig les bogeries que fem quan estem junts. I sé que les seguirem fent. Martí, Cora, Aina, Sensi, Samu i Aleix, seguim.

Gràcies al Palau de la Música i tots els 20 anys als seus cors, que han aportat la música que tan necessito. I a Voxalba, pels dilluns de música quan més els necessitava durant l'escriptura.

I a la meva petita i guai família. A me mare per aguantar-me, al Biel i a la meva cosina Anna a qui admiro profundament. I és clar, a la Mireia, de qui sempre desitjaré ser una mica més com era ella.

Contents

Chapter 1

Introduction

1.1 Superconductivity

Superconductivity is a phase present at low temperatures observed in a wide range of materials, from pure metals until oxides and even graphene. It was first discovered by Kammerling Onnes in 1911, after him and his team achieved the liquefaction of helium [1]. They detected zero electrical resistance in pure mercury when it was cooled below 4.2K, which meant the beginning of a new field of research in materials [2]. After the first observation in mercury, many pure elements showed perfect conductivity each below a specific temperature, called critical temperature.

In 1933, Meissner and Ochsenfeld discovered another important characteristic of superconductors, called the Meissner effect: below a certain value of applied magnetic field, they are able to expel the magnetic field from their interior [3]. Moreover, this effect proved superconductivity to be a thermodynamic state, since the field was expelled not only when applied on the superconducting material but also if the material was cooled into the superconducting state after applying the magnetic field.

There is also a limit in the current density that a superconductor can withhold without suppressing the superconducting state. Therefore, we can say that the superconducting state is limited by a critical temperature, a critical external magnetic field and a critical current density. In the infancy of superconductivity, the most limiting factor in terms of building materials for applications was the low critical temperatures of the studied metals and compounds, which were in the range of 4-20K.

Besides the phenomenological study of superconducting materials, a lot of effort was also made to develop suitable theories that could explain superconductivity. In 1935 the so-called London brothers proposed the London

equations, which describe the electromagnetism in superconductors beginning from Maxwell equations and Drude's model [4].

From a thermodynamic point of view, it is necessary that the superconducting state presents a lower Gibbs free energy (G) than the normal state. In a model proposed by Gorter and Casimir, this was considered to describe the condensation energy (E_c) as the energy difference between the SC and normal states, also specifying the thermodynamic critical field ($\mu_0 H_c$):

$$Ec = G_{SC} - G_N = \frac{\mu_0 H_c^2}{2} \cdot V \tag{1.1}$$

where μ_0 is the permeability of vacuum and V the volume of the superconductor.

In 1957 the first microscopic theory of superconductivity was introduced by Bardeen, Cooper and Schrieffer [5]. The so-called BCS theory explains the lower energy of the superconducting state in terms of the condensation of electrons into pairs, bound together at low temperatures, called Cooper pairs. These paired electrons have a weak attractive interaction with the lattice and form a boson-like state that has the effect of achieving a macroscopic phase, generating the superconducting properties. Thus, an energy gap is created between the superconducting state and the normal state, and the perfect conductivity is explained by the superconducting electrons not having available energy states where they could scatter, creating resistivity. The thermodynamic limit is reached when the kinetic energy of the charge carriers overtakes the binding energy of Cooper pairs, which is called depairing current.

The BCS theory explained the behaviour of the so-called conventional superconductors. Nonetheless, in 1935 a new type of superconductors had been described by Rjabinin and Scubnikov [6]. From a phenomenological point of view, this two types of superconductors are distinguished by their behaviour when subjected to a magnetic field, as depicted in Fig.1.1. Type-I superconductors exhibit perfect diamagnetism below the critical magnetic field H_c. Above this boundary, the material is in a normal state and the magnetic field is able to penetrate the whole material. In type-II superconductors, three differentiated regions exist. Below a small field, named lower critical field or H_{c1}, the material is in a Meissner state, excluding all magnetic field from its interior. Above H_{c1}, magnetic field penetrates the material in the shape of quantized cylindrical flux lines, called vortices. This vortices are normal regions generated by superconducting currents flowing in a perpendicular plane to the applied field, and allow the material to remain superconducting below T_c. This region in the H-T diagram is called the mixed-state, which is lost when surpassing the upper critical field or H_{c2}, above which the material is in the normal state.
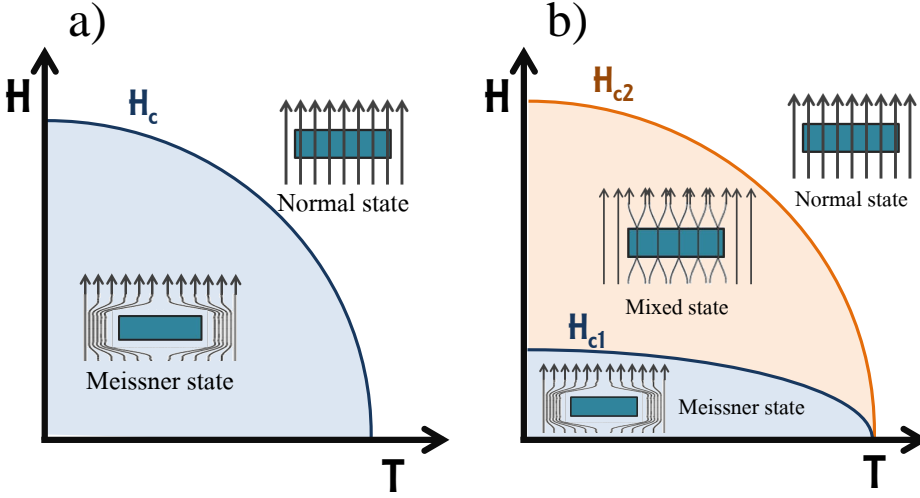
FIGURE 1.1: Depiction of magnetic flux behaviour in the H-T diagram for (a) Type-I superconductors and (b) Type-II superconductors.

According to the phenomenological model developed by Ginzburg and Landau in 1950 [7], the behaviour of the two types of superconductors can be explained by taking into consideration the energy of the boundary between the normal and superconducting state. The ratio between the magnetic penetration depth, λ, and the coherence length, ξ, defines the Ginzburg-Landau parameter, κ:

$$\kappa = \frac{\lambda}{\xi} \begin{cases} \kappa < \frac{1}{\sqrt{2}}: \text{positive boundary energy: type-I SC} \\ \kappa > \frac{1}{\sqrt{2}}: \text{negative boundary energy: type-II SC} \end{cases} \quad (1.2)$$

When the coherence length is bigger than magnetic penetration, boundary energy is positive and there is only one critical field, giving type-I superconductors. The negative boundary energy in the case of type-II makes the introduction of normal-core vortices inside of the superconducting material energetically favourable. The parameters λ and ξ are characteristic for each material, and low temperature superconductors consisted on both type-I and type-II superconductors. Elseway, all the high-temperature superconductors discovered until now belong to type-II.

1.1.1 High Temperature Superconductors

1986 brought a new breakthrough in superconductivity. The first material with a high critical temperature was discovered, a cuprate of the family of

(La,Ba)CuO$_4$ compounds, with a T$_c$ of 30K [8]. One year later, the first material with a critical temperature above the boiling point of nitrogen was reported, the cuprate YBa$_2$Cu$_3$O$_{7-\delta}$ (YBCO) [9], and very soon other cuprate families (Bi-based, Tl-based and Hg-based superconductors) were also discovered with even higher T$_c$ up to 135K for the best Hg-based cuprate. These new materials implied much broader possibilities for superconducting applications, since working with liquid nitrogen is economically and technically viable. The field of superconductivity experienced a boom in scientific research and general public interest, with big expectations for the implementation of superconductors into a plethora of applications. Since then, other superconductors with rather high critical temperature have been discovered, such as MgB$_2$, iron-based materials and more recently the family of hydrides, that under high atmospheric pressure present very high critical temperatures. Currently the record is hold by LaH$_{10}$, with T$_c$=250K under 170 gigapascals [10]. Nonetheless, YBCO and its family of cuprates remain as the most promising materials due to their high upper critical field and high current densities.

In order to attain their full potential, the properties of the mixed state need to be thoroughly studied. In the mixed state of type-II superconductors, vortices with a normal core penetrate the superconducting material. These normal-core vortices are surrounded by superconducting currents which generate a flux quantum of ϕ_0=2.07·10^{-15}Wb. Therefore, they experience a Lorentz-like force, comparable to the force felt by a charge in movement:

$$\overrightarrow{F_L} = \overrightarrow{J} \times \overrightarrow{B} \tag{1.3}$$

resulting in a movement of vortices perpendicular to the magnetic field and current directions. Since we would be moving the normal electrons of the core, vortex motion would imply dissipation and the critical current density in the superconducting material would drop to zero. Luckily, the Lorentz-like force can be counteracted by placing the vortices in non-superconducting sites within the material. This is thermodynamically favourable, as the system regains the condensation energy lost when the vortex core is penetrating the superconducting material. Thus, the arrangement of vortices in these defect sites will create a pinning force, opposed to the Lorentz-like force, enabling dissipation free current through the material as long as the pinning force is stronger than the Lorentz-force, so, as long as the vortices are pinned. The limit of zero resistance current flow in the mixed state is at F_p=F_L=J_cxB, defining the critical current density, J_c. At this point, vortices will start to move and current will dissipate, although the material will remain in a superconducting state until the thermodynamic limit of depairing current is reached.

As shown by Eq.1.3, the Lorentz-like force can increase, overcoming F_p, both by augmenting current density or magnetic field. Moreover, at high temperatures vortices can move due to thermal fluctuations. Overall, in the H-T diagram there is a boundary between the region where vortices are pinned, behaving like a vortex solid and $J_c \neq 0$, and the region where vortices move, considered to behave as a liquid of vortices, with $J_c = 0$. This is a thermodynamic transition named irreversibility line, and marks the limit of application for type-II superconductors.

The position of the irreversibility line is different for each material and can also be modified by increasing the pinning force. As shown in Fig.1.2 for pristine materials, YBCO presents one of the highest irreversibility lines, making it a good candidate for applications.
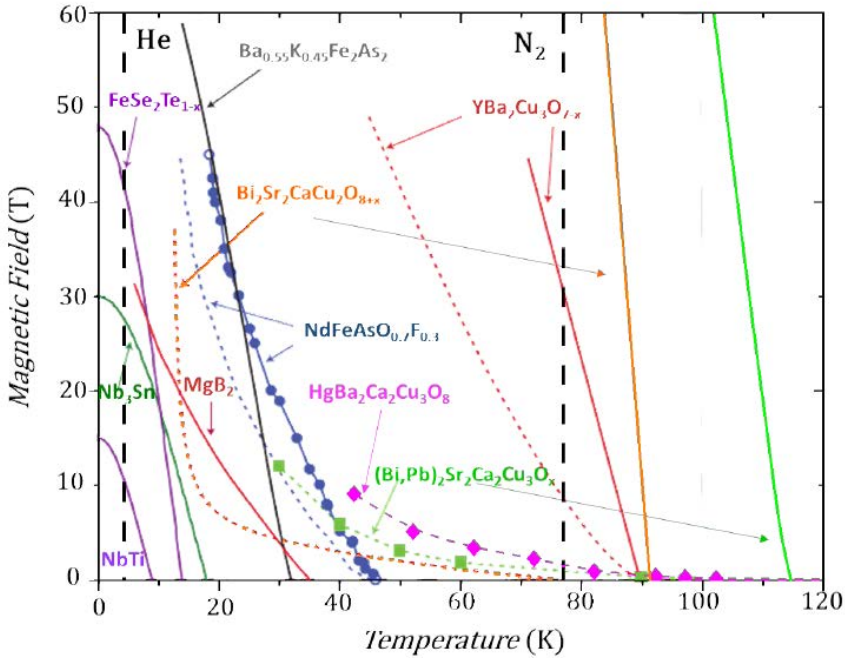
FIGURE 1.2: Type-II superconductors H-T phase diagram showing their irreversibility lines (dashed lines) and upper critical field (straight lines). Black dashed lines show the boiling point of helium and nitrogen. Data adapted from [11–14]

It should also be taken into account how the vortices feel repulsive forces among them, producing an homogeneous hexagonal lattice as first described by Abrikosov in single crystals without additional defects [15]. However, when a superconductor is subjected to an increasing magnetic field, and due to the opposition of pinning force with Lorentz-force, a magnetic gradient is

created inside of the superconductor. This enables us to explain the electro-magnetic behaviour of vortices with the Critical State Model, which describes how hysteresis in the magnetization loop can be used in thin films to calculate the critical current density [16, 17], according to the formula:

$$J_c = \frac{3m}{a^3 t} \cdot A_{corr} \tag{1.4}$$

with m being the magnetization obtained from the magnetic induction mea-surements, a and t the width and thickness from a thin film sample, respec-tively.

1.1.2   YBa$_2$Cu$_3$O$_7$

Within type-II superconductors, one material attracts special attention due to its outstanding properties: YBa$_2$Cu$_3$O$_{7-\delta}$. It has a high T_c, above the boiling point of liquid nitrogen, it can carry very high current densities and has a very high irreversibility line, therefore maintaining high J_c until large external magnetic fields. This makes it one of the most promising materials for appli-cations of superconductors at high temperatures but also at low temperatures and very high magnetic fields, as well as the focus of this thesis. YBCO is a ceramic oxide with a crystalline structure based on a triple perovskite cell. The structure of its unit cell is shown in Fig.1.3.

FIGURE 1.3: Depiction of YBCO unit cell structure.

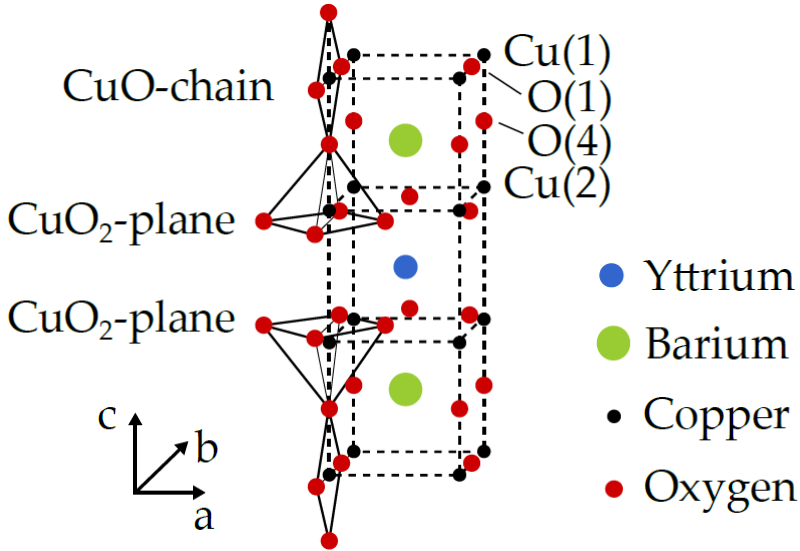The whole unit cell is comprised by three perovskite ABX_3 pseudocubic cells, where X is the anion, in this case oxygen, occupying the edges, Cu corresponds to cation B, which occupies the vertexes and A is the larger cation, in this case barium in the first and third cell and yttrium in the middle one. Depending on the oxygen deficiency indicated by δ, the structure of the material will be orthorhombic ($0 \leq \delta \leq 0.65$) or tetragonal ($0.65 < \delta \leq 1$). YBCO presents superconductivity only with the orthorhombic structure, and the T_c reaches its maximum value when $\delta \approx 0.07$. Therefore, when synthesizing YBCO, an oxygenation step is performed to achieve an optimal doping. In this formulation, the oxygen vacancies are ordered, giving two differentiated layers of Cu-O. There is a layer consisting of CuO chains parallel to the b-axis, followed by two layers of CuO_2 planes. This stacking of CuO_2 planes is found in all compounds of the cuprate family and is thought to be the key for superconductivity in these materials, with superconductivity being carried out by the CuO_2 planes. The CuO chains serve the vital function of charge reservoirs, providing proper carrier density transfer to the CuO_2 planes. However, this structure is responsible for the high anisotropy of YBCO, with the critical current in the ab direction largely exceeding that in the c-axis direction. Furthermore, it was shown that due to the short coherence length of YBCO, the critical current density is lost in the grain boundaries with very small misortientation angles between crystalline grains [18]. The intrinsic anisotropy of YBCO and the requirement for low grain boundary angles in every directions make of furthermost importance the high epitaxy of YBCO for applications. This is, in order to maintain a high J_c, the material needs to have a biaxial texture, being oriented both in out-of-plane and in-plane directions.

1.1.3 Coated Conductors

In order to take advantage of the full potential for applications of YBCO, the material has to be obtained in long tapes. This means that a ceramic (and therefore brittle) material needs to be highly epitaxial in a thickness of 2-3μm and lengths of hundreds of meters or kilometres. This is a huge technological challenge that has been achieved thanks to the coated conductor technology, first demonstrated in 1991 [19].

The common structural features of a coated conductor are the metallic substrate, one or more oxide buffer layers, the superconducting material and a capping layer. The metallic substrate provides flexibility and in general good mechanical properties, and although they are textured, they usually have a very different lattice parameter than YBCO and therefore cannot act as a texture template. The intermediate buffer layers can serve many functions, such as preventing reactivity with the substrate, providing a smooth surface and

very importantly acting as a textured template for the heteroepitaxial growth of the superconducting material. Finally, the capping layer provides protection from environment and can also be important for heating diffusion purposes. Several companies exist around the world which provide coated conductors of various rare earth cuprates (REBCO) materials, synthesized through different production processes. Nonetheless, there are still some obstacles for the commercial viability of superconductors. The two main difficulties are the reluctance of electrical companies to implement new untested technologies (in this cased based on superconducting materials) and the high cost of the coated conductors and final superconducting devices. There has been many efforts to test the technological and economical feasibility of superconducting coated conductors, which are a good step forward for this technology. Two good examples are the Jeju island and Ecoswing projects.

South Corea has invested strongly on the development and installation of HTS CCs. One of their successful installations was carried out in Jeju island, where a 500m YBCO coated conductor was tested and put into operation in the Korean electrical power corporation (KEPCO) grid. The DC HTS was designed to work at 80kV and 156MW and it contains two cryostat layers to control the YBCO temperature. The ultimate goal is to design cables both for long distance DC transport, operating at high voltages, an medium voltage cables to operate in dense cities where overhead transmission is not possible and conventional cables are close to saturation due to their size [20–22].

More recently, the first windmill generator based on a superconducting rotor was manufactured and successfully put into operation. The Ecoswing project used tens of kilometers of coated conductors fabricated by Theva which were winded in a total of 40 poles, and cooled by GM-cryocoolers under vacuum to temperatures lower than 30K, in order to ensure a high I_c and safety of operation. Although an already existing standard windmill structure was used, the smaller dimensions of the superconducting-based system could be appreciated, and the final operation provided with 3.6MW of power [23, 24].

Such projects are a big step in the push towards implementing coated conductors in those fields which can greatly benefit from their characteristics. Projects funded by public research serve the important function of displaying the feasibility of the final products, providing a full proof of concept, and making the technology available to possible interested companies. Nonetheless, further improvements on the cost and throughput are necessary to continue on the current path.

We must also take into account that different applications of coated conductors have different requirements in terms of working temperature and magnetic fields. Fig.1.4 summarizes the working region of different applications for HTS. While coated conductors as transmission cables will work at 77K
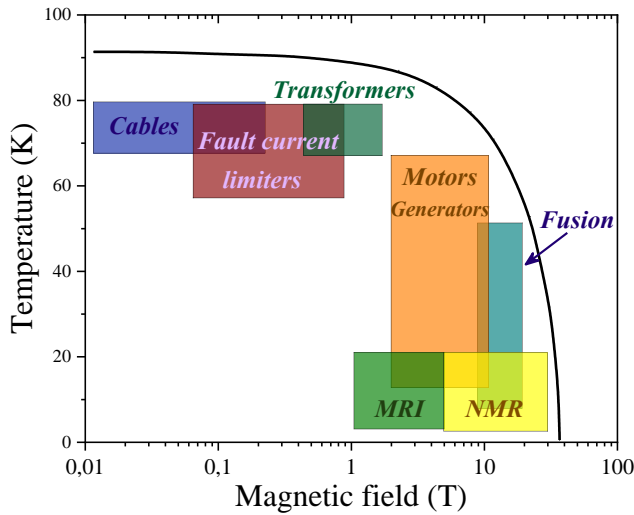
FIGURE 1.4: Working region of temperature and magnetic field for different applications of coated conductors. Black line indicates the irreversibility line of YBCO. Adapted from [25].

and very low magnetic fields, applications such as generators for windmills or fusion and NMR magnets will require to operate at high magnetic fields, although at lower temperatures. Therefore, vortex pinning becomes a very relevant parameter in order that a non-vanishing critical current density is maintained at such high magnetic fields. As it was introduced in section1.1.1, both by increasing magnetic field or current density, the Lorentz-like force that can move vortices and therefore dissipate current, is increased. To counteract this force, we can increase pinning force by providing sites inside of the superconducting material which are in a normal state and therefore can act as pinning centers. Besides the defects usually encountered in crystalline lattices, we can nanoengineer the material to include pinning sites in order to increase the J_c of the coated conductors working under medium and high magnetic fields. The possibility of synthesizing such nanocomposite films has been largely investigated and will be introduced in the following section.

1.2 Nanocomposites

Since Richard Feynmann inspired the field of Nanoscience and Nanotechnology from his lecture "There's plenty of room at the bottom" in 1959 [26], and

the development of Scanning tunnelling microscopy in 1981 and other discoveries put these ideas in the scope of many developments, the study of materials at the nanoscale has blossomed. We now have many techniques that allow us to investigate these materials in the scale of nanometers, opening the door to studying their potential.

A nanocomposite material is defined as a solid containing several phases in which one or more of these phases have one or more dimensions with a length of 100 nanometers or less. In the case of superconducting materials, we are interested in the opportunity to include nanometric defects in the larger crystalline lattice in order to increase vortex pinning.

Origin	Name	Dimensionality	Candidates for VP
Natural	Grain boundaries	1D	No
Natural	a/b grains	3D	Depending on size
Natural	Anti-phase boundaries	2D	Depending on size
Natural	Twin boundaries	2D	Only in H ∥ c
Natural or induced	Stacking faults	2D	Yes
Natural	Oxygen vacancies	0D	Yes
Natural	Dislocations	1D	H ∥ Dislocation axis
Artificial	Nanorods	1D	Yes
Artificial	Nanoparticles	3D	Yes

TABLE 1.1: Possible defects on the YBCO structure and their characteristics.

During the growth process of YBCO or other REBCO materials, many crystalline defects are generated. The density and type of flaws in the crystal lattice will depend on the growth methodology, and some of these naturally occurring defects are able to act as pinning centers, such as stacking faults or twin boundaries. Other type of defects, such as high-angle grain boundaries or large a/b grains are not pinning sites and can block current percolation. We will attempt to maximize the defects with potential for vortex pinning obtained during growth, but we can also artificially induce more defects to provide additional pinning force to increase critical current densities at high magnetic fields. Therefore, the synthesis process can introduce artificial defects, obtaining above-mentioned nanocomposites with enhanced pinning capabilities. Table 1.1 includes a list of possible artificial and natural defects and their potential as pinning centers.

The defects can also be classified depending on their dimensionality, which is relevant to distinguish between isotropic and anisotropic pinning. The ones classified as 0D and 3D, will have the same pinning ability independent of the direction of magnetic field, and therefore contribute to isotropic pinning. On the other hand, 1D and 2D defects will contribute differently to the pinning force depending on magnetic field direction, sometimes only being effective in very specific orientations. In this case they will contribute to anisotropic pinning.

Another important aspect of possible pinning centers is their dimensions. An effective pinning site requires local reduction of superconductivity in a nanometric region, with similar size as the diameter of the vortex (equivalent to two times the coherence length of the material). This size is of approximately 2nm in YBCO at low temperatures, and therefore when synthesizing a nanocomposite with nanorods or nanoparticles, 5nm should be the aimed diameter for the artificially introduced defects. Nonetheless, the system is more complex, since when we introduce nanophases to the growth process, the growth of the crystalline lattice will need to accommodate these phases, sometimes creating additional defects in the structure. These induce defects, such as stacking faults, can also act as pinning sites. Therefore, the introduced nanoparticles or nanorods can act directly as pinning centers if their dimensions are small enough, but bigger particles can also increase the final pinning force of the films by inducing defects in the lattice, therefore acting as indirect pinning sites.

The modification of superconducting materials in order to improve vortex pinning has been an active research field for many years [27]. Early research began with the introduction of Y211 grains in bulk single crystals[28]. Also in single crystals, irradiation with protons, electrons, neutrons and heavy ions demonstrated the richness of the YBCO vortex pinning potentiality [29, 30]. In thin films, one of the first techniques used was surface decoration with nanodots of different oxides, which are able to create growth defects, enhancing pinning [31–33]. Good improvement in critical current density was also accomplished with the incorporation of Y211 nanoparticles into the YBCO matrix, first demonstrated in 2003 by different groups[34, 35]. Therefore, a large effort has been made since then to investigate how to add nanoparticles and nanorods through different growth methodologies for YBCO and other REBCO materials [36–39].

The materials used to synthesize these nanocomposite films need to fulfil different requirements. They must present stability in front of the growth conditions, as well as no reactivity with YBCO, including no ionic substitution in the YBCO matrix and no formation of other secondary phases. Some of the most commonly used materials are:

- BaMO$_3$ perovskites, with M= Zr, Hf or Sn.

- Related Y-Ba-Cu phases such as Y$_2$BaCuO$_5$.

- Rare earth oxides, RE$_x$O$_y$ with RE= Y, Gd, Ho, Er and Dy.

- Double perovskites such as Ba$_2$RE(Ta,Nb)O$_6$

Using some of these materials, YBCO films with small diameter ($\sim$5nm) nanorods with lengths up to the whole film thickness can be obtained by different techniques such as pulsed-laser deposition, by simultaneously depositing the REBCO phase and the nanorod phase in certain conditions. In the case of nanoparticles, they can be introduced both by physical and chemical deposition methods, and there is a large variety in size and orientation that can be investigated. Furthermore, in metal-organic decomposition methods, the nanoparticles can either be synthesized simultaneously to the YBCO by spontaneous segregation, or else they can be synthesized ex-situ and incorporated in the YBCO precursor solution. This variability in methods and sizes gives as well very different defect landscape scenarios.

It is clear that YBCO nanocomposites is an extensive field of research. The study of the growth of nanocomposites depends greatly on the chosen growth methodology. In our case, we will focus on synthesis through chemical solution deposition methods. This choice is motivated by the need of coated conductors to have a low cost and high throughput production. Therefore, if we combine enhanced pinning of nanocomposites technology with a low cost production method, we will be one step closer to an extended use of superconducting materials.

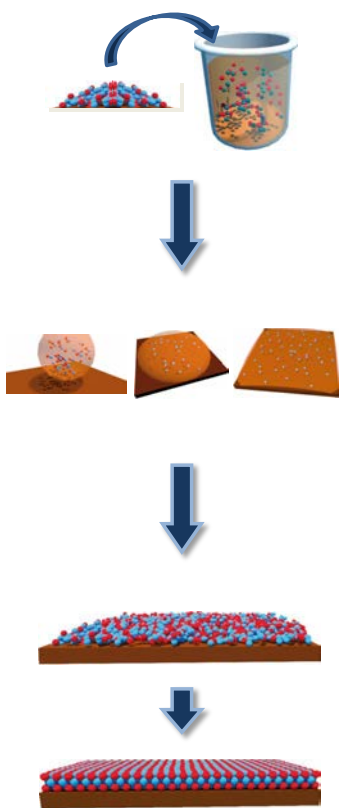## 1.3   Chemical solution deposition techniques

Chemical solution deposition (CSD) is a method for thin film growth with a lot of potential towards the manufacturing of functional materials with a lot of different properties [40, 41]. The main advantage of this process is the ability of synthesizing complex oxides through a simple and yet versatile methodology that does not require expensive equipment and often can be carried out under atmospheric pressure. In this sense, it is also beneficial for the growth of superconducting thin films, in comparison to the so-called physical methods such as pulsed laser deposition (PLD), which requires high vacuum and the use of high-frequency lasers.

From an historical perspective, CSD was developed in the mid of the twentieth century to synthesize coatings of SiO$_2$, soon followed by other simple oxides such as TiO$_2$ and Al$_2$O$_3$ [42–44]. With the discovery of various functionalities for perovskite oxides, CSD also evolved to synthesizing more complex

materials, with films of $PbZr_xTi_{1-x}O_3$ (PZT) being one of the first examples [45, 46]. Many properties of strongly correlated oxides, discovered in bulk samples, were soon studied in thin films, and this method provided methodologies apt both for small scale research and for large scale commercial devices. Some of the main interests in the field of functional oxides growth through CSD are ferroelectric thin films with applications in different kinds of memory devices [47, 48], as well as piezoelectric materials for sensors and actuators [49].

The chemical solution deposition process consists mainly on three steps:

- **Solution preparation:** Precursors of the cations present in the final material are dissolved in one or more solvents through different chemical synthesis procedures, obtaining a coating solution with the desired concentration and rheological properties.

- **Deposition:** The coating solution is deposited onto the substrate through various techniques such as dip-coating, spin-coating, spray coating or others. The deposition conditions can be regulated in order to optimize the film thickness and homogeneity.

- **Processing and crystallization:** The gel film obtained through deposition is subjected to different processing conditions until crystallization of the final material. This step is often divided into two different processes, pyrolysis and crystallization. The pyrolysis is performed at intermediate temperatures, decomposing the organic components of the sample and generating for example metal oxide particles of the metal precursors. Crystallization of the desired functional phase is often performed at higher temperatures and a variety of atmospheric conditions, placing the sample in optimal processing conditions to obtain the desired crystalline oxide.

Chemical solution deposition can also be classified depending on the type of chemical reactions involved on the process, which will change according to

the type of precursors used. Therefore the process can be considered metalorganic decomposition when different types of carboxylates are used, sol-gel reactions with alkoxide precursors or the so-called hybrid routes, with both alkoxide and carboxylates and which are usually carried out to obtain polymers.

1.3.1   CSD for YBCO growth

Since the discovery of $YBa_2Cu_3O_{7-\delta}$, chemical solution deposition was studied as a possible method to synthesize thin films of this material. The starting precursor solution needs to contain Y, Ba and Cu in the desired stoichiometry, and the deposited film undergoes a pyrolysis treatment before the final crystallization step. Through the most common carboxylates precursors, $BaCO_3$ is obtained after pyrolysis. Due to the high stability of this product and thus the difficulty to fully eliminate it during the growth of YBCO, the TFA-MOD process was developed [50]. This method bypasses the barium carbonate problem by using trifluoroacetate (TFA) precursors. The presence of fluorine generates BaF_2 instead of $BaCO_3$, and therefore the YBCO is grown through a solid-gas reaction between YBCO precursors and water vapor, releasing HF gas [51, 52].

TFA methodology has been successful in achieving epitaxial YBCO films with very high critical current densities, and therefore is the most investigated CSD method for REBCO growth. It has also shown compatibility with the growth of nanocomposite films, with many studies demonstrating enhanced vortex pinning by the introduction of nanoparticles [35, 53].

The drawbacks of TFA-CSD are the release of harmful HF during synthesis and most importantly the limited growth rate due to the solid-gas nature of the reaction. The growth rate limit is of $\sim$1nm/s [54].

Other CSD processes have been investigated, using non-fluorinated precursors such as acetates in acid [55, 56] or aqueous solutions, acetylacetonates[57], or through polimer-assisted deposition[58, 59]. Many of these routes have shown lower properties than the TFA process and a lower number of studies exist[60, 61].

Nonetheless, it would be an important step forward to develop methodologies that can overcome the limited growth rate of 1nm/s. In this sense, this thesis is based on an idea funded by an ERC Advanced grant, which envisages a way to combine CSD methodologies with ultrafast growth of YBCO. The breakthrough is to use a liquid as intermediate for the formation of YBCO. In general, a reaction involving a liquid reactant is much faster than a solid-gas reaction.

The growth of YBCO thin films through a liquid has been previously used only in liquid phase epitaxy (LPE), hybrid liquid phase epitaxy (HLPE) and more recently reactive co-evaporation and direct reaction technique (RCE-DR).

The new methodology is called transient liquid assisted growth, which was first reported in Soler's thesis [62], and will be detailed in Chapter 2. The combination of simple CSD methodologies, ultrafast growth rates and nanocomposite technology would meet all the requirements for low-cost, high throughput and good superconducting properties coated conductors.

1.4   Thesis goals and content

This thesis was developed in the framework of studying transient liquid assisted growth methodology (TLAG) for the growth of YBCO thin films. This process is based on well known chemical solution deposition techniques but is newly combined with the presence of a liquid as a catalyst to boost growth rates. The main goal of this thesis is to grow nanocomposite films through TLAG, therefore taking advantage both from the improved pinning of nanocomposites and the characteristics of TLAG. This novel methodology is still under development and therefore this thesis was involved with the general study of the reactions and processes of TLAG as well as going forward in including nanoparticles. Furthermore, this project goals also includes making this technique compatible with coated conductor technology, and thus we investigated how to grow thick films and different buffer layers.

The content of this thesis is structured as follows:

- **Chapter 2** details the experimental methodologies and gives a theoretical introduction to transient liquid assisted growth.

- **Chapter 3** gives the results on nanocomposite films grown through temperature route. The growth conditions were optimized in order to obtain epitaxial films, and the superconducting properties were analysed and related to the growth conditions and presence of nanoparticles.

- **Chapter 4** describes the growth of nanocomposite films through the PO_2-route. Epitaxial films were obtained and the possibility to include a thin seed layer was investigated. The crystalline orientation of the nanoparticles was analysed as well as the superconducting properties and the enhanced vortex pinning.

- **Chapter 5** includes the first studies on thick films and several buffer layers. Different compounds grown through CSD were investigated and

their reactivity with YBCO was analysed. The compatibility of buffer layers grown through PLD and commercial tapes with YBCO was also explored, giving promising preliminary results that need to be further investigated.

Chapter 2

Transient Liquid Assisted Growth methodologies and principles

The aim of this chapter is to introduce the reader to experimental details of sample preparation as well as the principles of transient liquid assisted growth (TLAG). We will explain the methodologies of chemical solution deposition and how they were adapted to prepare nanocomposite films. The methods used to prepare the precursor films, such as chemical solution preparation, deposition through spin coating and pyrolysis, are well established in literature and therefore their principles will be briefly explained while giving details on how they were adapted for this thesis. A small section on nucleation and crystal growth will introduce the necessary concepts to present a discussion on TLAG. This methodology has been developed by SUMAN research group at ICMAB, under the funding of an advanced ERC grant. The novelty of this process involves a big effort on elucidating the growth mechanism and factors involved on the YBCO nucleation, a research that was initially studied in Soler's thesis [62], was extended in Rasi's thesis[63] and in the present work, and will continue in Banchewski thesis (to be defended in summer 2020). These four PhD thesis worked quite a long time in parallel and produced a publication that describes and analyses TLAG [64]. Nowadays, the continuation of this research is still carried on in SUMAN group with 3 additional PhD thesis. In particular, this chapter will summarize our knowledge on the growth mechanism understanding up to now and the different crystallization routes. The insight on TLAG principles is necessary to put in context the following chapters dedicated to nanocomposite films.

2.1 Chemical solution preparation and deposition

Chemical solution deposition requires several steps to obtain a final crystalized film. The first of them, preparing a solution with the desired precursors, is usually simple in procedure but requires a high degree of control of many different factors that might affect all the subsequent steps. In a first level of requirement, one needs to obtain a solution where all the metals are dissolved in the correct stoichiometry. But furthermore, the chosen solvents, metal precursors, concentration and way of preparation will influence viscosity, contact angle, density, surface tension, and other solution parameters that need to be controlled and reproducible in order to obtain a precursor solution that is compatible with spin coating, the deposition technique used in this thesis. Based on literature and on many experiments described in more detail in Soler's thesis [62], a precursor solution was optimized for YBCO growth through TLAG.

2.1.1 YBCO precursor solution preparation

The acetates of each metal: $Y(CH_3CH_2COO)_3$, $Ba(CH_3CH_2COO)_2$ and $Cu(CH_3CH_2COO)_2$ where used as the precursor metalorganic salts. They were chosen due to their good solubility in the solvents, long term stability and commercial availability. Before solution preparation they were dried on a vacuum oven at 55º overnight.

The three acetates were dissolved in a round bottom flask at 50ºC in propionic acid while circulating nitrogen into the flask during 4 hours. After complete dissolution, the solution was filled up to reach the desired precise concentration. This is the so-called mother solution, which was stable in storage up to 4 weeks. The final solution is obtained by mixing equal volume of the mother solution and methanol. Therefore the final solvent mixture is 50% CH_3OH and 50% $CH_3CH_2CH_2COOH$ (propionic acid). Due to the rheological properties of the solvents, solutions with higher percentage of methanol produce thicker films on deposition, but after pyrolysis the films are inhomogeneous. Therefore, the mixing of both solvents with 50% in volume provides solutions with contact angle=10-12º and a viscosity of 6-8mPa·s, which gives homogeneous films after pyrolysis. A small amount of additive (5% in weight) such as triethanolamine (TEA) can be added to increase the thickness of the film. Typically the concentration of the mother solution is 2M, which will diminish to 1M in the final solution. This concentration will give films of 200nm after pyrolysis without TEA, and 250nm with the additive, which will decrease to 100nm and 125nm after growth, respectively.
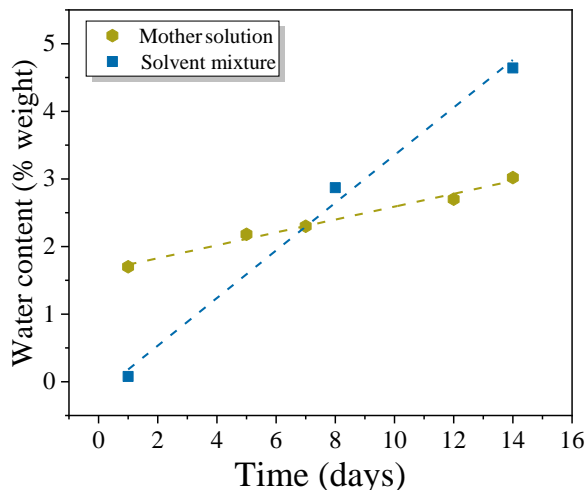
FIGURE 2.1: Percentage of water in solution measured by Karl-Fischer, in the mixture of methanol and propionic acid and in the YBCO mother solution with methanol as the only solvent.

Fig.2.1 shows the increasing percentage of water in a mixture of propionic acid and methanol versus a mother solution containing only propionic acid as a solvent. An estherification reaction is possible between the two used solvents:

$$CH_3OH + CH_3CH_2CH_2COOH \rightarrow CH_3CH_2CH_2COOCH_3 + H_2O \qquad (2.1)$$

and thus water will be produced in the solvent mixture at an approximate rate of 0.1% in weight per day. The effect of water in solution can be observed in Fig.2.2. Percentages above 2% were found to have a direct correlation with misorientation of YBCO and random nucleation.

This result shows the importance of the precursor solution for the success of all the different steps. By producing a mother solution and mixing with methanol only before deposition, this reaction can be strongly minimized.

2.1.2 Nanoparticles solutions preparation

All the pre-formed nanoparticles used in this thesis were obtained in collaboration with the department of inorganic chemistry at *Universitat Autònoma de Barcelona*. The preparation of colloidal solutions of nanoparticles is an extensive research field in itself, and in particular the work performed in UAB to obtain nanoparticles compatible with the requirements of YBCO growth has
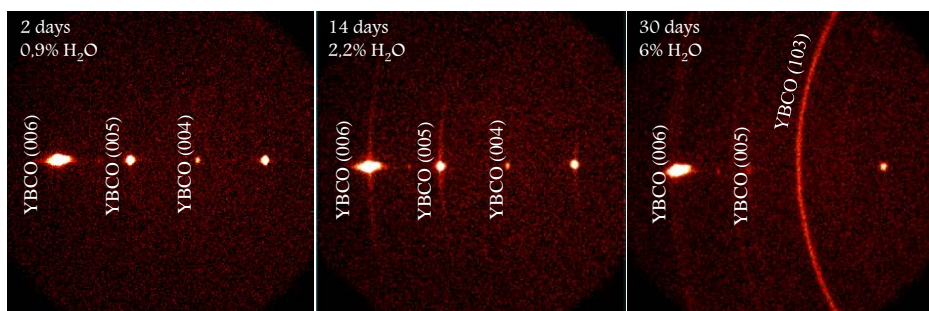
FIGURE 2.2: 2D X-ray of grown YBCO films with different water content. More details on X-ray analysis can be found in Appendix A.

required overcoming challenges such as a good control of the size of the particles and their stabilization in alcoholic media in high concentrations. Here we will include the experimental details of the nanoparticles with best compatibility with our methodologies, which in particular were synthesized by Natalia Chamorro in the case of $BaMO_3$ nanoparticles and by Jordi Martinez-Esain in the case of LaF_3 (both developing their PhD thesis also during this period).
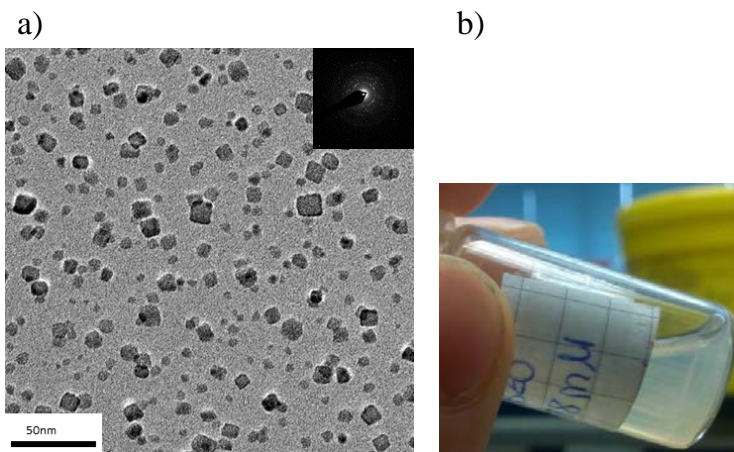
Synthesis of $BaZrO_3$ nanoparticles

FIGURE 2.3: a) TEM image of cubic $BaZrO_3$ nanoparticles after synthesis. b) Image od the coloidal solution containing dispersed nanoparticles.

$BaZrO_3$ nanoparticles were synthesized through solvothermal synthesis, a method that has been successful for this type of nanoparticles [65, 66], and

was studied in the inorganic chemistry department at UAB in the last 3 years. This method uses high temperature and pressures to perform the nanoparticle synthesis reaction and is able to tune the phase, shape and size through controlling different factors such as reaction time, temperature and additives. $Ba(OH)_2 \cdot 8H_2O$ and $Zr(OCH_2CH_2CH_2CH_3)_2$ are placed in an autoclave with 10ml of ethanol as solvent, 1ml of NH_3 and 6ml of triethileneglycol, at 180ºC during 1 hour. Triethileneglycol molecules are used as surfactants, stabilizing the small nanoparticles. These molecules will be attached to the nanoparticles surface in the final colloidal solution. After completion of the reaction, nanoparticles are separated from the reaction mixture through centrifugation, and after the proper cleaning process they are re-dispersed in ethanol. The concentration of the final solution ranges 100-150mM in $BaZrO_3$.
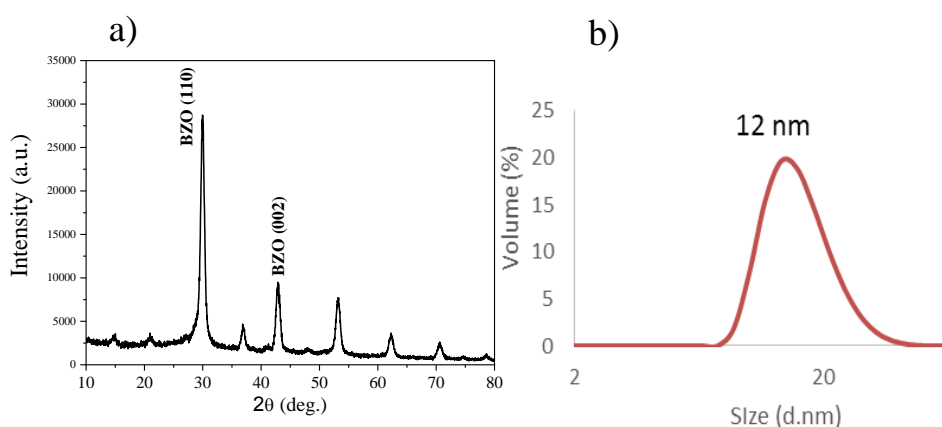

FIGURE 2.4: a) X-ray pattern of synthesized $BaZrO_3$ nanoparticles. b) Corresponding DLS spectra.

Fig.2.3 (a) shows a TEM image of the final nanoparticles, where their cubic shape and their crystallinity can be appreciated. A picture of the final colloidal solution is shown in Fig.2.3 (b). Fig.2.4 (a) presents the powder X-ray diffraction pattern of the dried nanoparticles showing their phase purity and crystallinity.

To measure the size of the nanoparticles, two different methods are applied. The size of the crystalline nanoparticles is determined directly from TEM images, but to take into account the full diameter which also includes the triethylene glycol molecules attached to the surface, dynamic light scattering (DLS) measurements were performed to determine the hydrodynamical diameter. This method is probing a higher volume of sample, and so, besides giving the value of particle diameter, it will detect the distribution of sizes and possible

different families of nanoparticles size, thus detecting possible agglomeration.
The mean size of BaZrO$_3$ nanoparticles is 10nm as determined by TEM. Fig.2.4
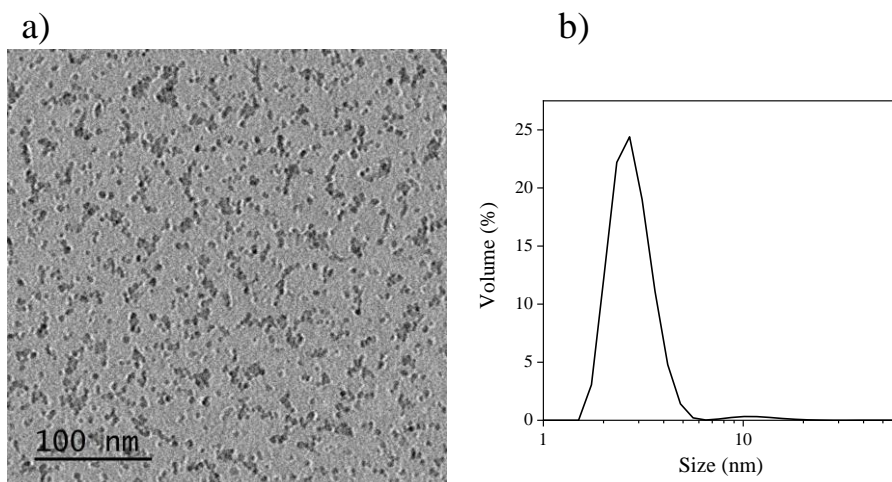(b) shows a typical DLS measurement presenting a mean size of 12nm.

a)   b)

FIGURE 2.5: DLS and TEM images of BaZrO$_3$ nanoparticles of 4nm in diameter.

In this thesis two different sizes were used. The 12nm diameter nanopar-
ticles and smaller nanoparticles with 4nm in diameter. These small nanopar-
ticles were synthesized by substituting the 1ml of NH$_3$ added to the reaction
mixture by 3.3ml of triethanolamine. Their TEM and DLS measurements are
shown in Fig.2.5.

Synthesis of BaHfO$_3$ nanoparticles

BaHfO$_3$ nanoparticles were synthesized through the same procedure as BaZrO$_3$
by replacing Zr(OCH$_2$CH$_2$CH$_2$CH$_3$)$_2$ with its hafnium equivalent. The met-
alorganic precursors were dissolved in 1ml of NH$_3$, 7ml of TREG and 9ml
of ethanol and heated to 180ºC in the autoclave. The reaction was carried
out during 1 hour and the resulting nanoparticles were separated from the
reaction mixture through centrifugation. A cleaning step was performed by
dispersing the nanoparticles in ethanol and centrifuging the mixture for 20
minutes. Fig.2.6 (a) shows the TEM of the resulting spherical nanoparticles,
with a diameter of 4.8±1.8nm. The diameter calculated with DLS is 3.7nm.
The concentration of BaHfO$_3$ after re-dispersion ranges from 70 to 120mM.
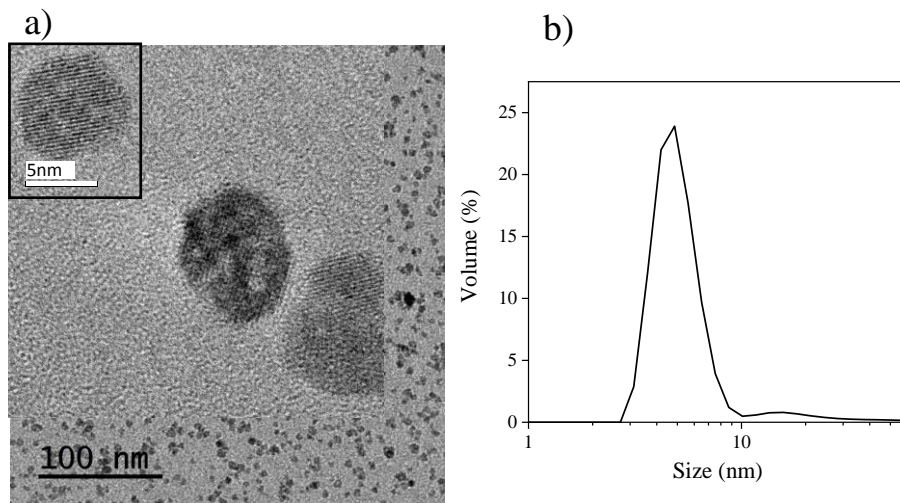
FIGURE 2.6: TEM images and DLS measurement of as-synthesized BaHfO$_3$ nanoparticles.

Synthesis of LaF$_3$ nanoparticles

Details of the study of this family of nanoparticles can be found in [67] and [68]. The method consists of co-precipitation with citric acid in water. Citric acid was dissolved in H$_2$O and neutralized with N(CH$_3$)$_4$OH. Afterwards, the precursor lanthanum acetate hydrate was added to the solution and then heated under stirring to 100ºC. At this temperature, NH$_4$F was incorporated and the reaction mixture was kept stirring for 2 hours. After cooling, the synthesized nanoparticles were separated from the reaction mixture by adding acetone and centrifugation. The nanoparticles were re-dispersed in methanol obtaining a solution 90-120mM in LaF$_3$, compatible with YBCO mother solution.

2.1.3 Stabilization of the nanoparticles solutions in the YBCO precursor solutions

The chemical solutions used in the case of nanocomposite films require the presence of both the precursors for YBCO and the nanoparticles. In our case, we use colloidal solutions with pre-formed nanoparticles that can be stabilized in the YBCO solution. The conditions for this mixing are compatibility of the solvents and no unwanted reactions between the different components. The use of a mother precursor solution in propionic acid allows us to mix the nanoparticles solution as part of the mixing volume of methanol, since their solvent is ethanol, which can substitute methanol in small amounts without
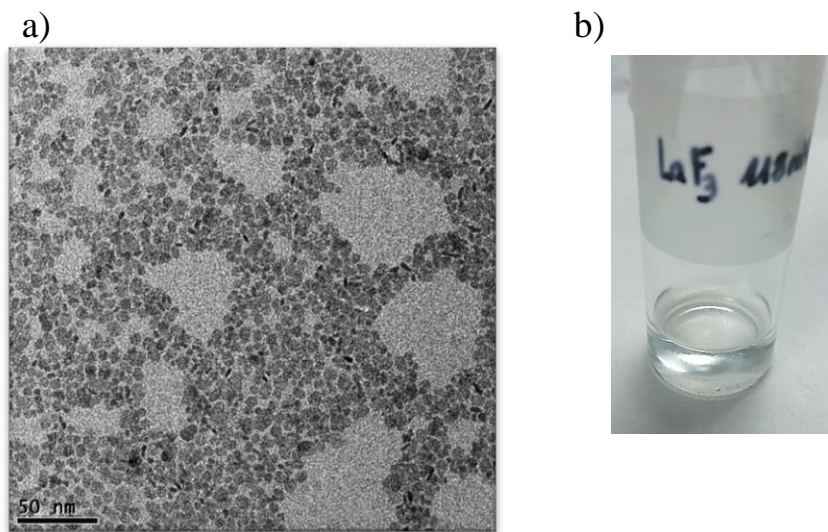
a)   b)

FIGURE 2.7: a) TEM image of LaF$_3$ as synthesized and b) picture of the transparent
coloidal solution.

any discernable change in the solutions properties. Therefore, the concentration of YBCO can remain constant while changing the concentration of nanoparticles as desired as long as the volume of nanoparticles solution required is equal or lower than the volume of the mother solution.

The solution of 12nm BaZrO$_3$ was first mixed with YBCO precursor solution with immediate precipitation of nanoparticles. As shown in Fig.2.8 b), the solution became turbid. 12 hours after mixing both solutions, shown in picture number 2, a white precipitate was deposited at the bottom of the flask. Nonetheless, the nanoparticles redissolved completely 2 days after the mixing. In order to solve this problem, N. Chamorro performed a study on different times of an extra-centrifugation step after synthesis and re-dispersion. As can be observed in Fig.2.8 a), the DLS measurement without any extra-centrifuge shows two size families, indicating some aggregation of the synthesized particles. By the extra centrifuging step, the aggregated particles, which show a very big DLS radius, are eliminated. The process was optimized to 20 minutes, preventing any precipitation when mixing with YBCO solution. When BaZrO$_3$ of smaller size (4nm) were used, as well with the BaHfO$_3$ nanoparticles, the extra-centrifugation step was also performed, enabling the obtention of YBCO precursor solutions with homogeneously dispersed nanoparticles stable for several weeks.
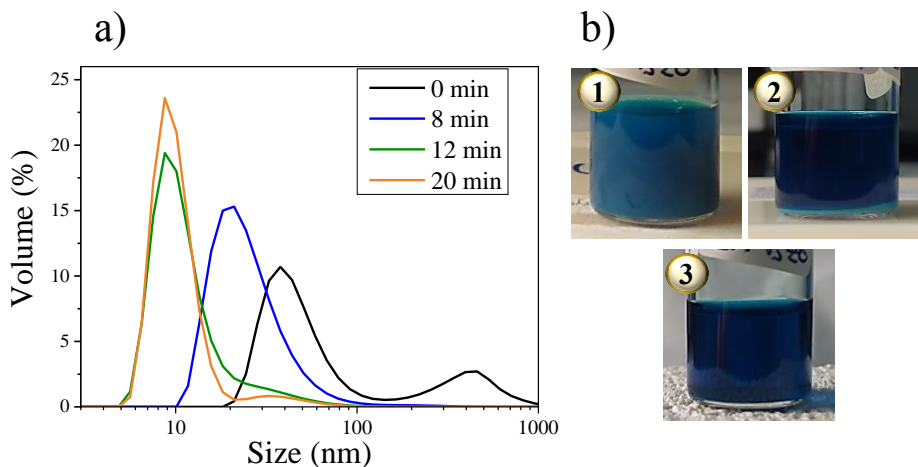
FIGURE 2.8: a) DLS measurements of BaZrO$_3$ solutions after different times of extra-centrifugation b) Pictures of YBCO solution mixed with BaZrO$_3$ after 1: immediately after mixing, 2:12 hours after mixing, and 3: 2 days after mixing

FIGURE 2.9: Image of a YBCO precursor solution with a 12% molar LaF$_3$ nanoparticles content.

In the case of LaF$_3$ the stabilization of the nanoparticles in the YBCO solution was very straight-forward. The mother solution was mixed with the colloidal solution and the remaining volume of methanol, obtaining completely stable solutions, such as the one shown in Fig.2.9.

2.1.4   Deposition

After an appropriate precursor solution has been obtained, it needs to be uniformly distributed on top of a substrate in the shape of a film, in order to start the crystallization process. There are several methods to obtain the deposited

solution; to study the process in a small scale we choose to deposit our films on single crystal substrates, and therefore we use the spin-coating technique, inexpensive and effective in obtaining homogeneous depositions.

Spin coating

This technique consists of depositing an excess of solution on top of a substrate and creating a flat film through rotation of this substrate, as the scheme shows in Fig.2.10. It has the advantage of being inexpensive and simple, and it has been widely used specially with small single crystal substrates [69]. The thickness of the obtained films (h) depends on the rheological characteristics of the deposited solution, and can be calculated as:

$$h = \frac{c}{2\omega\rho_s}\left(\frac{3\eta\rho_l}{t}\right)^{1/2} \tag{2.2}$$

where c is the mass concentration, ρ the density of solid and liquid phases and η is the viscosity, while ω and t are parameters of the spin coating such as angular velocity and time of spinning [70]. The solution is dispensed manually with a syringe, ensuring full coverage of the substrate, and the rotation is started through a fast ramping stage until reaching the final velocity, typically in the range of thousands of rpm.
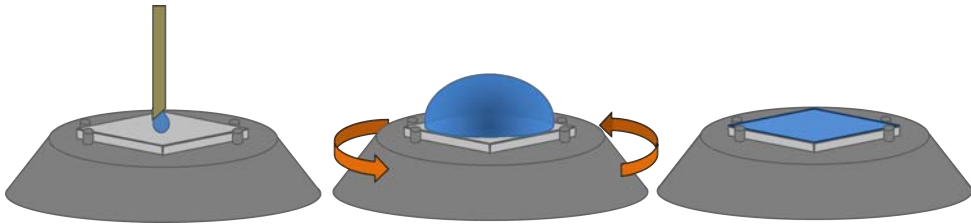

FIGURE 2.10: Schematic drawing of the spin-coating process.

After a holding time adequate to reach a uniform film, the spinning is stopped. Parameters such as rotation speed, ramping time and holding time will influence final film thickness and homogeneity. Two processes create the thinning of the film: fluid flow and solvent evaporation. During the first seconds the thinning will be governed by fluid flow, which will eliminate solution through centripetal force. Afterwards, solvent evaporation will be the major source of film thinning. Since the physics of fluid flow favours coating homogeneity, the final result is a flat uniform dense film. Usually the edges of the film have a higher thickness due to surface tension, which makes more difficult the de-attachment of the liquid from the boundaries. Other defects that can occur during spin coating are the presence of contaminant particles, both

airborne or present in the coating solution, which will create a flow defect and therefore film inhomogeneity surrounding the particle. This kind of defect is called comet, and to avoid it all coating solutions are filtered before depositions with a 0.22μm filter. Other possible defects are the so-called striations, which are radial thickness undulations, created by surface tension inhomogeneities during solvent evaporation. The presence of these inhomogeneities will depend on the used solvent.
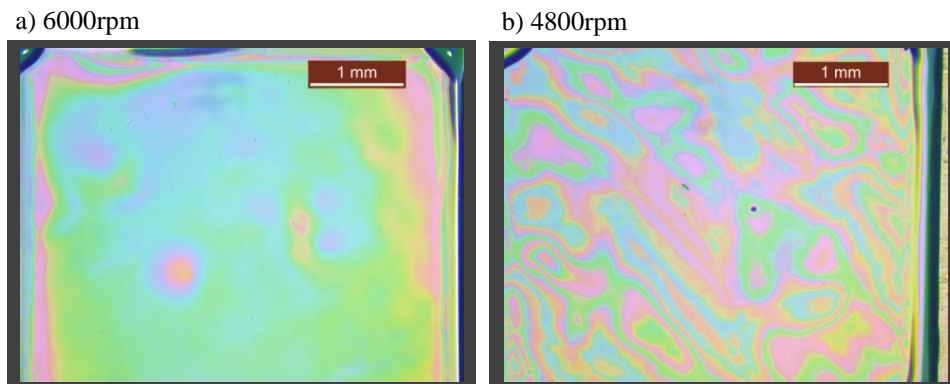
a) 6000rpm   b) 4800rpm

FIGURE 2.11: Optical microscopy images of as-deposited films obtained with different rotating speeds, (a)6000rpm and (b)4800rpm.

The experimental parameters chosen to obtain our films were to deposit 15μl of YBCO precursor solution with a syringe on top of the substrates. The spinning conditions were: ramping up with 1 second to 6000rpm and a holding time of 2 minutes. After the spinning process was completed, the sample was placed on a hot plate during 2 more minutes at 70ºC to ensure complete solvent evaporation. This whole process was done under a nitrogen atmosphere ensuring a humidity level below 10%, in order to avoid the incorporation of water in our films, detrimental for the pyrolysis step. Fig.2.11 shows optical microscope images of films deposited with different spinning velocity. With the rheological characteristics of our solutions, with viscosity ranging between 6 and 8mPa·s and contact angles of 10-12º, this velocity is a relevant parameter to obtain homogeneous depositions. The film deposited at 4800rpm presents thickness inhomogeneities which are avoided when a higher spinning velocity of 6000rpm is used.

Deposition homogeneity and thickness is highly related to solution rheological characteristics. In this work, the proportion between methanol and propionic acid were optimized to obtain homogeneous films. Solutions with 100% of methanol gave rise to inhomogeneous films, while high percentage of propionic acid decreased the thickness of the films. Therefore the use of

different solvents is a useful way to avoid defects such as striations while maintaining acceptable thicknesses.

The same procedure was used for both pristine YBCO precursor solutions and solutions with pre-formed nanoparticles. No differences were observed during the deposition step.

Single crystal substrates

Epitaxial growth of thin film relies on a low mismatch between lattice parameters of the substrate and the grown layer. Therefore it is important to choose a substrate that has the desired cell parameters and, furthermore, has a flat surface, a good wettability with the coating solution and small thermal expansion coefficient. Commercially available single crystal substrates are good candidates for small-scale investigations due to their high crystalline quality, very small roughness (<0.1nm), and commercial availability. In this thesis two different substrates were acquired from Crystech, $SrTiO_3$ (STO) and the double perovskite $(LaAlO_3)_{0.3}(Sr_2AlTaO_6)_{0.7}$ (LSAT). Mismatch is calculated through the equation:

$$\varepsilon = \frac{a_{substrate} - a_{film}}{a_{film}} \tag{2.3}$$

Taking into account literature references for YBCO of a=3.85Å, the calculated mismatch is presented in table 2.1. These small mismatch values will allow us to grow epitaxially aligned YBCO.

	Structure	a-parameter (Å)	mismatch (%)
STO	cubic	3.905	1.56
LSAT	cubic	3.86	0.26

TABLE 2.1: Lattice parameter and mismatch with YBCO of different substrates.

In order to ensure atomically flat terraces on the surface, before use, the substrates were subjected to a standard thermal treatment at 900ºC during 5 hours under a flow of 0.5l/min of pure oxygen [71].

2.2 Pyrolysis process

After deposition of the precursor solution through spin coating techniques, we obtain a dried gel film consisting of an inorganic network bound to organic
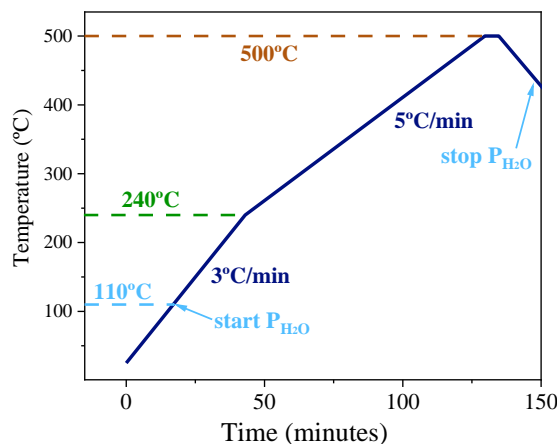
FIGURE 2.12: Schematic representation of the pyrolysis profile used for pristine TLAG films.

groups and with solvent molecules entrapped in the structure. Before crystallization of the final film, an intermediate step is necessary to eliminate all the organic components of the sample. This process is called pyrolysis, defined as the decomposition of organic compounds through calcination at medium temperatures and under a controlled atmosphere. During pyrolysis the dried gel film will convert to an amorphous matrix or a film with nanocrystalline phases. The film will also suffer a major shrinkage due to the elimination of the organic compounds into volatile species. Many factors will influence this decomposition, such as solution formulation, film thickness, atmosphere, heating ramp and organic components composition.

The necessary profile for complete decomposition of organic molecules in our films is shown in Fig.2.12. This profile has been established after careful analysis of thermal decomposition analysis (TGA) and in-situ FT-IR performed in Alba synchrotron [62]. An atmosphere of oxygen is used and H_2O pressure of P_{H_2O}=7mbar is added above 110ºC to prevent sublimation of copper propionate and remaining of copper acetate present in solution. Different heating ramps are designed to avoid very fast film shrinkage, which would create cracking and buckling of the film. After the pyrolysis treatment is completed, Y and Cu have decomposed to their corresponding oxides Y_2O_3 and CuO, while in the case of barium, the stable compound is $BaCO_3$. This product is stable in a wide range of temperatures and in order to form YBCO we will need to decompose it in the following treatment, assuring that no carbon contamination is left in the samples. The presence of $BaCO_3$ was thought to be an impediment for the formation of YBCO due to the difficulty to eliminate
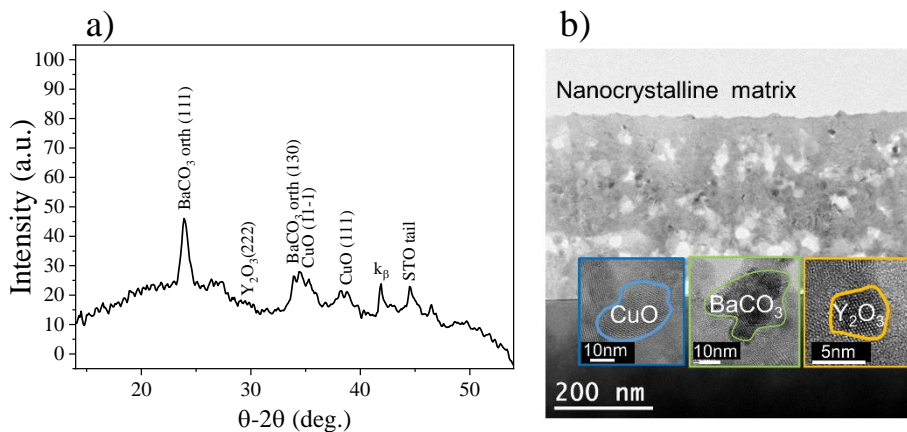
FIGURE 2.13: (a)θ-2θ X-ray diffraction pattern integrated from a 2D XRD image in a tilted substrate configuration of a pyrolysed film. (b)TEM images of a pyrolysed pristine film.

it, which lead to the development of techniques that avoided this compound such as the trifluoroacetates route, which has become the most used technique to grow YBCO from CSD methods. In the following sections we will demonstrate how transient liquid assisted growth is capable of decomposing $BaCO_3$ effectively. The final products of pyrolysis are identified by X-ray diffraction as shown in Fig.2.13 a). The X-ray diffraction patterns of pyrolysed films are obtained in a tilted substrate configuration, where ω is kept out of Bragg configuration in order to eliminate the epitaxial peaks of the substrate and avoid their overlapping with the polycrystalline peaks from the film.

We observe the presence of polycrystalline CuO and $BaCO_3$, while Y_2O_3 is harder to identify due to its small particle size. Fig.2.13 b) shows a TEM image of a pyrolysed film with details on the three components of the film. All three compounds present small grains sizes in the tenths of nanometers range. An important factor to take into account is the structure of $BaCO_3$. Two different structures, orthorhombic and monoclinic, are stable at this temperature range. The studies on barium carbonate elimination have shown how the monoclinic phase converts to orthorhombic $BaCO_3$ before decomposition can occur, and therefore orthorhombic BCO is preferred due to its simplified elimination. More details on this reaction will be given in the following section. Different conditions need to be controlled in order to avoid the presence of monoclinic $BaCO_3$, such as keeping water content in the precursor solution below 6% and using an atmosphere of wet oxygen during pyrolysis.

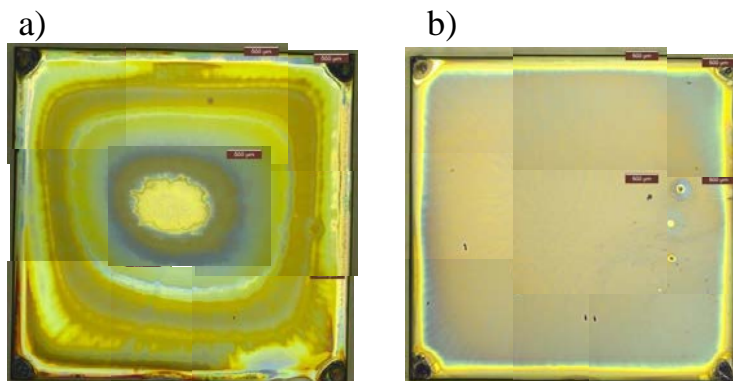### 2.2.1 Pyrolysis of BaZrO₃ and BaHfO₃ nanocomposite films.

FIGURE 2.14: Optical microscope images of films with 12%BaZrO$_3$, (a) With 5% of TEA added in the solution (b) Without additives.

When introducing pre-formed nanoparticles to our films, the pyrolysis step needs to be investigated to ensure that no undesired effects occur. Ideally, the nanoparticles, which are metal oxides, should remain inert during the process and maintain an homogeneous distribution in the final film, while their stabilization layer composed of triethileneglycol decomposes together with the other organic components. Nonetheless, inhomogeneities can take place due to the difference in solution, as well as aggregation or coarsening of the nanoparticles. Due to the similarity between BaZrO$_3$ and BaHfO$_3$, their pyrolysis process can be analysed simultaneously. Optical microscopy images after pyrolysis of a YBCO precursor solution with 12% molar of BaZrO$_3$ reveal a clear inhomogeneity of the films, as shown in Fig.2.14 a).

An optimization of the precursor solution was performed and the best results were obtained when the additive TEA was eliminated, as shown in Fig.2.14 b). The interaction of TEA in combination with the nanoparticles colloidal solution creates striations and changes in thickness, and therefore all the nanocomposite films were synthesized without its addition.

The crystalline phases present in the homogeneous pyrolysed films were analysed through X-ray diffraction. In order to eliminate the Bragg peaks of the substrate from the spectra and avoid their overlapping with the polycrystalline peaks from the film, the X-ray pattern was obtained with a tilted substrate. In Fig.2.15 we identify the desired YBCO precursors: orthorhombic BaCO$_3$, CuO and Y$_2$O$_3$. However, the two peaks corresponding to BaZrO$_3$ are not detected. The film shown in Fig.2.15 corresponds to a sample with three layers of pyrolysis of a solution with 24%BaZrO$_3$ of 12nm in diameter. This film was done in order to maximize the signal from the nanoparticles
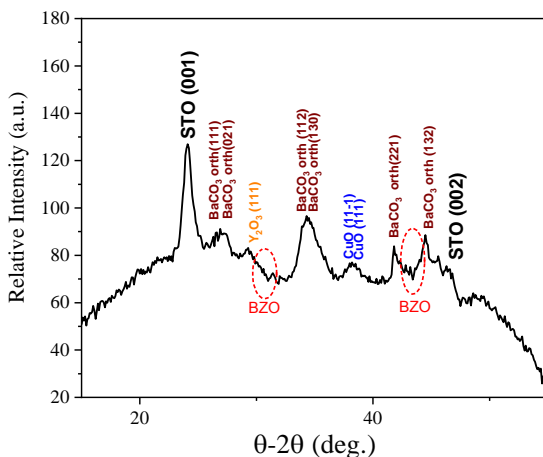
FIGURE 2.15: Integrated θ-2θ XRD from 2D GADDS of a 3 layers pyrolysed film with 24%BaZrO$_3$ of 12nm in diameter obtained with a tilted substrate configuration.

phase, yet they correspond to a concentration of 0.24M in the solution of 1M YBCO, which in comparison will be 0.5M in Y$_2$O$_3$ or 3M in CuO. The size of the particles can also be an impediment to the intensity of their diffraction peak, according to Scherrer's equation, which indicates that smaller crystallite sizes will have a broader diffraction peak and therefore a lower intensity for the same diffracting volume.

To further investigate the presence of crystalline BaZrO$_3$ nanoparticles, a pyrolysed nanocomposite film was analysed through electron energy loss spectroscopy (STEM-EELS), in collaboration with Dr. Roger Guzmán from SUMAN group. The results are shown in Fig.2.16. There is a homogeneous distribution of the precursor phases observed by XRD, although in the case of CuO, the particle size increases near the substrate. The signal for zirconium confirms the presence of BaZrO$_3$ nanoparticles of 8-12nm in diameter also homogeneously distributed thorough the film. The film morphology is very compact with no observable pores.

This measurement proves that the nanoparticles have not aggregated or dissolved during the pyrolysis process, showing a film suitable for growth of crystalline nanocomposites. However, the crystallinity of these particles could not be confirmed. It is possible that the small size and random distribution of the nanoparticles does not provide enough diffraction volume in order to be detected by our XRD scans. Another possibility is the partial amorphisation of the nanoparticles. Depending on the organic ligands and solution characteristics, the surface of the nanoparticles might be greatly affected [72]. Thus, the ligands and solution might have altered the nanoparticles surface
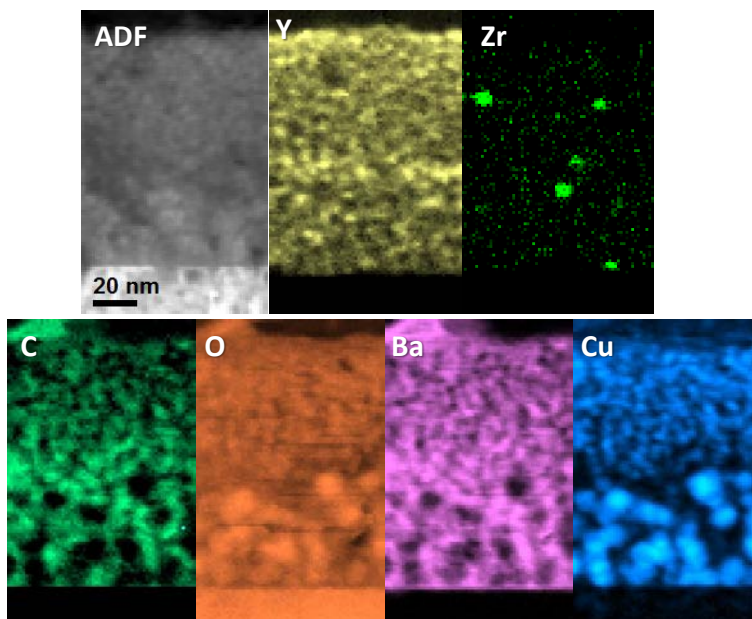
FIGURE 2.16: Annular dark-field STEM image and EELS spectroscopy for different elements of a 12%BaZrO$_3$ single layer pyrolysis.

previously to deposition, affecting the outcome of XRD analysis after pyrolysis. This effects should be confirmed by further studies of different ligands and solutions of nanoparticles. Their crystallinity will be further investigated in the chapters devoted to studying the growth of these films. The pyrolysis of films with BaHfO$_3$ nanoparticles gave very similar results than the ones presented above and therefore are also useful for the following crystallization steps.

2.2.2 Pyrolysis with LaF$_3$ nanocomposite films

The standard pyrolysis treatment presented in Fig.2.12 was performed on films containing 12% molar LaF$_3$ nanoparticles. As shown in Fig.2.17 a) the obtained YBCO precursor phases after pyrolysis are the same as in pristine films. In this case, the presence of crystalline LaF$_3$ was also confirmed. Fig.2.17 b) shows the homogeneous deposition and pyrolysis of these films.

A LaF$_3$ pyrolysed sample was also analysed through STEM-EELS spectroscopy. The images shown in Fig.2.18 display a quite compact structure with some pores. All the elements are homogeneously distributed and CuO shows the biggest grain size with diameters ranging from 20 to 30nm approximately. Lanthanum corresponding to the nanoparticles is also detected, with
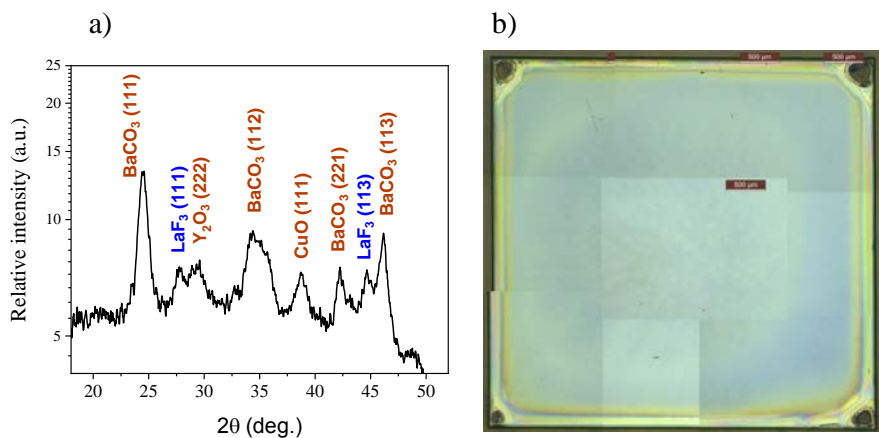
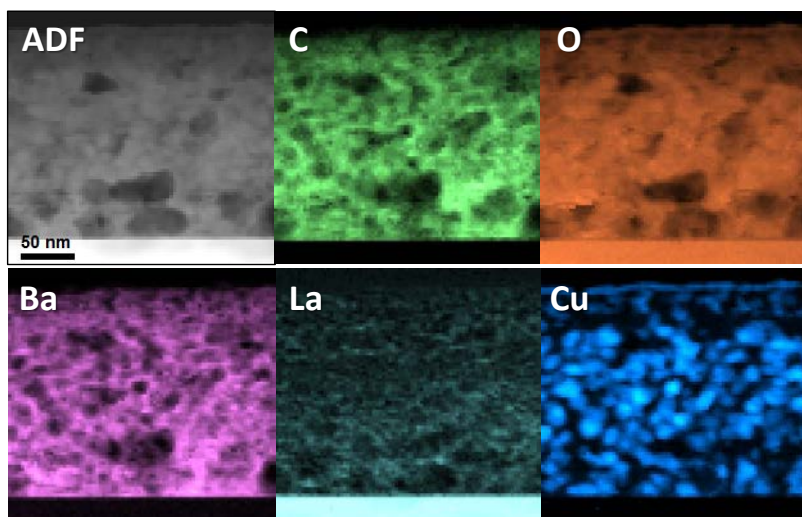FIGURE 2.17: (a) XRD pattern and (b) an optical microscope image of a 12%molar-LaF$_3$ pyrolysed film.

FIGURE 2.18: Annular dark-field STEM image and EELS spectroscopy for different elements of a 12% molLaF$_3$ single layer pyrolysis.

a homogeneous distribution along the film, although individual particles cannot be observed, probably due to their small size in the limit of EELS detector resolution. LaF$_3$ nanoparticles fulfil all the requirements at the pyrolysis stage to be able to continue to growth experiments.

2.3 YBCO crystallization techniques

In order to understand the crystallization of YBCO thin films we need to introduce basic concepts of nucleation and growth of crystalline films which will then be applied to the specific case of transient liquid assisted growth. In the sections devoted to solution preparation and the pyrolysis step we have explained the details concerning pristine and nanocomposite films. In this section we will explain the theory, experimental details and some experiments only on pristine films. The growth of nanocomposites will be analysed in detail in the next two chapters which constitute the main result body of this thesis.

2.3.1 Nucleation and crystal growth

YBCO is a crystalline material, thus, we rely on the process of crystallization to obtain our final films. As in any chemical transformation, there must be a decrease in Gibbs free energy which makes the reaction favourable. In the case of crystallization, the process relies on the higher stability (lower Gibbs free energy) of the crystalline phase with respect to the amorphous (liquid or solid) precursor phase. The specific conditions in which the formation of the crystalline phase may occur depend on each material and will be discussed later on, but the mechanisms and driving force for this process can be understood independently from the conditions. Crystallization can be divided in two major steps: nucleation and growth.

Nucleation

Nucleation is the process of forming small initial crystals from a solution or other precursor phases. The difference in Gibbs free energy between a system with no aggregates to a system with nucleated aggregates can be defined as:

$$\Delta G = G_2 - G_1 = ((M - n)\mu_1 + n\mu_2 + S(n)\gamma) - M\mu_1 \tag{2.4}$$

with the term $S(n)\gamma$ being the product of surface area $S(n)$ and specific surface energy γ. The equation can be expressed as:

$$\Delta G = -n\Delta\mu + S(n)\gamma \tag{2.5}$$

where μ is the chemical potential, M is the number of monomers in the initial state and n the number of aggregates of a new phase [73]. Therefore, the process of producing new aggregates of a new phase, i.e. the nucleation process, will be favourable when $\Delta\mu$ >0. This therm is the so-called supersaturation, the difference between chemical potentials of the old and the new

phase, and is the driving force for the formation of nuclei. In the case of nucleation from solutions, the chemical potential is related to the ionic activity and thus the concentration of the solutes, and therefore can be expressed as:

$$\Delta\mu = kTln\frac{C_\delta}{C_{eq}} \qquad (2.6)$$

where C_δ is the actual concentration of the solute in solution and C_{eq} is the equilibrium concentration. It can be deduced from this expression that the bigger the difference between solute concentration and equilibrium concentration, the higher the supersaturation will be and therefore the driving force for nucleation will be increased. It has to be taken into account that a certain barrier, the activation energy, needs to be overcome in order to have stable nuclei. In a nucleation process, this energy barrier is related to the size of the clusters, considering that, as can be seen in equation 2.5, the surface energy of the aggregates works against the formation of nuclei. Smaller clusters will tend to dissolve while only the clusters that surpass a certain critical radius will become stable and continue growing [74]. Critical radius r* is described as:

$$r^* = \frac{2\gamma V_M}{\Delta\mu} \qquad (2.7)$$

where V_M is the molar volume of the crystal. Through this equation we can recognize how an increase in supersaturation will decrease the required size to form stable nuclei, the critical radius, thus increasing the nucleation rate. This results in a metastable zone above the solubility line, which is the thermodynamic equilibrium boundary of solubility. Above this line, $\Delta\mu>0$, as shown in Fig.2.19, indicating that nucleation is thermodynamically favourable. However, in the yellow area where $\Delta\mu$ is small but positive, the precursor phase is kinetically stable, since the formation of new nuclei is prevented by the activation energy. This results in a so-called induction time, the mean time for nucleation to occur. This kinetic barrier can have very high values, such as one nucleation event per year, at very low supersaturation. As can be seen in the graph, when increasing supersaturation there is a steep increase in the nucleation rate when activation energy decreases, and in a very narrow window the induction time is reduced to zero. In this sense, it is evidenced how supersaturation is strongly governing nucleation, and how small changes in the processing conditions that affect supersaturation can drastically change nucleation rate.

In this sense, nucleation rate is also strongly influenced by temperature. On one hand, increasing temperature increases solubility, and therefore for a given concentration, it will decrease supersaturation. On the other hand,
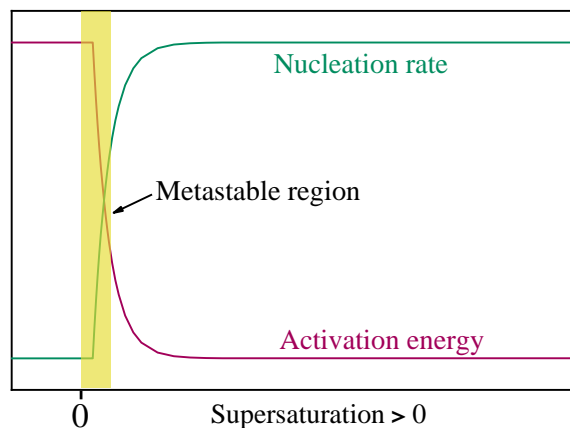
FIGURE 2.19: Schematic representation of nucleation rate and activation energy with increasing supersaturation. Marked in yellow is the kinetically induced metastable region.

atomic mobility, related to diffusion, will increase with increasing temperature, and a good atomic diffusion in solution is needed in order to create nucleation events. These two opposing factors are exemplified in the dependence of nucleation rate and induction time with temperature, as shown in Fig.2.20. It can be seen that any given system will have a maximum of nucleation rate between the region where diffusion is small and a region at high temperatures where supersaturation is too low, and interfacial free energy, related to activation energy, will change the nucleation rate values as well.
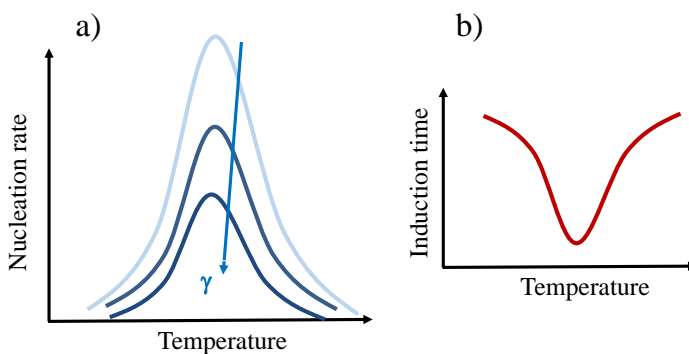

FIGURE 2.20: (a) Nucleation rate dependence with temperature at different interfacial energies, γ. (b) Induction time dependence with temperature. Adapted from [75].

Besides the factors that affect nucleation rate, we need to discuss the possible crystalline orientations, since the growth of epitaxial films is necessary

for the applications of YBCO. Nucleation can be classified in two different types depending on the orientation of crystals: homogeneous nucleation or heterogeneous nucleation. The formation of crystals at the substrate surface, following a given epitaxial orientation, is the so-called heterogeneous nucleation. This type of nucleation has a lower surface energy and therefore is thermodynamically more stable than homogeneous nucleation. Nonetheless, when supersaturation is very high and therefore the driving force for nucleation is also large, homogeneous nucleation away from the growing interface may occur, leading to many crystals with no specific orientation. Therefore, heterogeneous nucleation is favoured at low supersaturation values, where there is a lower nucleation rate. In the growth of thin films, epitaxial orientation is also favoured by using low mismatch substrates. In the case of complex oxides such as cuprates, different epitaxial orientations are possible, which increases the complexity of the system. Once more, the control of supersaturation will be crucial to avoid the undesired homogeneous nucleation or other undesired epitaxial orientations, which will be discussed in the next subsection.

Crystal growth

After nucleation has occurred, the next step in obtaining a crystallized film is the continuing growth of these nuclei. The driving force for crystal growth is as well supersaturation; if supersaturation is low enough for heterogeneous nucleation, three different mechanisms can take place for growing a crystal [73].
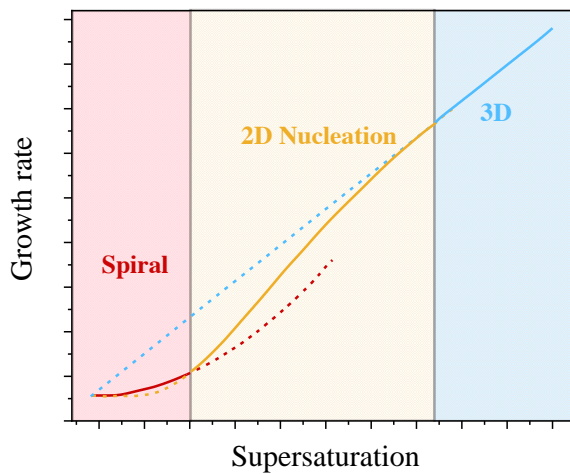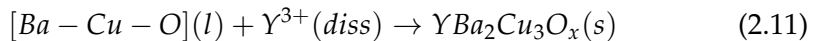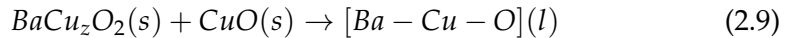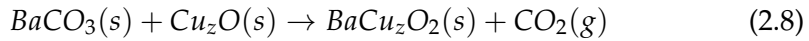

FIGURE 2.21: Growth rate versus supersaturation of the three possible crystal growth mechanisms. Filled lines represent the dominant mechanism. Adapted from [73].

Fig.2.21 shows the growth rate of the three possible mechanisms, a continuous line marking the range in which they are the dominant ones. At very low supersaturation, the very low driving force will only allow growth at screw dislocations positions, created by defects in the substrate or the nucleation, which will result in spiral growth around these dislocations. In a medium range supersaturation, the most common mechanism is observed, in which there's enough energy to create a new layer on top of the already grown crystal. Once a new layer is nucleated, it will grow until completion and then the process will repeat itself. Therefore, this growth mechanism is called 2D nucleation. On the higher supersaturation range, the mechanism that presents the highest growth rate will occur, which is called 3D or normal growth and involves growth in the three possible crystallographic directions. These three regimes also depend on the substrate used. In particular, depending on the surface energy of the substrate and that of the nuclei surfaces, a 2D or a 3D nucleation is favoured [76].

2.3.2 Reactions and concepts of TLAG

Transient liquid assisted growth is a novel methodology that exploits the presence of an eutectic liquid in the BaO-CuO system in order to crystallize YBCO from the yttrium supersaturated liquid in a region of the phase diagram where YBCO is the stable phase. Hence, nucleation occurs in the Ba-Cu liquid where Y_2O_3 dissolves and the driving force is the supersaturation of yttrium in the liquid. Since the starting point is a nanocrystalline matrix with Y_2O_3, CuO and $BaCO_3$, several reactions and processes must occur in order to reach the final epitaxial film. Furthermore, different processing routes can carry out these reactions in different ways. Nonetheless, we can understand the process as a series of reactions starting from the pyrolysis precursors:

$$BaCO_3(s) + Cu_zO(s) \rightarrow BaCu_zO_2(s) + CO_2(g) \tag{2.8}$$

$$BaCu_zO_2(s) + CuO(s) \rightarrow [Ba - Cu - O](l) \tag{2.9}$$

$$Y_2O_3(s) \rightarrow Y^{3+}(diss) \tag{2.10}$$

$$[Ba - Cu - O](l) + Y^{3+}(diss) \rightarrow YBa_2Cu_3O_x(s) \tag{2.11}$$

In reaction 2.8 the valence state of Copper will be CuO or Cu_2O depending on the PO_2-T conditions, as well as $BaCuO_2$ which is an intermediate at higher

PO_2 while at lower PO_2, $BaCu_2O_2$ will be the obtained product. The elimination of $BaCO_3$ is crucial for the whole process and therefore we will first explain in detail this reaction, to then focus on the phase diagram of YBCO.

From an historical perspective, the liquid formed by Ba and Cu has been known for many decades, and since the discovery of high temperature superconductors in 1986, it has been exploited in different ways. Several methods grow YBCO from the equilibrium liquid, and have provided relevant knowledge to the current state of the art. Here we list some of these methods.

- **Melt textured growth**: In the case of bulk YBCO, melt-textured growth techniques rely on the incongruent melting of YBCO in Y211 particles and BaO-CuO liquid. Upon cooling, the Y211 supersaturates the Ba-Cu flux, growing YBCO large bulk textured crystals at rates of 200-800nm/s [77, 78].

- **LPE**: Liquid phase epitaxy (LPE) was developed to grow YBCO single crystals and later adapted to films. A melt of the BaO-CuO liquid is generated in a crucible and a certain amount of rare earth, usually that amount that is soluble for the particular temperature, is later supplied [79, 80]. A decrease of the temperature of the system increases supersaturation, so YBCO nucleates epitaxially in a low mismatch substrate. This method is characteristic for using very small supersaturation values.

- **HLPE**: A development of LPE is called Hybrid liquid phase epitaxy (HLPE)[81], which consists of depositing a layer of Ba and Cu with the desired liquid composition, and to this stable liquid phase deposit the rare earth element, which will diffuse to the growing interface and grow YBCO epitaxial films, displacing the liquid interface. This method is performed by pulsed laser deposition techniques.

- **RCE-DR**: More recently, RCE-DR, which stands for reactive co-evaporation and direct reaction method was developed in Corea [82]. This method uses gadolinium as the rare earth metal, which in difference of yttrium presents a stable liquid in the ternary phase diagram. The metals are deposited by CVD, and first the film is heated at a low PO_2 where the liquid phase is created, to then increase the oxygen pressure to a region where GdBCO will nucleate.

All the previously described methods rely on liquids in equilibrium, but the novelty of TLAG is working with out-of-equilibrium liquids in a process where kinetic factors dominate the occurring reactions. TLAG is also combining liquid-mediated growth with chemical solution deposition, which will

bring together the high growth rates obtained by growing through a liquid phase and the simplicity of chemical methods which are necessary for an inexpensive scaling of the process. Furthermore, it is the only technique in which the employed liquid is obtained only through kinetic factors, since the working conditions place the system in a region of the phase diagram where the equilibrium phase is YBCO. To understand the process better we will analyse the different steps of this methodology.
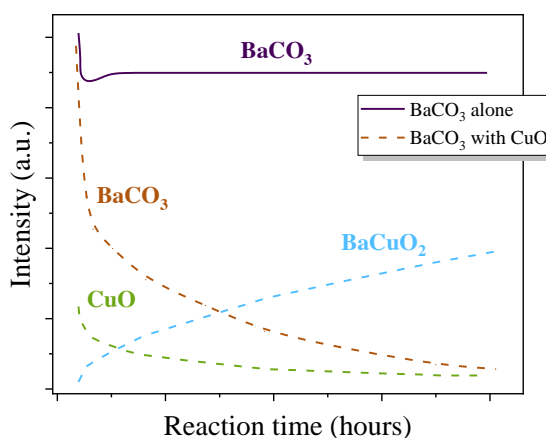
BaCO$_3$ elimination

FIGURE 2.22: Intensity from XRD patterns of different species after being heated to 950ºC with several dwell times (reaction time). Adapted from [83].

The previously introduced liquid-based methods start the synthesis from the oxides or metal of each element, deposited through different physical techniques. Using chemical solution deposition, dissolved yttrium and copper will react to form their corresponding oxides during pyrolysis, but barium will react to form barium carbonate. This is a very stable compound in a wide range of pressures and temperatures, and was initially thought to be an impediment to grow YBCO through CSD routes due to the high required temperatures for BaCO$_3$ decomposition and possible accumulation of carbon in grain boundaries, detrimental to superconducting properties [84]. Methods such as the tri-fluoro-acetate route were developed, in which the preference to form BaF$_2$ instead of BaCO$_3$ in the presence of fluorine was exploited in order to avoid the formation of barium carbonate . The reaction path to reach YBCO will be a solid-solid reaction mediated by HF gas exchange through different intermediates [85, 86]. In our case, as discussed in the section devoted to the pyrolysis step, pyrolysed films will contain BaCO$_3$.

The decomposition reaction of metal carbonates such as $BaCO_3$ is:

$$BaCO_3(s) \rightarrow BaO(s) + CO_2(g) \tag{2.12}$$
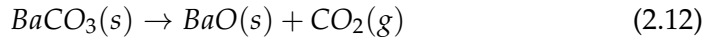
But often, a complex system might show reactions between the different components. This is the case when alkaline metals are placed together with transition elements. When decomposing $BaCO_3$ on its own to obtain BaO, the required temperature might reach 1350ºC depending on the morphology and PO_2 conditions. In the presence of CuO, the reaction 2.8 becomes possible at lower temperatures. Fig.2.22 shows the decomposition of barium carbonate with time with and without presence of CuO. The experiment by Itoh and al. [83] was performed at 900ºC. It can be observed how when CuO is present, the reaction to form $BaCuO_2$ is favourable. However, $BaCO_3$ alone doesn't decompose. This fact is key for our process since we will rely on this reaction to eliminate $BaCO_3$.

We need to take into account that when obtaining $BaCuO_2$, the study of the binary system between CuO and $BaCuO_2$ will become relevant. This system shows the presence of a liquid phase with an eutectic composition of 3(BaO):7(CuO) as has been studied extensively in literature [60, 87, 88], and as shown in Fig.2.23 for atmospheric pressure.
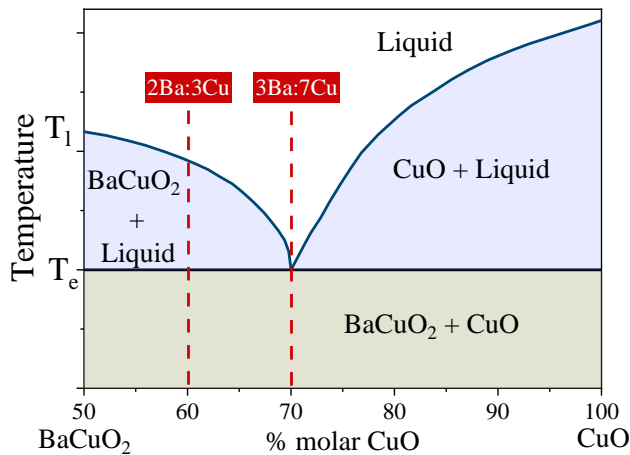

FIGURE 2.23: Phase diagram of the eutectic system between $BaCuO_2$ and CuO under atmospheric conditions. Adapted from [87].

According to the defining characteristic of eutectic systems, the melting point of the components (in this case CuO and $BaCuO_2$) is always lower when mixed, in comparison with their individual melting points. Moreover there's

a characteristic composition in which the melting occurs at a single temperature similarly to pure compounds. For all other compositions, at this temperature the melting of the components in the eutectic relationship will occur, while the component in excess will remain solid. By further increasing the temperature, all the system will become liquid, when reaching the so-called liquidus line. Such systems are common for many metals and oxides, and their properties are used in many industrial processes such as the synthesis of stainless steel.

In equilibrium conditions, the specific temperature at which the system will become liquid depends on the composition and the PO_2. In our process, we work in non-equilibrium conditions and therefore kinetic factors related to the previous elimination of $BaCO_3$ such as the heating ramp will also influence the specific conditions at which the liquid will be formed. Furthermore, we are discussing a binary case but our films contain Y_2O_3, which changes the phase diagram to a ternary diagram in which the thermodynamic stable phase in the processing conditions is YBCO. This phase diagram will be discussed in the following subsection, while we take into consideration the binary phase diagram of CuO and $BaCuO_2$ to discuss the elimination of barium carbonate.

The elimination of barium carbonate was studied via in-situ XRD experiments performed in Soleil synchrotron. Phase evolution of the samples could be followed during heating or pressure changes through fast acquisition of XRD patterns every 100ms.

First of all, in order to demonstrate the importance of barium carbonate structure, Fig.2.24 shows the evolution with temperature of two different samples, both with 3:7 Ba:Cu stoichiometry. The one in the upper panel corresponds to a pyrolysis where all of the barium carbonate has an orthorhombic structure, while the one shown on the lower panel presents a mixture between orthorhombic and monoclinic barium carbonate. When both samples are subjected to the same thermal treatment, the film containing only orthorhombic $BaCO_3$ will decompose at lower temperature, whereas the mixed composition sample will first start a reaction to convert the monoclinic $BaCO_3$ to an orthorhombic structure before the decomposition can occur. This is indicating that the necessary reaction between CuO and $BaCO_3$ only occurs when this compound presents an orthorhombic structure. Therefore, in order to not delay the elimination of barium carbonate, the pyrolysis process has been optimized to obtain films with solely orthorhombic $BaCO_3$, and all the following experiments were performed with the single composition of this compound.

Fig.2.25 shows the evolution of species present in two different films. The first sample has the YBCO stoichiometry of 1Y:2Ba:3Cu and the second corresponds to the eutectic relationship between Ba and Cu of 3:7 and a total stoichiometry of 1Y:2Ba:4.66Cu. Both films were heated at 5ºC/s under a PO_2
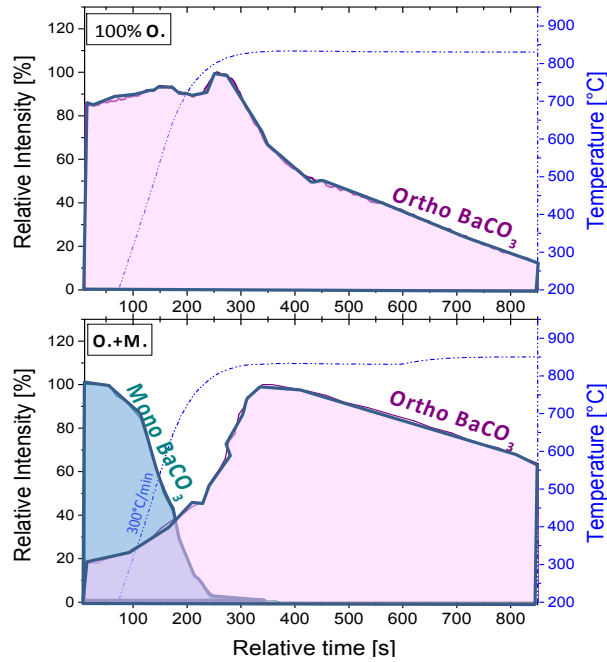
FIGURE 2.24: Species evolution as integrated from synchrotron in-situ XRD, showing their intensities through heating at $PO_2=10^{-3}$bar of a sample with only orthorhombic $BaCO_3$ and another with mixture between orthorhombic and monoclinic $BaCO_3$.

of $1 \cdot 10^{-3}$bar. Sample a) shows the formation of $BaCuO_2$(s) when CuO and $BaCO_3$ start diminishing their intensity, thus creating this intermediate phase which at 650°C starts to disappear at expenses of YBCO growth. We can also observe how barium carbonate is still reacting during the growth of YBCO, indicating that the elimination of $BaCO_3$ is the slowest reaction of the system and therefore the rate determining step.

In the case of the sample with eutectic stoichiometry in Fig.2.25 b), formation of $BaCuO_2$(s) is not observed. The diminishing of barium carbonate intensity directly leads to the formation of YBCO. Nonetheless, there is a certain delay between the onset in the elimination reaction of $BaCO_3$ and the beginning of YBCO growth, which could indicate the presence of an amorphous liquid phase, undetectable through X-ray diffraction. Furthermore, the different behaviour with respect to the formation of $BaCuO_2$ could be explained by the binary eutectic system presented in Fig.2.23. When using Ba:Cu 2:3 relationship, an excess of $BaCuO_2$ exists with respect to the eutectic composition. Therefore, above the eutectic temperature there will be solid $BaCuO_2$ until crossing the liquidus line at higher temperatures. On the other hand, when
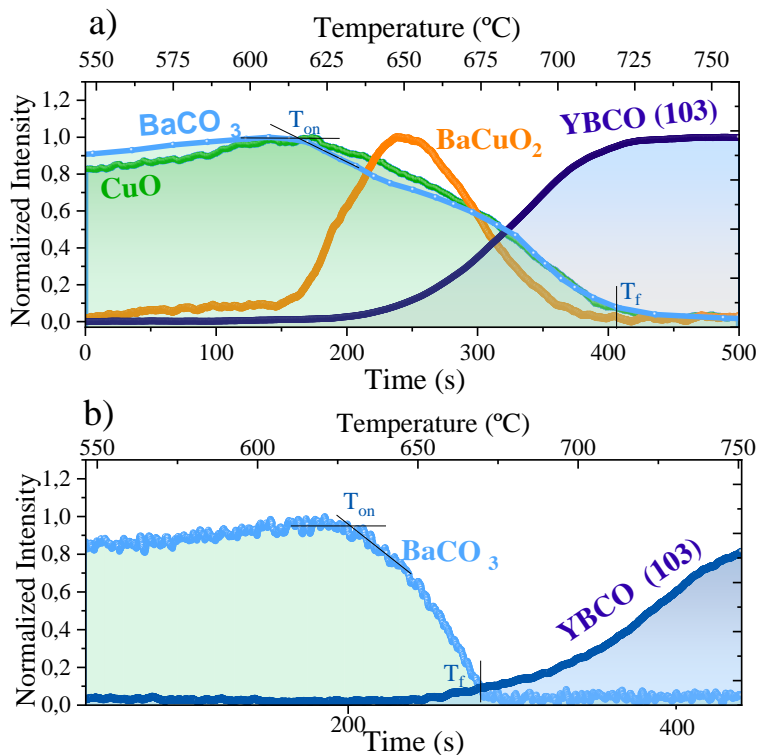
FIGURE 2.25: Species evolution as integrated from synchrotron in-situ XRD, showing their intensities through heating at $PO_2=10^{-3}$bar with Y:Ba:Cu stoichiometry of (a) 1:2:3 and (b) 1:2:4.66.

using the eutectic composition there will be no solid phases above the eutectic temperature.

The two samples with different compositions also differ on the reaction temperatures and time needed to eliminate barium carbonate. While sample a) has the onset of $BaCO_3$ decrease at 620ºC and complete elimination is reached at 720ºC, with a total reaction time of 220s, sample b) has the onset at 630ºC and is vanished at 670ºC, giving a total reaction time of 90s. Thus, the reaction is much faster when the eutectic composition is used. It is important to note that the elimination of $BaCO_3$ is completed at low temperatures for both films, making the growth of YBCO through this approach feasible since it will not be impeded by the presence of barium carbonate.
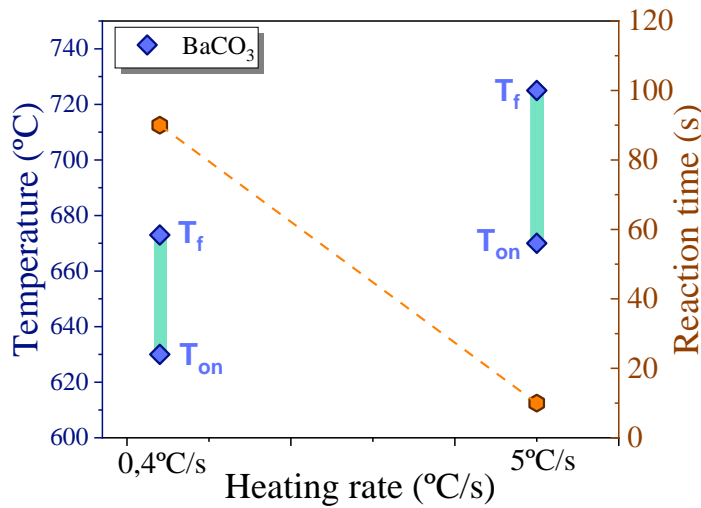
FIGURE 2.26: Data extracted from in-situ XRD, showing onset and final temperatures of $BaCO_3$ elimination for different heating ramps, as well as the different reaction times in the left y axis. Experiments performed with a 3:7 liquid composition with $PO_2=1\cdot10^{-3}$bar.

Other factors to take into account when analysing the BCO elimination are the heating ramp and the PO_2. Fig.2.26 displays the onset and final temperatures of this reaction together with the corresponding reaction times for samples of the eutectic composition grown at two different heating rates. We observe how faster heating rates delay the onset temperature. This indicates the existence of a certain induction time to start the decomposition reaction, since thermodynamically the reaction is favourable already at 630°C as shown in the 0.4°C/s heating ramp, but will start at 670°C when using 5°C/s. Nonetheless, the kinetics of the conversion are enhanced at higher temperatures and therefore the reaction time will be shortened from 90s to 10s at 5°C/s. These results show how we perform this reaction in out-of-equilibrium conditions and demonstrates the importance of kinetic factors such as heating ramp.

A similar plot can be drawn for different PO_2 conditions. In this case Fig.2.27 a) shows the onset and final temperatures of films with stoichiometric YBCO composition. This composition allows us to also investigate the different behaviour of the $BaCuO_2$ intermediate. These experiments were performed with a heating ramp of 0.4°C/s. Both the reaction time and the temperature range increase when increasing PO_2. Additionally, $BaCuO_2$ is also observed in a wider temperature range for higher PO_2 and is not detected in the experiment
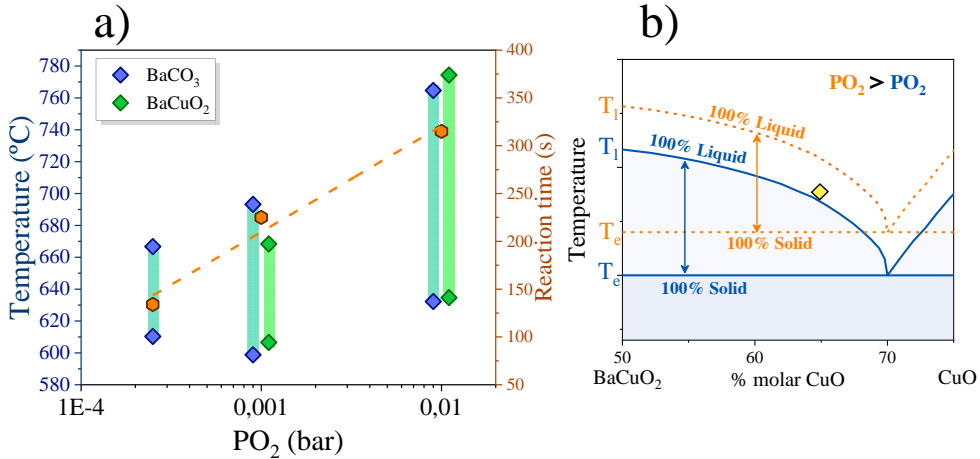
FIGURE 2.27: Onset and complete elimination temperatures for $BaCO_3$ and formation and elimination temperatures of $BaCuO_2$ at different PO_2, as well as reaction time for $BaCO_3$ elimination. Experiments performed at 0.4ºC/s with samples of 2:3 Ba:Cu stoichiometry.

performed at $2.5 \cdot 10^{-4}$bar. These observations are in accordance with the eutectic temperature evolution with PO_2 [60], as schematically shown in Fig.2.27 b). At higher PO_2, which gives a higher eutectic temperature, the system is further away from the liquidus line at a given temperature than at lower PO_2, which leads to higher fraction of solid $BaCuO_2$ when $BaCO_3$ is eliminated and a higher temperature to fully eliminate both species, i.e. a higher liquidus temperature. This is, when a sample is placed at the conditions marked by the yellow point, depending on the PO_2 it will transform to full liquid phase or it will have $BaCuO_2$ if its below the liquidus line. At lower PO_2 where the eutectic temperature is low enough, all the $BaCO_3$ is directly converted to liquid fraction and no $BaCuO_2$ is detected. This is a clear indication of how important the presence of the Ba-Cu liquid is for the kinetics of $BaCO_3$ elimination. When the liquid fraction is important, both the temperature and time of the reaction are lowered. This knowledge is essential in order to tune and understand the growth of YBCO taking into account the different steps of the process.

A different scenario is possible when PO_2 is lowered below the limit of YBCO stability. Fig.2.28 shows the phase evolution analysis of a sample with eutectic composition heated at $PO_2 = 1 \cdot 10^{-5}$bar. It can be observed how at this low oxygen pressure, the first reaction to occur is the reduction of copper from Cu^{2+} to Cu^{1+}. Afterwards, we encounter the following reaction:
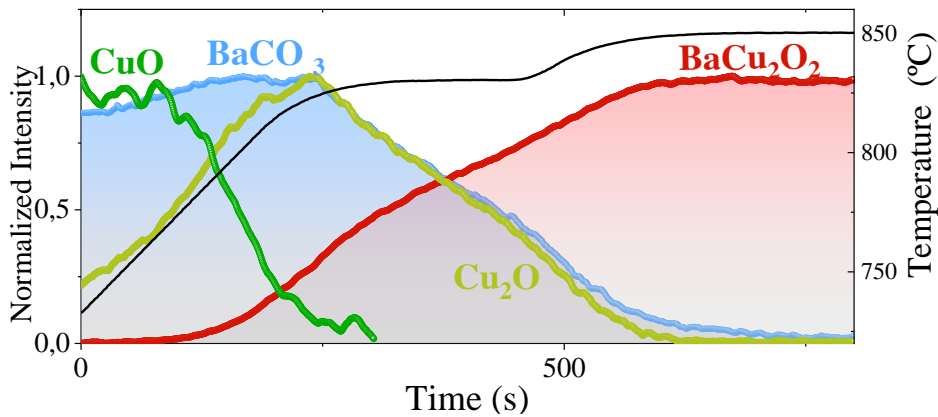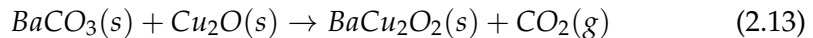
FIGURE 2.28: Species evolution for a sample heated under a PO_2 of 10^{-5}bar.

$$BaCO_3(s) + Cu_2O(s) \rightarrow BaCu_2O_2(s) + CO_2(g) \qquad (2.13)$$

which is observed in Fig.2.28. No liquid phase is detected and we are below the instability line of YBCO, and therefore, in this case, we demonstrate that it is also possible to eliminate $BaCO_3$ without the formation of YBCO, and again the reaction time is increased ($\sim$330s) when there's no liquid phase involved.

YBCO phase diagram and growth conditions

After demonstrating the successful elimination of $BaCO_3$ under different conditions and conversion to the desired intermediate phases, the next step in the process is synthesizing YBCO. We have introduced the binary phase diagram of Ba and Cu, but our system contains yttrium and therefore the phase diagram that shows the thermodynamically stable phases is shown in Fig.2.29. The straight lines show the stability region of YBCO while dashed lines display other phase changes relevant to our process, such as the eutectic line of Ba and Cu. The line between pyrolysis precursors and YBCO is not a thermodynamic stability line but the region where YBCO is first detected when heating. According to the equilibrium phase diagram, the only stable phase below the temperatures of peritectic melting and stability line, is YBCO. But the growth process of TLAG is not performed at thermodynamic equilibrium.

Kinetic factors play a dominant role, which affects the path to nucleate YBCO. When the precursor films are placed in conditions of high temperature, $BaCuO_2$, CuO and Y_2O_3 should react to form YBCO, in a solid-solid reaction. Nonetheless, the induction period to form the new stable phase from solid precursors is much higher than the reaction between $BaCuO_2$ and CuO
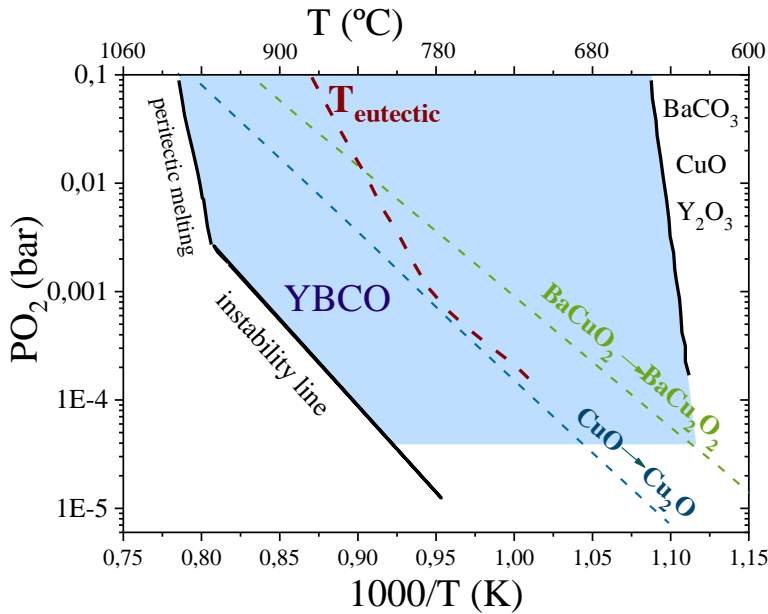
FIGURE 2.29: Phase diagram of YBCO with data obtained from [89–94], and super-imposed data from other reactions.

to form a liquid phase. Thus, the system will kinetically prefer forming a liquid, which will serve as a solvent for Y_2O_3. The dissolved yttrium will diffuse to the substrate or the growing interface where YBCO will be formed. In this way, the liquid used during growth is called transient liquid because its not thermodynamically stable and only exists due to the kinetic hindrance to solid-solid reactions. The preferred path of the system will be to nucleate YBCO from the liquid supersaturated in yttrium. The high diffusivity in the liquid is also what will allow very high growth rates.

In this scenario, the driving force for nucleation is the supersaturation of yttrium in the Ba-Cu melt. As has been previously discussed, supersaturation is the difference between the actual concentration (C_δ) and the equilibrium concentration(C_e) of the solute (in our case Y), which will depend on temperature.

Fig.2.30 shows the phase diagram with temperature of the ternary system of $BaCuO_2$:CuO 2:1 and varying Y_2O_3 composition, as adapted from [95]. Again, this diagram shows the equilibrium species, but in our case the film contains Y_2O_3 nanoparticles, originated during pyrolysis, which will be present when the Ba-Cu liquid is formed. By inferring the liquidus line of Y_2O_3+L (green dashed line), we can conclude that the maximum yttrium dissolved in the liquid will be of about 10%. On the other hand, the equilibrium concentration
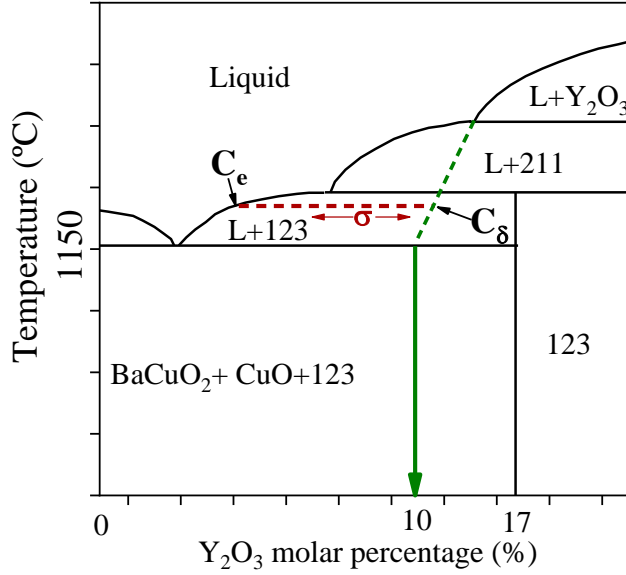
FIGURE 2.30: Phase diagram of Y_2O_3 and $BaCuO_2$+CuO, reproduced from [95] and with the Y_2O_3 liquidus line extended.

will depend on temperature and Ba-Cu composition. We can calculate the relative supersaturation as

$$\sigma = \frac{C_\delta}{C_e} - 1 \tag{2.14}$$

Fig.2.31 shows a schematic representation of the mechanism for YBCO nucleation in TLAG. After the $BaCuO_2$-CuO liquid has been formed due to kinetic factors, Y_2O_3 nanoparticles undergo three differentiated steps. First, they dissolve, creating a supersaturated solution. The dissolved yttrium atoms diffuse to the substrate or growing interface, where surface kinetics will play a role in the yttrium mobility and diffusion to the nucleation site.

All three steps have very fast kinetics. The small size of yttrium oxide and high temperatures allow a very fast dissolution. The diffusion of Y in the liquid was estimated to $4 \cdot 10^{-10} m^2/cm$ at 870ºC by Kursumovic et al.[96], which for the short distances in our thin films will make this process very fast. Instead, the surface kinetics related to the movement of yttrium atoms from the moment they attach to the surface until they become part of the YBCO crystal are expected to be slower. In summary, the three processes are fast enough to allow very fast growth rates, with the last process of surface kinetics expected to be the rate determining step.
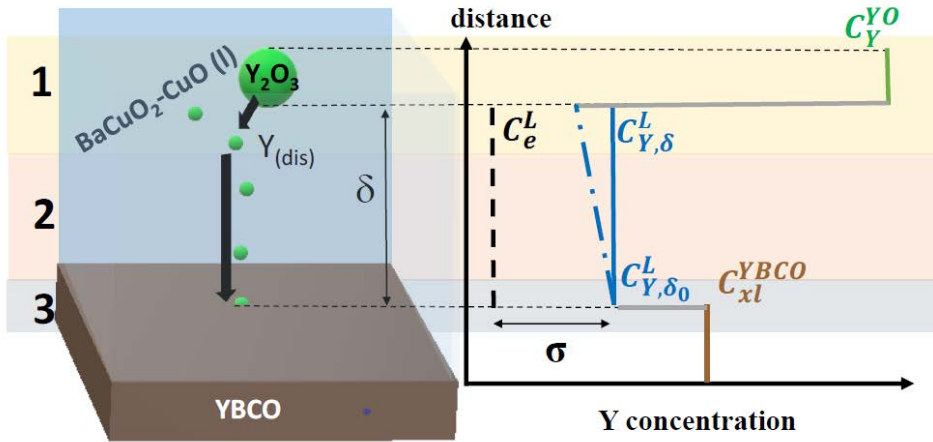
FIGURE 2.31: Schematic representation of YBCO nucleation in the Ba-Cu melt. On the right, the different concentrations of yttrium in the different steps. C_Y^{YO} is the concentration of Y in Y_2O_3. C_{Y,δ,δ_0}^L the concentration in the liquid at different distances from the substrate, C_e^L the equilibrium yttrium concentration in the liquid and C_{xl}^{YBCO} the concentration in YBCO

When YBCO nucleation occurs, we will find in our films different possible orientations. If supersaturation is too high, homogeneous nucleation is favourable and therefore randomly oriented crystals will dominate the film. In order to achieve good superconducting properties it is necessary to have a bi-axially aligned crystalline structure with the substrate. Therefore, we will tune the conditions necessary to work in a range of supersaturation that allows heterogeneous nucleation in closely matched single crystal substrates. In the case of YBCO, although the substrates are chosen to match the a/b lattice parameter to grow a c-axis aligned structure, the c-parameter can be divided in three sub-units which have a very similar length to the a/b parameter. This allows a possible epitaxial growth with the c-axis parallel to the substrate, which results in the so-called a/b oriented grains. Nucleation of a/b grains needs to be avoided due to their detrimental effect on the percolation of superconducting currents, since J_c is strongly suppressed when crossing a/b planes.

Fig.2.32 displays the Gibbs free energy of c-axis oriented and a/b oriented nucleation for different supersaturations. Higher supersaturation lowers the thermodynamic barrier to grow nuclei in any orientation, and therefore above a certain value both nucleations will co-exist. But at low supersaturation, the different surface energy of c-axis grains versus a/b grains will play a predominant role. The interfacial surface energy of c-axis orientation is lower,
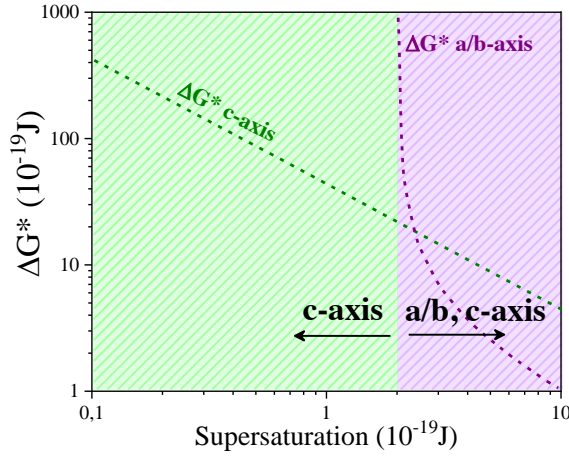
FIGURE 2.32: Gibbs free energy of different YBCO epitaxial orientations depending on supersaturation, reproduced from [97].

also changing with different substrate mismatch. Thus, the activation energy will be lower for this nucleation and the film will be predominantly c-axis.
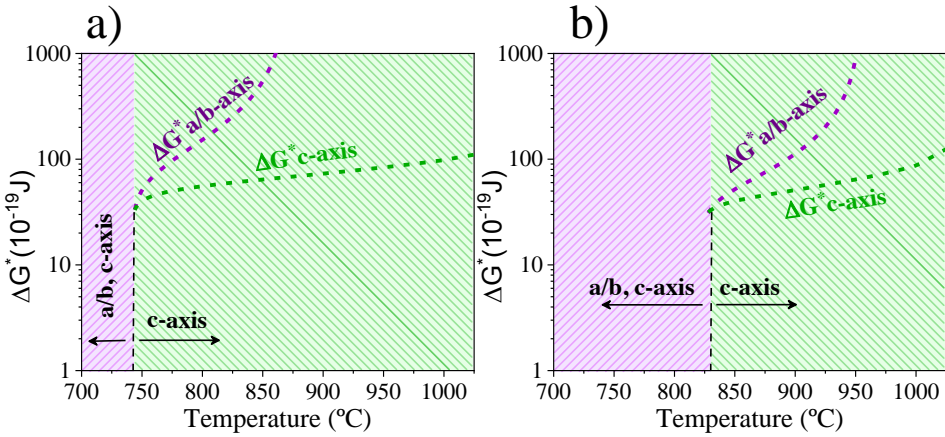

FIGURE 2.33: Gibbs free energy depending on temperature of c-axis and a/b nucleation for (a) 3:7 liquid composition and (b) 3:5 liquid composition.

Another factor which plays a role on the epitaxial orientation of the film is Ba-Cu liquid composition. When using the eutectic liquid composition, we are increasing the equilibrium concentration (C_e) of yttrium with respect to the 2-3 composition. Therefore, for the same amount of Y_2O_3 the relative supersaturation will be lower in the eutectic composition, as shown in equation

2.14. Thus, the lower supersaturation will result in a lower Gibbs free energy for c-axis nucleation. Fig.2.33 shows the Gibbs free energy barrier for nucleation of two different liquid compositions. It can be observed how the crossover between a/b and c-axis mixed nucleation to predominantly c-axis occurs at lower temperatures for lower supersaturation 3:7 composition.
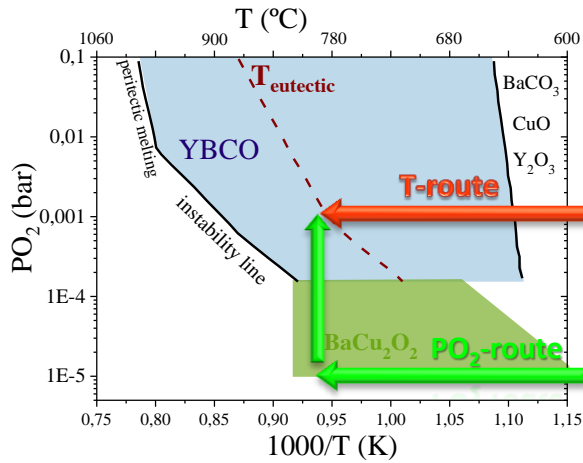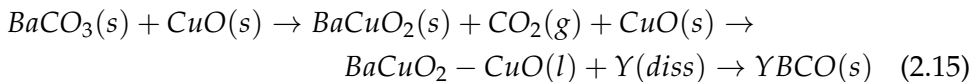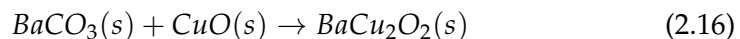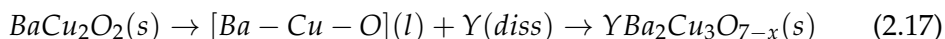

FIGURE 2.34: YBCO phase diagram with marked processing pathways to grow YBCO. In red, the conditions for temperature route. In green, the two steps necessary for the PO$_2$ route.

All the characteristics of this process also make possible two different pathways to grow YBCO, depending on the route chosen to arrive to the desired growing conditions in the phase diagram. Fig.2.34 indicates two possibilities. The first one is perhaps the most studied and intuitive, the so-called temperature-route: the sample is heated under a constant oxygen pressure until reaching the final temperature. In the PO$_2$ route, two different steps are necessary. First, the sample is heated at low oxygen pressures, where neither the Ba-Cu melt or YBCO are stable, and subsequently a fast jump in PO$_2$ is performed to arrive to the final conditions. The reactions followed in each case will be different. For T-route:

$$BaCO_3(s) + CuO(s) \rightarrow BaCuO_2(s) + CO_2(g) + CuO(s) \rightarrow$$
$$BaCuO_2 - CuO(l) + Y(diss) \rightarrow YBCO(s) \quad (2.15)$$

And in PO$_2$ route:

$$BaCO_3(s) + CuO(s) \rightarrow BaCu_2O_2(s) \quad (2.16)$$

$$BaCu_2O_2(s) \rightarrow [Ba - Cu - O](l) + Y(diss) \rightarrow YBa_2Cu_3O_{7-x}(s) \qquad (2.17)$$

More importantly, in T-route reactions take place consecutively, and due to $BaCO_3$ elimination being the rate limiting step, the growth of YBCO will occur simultaneously to the elimination. On the other hand, the PO_2-route is separated in two processing steps that disentangle the barium carbonate reaction from the YBCO growth. This route is exploiting the possibility to eliminate $BaCO_3$ in a region where YBCO is not stable and therefore the conditions will be tuned to fully decompose $BaCO_3$ before making the PO_2 step to the final growing conditions. Also, no liquid phase is stable at the PO_2 where the elimination is completed, but increasing the oxygen partial pressure will generate the liquid and, immediately after, the YBCO growth. The transient characteristic of the liquid is kept in both routes, reached as an intermediate in the same conditions where YBCO is grown. At the moment, SUMAN group is investigating the possible existence of a [Ba-Cu-O] liquid with Cu^{1+} instead of Cu^{2+} depending on the processing conditions. The experimental details and some results of each route will be presented to set the basis for later chapters on nanocomposite films.

2.3.3 Temperature route

The oven used for T-route processing is a rapid thermal annealing commercial furnace from Annealsys company.
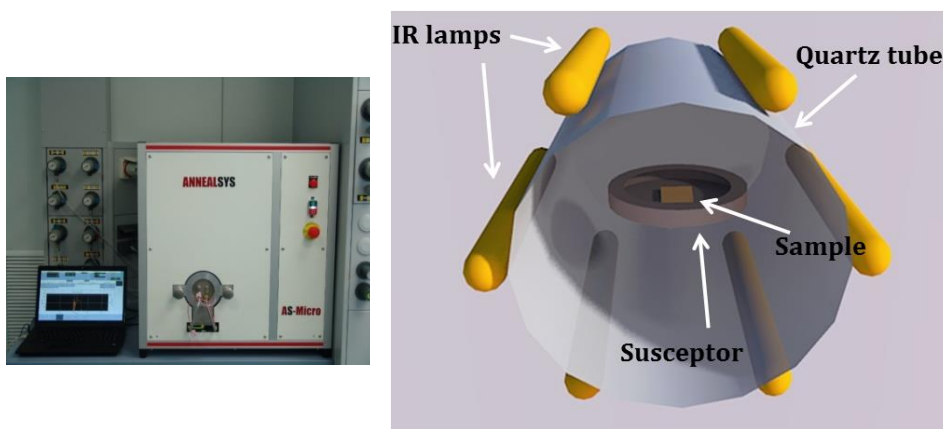

FIGURE 2.35: A picture of the rapid thermal annealing furnace located in ICMAB's clean room together with a scheme of the sample chamber.

Fig.2.35 shows a picture of the furnace located in the ICMAB's clean room facilities. It depicts as well the sample chamber of the furnace, which consists of a quartz tube surrounded by six infra-red lamps that will provide the rapid heating, and a graphite susceptor coated with silicon carbide where the sample is placed. Special power converters allow very high heating ramps with excellent control of temperature. The factor limiting the heating ramp is the SiC susceptor crack formation which allows up to 60ºC/s.

The most relevant factors that have been studied in order to obtain fully epitaxial samples with good superconducting properties are: growth temperature, PO_2, heating ramp and liquid composition. The influence of all these parameters in pristine films has been studied in detail in Soler's thesis [62], which has been running quite in parallel with this one. For the purpose of this work, we need an understanding of the factors that influence nucleation and a set of conditions in which pristine films are fully epitaxial and present good superconducting properties to provide a starting point in the study of nanocomposites. In the case of temperature route, the conditions for epitaxy depend strongly on the used liquid composition. Growth temperature was optimized for each composition in order to have a low supersaturation to favour c-axis growth, as shown in Fig.2.32 and Fig.2.33. Due to the fast kinetics of the reactions carried out to obtain YBCO, heating ramp was found to have a very relevant impact on film texture since the speed on reaching final temperature might allow for the reactions to start during heating.
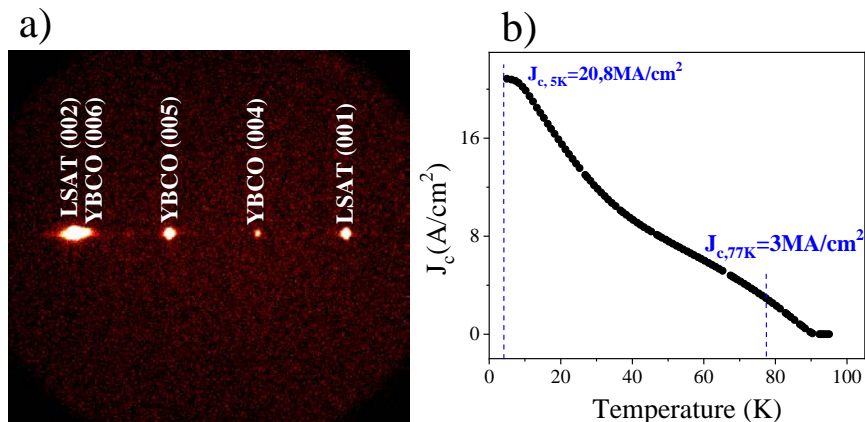

FIGURE 2.36: (a) 2D-XRD pattern of a pristine film of 2-3 liquid composition grown at 20ºC/s until 835ºC with a dwell time of 2min under a $PO_2 = 1 \cdot 10^{-2}$bar. (b) SQUID measurement of critical current density versus temperature of a YBCO pristine film grown through T-route.

Fig.2.36 a) shows a 2D X-ray scan where the epitaxial texture of YBCO can be appreciated in a YBCO film of 123 stoichiometry (2:3 liquid stoichiometry) grown on LSAT substrate in the RTA furnace at 20ºC/s to 835ºC, with a $PO_2 = 1\cdot10^{-2}$bar and 2 min dwell. These conditions were found to be reproducible and as shown in Fig.2.36 b) gave excellent superconducting properties. High growth rates were demonstrated by in-situ X-ray measurements performed in Soleil synchrotron.
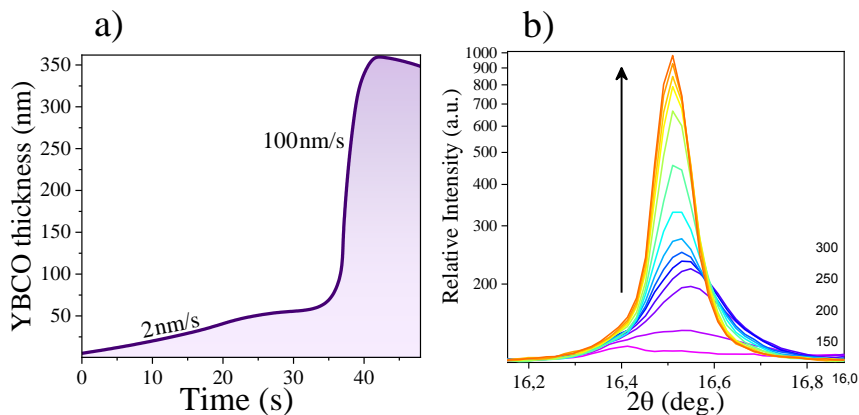

FIGURE 2.37: (a) Grown thickness of epitaxial YBCO inferred from in-situ XRD analysis of a 3-7 sample grown at 5ºC/s in a T-range between 750ºC and 860ºC and $PO_2 = 1\cdot10^{-3}$bar. (b) Peak evolution of the (005) epitaxial peak.

Fig.2.37 shows the calculated grown thickness from the YBCO (005) peak intensity during heating. It can be observed how in a first stage the growth rate is limited to 2nm/s. When higher temperatures are reached, the growth rate increases until 100nm/s, a value that shows the potential of transient liquid assisted growth as a methodology of great throughput.

Most of the efforts on developing this growth method have been dedicated to YBCO material. Nonetheless, almost all the REBCO family of compounds (except Pr123) present a superconducting phase, with different equilibrium phase diagram, T_c and irreversibility lines. Critical temperature is an intrinsic property of each material, which increases with decreasing size of the rare earth elements [98]. GdBCO has been widely studied precisely due to its high T_c which can reach up to 95K [99]. A high T_c also entails a higher critical current density at a given temperature. Therefore, using gadolinium instead of yttrium can be seen as a way to increase current densities in general due to the increase of the irreversibility line. Nonetheless, due to the smaller size of gadolinium, the stabilization of GdBCO is harder than its YBCO counterpart and usually requires higher temperatures[99].
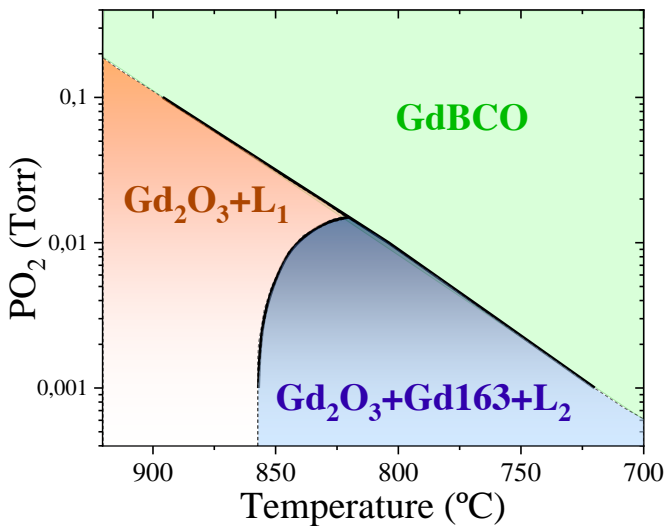
FIGURE 2.38: Phase diagram of GdBCO with temperature and oxygen partial pressure. Adapted from [100].

Further differences are found when observing the phase diagram shown in Fig.2.38. While the liquid formed between Ba and Cu oxides is not stable in the ternary phase with yttrium in most of the studied conditions, there is a region in Gd phase diagram in which the melt and Gd_2O_3 coexist. This has been exploited in the RCE-DR method developed in Corea, which crystallizes GdBCO from the liquid formed at low pressures when increasing PO_2 [82]. The peritectic melting and phase stability lines are also at higher temperatures in the case of GdBCO.

We performed a series of experiments with GdBCO and mixed Y and Gd composition in order to test the compatibility of TLAG with other rare-earth cations. The temperature route was used, growing films on top of STO substrates in the RTA furnace. This route ensures the use of the same TLAG principles for Y and Gd, since in the PO_2 route we might have to consider the stable liquids of the GdBCO phase diagram.

Fig.2.39 shows the percentage of epitaxial gadolinium phase with respect with other orientations or phases. The epitaxy percentage was estimated as: $\frac{I(005)}{I(005)+I(103)} * 100$ .The experiments were performed with $GdBa_2Cu_3O_{7-x}$ composition, $Gd_{0.5}Y_{0.5}Ba_2Cu_3O_{7-x}$ and pure yttrium samples for comparison. Fig.2.39 a) shows how both Gd and $Gd_{0.5}Y_{0.5}$ films have a strong preference for a PO_2 of 10^{-3}bar, while YBCO maintains a fully epitaxial orientation for both
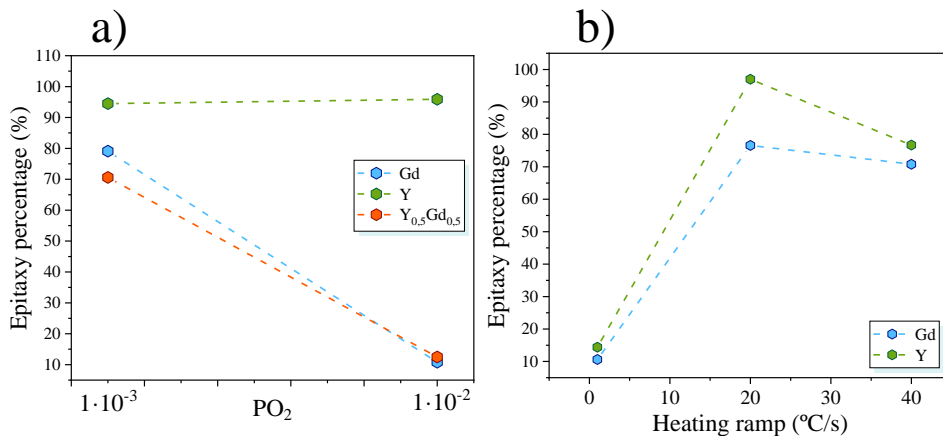
FIGURE 2.39: (a) Epitaxy percentage of films with different rare earth compositions
at different PO_2 conditions. Epitaxy percentage is inferred from XRD patterns taking
into account the intensities of all the detected phases and orientations. (b) Epitaxy
percentage of yttrium and gadolinium samples at different heating ramps.

pressures. In the case of heating ramp, a medium range speed is preferred
by both Gd and Y as observed in Fig.2.39 b). While at low heating ramps of
1°C/s random nucleation occurs, at high heating speed the presence of sec-
ondary reacting phases hinders the achievement of fully epitaxial samples.
Once the most favourable heating ramp and PO_2 conditions were chosen, a
more careful optimization of growth temperature was performed.

At 20°C/s and a $PO_2=10^{-3}$bar, a scan in temperatures from 795°C until
860°C was performed, as shown in Fig.2.40. In Fig.2.40 a) the percentage of
epitaxy can be observed for the different rare earth compositions. In this case
all the phases shown in Fig.2.40 b) were taken into account for epitaxy per-
centage calculation. We identify how YBCO reaches a fully textured film at
810°C, while the gadolinium and mixed phases are limited to a 78% of epi-
taxy in the best case-scenario. To understand this behaviour for the GdBCO
samples, Fig.2.40 b) shows the different phases and orientations competing
with epitaxial GdBCO and their presence at different growth temperatures. It
can be discerned how at 795°C the sample is mainly random GdBCO, which
decreases significantly above this temperature. Even so, there are other com-
peting phases, such as Gd211 and unidentified reactivity phases that appear
at higher temperatures. It has been investigated in the case of yttrium that the
211 phase appears as a side effect of reactivity of the liquid with the substrate,
since the liquid is formed by Ba and Cu, which reacts forming solid solutions
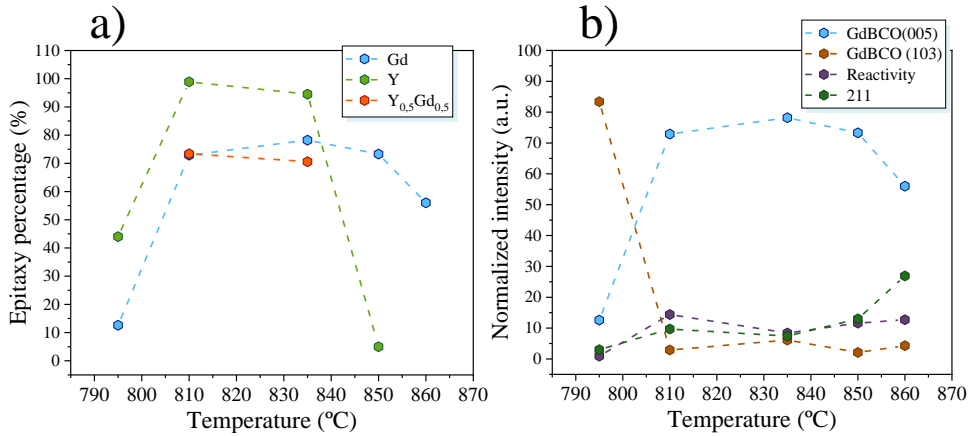
FIGURE 2.40: (a) Epitaxy percentage of samples with different rare earth composition grown at different temperatures, at $PO_2 = 10^{-3}$ bar and 20°C/s heating rate. (b) Intensity of the different phases present at different temperatures of the GdBCO samples.

with titanium and other elements from the substrate, while the excess of yttrium, or in this case gadolinium, reacts to form the 211 phase. The intensity of these phases increases with temperature, hindering the formation of epitaxial GdBCO. We conclude that Gd requires higher temperatures to be fully epitaxial but because higher temperatures create reactivity with the substrate, a non-reactive buffer would be needed in order to achieve fully c-axis films. Possible buffer layers will be investigated in the last chapter of this thesis.

Difference in the morphology of the films can also be appreciated through SEM images shown in Fig.2.41. The most homogeneous and non-porous film is achieved at 835°C, but at higher temperatures grains with different morphology and big holes can be observed, probably due to the presence of reactivity near the substrate or by bad wetting conditions of the liquid at these high temperatures. Both bad wetting and the presence of reactivity phases is very detrimental for superconducting properties, specially for such thin films, and therefore no sample had relevant T_c or J_c. With this preliminary experiments we have demonstrated that GdBCO is compatible with transient liquid growth methodologies, opening the door to tuning properties of the materials through changes in the rare earth metal. Nonetheless, further optimization and understanding of the process involving gadolinium is needed in order to achieve films with good superconducting properties.
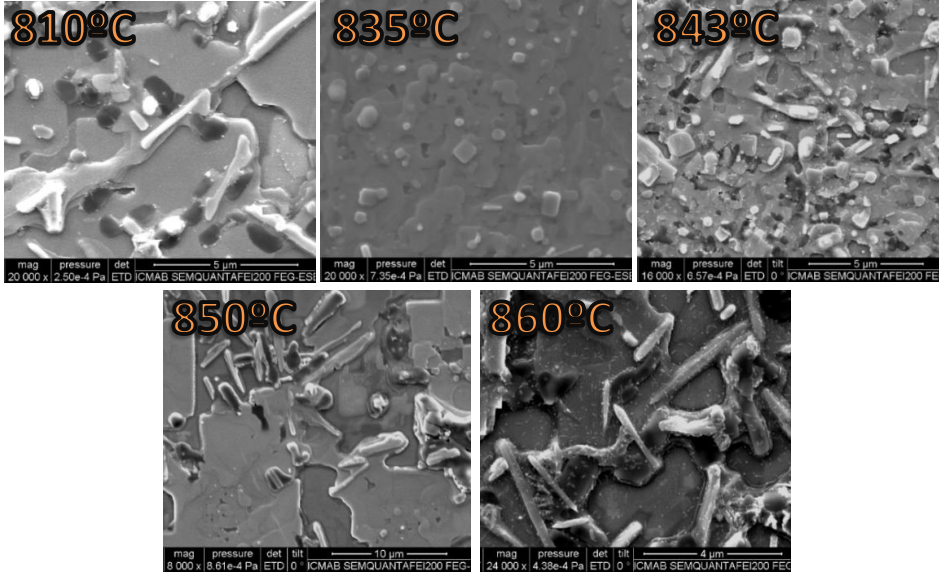
FIGURE 2.41:   SEM of GdBCO samples grown at different temperatures, at
$PO_2 = 10^{-3}$bar and 20ºC/s heating rate.

2.3.4   PO$_2$ route

Growing samples through a change in PO_2 conditions was also performed
in the rapid thermal annealing furnace. In this case, the chamber is placed
under a reduced total pressure of $P_{tot} = 1 \cdot 10^{-3}$bar in order to reach the desired
$PO_2 = 1 \cdot 10^{-5}$bar which is not accessible at atmospheric total pressure. Then the
heating step is performed and at the desired final temperature, the mass flows
and pumps are switched to atmospheric total pressure and the final PO_2. A
sensor inside the chamber provides reading of the PO_2, which shows that the
pressure change is achieved in less than 3 seconds. The factors influencing the
final characteristics of the film in this route are, more importantly, the final and
initial oxygen pressure as well as the growth temperature, but also the heating
speed that will influence the barium carbonate elimination and coarsening of
the intermediate phases, and total pressure and flow at the low pressure stage
which might play a role in the effective displacement of CO_2, necessary for
the barium carbonate reaction.

Here we present the best conditions found for this route in the rapid ther-
mal annealing furnace. Fig.2.42 a) shows the 2D X-ray diffraction pattern of
a fully epitaxial film grown on STO substrate, by heating a 3:7 composition
sample at a $PO_2 = 1 \cdot 10^{-5}$bar with a heating rate of 0.4ºC/s until 830ºC, keep-
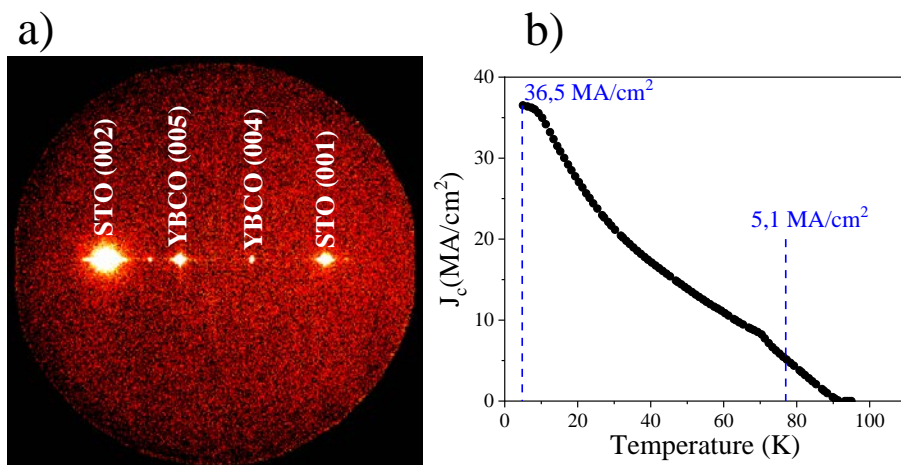ing a dwell of 5 minutes, and then performing a fast pressure jump until

FIGURE 2.42: (a) 2D-XRD sample grown on STO through PO_2 route, with a 3:7 composition, and processing conditions of heating the sample at a $PO_2=1 \cdot 10^{-5}$bar with a heating rate of 0.4°C/s until 830°C. Second step is a fast jump to $PO_2=1 \cdot 10^{-3}$bar. (b) SQUID measurement of J_c vs temperature for a film grown with the same conditions as (a).

$PO_2=1 \cdot 10^{-3}$bar and maintaining a dwell of 5 minutes at the same temperature. The critical currents achieved with this process are outstanding, such as shown in Fig.2.42 b), reaching a J_c=5.1MA/cm^2 at 77K and self-field. This is a good starting point to begin investigating the growth of nanocomposite films as will be done in the following chapters. It is also important to state that the PO_2 route has been under development for a shorter time than the temperature route and there is still a lot of work to be done to improve the understanding and the control of the factors that govern this route.

In any case, the growth rate of YBCO grown through this processing methodology could be measured by in-situ X-ray diffraction in the same manner as the temperature route. As it is displayed in Fig.2.43, we could demonstrate a growth rate of 100nm/s in almost all the growth stage. This confirms that YBCO material can also grow at very high speed when a liquid is formed using the PO_2 route.

From the knowledge gathered with the films grown in the rapid thermal annealing furnace, a new personalized oven was built in the group specifically to satisfy the requirements for performing PO_2-route experiments. This furnace is located in the laboratory of MATGAS belonging to SUMAN group, and consists of two pumping lines, one with a turbo-molecular pump and another only with a rotatory pump, which are connected to the furnace quartz tube
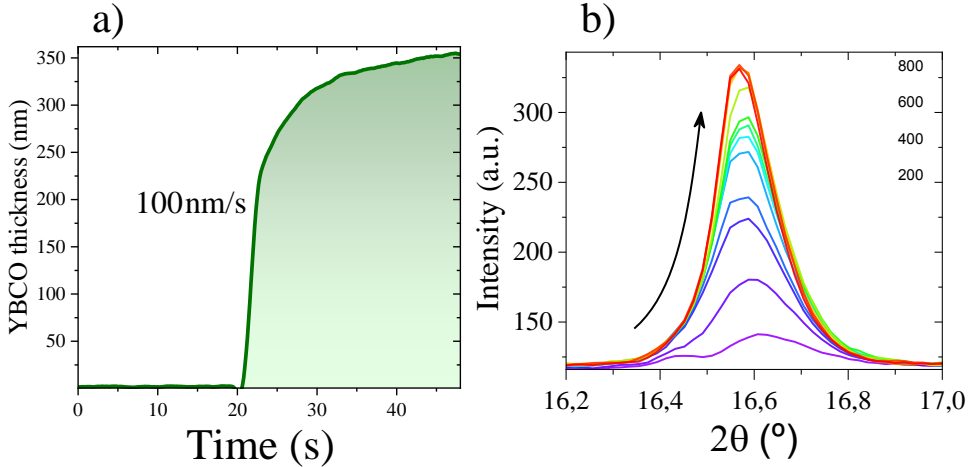
FIGURE 2.43: (a) Epitaxial YBCO thickness calculated from in-situ XRD. The sample was grown by performing a PO_2 jump from 10^{-5}bar to $2.5 \cdot 10^{-4}$bar at 830ºC although T fluctuations decreased temperature until 750ºC after the pressure jump. (b)Peak evolution of the (005) epitaxial peak from the same sample as (a).

through a needle valve and an electro-valve. The needle valve allows regulation of the pressure given by each pumping system while the electro-valves provide a fast switching between the two pumping circuits. Two pressure meters are located close to the tube entrance in order to have in-situ reading of the pressure inside the sample chamber, while performing the different steps of the process.

Fig.2.44 shows a picture of this furnace. At the other end of the tube, we observe the connection for a thermocouple attached to the crucible where the sample is placed. Additionally, a reservoir is connected to the rotatory pump circuit in order to make the pressure jump faster and reproducible. The advantage of this furnace is that thanks to the vacuum connections in all the system and the characteristics of the two pumps, the available pressures have a higher range than in the rapid thermal annealing furnace. Furthermore, by having a higher evacuation flux, the barium carbonate elimination reaction can be carried out easily for thicker films. The use of this furnace will be discussed in the last chapter for the growth of thick films.
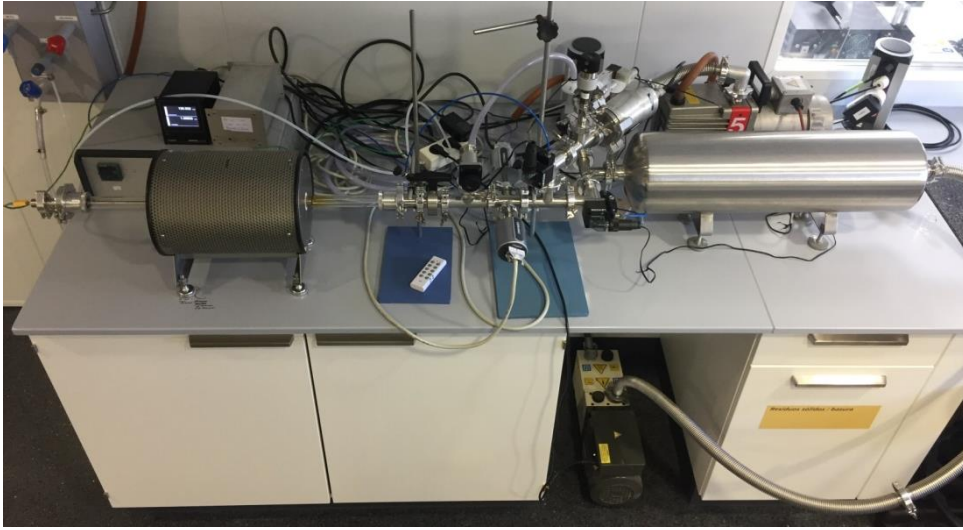
FIGURE 2.44: Picture of the Matgas furnace used for PO$_2$-route experiments.

2.4   Oxygenation

YBa$_2$Cu$_3$O$_{7-\delta}$ is very sensitive to oxygen content, affecting both its structure and its superconducting state. When δ is between 1 and 0.65, YBCO will present a tetragonal phase which is not superconducting. For δ between 0.65 and 0, the structure is orthorhombic and the T$_c$ depends strongly on the oxygen content, as shown in Fig.2.45 a).
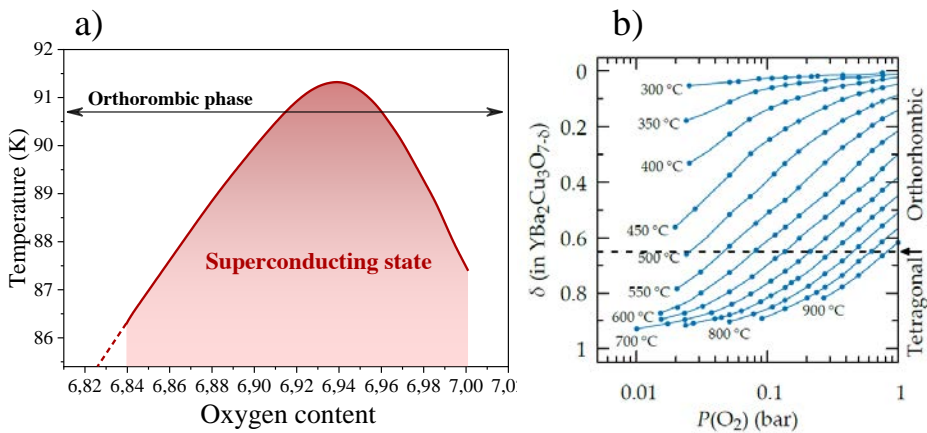

FIGURE 2.45: (a)Critical temperature of YBCO dependence with oxygen content, adapted from [101]. (b) Oxygen content in YBCO dependence with PO$_2$ at different temperatures. Reproduced from [102].

In order to obtain films with an optimally doped composition for the maximization of critical temperature, an oxygenation step is performed after growth. After growing YBCO through both the temperature and PO$_2$ route, the material is in a tetragonal structure due to the low oxygen pressure used during growth. The oxygen content in the structure will depend on PO$_2$ and temperature as shown in Fig.2.45 b). Therefore, the sample is placed in a tubular furnace and heated to 450ºC at 10ºC/min, to keep the final temperature during 210 minutes under a flow of oxygen of 0.6l/min and total pressure of 1 bar. This procedure ensures a high oxygen content of the films, as has been proven by hall measurements and in-situ resistance measurements performed by Dr. A. Stangl [62].

2.5   Conclusions

This chapter has given all the necessary information to understand transient liquid assisted growth and the experimental methodologies required for every step. The synthesis of precursor solutions have been described, which follows well established procedures common for chemical solution deposition. A mixture of solvents is necessary to achieve homogeneous depositions and a control of water content is vital to avoid unwanted nucleation further along the process. Synthesis of BaZrO$_3$ and BaHfO$_3$ through solvotermal methods was optimized to obtain small nanoparticles down to 4nm in diameter dispersed in alcoholic solutions, while LaF$_3$ is synthesized through a co-precipitation method. We described the necessary stabilization of nanoparticles colloidal solutions in YBCO precursor solutions as a first step to obtaining nanocomposite films. The thermal treatment of pyrolysis was detailed both for pristine films and nanocomposites, showing the obtained phases as well as the stability of nanoparticles during this step. Since TLAG is a novel process only reported before in Soler's thesis [62] and Rasi's thesis [63], which worked quite in parallel with this work, we have provided a theoretical basis and detailed explanation of the different reactions and processes involved. Barium carbonate elimination reaction has been studied by in-situ synchrotron X-ray diffraction experiments, to prove that we can effectively eliminate this compound in different processing conditions. After a careful explanation on the binary eutectic phase diagram and ternary phase diagram of YBCO, the temperature route and PO$_2$ route have been presented. Ultra-high growth rates of even 100nm/s have been demonstrated for both processing routes, as well as their very good J$_c$ self-field values at 77K of 3MA/cm^2 in temperature route and 5MA/cm^2 in PO$_2$ route. We have also investigated the possibility to extend this method to other rare earth metals like gadolinium, showing promising results which need to be further investigated.

With this chapter as a basis for the theoretical framework and experimental methodologies, we can move on to the main results body of this thesis which is the growth of nanocomposite films through transient liquid assisted growth.

Chapter 3

Nanocomposite films through Temperature route

This chapter investigates the introduction of pre-formed nanoparticles in the growth of YBCO thin films through the temperature route of TLAG. The goal is to obtain nanocomposite films in which the homogeneously dispersed nanoparticles act as vortex pinning centres, increasing critical current density at high magnetic fields. Different nanoparticles will be investigated, such as LaF_3, $BaZrO_3$ and $BaHfO_3$. We will study the stability of these particles during the growth of YBCO, as well as the necessary optimization of the processing conditions in order to obtain epitaxial films. We will also address the relationship between the introduced nanoparticles and the different kind of defects found in the YBCO matrix. Overall, we will discuss all the factors involved in obtaining a nanoengineered nanocomposite film through the new CSD methodology of transient liquid assisted growth.

3.1   Introduction of preformed nanoparticles in YBCO growth

As introduced in Chapter 2, the so-called Temperature-route relies on heating at constant PO_2 to achieve c-axis oriented YBCO films. Previous work investigating pristine films has shown that controlling supersaturation of yttrium in the liquid is key to achieve epitaxial films, as well as liquid stoichiometry [62, 64], and that processing conditions such as heating ramp, growth temperature and PO_2, have an influence on the final texture of the films. In this chapter we will study how the texture and properties of YBCO films are influenced when small pre-formed nanoparticles are introduced, and which are the optimal

conditions to grow biaxially oriented YBCO nanocomposite samples. There-
fore, the starting conditions for this investigation are the ones which produced
pristine samples with the highest texture and properties. For the stoichiomet-
ric liquid composition (2:3), a heating ramp of 20°C/s and a dwell of 2min at
835°C with a $PO_2=1\cdot10^{-2}$bar were used to grow YBCO on LSAT substrates,
which have a 0.26% of mismatch, achieving fully c-axis epitaxial films with
critical currents up to 3MA/cm^2 in pristine films. The eutectic liquid compo-
sition (3:7) will be investigated in the last section of this chapter. High heating
ramps are used to advantageously tune the kinetic factors. Rapid heating
prevents the $BaCO_3$ elimination to start where this reaction is already thermo-
dynamically favourable. Instead it will occur at higher temperatures, where
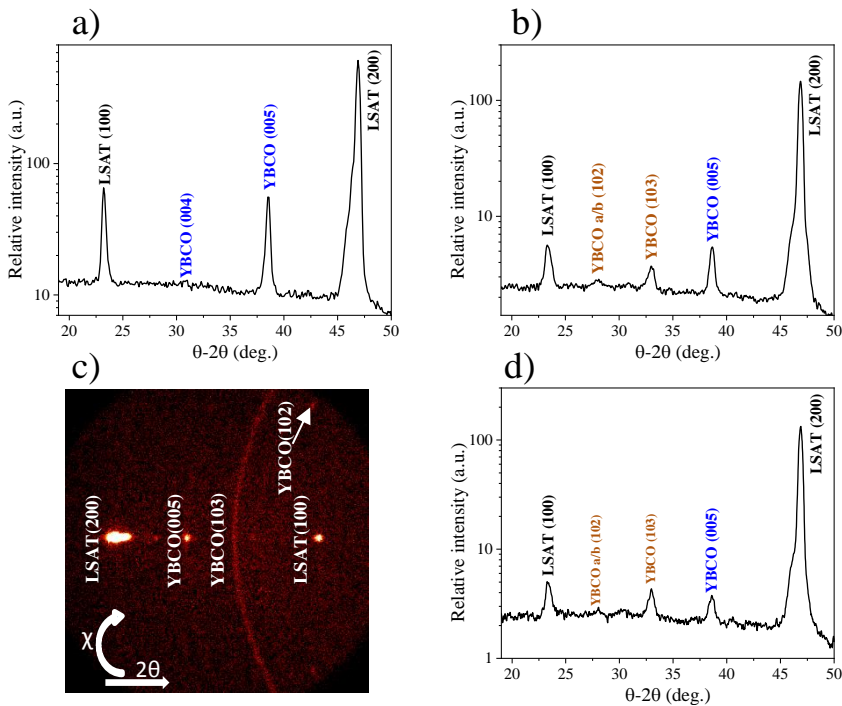supersaturation is reduced and c-axis nucleation is promoted.

FIGURE 3.1: Integrated X-ray diffraction patterns of (a) a pristine film, (b) a 12%mol-
LaF$_3$ nanocomposite and (d) a 12%molBaZrO$_3$ nanocomposite, all grown at 20°C/s
at 835°C. (c) 2D-XRD pattern as obtained by GADDS of sample (d).

LaF$_3$, BaZrO$_3$ and BaHfO$_3$ nanoparticles were chosen to begin with nanocom-
posite studies due to their small size and high dispersibility, as well as their
stability in alcoholic solutions compatible with YBCO precursor solutions. Py-
rolysed nanocomposite films containing 12%mol LaF$_3$, BaZrO$_3$ and BaHfO$_3$
were grown with the specified conditions. Details of the pyrolysis process can

be found in Chapter 2. Fig.3.1 shows the integrated X-ray scans for a 12%LaF$_3$ (b) and 12%BaZrO$_3$ (d) as well as a pristine film for comparison (a). In Fig.3.1 (c), the original 2D spectra of (d) can be observed, which shows the intensity both in 2θ and χ. More details of X-ray diffraction analysis can be found in Appendix A. Both nanocomposite films exhibit a significant increase in random nucleation, evidenced by the presence of the (103) reflection. Moreover, a small contribution of a/b oriented grains is also detected, with the (102) reflection appearing at an angle of $\chi = 12°$ in the 2D-XRD image. Therefore, the introduction of nanoparticles is affecting the YBCO nucleation, and tuning and optimization of the process are required to accommodate the nanoparticles to epitaxial growth. Both TFA and fluor-free chemical solution deposition methodologies have reported how introducing nanoparticles can lead to random nucleation of YBCO [103, 104].
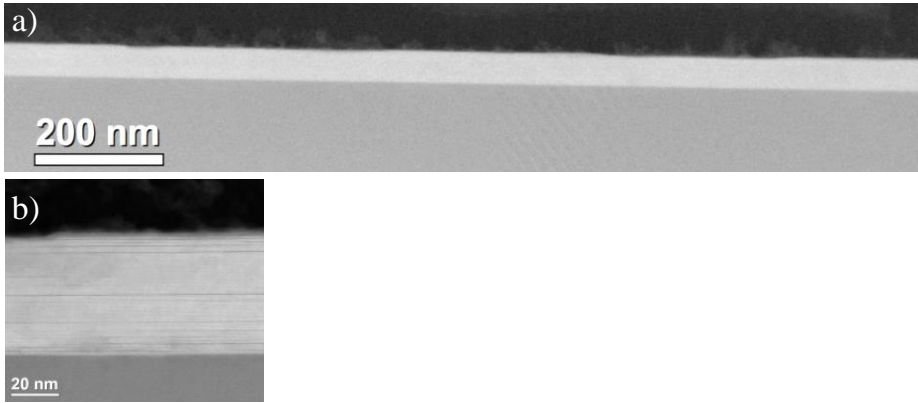

FIGURE 3.2: Scanning Transmission Electron Microscopy of a 50nm PLD YBCO film

C-axis growth relies on heterogeneous nucleation at the substrate interface due to the low mismatch of the substrate lattice parameter with the YBCO a/b lattice parameter. The presence of nanoparticles near the substrate interface can affect the nucleation of YBCO. Furthermore, the effect that small nanoparticles can have on supersaturation conditions is unknown. When using stoichiometric relationship of YBCO, the 2:3 composition of the liquid will entail a higher supersaturation than the eutectic liquid, and therefore the Gibbs free energy of c-axis and a/b nucleation will be closer, favouring both nucleations as explained in section 2.3.2. We also have to take into account that TLAG is already a relatively high supersaturation method due to the fact that all yttrium is already present in the film when the liquid is formed, as opposed to other methods such as HLPE, that introduces yttrium during growth and therefore have a smaller supersaturation[81]. If the supersaturation value of

epitaxial pristine films grown under these conditions is close to the limit area with mixed c-axis and a/b axis nucleation, the system will be more sensitive to perturbing factors such as the introduction of nanoparticles, shifting the equilibrium to a higher amount of random and a/b nucleation.

   To promote c-axis nucleation, a 50nm YBCO layer grown by Pulsed Laser Deposition (PLD) was deposited on the single crystal substrates. The conditions previously studied by other members of the group were used to grow homogeneous epitaxial 50nm YBCO PLD films on top of STO substrates, such as the one shown in Fig3.2. These films were chosen because of their good epitaxial texture and homogeneous surface which makes them good candidates as buffer layers. The idea behind using YBCO as a buffer layer has two advantages. Gibbs free energy for c-axis nucleation depends on the mismatch with the substrate. Therefore, homoepitaxy (epitaxial growth of a material on top of itself) is the most advantageous possible case, since the mismatch will be zero. Furthermore, it prevents the direct contact of nanoparticles with the substrate, avoiding direct YBCO nucleation on the nanoparticles and allowing more percolation paths for superconducting currents.

   The precursor solution was deposited on top of the YBCO PLD buffer layers. The resulting pyrolyzed films were grown in the same conditions as described previously. The epitaxial fraction of the films was measured as: % of epitaxy = $\frac{A(005)}{A(005)+A(103)}$. As shown in Fig.3.3, the epitaxial fraction of the films increased specially for LaF$_3$ nanocomposites where a 100% of epitaxy was achieved. In the case of BaZrO$_3$ and BaHfO$_3$, a 30-40% of random nucleation remained.

   It becomes apparent that to achieve a biaxial texture of BaZrO$_3$ and BaHfO$_3$ nanocomposites, the growth conditions of the films will need to be optimized. Nonetheless, before changing the processing parameters, we studied the stability of the nanoparticles during growth to ensure that the nanoparticles introduced in the precursor solution remained stable after the growth of YBCO.
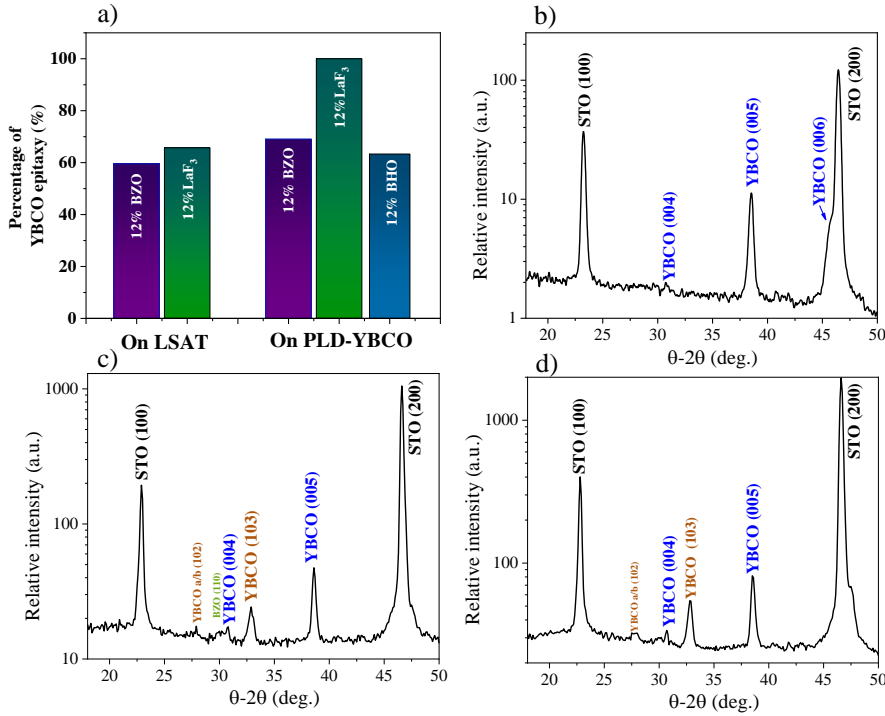
FIGURE 3.3: (a) Epitaxy percentage of 12%mol LaF$_3$, BaZrO$_3$ and BaHfO$_3$ films grown on LSAT and on YBCO PLD buffer layers. Integrated XRD of nanocomposite films grown on YBCO PLD buffer layers of (b)LaF$_3$, (c)BaZrO$_3$ and (c)BaHfO$_3$.

3.1.1 Nanoparticles stability

The use of pre-formed nanoparticles allows a good control of the crystalline phase, the size and the shape of the particles to be introduced as artificial pinning centers. However, these nanoparticles are exposed to processing conditions that could alter their characteristics, specially due to the presence of the [Ba-Cu-O] liquid which has shown to be highly corrosive [105]. We have shown in Chapter 2 how the nanoparticles remain stable after pyrolysis. After growth of the nanocomposite films, X-ray diffraction is inconclusive in identifying the nanoparticles. No peak belonging to the LaF$_3$ or BaZrO$_3$ phases is observed in Fig.3.1, but due to the small size of the nanoparticles and their small volume percentage in the final film, it can be difficult to identify the nanoparticles by X-ray diffraction.

To test the stability of the nanoparticles during YBCO growth and ensure the presence of LaF$_3$ and BaZrO$_3$ phases in the final film, the following experiment was performed. 5 layers of nanoparticles solution were deposited on top of LSAT substrates and then subjected to pyrolysis conditions. Once a
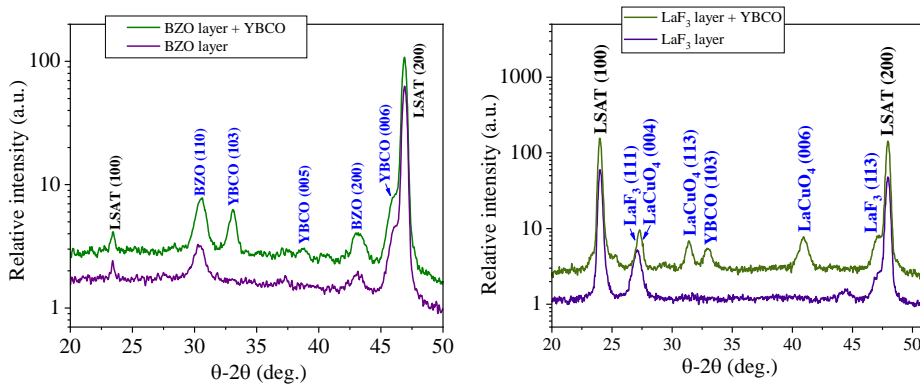
FIGURE 3.4: X-ray diffraction patterns for (a)BaZrO$_3$ and (b)LaF$_3$ only-nanoparticles films before and after YBCO growth on top.

film of solely nanoparticles was obtained, the YBCO solution was deposited on top and pyrolyzed again. Thus, we ensured that there was enough volume of nanoparticles phase to be observed by X-ray diffraction. As seen in Fig 3.4 the films of NPs after pyrolysis (with no YBCO on top) showed the LaF$_3$ and BaZrO$_3$ phases.

LaF$_3$ stability

When nanoparticles films with YBCO precursors on top were subjected to growth conditions, two different behaviours were observed. In the case of BaZrO$_3$, the peaks corresponding to the BaZrO$_3$ phase remained unchanged and YBCO peaks were also present. No reaction between the two materials was observed. On the other hand, the LaF$_3$ film exhibited three different phases. LaF$_3$ peaks could still be identified, but a phase containing La and Cu appeared, identified as LaCuO$_4$. This phase has been previously identified as a product of reaction between La$_2$O$_3$ and CuO at temperatures above 1000ºC [106]. In this case the La-Cu containing phase is identified at lower temperatures, indicating that the liquid formed during YBCO growth reacts with LaF$_3$. Indeed, this result is not surprising given the corrosive nature of the [Ba-Cu-O] liquid. Early research on melt-textured YBCO growth faced the problem of many crucible materials being very reactive when in contact with BaCuO$_2$-CuO liquid at high temperatures. Precisely, barium zirconiate was proposed as a solution to the crucible corrosion problems [105, 107]. To eliminate the possibility of LaF$_3$ nanoparticles being unstable due to atmosphere and temperature conditions during the growth process, a film of only nanoparticles was subjected to a thermal treatment of 20ºC/s until 835ºC at
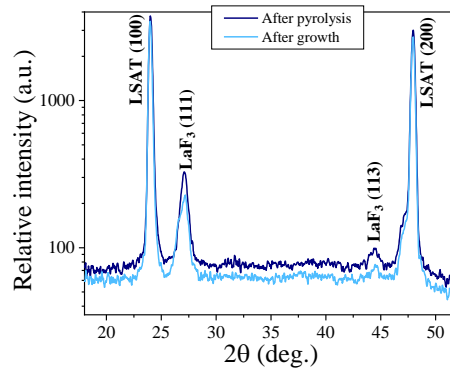
FIGURE 3.5: X-ray diffraction pattern of LaF$_3$ nanoparticles after being exposed to growth conditions.

PO$_2$=1·10^{-2}bar. As shown in Fig.3.5 the nanoparticles remained stable under these conditions.
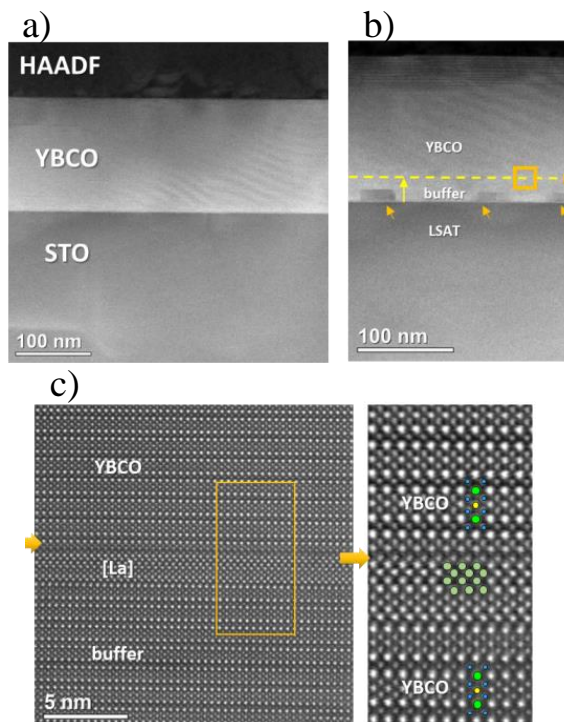

FIGURE 3.6: STEM of a YBCO nanocomposite film with LaF$_3$ nanoparticles grown on top of a YBCO buffer layer. (a) and (b): Low magnification images. (c): Different magnification images of the area marked in yellow in (b), showingLa$_2$O$_3$.

To confirm reactivity between LaF_3 and the transient liquid, Scanning Transmission Electron Microscopy was used due to its ability to analyse with atomic resolution the composition and structure of these nanocomposites. Fig.3.6 (a) shows a low magnification scan of a LaF_3 nanocomposite film where epitaxial YBCO is identified. With higher magnification, no LaF_3 nanoparticles were observed in Fig.3.6 (b). Instead, La_2O_3 intergrown layers only 3-4 unit cells thick were identified epitaxially aligned with the YBCO planes.

Lanthanum originating from the nanoparticles has reacted to form long lanthanum oxide layers only a few nanometers thick. In this case we observe La_2O_3 as a product of the reaction between [Ba-Cu-O] liquid and LaF_3 instead of $LaCuO_4$. Both products are stable phases and possibly depending on the local stoichiometry and composition of the system different reaction products can be detected. Both observations (X-ray diffraction in Fig.3.4 and TEM images in Fig.3.6) corroborate that LaF_3 is not stable in the presence of this liquid.
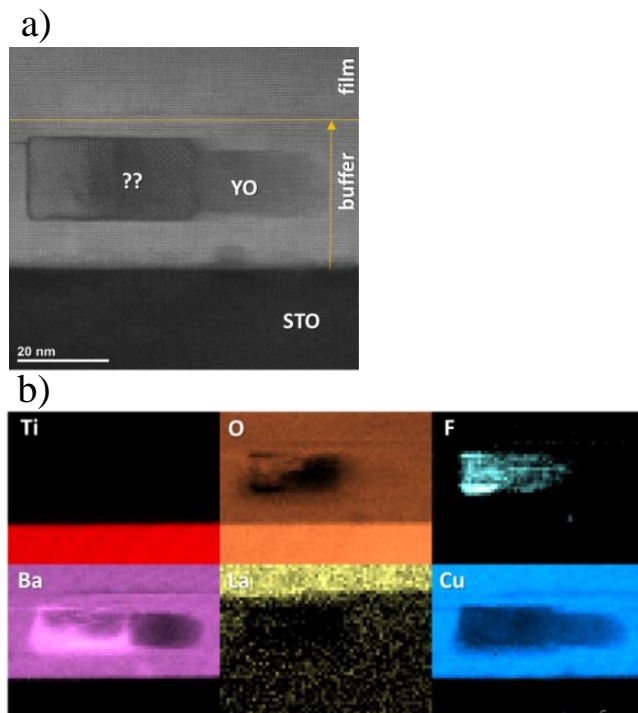

FIGURE 3.7: (a) STEM image of a particle inside a LaF_3 nanocomposite film. (b) EDX maps of different elements present in the particle observed in (a).

In the case of fluorine coming from the reacted LaF_3, some particles of unidentified phase containing fluorine could be observed by EDX analysis

as shown in Fig.3.7. The exact composition of these particles could not be determined, but EDX images show the presence of fluorine and barium while no lanthanum remained. Therefore it is possible that the fluorine contained in LaF_3 nanoparticles reacted to form BaF_2. This product is found under these conditions in other methodologies such as TFA-YBCO growth [86]. It is interesting to note that the phase containing fluorine was observed in the first 50nm of the film, therefore where the PLD buffer layer was deposited. This observation tells us that the PLD buffer didn't remain completely stable during the thermal treatment. Considering these results, we can conclude that LaF_3 nanoparticles are incompatible with YBCO films through transient liquid assisted growth due to their reactivity in the presence of [Ba-Cu-O] liquid.

BaZrO$_3$ stability

In the case of $BaZrO_3$ nanoparticles, STEM analysis were also performed for these nanocomposite films to observe the behavior of the nanoparticles during growth. Fig.3.8 shows a film grown on top of a YBCO PLD buffer. The layer of YBCO consists of polycrystalline grains on top of the un-disturbed buffer layer. In the image of the interface between buffer layer and YBCO, we find the presence of agglomerated BZO nanoparticles. They maintain their original size but during the process they have deposited on top of the buffer layer before any new YBCO grain was grown. Concerning nanoparticles stability, no other phase containing zirconium could be observed. This confirms that $BaZrO_3$ phase does not decompose during the contact with the transient liquid. In fact, in the field of YBCO singe crystals growth, the material that was found to be most stable and subsequently used as a crucible was $BaZrO_3$ [107]. Therefore, our results agree with previous research on finding that $BaZrO_3$ shows no reactivity with the $BaCuO_2$-CuO liquid, remaining stable during growth, while other materials, in this case LaF_3 can be decomposed in the presence of this liquid. Furthermore, $BaZrO_3$ nanoparticles also maintained their original size of 10-12nm as shown in Chapter 2. The displacement of the nanoparticles to the growing interface between the PLD buffer and YBCO is possibly the reason of YBCO random nucleation.

In this section we have shown how introducing nanoparticles in TLAG YBCO can be challenging. In general, due to the growth mechanism through decomposition of barium carbonate and nucleation from a liquid, problems regarding reactivity of the nanoparticles and random nucleation of YBCO can arise. Some materials can be reactive with the liquid and therefore are incompatible with YBCO nanocomposite films growth, as such is the case for LaF_3 nanoparticles. The instability of these nanoparticles was severe in the presence of [Ba-Cu-O] liquid. On the other hand, $BaZrO_3$ and $BaHfO_3$
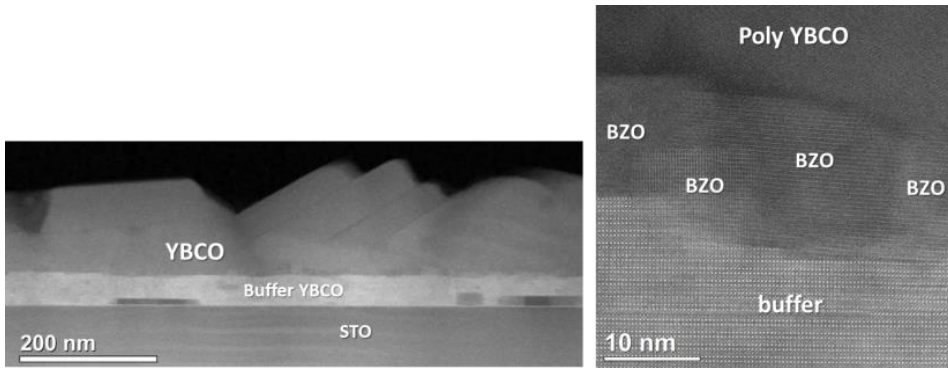
FIGURE 3.8: TEM images of a BaZrO$_3$ nanocomposite film
grown on top of a PLD YBCO buffer.

nanoparticles are more promising. They are stable in the presence of the liquid. Nonetheless, random nucleation was detected, which can be attributed to the fact that YBCO is growing from a highly supersaturated liquid. According to theory of nucleation from liquids, higher supersaturation increases nuclei density and growth rate, and thus the system can be more easily disturbed that when the supersaturation is lower and therefore nucleation is easier to control. In this case, there are different approaches we can follow to promote c-axis nucleation through tuning of the growth conditions. Therefore, in the next section we will concentrate our efforts on understanding and optimizing the growth of BaZrO$_3$ and BaHfO$_3$ epitaxial YBCO nanocomposite films.

3.2   Tuning nanocomposites growth conditions

3.2.1   Heating ramp study

To be able to tune growth conditions to achieve epitaxial films when the system is disturbed by introducing nanoparticles, we need to understand the growth mechanism and factors involved in TLAG. In this methodology there is an interplay between kinetic and thermodynamic effects that allows the formation of the BaCuO$_2$-CuO liquid in a region where it is not thermodynamically stable. In the binary system of Ba and Cu, a liquid phase is formed in the P-T of interest, but with the addition of Y$_2$O$_3$ the stable phase according to the equilibrium phase diagram is YBCO [94]. Nonetheless, when we reach the nucleation region for YBCO, there is a nucleation barrier for YBCO induced by a solid-solid reaction. Instead, the formation of the liquid is energetically

favourable (no barrier exists for liquid formation), and thus practically instantaneous, and once the liquid is formed, Y dissolves and the high diffusivity of Y dissolved in the liquid to the substrate interface will allow YBCO growth to take place. Therefore, we are relying on kinetic effects that initially favour the formation of the liquid instead of YBCO. Furthermore, the temperature and time for these reactions to occur will be determined by the elimination of $BaCO_3$. This reaction must occur before liquid formation and it is expected to be the slowest reaction of the system. By tuning the temperature at which $BaCO_3$ decomposes, we will be able to tune at which temperature the following reactions occur, and thus promote c-axis nucleation. More details on barium carbonate elimination and the different reactions of the system can be found in Chapter 2. One of the important parameters that can allow us to tune these reactions is the heating ramp. If the reactions of the process are happening in the heating stage, changing heating ramp should affect the final results. On the contrary, if $BaCO_3$ decomposition and subsequent reactions occur once the final temperature is reached, no effect should be observed when heating is altered. Rapid thermal annealing furnaces are a useful tool to conduct these experiments due to its ability to control heating ramps up to 60ºC/s.
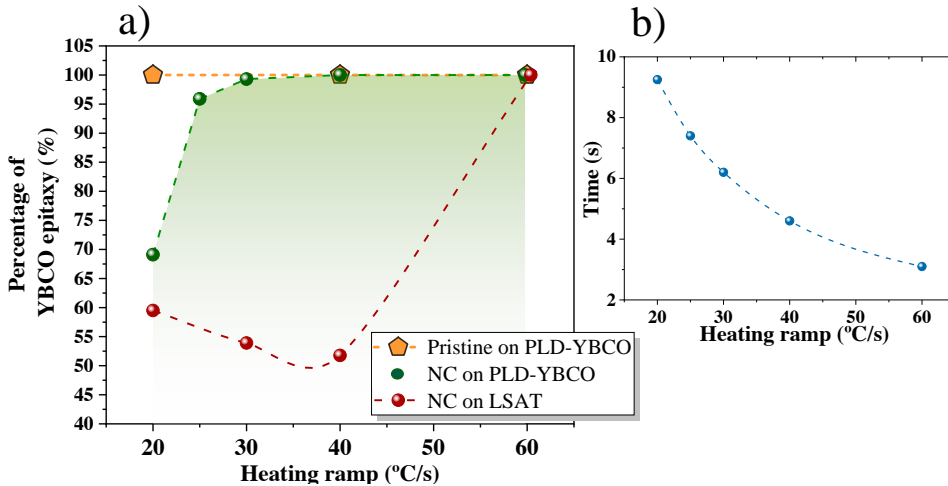

FIGURE 3.9: (a) Calculated epitaxial fraction for pristine and nanocomposite films grown with different heating ramps. (b) Required time to reach 835ºC from 650ºC at different heating ramps.

Nanocomposite and pristine films deposited on top of YBCO PLD buffer layers were grown at heating ramps ranging from 20ºC/s up to 60ºC/s, as well as nanocomposite films on top of LSAT single crystals. For all samples, a dwell of 2 min at the final growth temperature of 835ºC was performed, and

PO_2 was kept at $1 \cdot 10^{-2}$ bars during the whole process. The epitaxial fraction of the resulting films was calculated and is shown in Fig.3.9. Pristine films remained 100% epitaxial in all tested heating ramps. $BaZrO_3$ nanocomposite films on top of LSAT didn't show a significant increase in epitaxial fraction until a 60ºC/s ramp was used. In the case of nanocomposite films on top of YBCO PLD buffer layers the epitaxial fraction changed substantially with small changes in the heating ramp. 100% epitaxial films were obtained with heating rates beyond 25ºC/s. We know that 650ºC is the lowest possible temperature where $BaCO_3$ can decompose under these PO_2 conditions, according to Soler's thesis [62]. It is noteworthy that the time spent between 650ºC and the final temperature of 835ºC is only shortened from 11.8s at a heating ramp of 20ºC/s to 7.8s for 30ºC/s, as shown in Fig.3.9 (b). This is an indication of the fast kinetics involved in this process, and changes in the nucleation with diferent heating ramps indicate that $BaCO_3$ decomposition and subsequent YBCO formation is occuring during heating. As previously pointed out, by using higher heating ramps we were able to grow YBCO at higher temperatures where c-axis nucleation is promoted, as seen in Fig.2.32. Temperature can have two opposing effects on growth rate, since it increases yttrium diffusivity but lowers supersaturation, as shown in Fig.2.20. Since the supersaturation in this system is high, we probably are in the region where increasing diffusivity is increasing growth rate. These two factors, higher growth rates and higher tendency for c-axis nucleation, are able to overcome the random nucleation that was induced by the introduction of nanoparticles. A lower degree of aggregation of the nanoparticles due to a shortened reaction time could also play a major role in allowing c-axis nucleation on top of the PLD buffer layer.

Rocking curves were evaluated in order to test the crystalline quality of the films. Pristine and nanocomposite films were measured and are plotted in Fig.3.10. The values of full-width at half-maximum (FWHM) decreased with increasing heating ramps for $BaZrO_3$ nanocomposites, while remaining with values under 0.35º for pristine films. High FWHM values are an indication of deviations from the ideal Bragg conditions, created when the crystalline planes are not perfectly parallel to each other due to mosaicity or slight misorientation of epitaxial grains. In this case, increasing heating ramps produced nanocomposites with increased texture, supporting our hypothesis that we have been able to promote c-axis nucleation by inducing the reaction at higher temperatures. Pristine films didn't show any significant difference in the studied range of heating ramps, since their epitaxial fraction was found to be 100% for the whole range. Nanocomposite films reached the same values as pristine films with ramps above 30ºC/s. The observed values of 0.2-0.3º are signs of very high crystalline and texture quality, possibly related to the
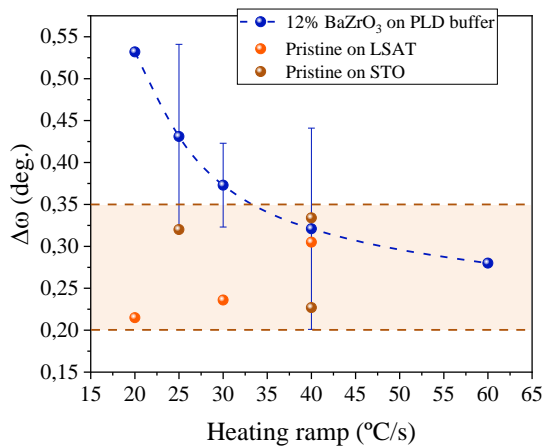
FIGURE 3.10: Rocking curve FWHM values calculated for pristine and BaZrO$_3$ nanocomposite films grown with different heating ramps.

low defect structure obtained through crystallization from liquids. Consequently, these values are lower than those reported for methodologies using vapor-solid (PLD) or gas-solid reactions (CSD-TFA) [108].
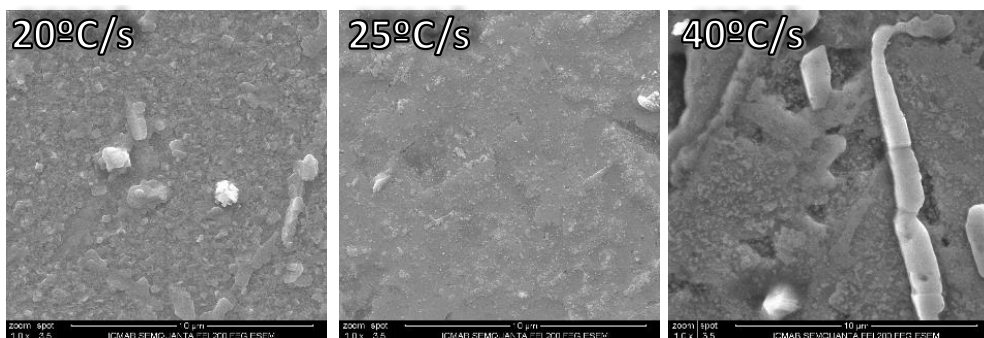

FIGURE 3.11: Scanning electron microscopy images of films grown under different heating ramps.

To improve our understanding of the effect that heating ramps have on nanocomposite films, Scanning Electron Microscopy (SEM) was used to investigate the morphology of the samples. Fig.3.11 displays the difference between films surfaces in a range between 20 and 40ºC/s. At 20ºC/s we can observe small randomly oriented grains, in agreement with X-ray diffraction patterns. At 25ºC/s the randomly oriented grains have disappeared and a

homogeneous non-porous sample is observed, but when heating ramp is increased up to 40°C/s, a somewhat disordered structure is detected. The sample shows some holes and grains on the surface which could affect the percolation of current in the film.
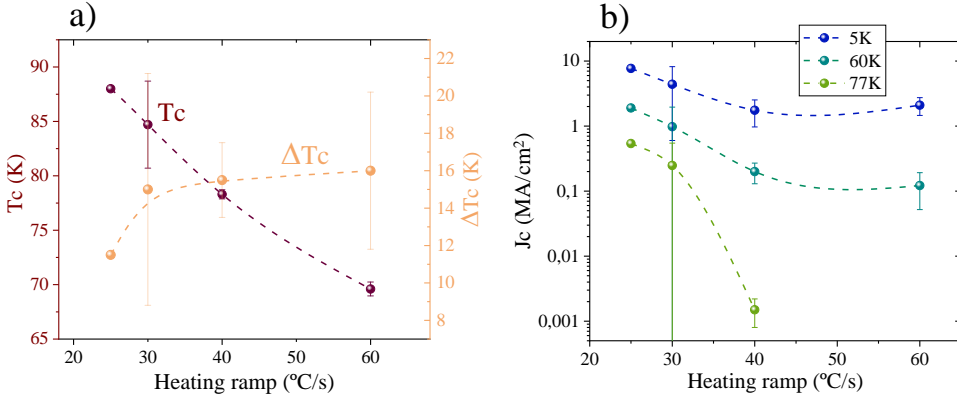

FIGURE 3.12: (a) T_c and ΔT_c measured by SQUID. (b) SQUID J_c measurements at different temperatures.

The superconducting properties of films with 95% or more epitaxial fraction were measured by SQUID magnetometry. As shown in Fig.3.12 (a), both T_c and ΔT_c showed a significant decrease with increasing heating ramps. A similar trend was observed for critical current density as shown in Fig.3.12 (b), and the highest J_c at 77K was 0.6MA/cm^2 and 10MA/cm^2 at 5K, observed for a sample grown at 25°C/s. Although these are not optimized values, it is a good starting point in our investigations. A good current percolation in superconducting films requires low angle grain boundaries, and so it is essential that the films be biaxially aligned to reach the full J_c potential [109]. In this case, the decrease in properties does not correspond to the observation of higher texture quality with higher heating ramps. Therefore, the reason behind a further improvement must lay in factors other than YBCO crystalline texture. Current percolation can be altered by many factors such as the presence of non-superconducting secondary phases and poor grain connectivity due to dewetting or pores, which we will need to investigate.

Critical temperature has a characteristic value for each superconducting phase, and therefore its measurement can give us information on the purity of the material. Nonetheless, depending on the measurement methodology we will obtain different information. When T_c is measured by dc-SQUID magnetometry, T_c values will be sensitive to percolative currents of the films and therefore it is not possible to discern which is the cause for a lowered T_c. On
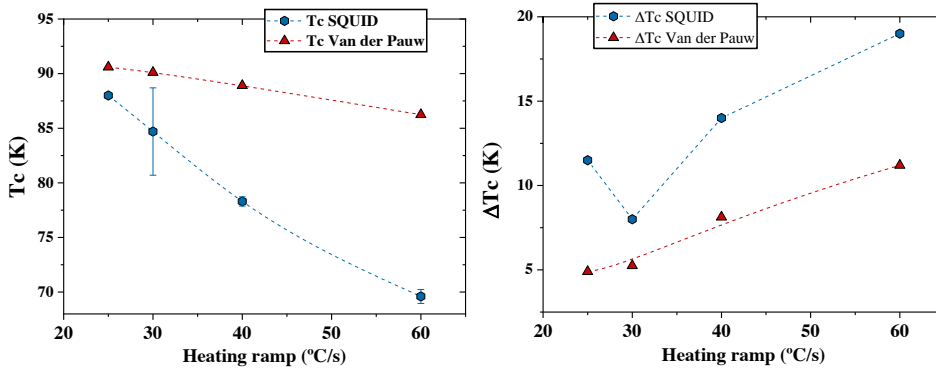
FIGURE 3.13: T_c and ΔT_c measurements by Vand der Pauw and dc-SQUID.

the other hand, transport measurements such as Van der Pauw do not rely on percolation inhomogeneities, and will mostly be sensitive to the intrinsic properties of the material. T_c and ΔT_c were measured by Van der Pauw method and compared to SQUID values as can be observed in Fig.3.13. T_c measured by Van der Pauw is higher in all the measured samples, and while T_c by SQUID is decreasing rapidly below 87K, T_c by Van der Pauw decreases much less with heating ramp, never dropping below 87K. ΔT_c shows a very similar trend, increasing with heating ramp for both measurement methods but being lower in all cases for Van der Pauw. This different values and behavior for Van der Pauw as compared to dc-SQUID are an indication that the observed decrease in properties for the SQUID results are due to current percolation problems as opposed to impurities of the YBCO matrix.

To investigate the possible reasons for the difference in properties depending on heating ramp, such as the presence of secondary phases, high resolution X-ray scans were measured in a wide θ-2θ range. In Fig.3.14 we can observe the patterns for 4 different films. The films show primarily c-axis oriented YBCO, with some other minor phases. It is also detected the peak corresponding to $BaZrO_3$ with (002) orientation. No peak corresponding to (110) BZO is observed, which might indicate that $BaZrO_3$ nanoparticles have a preferred orientation inside the YBCO matrix. The film grown at 60ºC/s presents several peaks corresponding to an epitaxial phase at positions 65º and 78º, which could not be identified. This secondary phase could be detrimental for the superconducting properties, but no clear trend is observed for
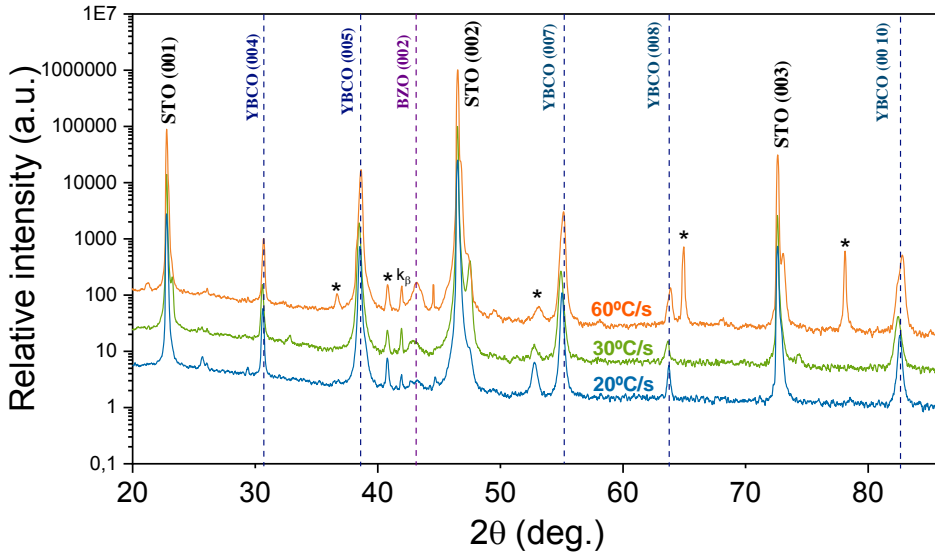
FIGURE 3.14: High resolution X-ray diffraction patterns of $BaZrO_3$ nanocomposite films grown on top od YBCO PLD buffer layers with different heating ramps. (*) mark unidentified peaks.

increasing heating ramps, with several minor peaks appearing for all the different ramps. More detailed and local characterization is needed to find a clear correlation.

In order to understand the influence of heating ramp at a microscopic level, STEM images were obtained for a film grown at 60ºC/s. It readily became apparent that the substrate suffers from a high amount of reactivity with the liquid phase. As shown in Fig.3.15 the $SrTirO_3$ substrate has dissolved in areas extending up to hundreds of nanometres. EDX scans in Fig.3.15 performed in areas where the substrate had reacted found large particles containing yttrium, barium and titanium embedded in the film, indicating that Ti atoms from the substrate have reacted with the [Ba-Cu-O] liquid and Y.

Different areas of the same sample showed different stoichiometry and morphology of these secondary phases. As shown in Fig.3.16 (a), also several hundreds of nanometers long particles of Y_2BaCuO_5 (Y211) were found near the substrate interface. Crystalline $BaTiO_3$ (BTO) was also identified in the shape of big particles of ~100nm in width embedded in the YBCO matrix, even far away from areas where the dissolution of the substrate was observed. Fig.3.16 (b) shows YBCO grown with different orientations around an area where the substrate has reacted in a steep step of ~150nm. Other areas of the sample,
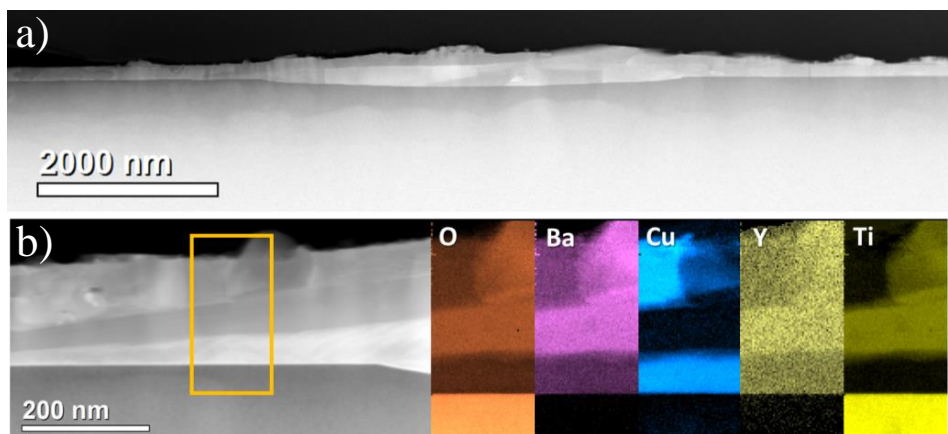
FIGURE 3.15: 12%BaZrO$_3$ nanocomposite film grown at 60ºC/s. (a)STEM image of a large are with substrate reactivity (b)STEM image and EDX analysis of several elements in the area marked with a yellow rectangle. Particles containing Ba, Y, Ti and O are identified.

such as the one shown in Fig.3.16 (c) present defect-free c-axis YBCO with no secondary phases or reactivity observed nearby. The products and extension of this reactivity are very inhomogeneous thorough the sample. Note that these films were grown on top of a 50nm PLD YBCO buffer. The observed reactivity indicates that the liquid dissolved first the buffer layer until reaching the substrate, since in addition, no evidence of an interface between the film and the buffer layer was found. The inhomogeneity of the film is a manifestation of out-of-equilibrium growth, where the fast kinetics of the liquid are playing a very important role, and the corrosive nature of the [Ba-Cu-O] liquid attacks specific points of the SrTiO$_3$ single crystal. From this system other phases such as BaTiO$_3$, a product of Ti atoms dissolution in the melt and stable at high temperatures, can be grown. We propose that when, locally, a certain amount of barium has been used to form BaTiO$_3$, the stoichiometry of the nearby elements will have an excess of yttrium, creating particles of Y211 which would not be stable under these conditions otherwise.

EDX quantification of the different secondary phases elucidated the elemental stoichiometry of some particles in the film, indicating that the BaTiO$_3$ particles were barium rich and some of them contained strontium, also coming from the substrate. Out of equilibrium growth occurs when the kinetic factors are more relevant than the thermodynamic ones, and in this case a supersaturated liquid can create the conditions necessary for a system in which the obtained phases do not correspond with the thermodynamically expected phases but with locally and kinetically favoured phases. Furthermore, the

inhomogeneity of the samples and the different stoichiometry found for the secondary phases can explain that properties have a systematic decrease with the heating ramp. As previously explained, $BaCO_3$ decomposition will start at higher temperatures when higher heating ramps are used, consequently, this will shift all the following reactions to higher temperatures too. Therefore, the transient liquid will also appear at higher temperatures, and what we are observing is that this corrosive liquid is more reactive at higher temperatures. A systematic increase of the heating ramp will result in an increase of the reactivity with the substrate, which at its turn will decrease critical current of the films due to the difficulties in current percolation created by the presence of extensive secondary phases.
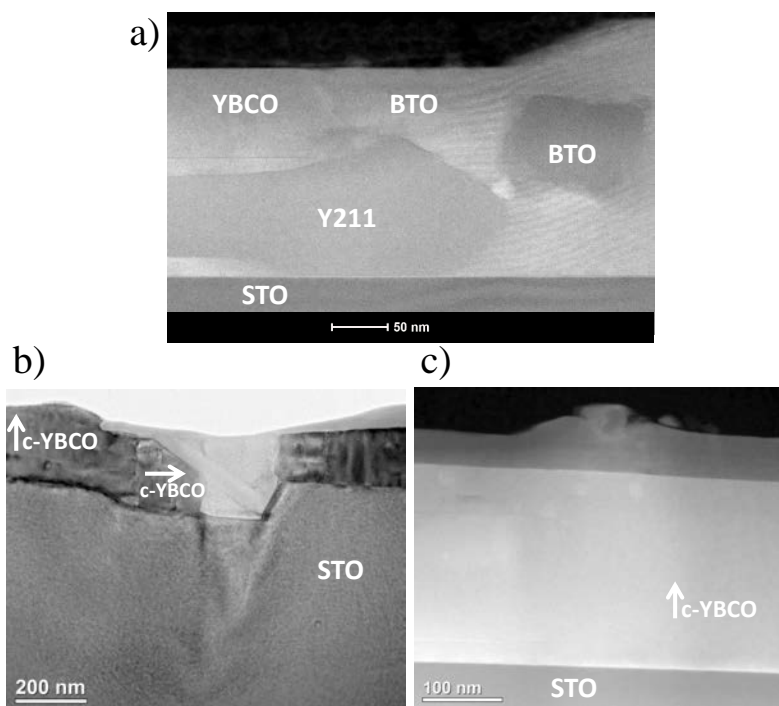

FIGURE 3.16: STEM images of several areas of a 12%$BaZrO_3$ nanocomposite film grown at 60ºC/s.

We have seen how heating ramps are a critical processing parameter in the growth of nanocomposite YBCO films through the temperature-route. On one hand, small variations in this parameter will greatly affect the texture of the films, being able to overcome the random orientation produced by the presence of nanoparticles. On the other hand, high heating ramps make the

transient [Ba-Cu-O] liquid appear at higher temperatures, creating reactivity with the substrate and therefore negatively affecting the superconducting properties. For the films presented in this chapter, the best conditions found are a compromise between these two competing effects: a ramp of 25ºC/s gives a J_c self-field at 77K of 0.6MA/cm^2 and 7.7MA/cm^2 at 5K. This value is in the range of other liquid-assisted methodologies, but could still be improved to reach more competitive values. To abandon the interplay between reactivity and c-axis orientation, we propose that a buffer layer inert to [Ba-Cu-O] liquids should be used. If such a buffer is found, heating ramp could be adjusted to obtain the best c-axis alignment and superconducting properties could reach its full potential without the presence of any secondary phases induced by liquid reactivity. A study on possible buffer layers is presented on Chapter 5.

3.2.2   Defect landscape dependence with heating ramp

We usually think of crystalline materials as perfectly ordered structures down to the atomic level. Nonetheless, a large amount of properties attributed to crystals such as photoluminescence, ionic conductivity or, in our case, vortex pinning in a superconducting material, wouldn't be possible without defects in the crystalline lattice. These flaws in the lattice can range from point defects to large inclusions of secondary phases, and their effect on properties will be different for every material. As has been discussed in the introduction, the study of defect structure is specially crucial in the case of YBCO, where critical current density values will depend on our ability to effectively pin vortices in nanometric non-superconducting areas of depressed superconducting order parameter [110–112].

To investigate defects at the nanoscale, Transmission Electron Microscopy (TEM) is a very powerful technique, able to identify structures at atomic scale and thus revealing any kind of irregularity in the crystalline structure, from small secondary phases to crystalline defects like stacking faults or anti-phase boundaries. It needs to be taken into account that TEM acquires images at a very local scale and therefore it is dangerous to extrapolate something observed in one image to the whole film. Nonetheless, through investigation of several samples and observation of lower magnification images we can understand the relationship between the defects observed by TEM and the properties of our films.

In this section, we want to briefly discuss which is the relationship between heating ramp used to grow nanocomposite films and the defects that the YBCO matrix presents, either attributed to the presence of nanoparticles
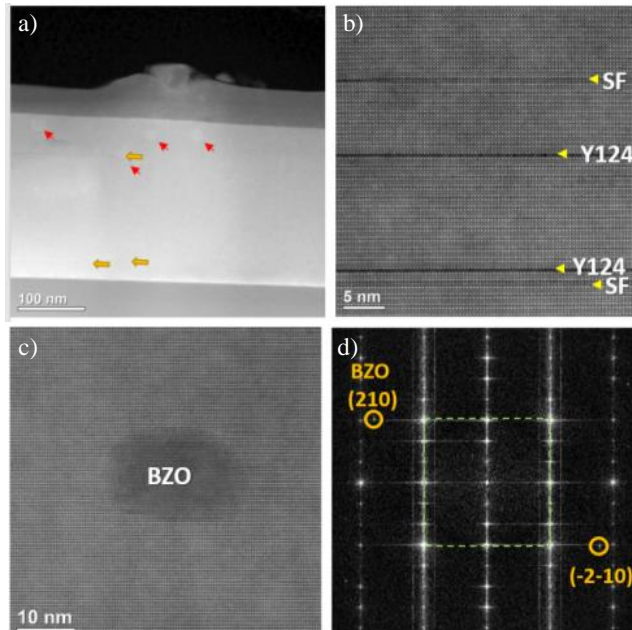
FIGURE 3.17: STEM images of a 12%BZO film grown at 60ºC/s. (a) Low magnification image with red arrows pointing to BZO nps. (b) Detail of Y124 (Y248) intergrowths. (c) A BZO np embedded in a defect-free YBCO matrix and (d) its diffraction pattern.

or intrinsic to the growth mechanism. We will focus on defects not related to reactivity which has already been discussed in the previous section.

Fig.3.17 shows different images of a 12%BaZrO$_3$ film grown at a heating ramp of 60ºC/s. The first relevant feature of the film is the high quality of the crystalline matrix. It is compact and homogeneous and no distortions are observed. This is in accordance with the rocking curves observed tendency to reach their lowest value for the highest heating ramp. As seen in Fig.3.17 (c) the nanoparticles embedded in the YBCO matrix don't induce distortions in the crystalline structure surrounding them. There's a small amount of Y$_2$Ba$_4$Cu$_8$O$_x$ (Y248) intergrowths, consisting on an extra Cu-O chain and which are one of the defects with the lowest formation energy and therefore it is a very common defect YBCO films grown through different methodologies [113, 114]. Also a less common perovskite intergrowth is observed in our films, the Y$_2$Ba$_2$CuO$_4$ phase consisting of an extra Y-Cu-O block. In some occasions these Y224 intergrowths are connected by (100) or (103) anti-phase boundaries (APB). This defect is a shift of the lattice so that every plane of the unit cell will be connected to a different one. The boundary in which the connection between different planes happen is called anti-phase boundary and
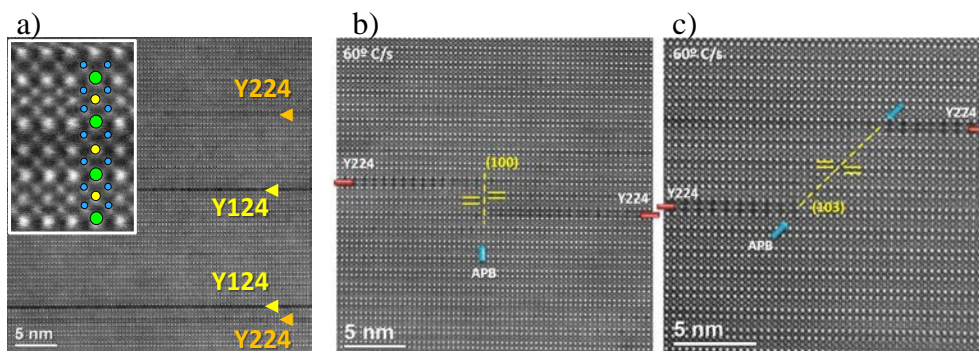
FIGURE 3.18: TEM images of a 12% $BaZrO_3$ film grown at 60ºC/s. (a)Y224 and Y248 intergrowths. (b) Two Y224 intergrowths connected by a (100) antiphase boundary and (c) by a (103) anti-phase boundary.

it has been reported only for very out-of-equilibrium growth methodologies such as sputtering and PLD [115]. The presence of APBs at this heating ramp indicates how TLAG is governed by kinetics factors far from thermodynamic equilibrium.
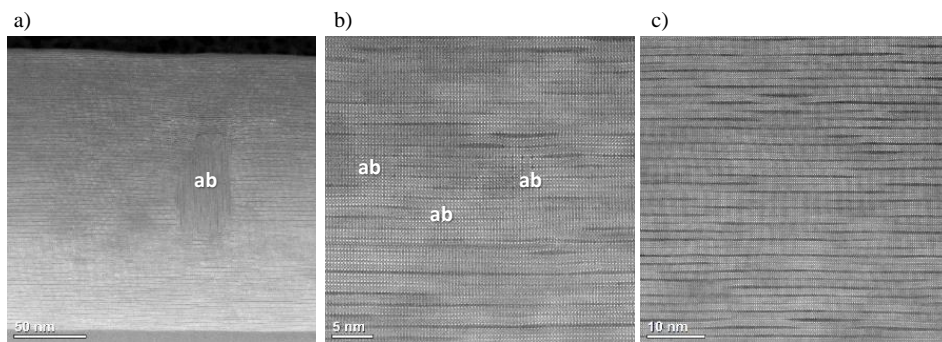

FIGURE 3.19: TEM images of a 12% $BaZrO_3$ film grown at 25ºC/s. (a) Low magnification image. (b) High magnification where small a/b grains are identified. (c) Detail of short stacking faults.

The defect landscape is very different for nanocomposite films grown at 25ºC/s, as can be observed in Fig.3.19. A high density of Y248 and stacking faults is detected in the whole thickness of the sample. Moreover, these stacking faults tend to be much shorter, which is believed to be beneficial for vortex pinning since the strain accumulated in the surrounding of the stacking fault is thought to be an effective pinning site as has been shown for TFA-CSD films

[116–118]. The presence of extra Cu-O chains (Y248 intergrowth) does not affect the Y123 stoichiometry of the film nor the values of T_c due to the formation of Cu vacancies and their corresponding oxygen vacancies in the Cu-O chains [119]. In Fig.3.19 (a) and (b) it is shown how the film also contains some small a/b grains, ranging between 5 to 20nm in size. The proximity in Gibbs free energy for nucleations other than c-axis at lower heating ramps might induce this a/b nucleation. However, such small misoriented grains are not detrimental to properties and could even act as pinning centers if their size is restricted to few nanometers. Regarding the role of preformed nanoparticles in the defect structure of the film, Fig.3.20 (a) and (b) shows the incoherent interface between nanoparticles and the YBCO matrix. Although not confirmed by XRD, the TEM image suggest that the nanoparticles are mostly randomly oriented in the YBCO matrix. Surrounding the nanoparticles, a high density of stacking faults is identified as well as bending of the YBCO matrix. It is clear that the nanoparticles are positively contributing to create artificial pinning sites by means of creating strain and associated defects which are effective at vortex pinning. Fig.3.20 (c) shows a big $BaZrO_3$ particle with a size of ~150nm. Such a large particle is reducing the cross-section for current percolation. Coarsening should be avoided in order to have maximum J_c and optimized vortex pinning performances. Fortunately, this kind of coarsening was not observed often as most of the detected particles maintained their original 10-12nm size. Nonetheless, strategies to avoid coarsening could further improve the properties of the films by keeping a high density of small artificial pinning sites.
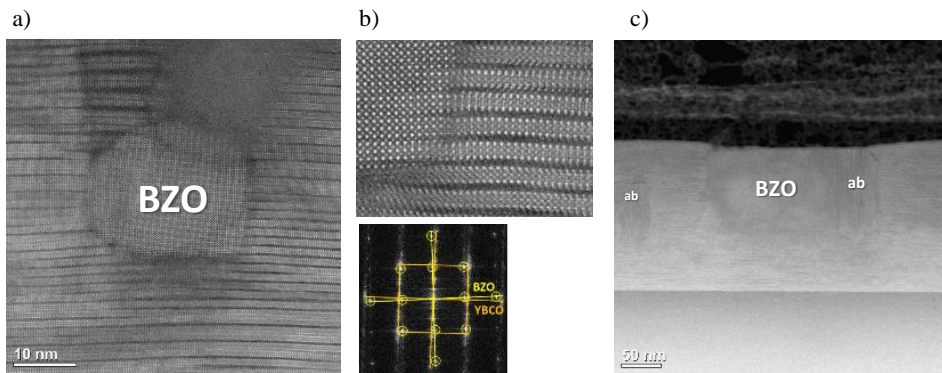

FIGURE 3.20: TEM images of a 12% $BaZrO_3$ film grown at 25ºC/s. (a) A small BZO nanoparticle embedden in the YBCO matrix. (b) Detail of the incoherent interface between BZO and YBCO. (c) A coarsened BZO nanoparticle.

If we compare nanocomposite films of the two presented heating ramps, it becomes apparent that processing conditions have a large effect on the defect landscape of the film. Films grown at 60ºC/s show a much lower density of defects, presenting features that correspond to out-of-equilibrium growth. When the heating ramp is lower, a much higher density of short stacking faults is observed, showing a landscape much more similar to other CSD techniques such as TFA. We also have discovered how the relationship between the YBCO matrix and the nanoparticles is different depending on the heating ramp. On one hand, at high heating ramps the nanoparticles are encapsulated by the YBCO crystalline structure without inducing any defects around them, while on the other hand, at 25ºC/s $BaZrO_3$ particles are generating plane distortions in their surroundings as well as a higher density of stacking faults. Thus, the interplay between defects created by the processing conditions and which of these conditions are better exploiting the potential of the nanoparticles to create a favourable defect landscape has to be taken into account in order to design the most optimal microstructure for an effective vortex pinning. TLAG is therefore a very flexible technology to nanoengineer defect landscapes.

3.2.3   Influence of PLD YBCO buffer layer thickness

As seen in section 3.2.1, reactivity with the substrate increases with heating ramps. In order to attack the substrate, the [Ba-Cu-O] liquid dissolves the YBCO PLD buffer layer until getting in contact with the substrate and causing undesired reactions. Also, we have demonstrated that this buffer layer is necessary to achieve epitaxial films with a minimum heating ramp of 25ºC/s. To better discern the role of the buffer layer on epitaxy and reactivity, films with 12%$BaZrO_3$ were grown on PLD buffers of 25nm, 50nm and 100nm in thickness. All resulting films had a good c-axis orientation.

As shown in Fig.3.21, the properties of these films were investigated with dc-SQUID measurements. Films with a 25nm buffer showed a decrease in T_c down to 70K, while films with 50nm and 100nm showed a T_c above 87K. J_c self-field showed an increase with increasing buffer thickness. As we have seen in section 3.2.1, a decrease in properties is possibly related to liquid reactivity with the substrate which causes large secondary phases and therefore affects the percolation of current in the films. These results support our previous findings. The probability of the liquid reaching the substrate will be higher for lower thicknesses of the YBCO PLD buffer, since less time is needed to dissolve the buffer. In the case of 25nm buffer layers, there will be more areas with reactivity and a worse percolation of current, while in 100nm buffer layers the reactivity will be more localized, as supported by these films
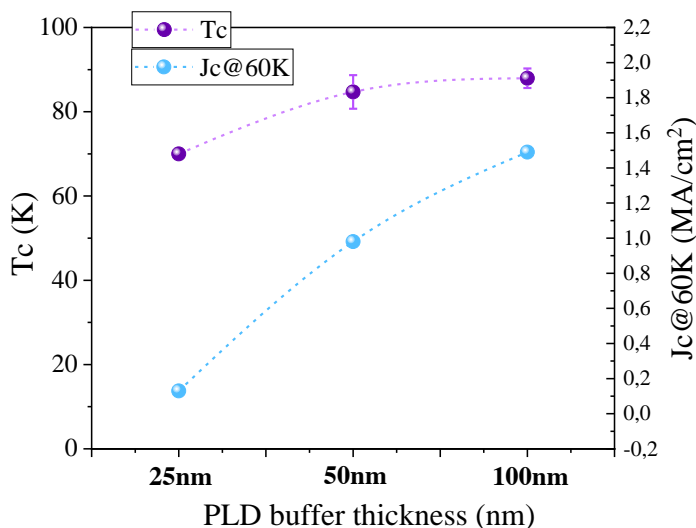
FIGURE 3.21: T_c and J_c at 60K of films grown on top of different YBCO PLD buffer thickness at 25ºC/s until 835ºC.

showing the best superconducting performances. It is to be expected that for a certain buffer thickness there will be no spots in which the liquid has been able to dissolve the full thickness of the layer, in which case no reactivity should be observed. To analyse if a 100nm buffer layer can avoid reactivity, TEM investigations were performed as shown in Fig.3.22
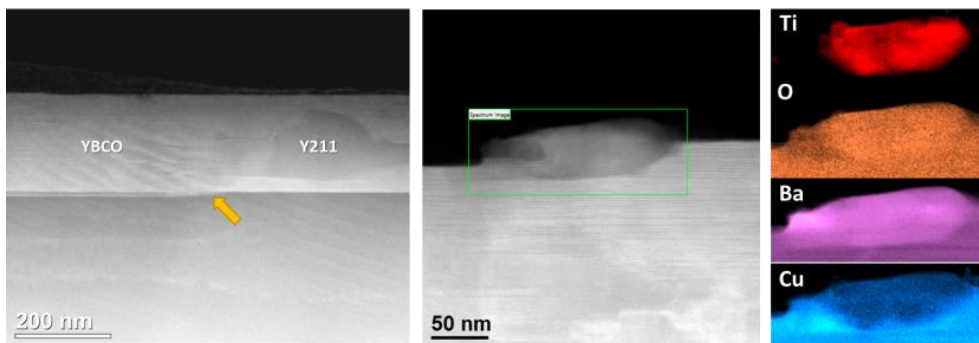

FIGURE 3.22: TEM images and EDX scans of a 12%BaZrO$_3$ film grown on a 100nm PLD buffer layer at 25ºC/s.

The film shows a good quality c-axis growth but we can also observe steps in the substrate surface and big Y211 particles, as well as some particles containing titanium at the film surface. The fast kinetics of liquid-related reactions are once more revealed. In the few seconds between liquid formation and complete YBCO growth when reactivity will no longer be possible, the liquid is able to locally dissolve 100nm of YBCO, react with the substrate and push products of this reaction to the film surface. This approach to prevent reactivity is therefore limited, since 100nm of buffer layer represents half of the film thickness and still presents reactivity. If we want to block the reaction between the liquid and $SrTiO_3$ or other substrates, a material that is inert to [Ba-Cu-O] liquid is needed. If no reaction is observed, properties will not depend on the buffer layer thickness. Furthermore, a thin YBCO buffer layer could still be used to improve the texture of nanocomposite films since we have demonstrated that a 25nm layer has the desired effects.

3.2.4 Films with increased percentage of nanoparticles

To investigate the effect of the density of nanoparticles in the YBCO, films with 24%$BaZrO_3$ were grown with different heating ramps and on top of 50nm PLD buffer layers. As shown in Fig.3.23 (a), the amount of random nucleation was influenced by the percentage of nanoparticles. Films grown at 25ºC/s were epitaxial in the case of 12%$BaZrO_3$ but had a substantial amount of random nucleation for 24%$BaZrO_3$. Full textured films with 24% of both $BaZrO_3$ and $BaHfO_3$ were achieved with ramps of 30ºC/s and higher. The effect that the introduction of nanoparticles has on the nucleation of YBCO is increased when the density of nanoparticles is higher, since more nucleation sites might be occupied by the nanoparticles at the growing interface. Nonetheless, a small increase in heating ramp can once again overcome this problem.

This allows us to prove once more how the processing conditions of this growth methodology can be finely tuned to achieve the desired orientation, since a small change in heating ramp and therefore in reaction temperature can obtain the desired effects. It is easy to envisage how a broader range of nanoparticles percentages on YBCO could be used by fine tuning the growth conditions. The versatility of this process is an important advantage for scalability.

The properties of these films were investigated with dc-SQUID. Fig.3.24 shows J_c self-field and T_c of 12 and 24% $BaZrO_3$ films grown at 30ºC/s. The mean values of nanocomposite films of every density grown with this heating ramp still need to be optimized regarding reactivity which causes current percolation problems. Nevertheless, we can compare the results between these two films grown under the same conditions to extract the effect of increasing
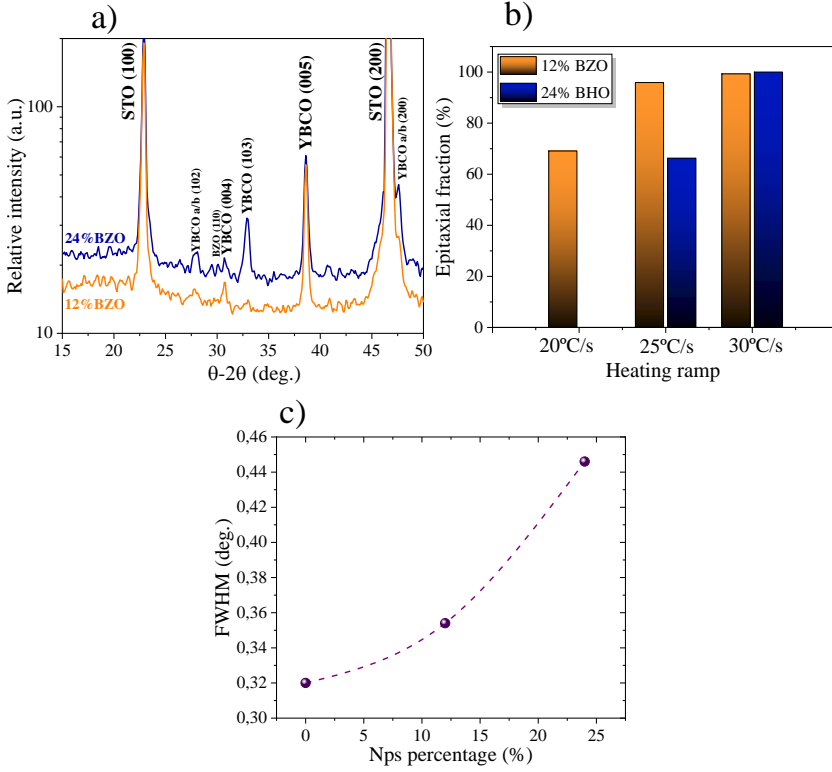
FIGURE 3.23: (a) θ-2θ patterns for 12 and 24% BaZrO$_3$ grown at 25ºC/s. (b) Measured epitaxial fraction for 12 and 24% BaZrO$_3$ and BaHfO$_3$ grown with different heating ramps. (c) Rocking curves of films grown at 30ºC/s with different BaZrO$_3$ percentage.

the molar percentage of nanoparticles. Both T$_c$ and J$_c$ were lowered in the 24%BaZrO$_3$ films in comparison with 12%BaZrO$_3$. A 12%BaZrO$_3$ film has a T$_c$ of 87.8K while in the 24%BaZrO$_3$ film is lowered to 86.2K. J$_c$ self-field at 5K is also reduced from 8.7MA/cm^2 to 6.2MA/cm^2. This decrease in properties attributed to the higher density of nanoparticles can have its origin in the fact that when nanoparticles are closer to each other the tendency towards aggregation or agglomeration is higher. Nonetheless, it is remarkable that TLAG nanocomposite films can accommodate up to 24% molar percentage of BaZrO$_3$ with only a slight decrease of the critical current density values. If we calculate the volume fraction that a 24% molar of BaZrO$_3$ occupies in a YBCO film by taking into account the volume of both unit cells, this high amount of secondary phase is occupying 9.2% volume fraction of the YBCO matrix. These results are evidencing the potential to obtain films with a high density of artificial pinning centers once the J$_c$ self-field values are optimized.
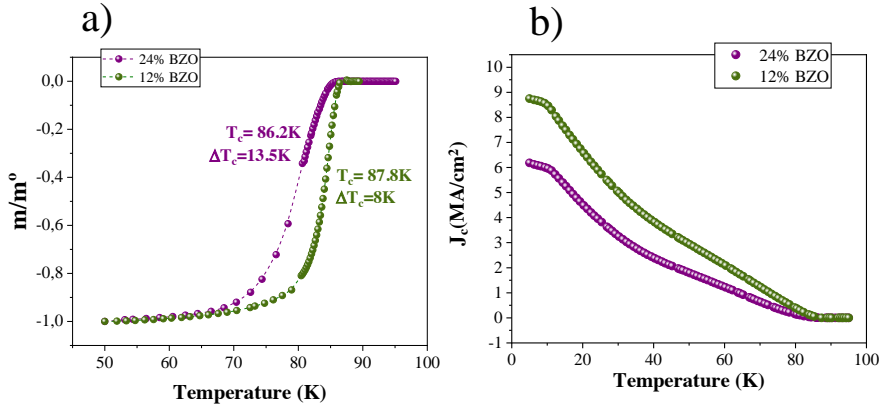
FIGURE 3.24: Properties of 12 and 24% BaZrO$_3$ films grown at 30ºC/s measured by SQUID. (a)T$_c$ and ΔT$_c$. (b) J$_c$ self-field versus T.

3.3   Growth of YBCO nanocomposites through eutectic liquid composition

In the two previous sections we have analysed the growth of YBCO nanocomposite films originating from chemical solutions with a relationship between Y:Ba:Cu of 1:2:3. This is the straightforward choice since it's the stoichiometry of the final product. Nevertheless, the other described methodologies working with the Ba-Cu liquid such as HLPE usually work with another stoichiometry, due to the characteristics of the BaCuO$_2$-CuO phase diagram. The relationship between Ba and Cu will establish liquid characteristics and if its different than the stoichiometric 2:3 relationship it will also imply and excess of one of the two metals. Furthermore, the amount of yttrium dissolved in the liquid, i.e. the supersaturation, will depend on the liquid composition. In this section we will analyse films with a Y:Ba:Cu relationship of 1:2:4,66. This composition keeps the stoichiometric relationship of Y with Ba in YBCO while having an excess of Cu. In this way, the relationship between barium and copper is 3:7.

We must consider the phase diagram of CuO and BaCuO$_2$ as shown in Fig.2.23 from [87]. These two components form an eutectic system that has a certain stoichiometry in which there's a congruent melting at the lowest possible temperature, called the eutectic temperature. Other stoichiometries will have a range of temperatures in which the liquid coexists with a solid

fraction before achieving complete melting at higher temperatures, the liquidus temperature. YBCO has a Ba:Cu stoichiometry of 2:3. We have demonstrated how we can grow through a transient liquid with this composition, but tuning the stoichiometry of the system could allow us to explore different supersaturation conditions and temperatures where the liquid is obtained. The eutectic composition, with a relationship of 3:7 between Ba and Cu was explored in Soler's thesis [62] and introduced in Chapter 2. We have shown how the eutectic composition has faster barium carbonate elimination with different intermediate phases as compared to 2:3 relationship in Fig.2.25. Another important difference is the lower temperatures required to have a Gibbs free energy promoting c-axis growth in the eutectic composition, as shown in Fig.2.33 due to the difference in supersaturation. After investigating different factors, the optimal conditions for epitaxial growth of pristine YBCO in eutectic liquid films were found to be at 770°C, with $PO_2=1\cdot10^{-3}$bar and a heating ramp of 20°C/s, on top of LSAT substrates. The remaining excess copper from the initial precursor solution is found as CuO particles on top of the film, not detrimental to texture or properties.

A film with 12%BaZrO$_3$ was grown in the same conditions as the investigated pristine layers. As shown in Fig.3.25 (c) the nanocomposite film is completely epitaxial. Fig.3.25 (b) shows the integrated X-ray pattern with no remarkable difference between the pristine film and the nanocomposite. SEM images also show a homogeneous film surface microstructure. Contrary to nanocomposite films grown with 2:3 composition, introducing pre-formed nanoparticles into the films didn't have any effect on the c-axis nucleation for the eutectic liquid composition. This result indicates how tuning the conditions towards lower supersaturation is crucial for the nucleation of c-axis YBCO. When supersaturation is high such as for 2:3 relationship, the Gibbs free energy for c-axis nucleation is similar or higher that the one for other orientations [97]. We are able to overcome this by lowering supersaturation through increasing temperature. For the same temperature, 3:7 composition has a much lower supersaturation, and therefore the lower Gibbs free energy towards c-axis nucleation avoids that small secondary phases such as the introduced nanoparticles affect the YBCO c-axis nucleation. Being able to use the same processing conditions both for pristine and nanocomposite films presents the clear advantage of more easily optimized and comparable properties, as well as avoiding higher heating ramps that intensify reactivity.

The properties of 3:7 nanocomposite films were measured by SQUID and compared to pristine layers as shown in Fig.3.26. T_c of 12%BaZrO$_3$ is 90.5K and for the pristine film is 87K. Although it might seem like the nanocomposite presents a higher T_c, we believe that these specific values are inside
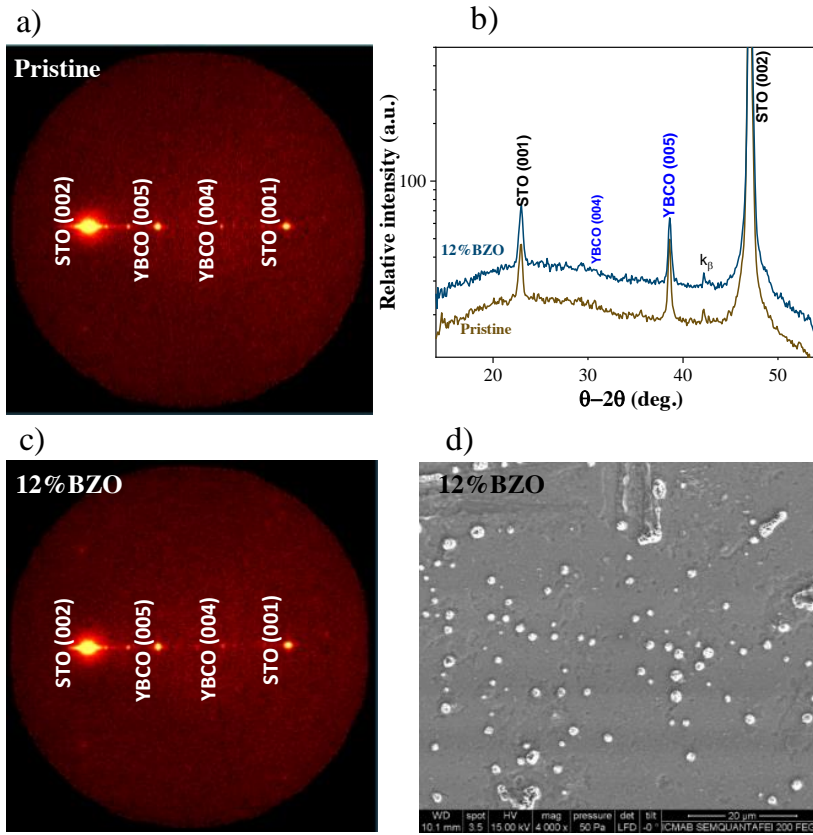
FIGURE 3.25: (a) and (c) 2D-XRD GADDS image frame from pristine and 12%BaZrO$_3$ films. (b) Integrated θ-2θ patterns. (d) SEM image of a 12%BaZrO$_3$ film grown from 3:7 liquid composition.

of the variability between samples grown in the same conditions. Thus, the addition of nanoparticles doesn't have any effect on the transition temperature. Both films present a rather large ΔT_c, which might be an indication of still current percolation problems in the samples. J$_c$ self-field at 5K is slightly larger for the pristine film but the values at 77K are very similar, of 1MA/cm^2 for the nanocomposite film and 0.9MA/cm^2 for the pristine one. This result confirms that TLAG films with preformed nanoparticles can attain the same J$_c$ self-field values than pristine films, therefore opening the possibility of exploiting all their potential benefits for vortex pinning when magnetic fields are applied. Nonetheless, the J$_c$ self-field at 77K value of 1MA/cm^2 is lower than values reported for other YBCO growth methodologies and should be optimized [104, 120].
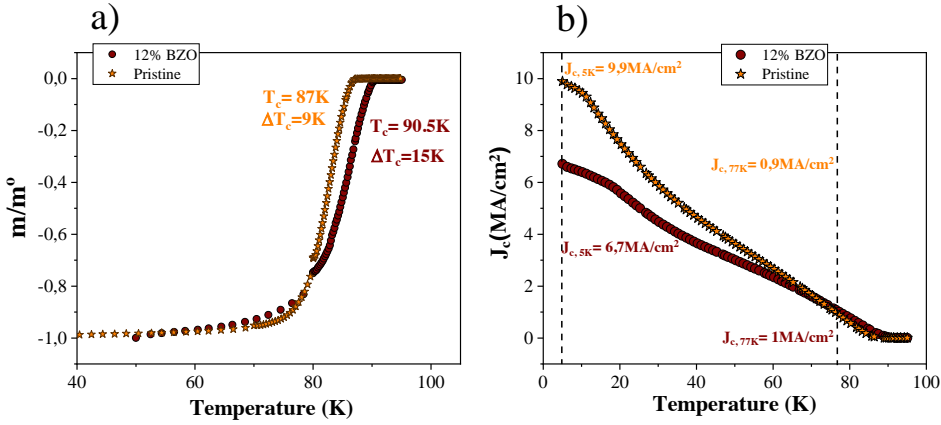
FIGURE 3.26: SQUID measurements for pristine and 12%BaZrO$_3$ films grown with 3:7 composition. (a) T$_c$ measurements. (b) J$_c$ self-field versus temperature.

Fig.3.27 shows SQUID measurements performed at 5K of critical current density versus an applied magnetic field reaching 5 Tesla. These SQUID measurements evaluate until which magnetic field the films can effectively pin vortices, preventing the dissipation of current. As shown in Fig.3.27 (b), which presents the normalized values for easier comparison, the J$_c$ plateau is very similar for pristine and nanocomposite films. The H* is an arbitrary value to evaluate the change between different pinning regimes. It is defined as the magnetic field in which J$_c$ has decreased until 90% of its maximum value. More details on this concept can be found in the introduction. In this case, H* is 0.07T for the nanocomposite film and 0.05T for the pristine film. This value is comparable to other methods of YBCO but the nanocomposite films lack a clear improvement of vortex pinning. More detailed analysis of measurements under magnetic field will be carried out in the following chapter.

Fig.3.28 shows TEM images of a 12%BaZrO$_3$ film of 3:7 composition. The layer is fully c-axis oriented, as confirmed by X-ray diffraction patterns, and the film is compact and homogeneous as observed in Fig.3.28 (a). Nanoparticles are homogeneously distributed, and the film presents a high density of long stacking faults. Small a/b grains embedded in the c-axis oriented matrix, such as shown in Fig.3.28 (c) were also found, similarly to those observed in pristine films [62]. These small a/b grains are not thought to have a detrimental effect on the properties due to their small size, which could enhance the vortex pinning capabilities of the film. The c-axis orientation and long stacking faults were observed in all the images obtained for this film.

However, some areas of the same sample showed nanoparticles aggregated or coarsened occupying the full thickness of the sample. As shown in Fig.3.29
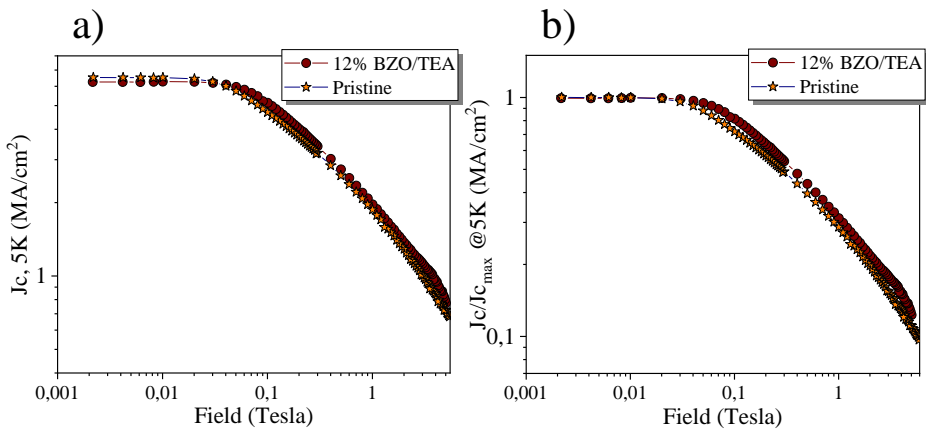
FIGURE 3.27: SQUID measurements of critical current density versus applied magnetic field of pristine and 12%$BaZrO_3$ films grown with 3:7 composition. (a) J_c values at 5K (b) Normalized J_c against maximum values at zero applied field.
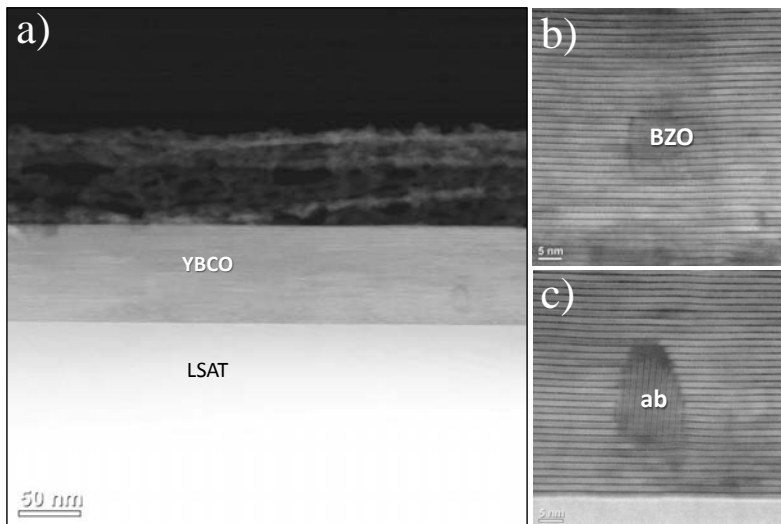

FIGURE 3.28: Low and high magnification TEM images of a
3:7 nanocomposite film grown at 770ºC.

the nanoparticles can aggregate to form big particles on top of the YBCO film. Some of the aggregates were smaller in size, only consisting of a few particles. Such aggregates can block the percolation path of the current and therefore lower the critical current density of the film. However, the measured J_c by SQUID is very similar for pristine and nanocomposite films, indicating

that these aggregates are not dominating the percolation characteristics of the films.
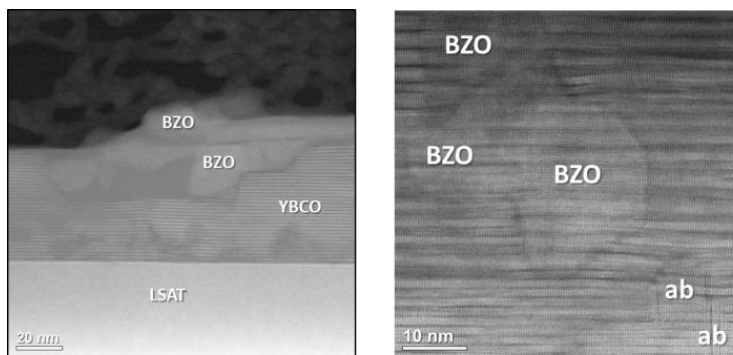
FIGURE 3.29: TEM images of $BaZrO_3$ aggregates in a 3:7 nanocomposite film.

We conclude that only a small fraction of the nanoparticles have aggregated, although quantification through TEM is difficult. Nonetheless, this aggregates need to be avoided in order to exploit the pinning abilities of the nanoparticles, which need to be of the same order of magnitude of the YBCO coherence length in order to act as pinning centers. Besides the possible problems caused by the aggregates of nanoparticles, Fig.3.30 shows other kind of microstructures found in the film. Some large a/b grains are observed which occupy the full thickness of the film and will therefore block the current transport as well. Also, we observe areas where two different YBCO grains have not merged and they are separated by voids of several hundreds of nanometers.
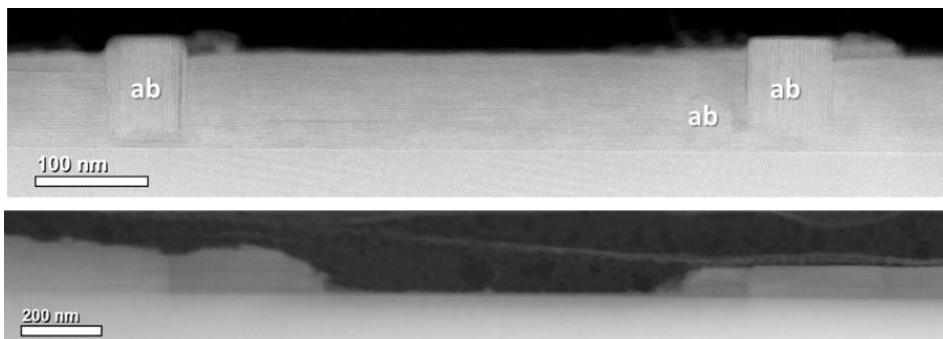

FIGURE 3.30: Granularity and big a/b grains observed by TEM in a 12%$BaZrO_3$ film of 3:7 composition.

This type of effects were also observed for pristine films grown under the same conditions in [62]. Its origin is attributed to bad wettability of the liquid during growth as well as low nucleation density created by the low supersaturation conditions, and thus we can conclude that the limited properties are due to induced porosity not related to the presence of nanoparticles. Since these effects are also observed in pristine films we believe they are the main reason for low critical current values and high ΔT_c. Therefore, in order to improve the superconducting performances of 3:7 nanocomposite films, one must first tackle the issues of liquid wettability affecting both the pristine and nanocomposite films. Strategies to investigate this problem could include increasing the yttrium content while maintaining the 3:7 relationship between Ba and Cu. This would increase the solid fraction of the system possibly increasing liquid viscosity during growth, as well as slightly increase supersaturation, augmenting the density of nucleation nuclei. Furthermore, increasing the thickness of the films could also decrease or get rid of wettability problems, since a bigger volume of liquid is less likely to separate into different droplets. In this sense the work on thick films presented in Chapter 5 could present solutions to the growth of pristine and nanocomposite films with 3:7 liquid.

3.3.1 In-situ X-ray studies

Transient liquid assisted growth process has been investigated by means of in-situ X-ray diffraction in Diffabs beamline at Soleil synchrotron. These studies helped to elucidate the reaction paths and growth rates of this methodology as has been described in [62] and Chapter 2 of this thesis. Experiments of in-situ X-ray diffraction were also carried out with films containing nanoparticles with the aim of understanding if the presence of preformed particles in the initial precursor film has any discernable effects on the growth reaction path and also to try to elucidate if the nanoparticles themselves suffer any changes during the growth process. To investigate the barium carbonate decomposition of nanocomposite films, samples with 24%$BaZrO_3$ and 24%$BaHfO_3$ were heated under the same conditions as pristine films. The evolution of $BaCO_3$ was followed by measuring the area of its main peak and plotted against temperature in Fig.3.31.

Both nanocomposite films show a similar onset temperature with pristine films of the barium carbonate elimination reaction, but the temperature at which the reaction is completed is higher in the case of nanocomposites. Barium carbonate is completely eliminated at 726°C in pristine films and at 772°C for both nanocomposite films. This accounts for different reaction times, raising the question of the nanoparticles possible effect on the growth mechanism.
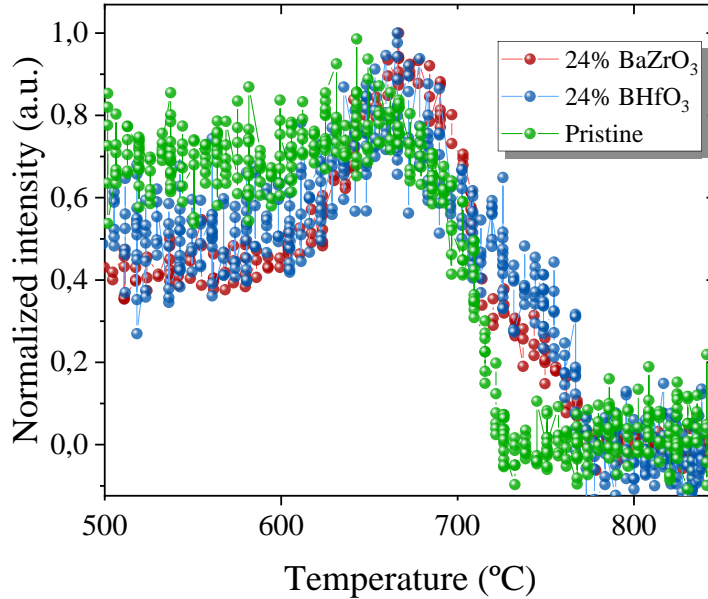
FIGURE 3.31: Evolution of integrated peak area through heating of barium carbonate phase in pristine and nanocomposite films. Heating speed of 5°C/s at $PO_2 = 1 \cdot 10^{-3}$bar.

$BaCO_3$ elimination requires the reaction between this compound and CuO, both present in the pyrolysed film in the shape of small particles. The presence of other materials in the precursor films could lower the area of contact between $BaCO_3$ and CuO and therefore delay the elimination reaction. With only this experiment to support this hypothesis, it is not possible to reach a conclusion, but it is an open question that should be taken into account in future experiments.

To follow the behaviour of the nanoparticles during YBCO growth, a film with 24%$BaZrO_3$ was placed in the chamber and heated at 5°C/s until 840°C at a $PO_2 = 1 \cdot 10^{-3}$bar. 5°C/s was the maximum allowed ramp of the system and a higher density of nanoparticles was used in order to ensure a high enough intensity of the nanoparticles peak.

An image was taken every 100ms during heating and cooling. The results of the experiment are shown in Fig.3.32, where the background has been subtracted for a better visualization of the main phases. YBCO starts to grow at 750°C, and the maximum conversion speed to c-axis oriented YBCO is reached at 840°C. In Chapter 2 we showed the growth rate of pristine films reaching
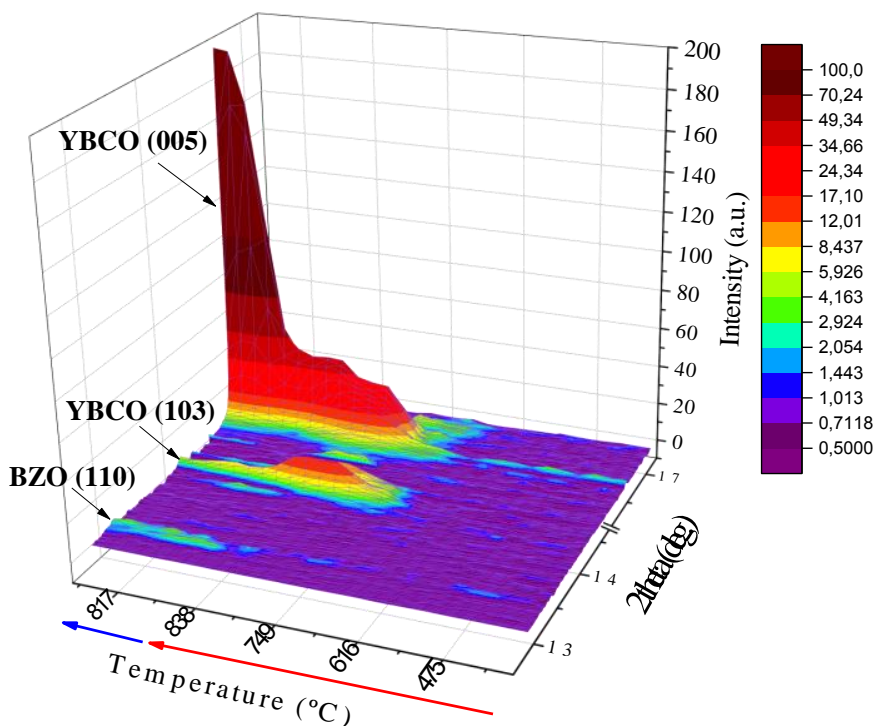
FIGURE 3.32: Integrated X-ray patterns versus temperature from in-situ synchrotron experiments, showing the evolution of (005) and (103) YBCO reflections and (110)BaZrO$_3$ reflection.

100nm/s, in the case of the nanocomposite film, the maximum rate was measured to be 90nm/s, a good agreement between both type of films, demonstrating that nanocomposite films can be grown at ultra-high rates through TLAG. In the first growth region, both YBCO(103) and YBCO(005) start to nucleate at a speed of 5nm/s. Above the eutectic line the system enters in the fast growth region where YBCO(005) is growing at 90nm/s and the randomly nucleated YBCO that had appeared in the previous region disappears, converting to epitaxial fraction. The conversion of randomly oriented grains to epitaxial orientation is rare and the mechanism for this conversion is an open research interest of SUMAN group. Other experiments have shown how these homogeneously nucleated grains can reorient at high temperatures thanks to the presence of the liquid. Furthermore, it is noteworthy that it can occur in such fast kinetics.

Regarding the nanoparticles, initial X-ray scans show no peak for the $BaZrO_3$ phase. As has been discussed in Chapter 2, TEM has shown that the nanoparticles are present with their original size in the pyrolysed films, but due to their small size or maybe due to a partial amorphisation of their surface, it is difficult to detect them by X-ray diffraction. In this experiment, we observed how the $(110)BaZrO_3$ peak, corresponding to randomly oriented nanoparticles, appears after YBCO has begun to grow. The nanoparticles peak reaches its maximum intensity at 840°C, 28 seconds after it is first detected, during the fast growth region of YBCO. There can be different explanations for this observation. One might think that at high temperatures the nanoparticles have more tendency to coarsen and therefore bigger particles will diffract more intensity than smaller ones. The fact that the appearance of the nanoparticles occurs during the growth of YBCO could indicate as well that the part of nanoparticles which are amorphous crystallize together with YBCO, therefore crystallizing at the same time as the material around it while being encapsulated by it. It is unclear at this point which is the real reason for this behaviour but it is interesting that the nanoparticles, while not affecting the final orientation of the film, are changing morphology or structure during the growth and therefore cannot be considered an inert part of the system.

3.4   Conclusions

In this chapter we have investigated the introduction of pre-formed nanoparticles to YBCO films grown through the temperature-route of TLAG. We have demonstrated that $BaZrO_3$ and $BaHfO_3$ nanoparticles are stable during growth while LaF_3 reacts with the [Ba-Cu-O] liquid and therefore is inadequate for the growth of nanocomposite films.

We have seen how the effect of the nanoparticles on nucleation is different depending on the liquid composition. While the presence of nanoparticles significantly increased the percentage of random nucleation in films of 2:3 liquid stoichiometry, 3:7 nanocomposite films remained epitaxial when grown under the same conditions as pristine samples. Therefore we have learned that nanoparticles can affect the growth mechanism of YBCO depending on supersaturation and reaction temperature.

In the case of 2:3 liquid composition, epitaxial films were achieved when a 50nm YBCO PLD buffer layer was used with heating ramps above 20°C/s. Tuning kinetic factors we can control the nucleation even when nanoparticles are present, as well as increasing the density of nanoparticles up to 24%$BaZrO_3$. The properties of these films decreased with increasing heating ramps due to the liquid reactivity with the $SrTiO_3$ substrates, which created

large secondary phases and therefore current percolation problems. A compromise is needed between high heating ramps to obtain c-axis texture and low heating ramps to avoid reactivity to achieve the maximum J_c self-field at 77K of 0.6MA/cm^2 at 25ºC/s. Further work should include the investigation of a non-reactive buffer layer which would get rid of this compromise. This issue will be addressed in Chapter 5.

Nanocomposites grown with 3:7 liquid composition reached the same properties as pristine samples, of 1MA/cm^2 at 77K grown at 20ºC/s. In this case the properties are limited by current percolation problems related to bad wettability of the liquid, which are also reported for the pristine films.

We have examined the defect landscape of the nanocomposite films finding that their microstructure and how nanoparticles introduce defects also depends on the growth processing conditions. The most favourable defect microstructure is found for films grown at 25ºC/s heating ramp, which present a very high density of stacking faults and where nanoparticles are inducing defects and distortions on the YBCO matrix.

In-situ X-ray studies have revealed how the BaCO$_3$ elimination requires longer reaction time when nanoparticles are present in the film. We have also shown how the XRD peak belonging to BaZrO$_3$ appears in the scans simultaneously to the growth of YBCO, opening the door to the possibility that nanoparticles recrystallize or coarsen during the growth process, as well as a growth rate of 90nm/s, in good agreement with pristine films values.

In conclusion, we have shown how pre-formed nanoparticles are compatible with YBCO growth through temperature-route of transient liquid assisted growth and that these nanoparticles can be favourable to create an optimum defect landscape for vortex pinning depending on the processing conditions. J_c self-field values can reach up to 1MA/cm^2 which still can be further optimized.

Chapter 4

Nanocomposite films through PO$_2$-route

Transient liquid assisted growth is a versatile methodology that allows different processing paths to arrive to the desired phase diagram conditions. In the previous chapter we have analysed how to obtain nanocomposite films through the so-called temperature route, that is, fast heating at constant PO$_2$ until reaching the desired final temperature. In this chapter we will analyse a different route, in which the heating stage is performed at very low PO$_2$ conditions where YBCO is not stable [94]. When the desired temperature is reached, a fast jump in PO$_2$ will place the system in conditions for epitaxial YBCO growth. This route has a reaction path that disentangles the decomposition of precursor phases from YBCO growth. Previous work on this route has shown that the best texture and performance is achieved when the 3:7 Ba:Cu stoichiometry is used[62, 64]. More details on the different reactions and conditions can be found in Chapter 2. In this chapter we will analyse how pre-formed and spontaneously segregated nanoparticles can be embedded on the YBCO matrix to form YBCO nanocomposites and which are the properties of the resulting films.

4.1 YBCO crystallization with pre-formed BaZrO$_3$ and BaHfO$_3$ nanoparticles

The processing conditions chosen to start this investigation were selected in accordance to the results presented in Soler's thesis [62]. The rapid thermal annealing furnace gave the most reproducible samples for 90nm pristine films grown on SrTiO$_3$. The first step of the treatment was heating until 830ºC with

a heating ramp of 0.4ºC/s and at a PO$_2$=10^{-5}bar to allow the full decomposition of BaCO$_3$. After a dwell of 5 minutes at the final temperature, a jump in PO$_2$ was performed until PO$_2$=10^{-3}bar keeping the temperature constant. At this final PO$_2$ YBCO is grown and finally temperature is decreased. The oxygenation step is performed at 450ºC in a separate furnace. Pyrolysed films with 12%mol BaZrO$_3$ and 12%mol BaHfO$_3$ on SrTiO$_3$ were grown under these conditions.
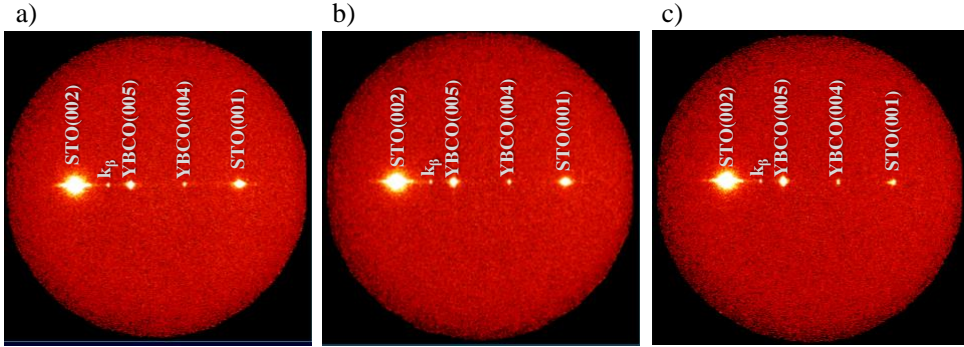

FIGURE 4.1: 2D XRD of films grown at 830ºC with PO$_2$ jump from10^{-5} to 10^{-3}bar of (a) a pristine film, (b) 12%mol BaZrO$_3$ nanocomposite and (c) 12%mol BaHfO$_3$ nanocomposite.

Fig.4.1 shows the 2D X-ray diffraction patterns for (a) a pristine films, (b) a 12%mol BaZrO$_3$ nanocomposite and (c) a 12%mol BaHfO$_3$. We can observe how all samples are fully c-axis textured with no trace of random or a/b nucleation.
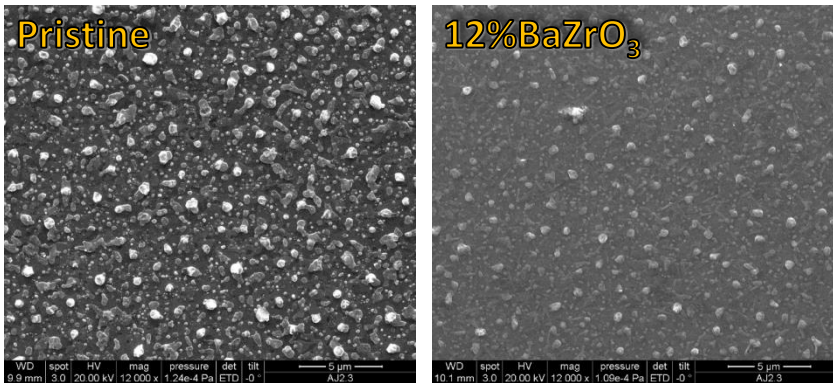
FIGURE 4.2: SEM images of films grown at 830ºC with PO$_2$ jump from 10^{-5} to 10^{-3} bar of (a) a pristine film and (b) 12%mol BaZrO$_3$ nanocomposite.

The surface microstructure of the films was observed by SEM as shown in Fig.4.2. The surface is homogeneous and non-porous, and many small particles are observed on the surface, which are identified as Cu-oxide due to the use of a 3:7 liquid that has an excess of copper with respect to YBCO stoichiometry. The SEM images show no significant difference between pristine and nanocomposite films, as well as in the case of XRD patterns. If the growth of YBCO through PO$_2$ route can accommodate small pre-formed nanoparticles with no change in the nucleation mechanism it will be easier to study and compare their properties and explore the full potential of nanocomposite films.

In order to test different nanoparticles densities and their possible effect on nucleation, films with BaZrO$_3$ and BaHfO$_3$ percentages ranging from 6 to 32% molar were grown using the same previously defined conditions.
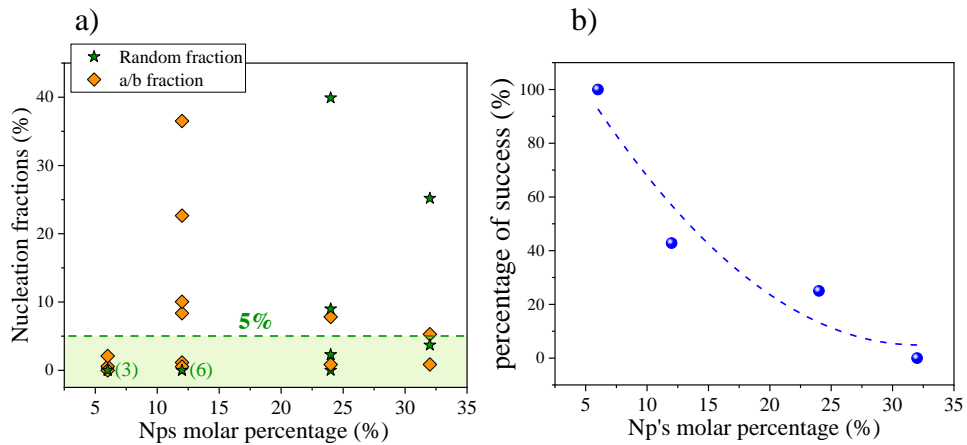
FIGURE 4.3: (a) Percentage of random and a/b nucleation for films grown with different nanoparticles percentages. (b) Total percentage of samples with random and a/b nucleation below 5%.

The resulting X-ray patterns were analysed to quantify the amount of random nucleation and a/b grains present in the samples. Random nucleation fraction was quantified integrating the area of YBCO peaks for the (005) and (103) reflections, with the formula:

$$Random fraction = \frac{Area(103)}{Area(103) + Area(005)} * 100 \qquad (4.1)$$

To measure a/b nucleation fraction we compared the intensities of the (102) peak for c-axis and a/b oriented grains, and the detailed methodology can be found in Appendix A. Since BaZrO$_3$ and BaHfO$_3$ are equal regarding size and

do not present any difference to the final texture of the film, the results of both nanocomposite samples are mixed and shown in Fig.4.3 (a).

The analysis of several samples reveals a certain irreproducibility that depends on the molar percentage of nanoparticles. We consider that a percentage of random or a/b nucleation of 5% or lower is not detrimental to the sample as will be explained below, when the properties are discussed. When 6% molar of nanoparticles are added, both a/b and random grains fractions remain below 5% in all samples. When the percentage of nanoparticles is increased until 12%mol BaMO$_3$ (M=Zr,Hf), not all samples exhibit the same nucleation. Although all films have virtually 0% of random nucleation, the amount of a/b grains varies between 0 and 37%. In the case of samples with 24% and 32% molar of nanoparticles, the a/b grains appear to be less important, only reaching up to 8% in some occasions, while in these cases the random nucleation increases in many samples arriving up to 40%. Therefore, there's a significant variability for samples grown under the same conditions. The percentage of success, understood as the number of samples which have both a/b and random nucleation below 5%, decreases when increasing the nanoparticle density as show in Fig.4.3 (b). In the case of 12%BaMO$_3$ films the unsuccessful samples present a/b nucleation while films with higher density of nanoparticles have a tendency towards random nucleation. In terms of Gibbs free energy for nucleation, the most stable crystalline orientation depends on supersaturation, as introduced in Chapter 2. At low supersaturation values c-axis nucleation presents the lowest energy, while a/b orientation has a similar energy range when supersaturation is slightly increased. Both of these epitaxial orientations are part of heterogeneous nucleation, which is more thermodynamically stable than homogeneous nucleation also at low supersaturation. When supersaturation is high, random or homogeneous nucleation will compete with epitaxial growth. Therefore, it seems like the addition of nanoparticles has a similar effect than increasing supersaturation, since within the same processing conditions, a small percentage of nanoparticles will induce a/b nucleation and in higher amount of nanoparticles, random nucleation will be more prevalent.

In order to analyse the effect of a/b nucleation on the resulting superconducting properties SQUID measurements were performed on 6% and 12% nanocomposite films. The obtained J$_c$ self field at 77K are shown in Fig.4.4 versus their amount of a/b grains. Two different areas can be clearly observed. When a/b nucleation is below 5%, the J$_c$ has a range from 1.3MA/cm^2 up to 2.2MA/cm^2. When a/b grains represent more than 5% of the film, J$_c$ is limited to 0.4MA/cm^2. It appears that there's not a progressive decrease of properties but rather a critical value above which the current percolation in the film is blocked by the a/b grains. The detrimental effect of a/b grains on J$_c$ has
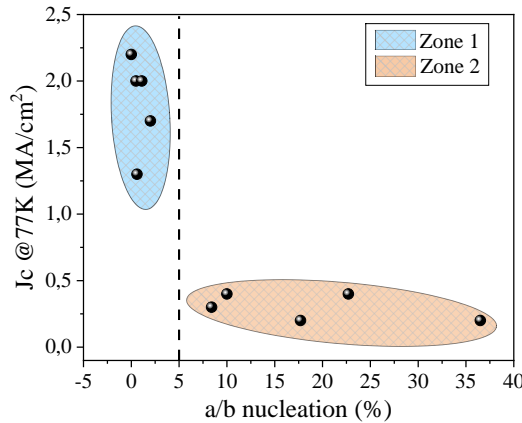
FIGURE 4.4: SQUID measurements of Jc-self field at 77K versus percentage of a/b nucleation in 6% and 12% BaMO$_3$ films.

been observed in other CSD methodologies such as TFA [51, 121–123]. Therefore, to achieve films with good superconducting properties we will need to eliminate a/b nucleation.

4.1.1 Superconducting properties: current percolation study

Fig.4.5 shows SQUID measurements for samples with less than 5% of a/b grains. Since there are no films that have both a/b and random nucleation below 5% in the case of 24% and 32% nanocomposites, we have chosen to include the samples with random nucleation above 5% to be able to analyse the SQUID measurements.

In general, there is a tendency towards decreasing superconducting properties with increasing nanoparticles density in both BaZrO$_3$ and BaHfO$_3$ nanocomposites. The values of T$_c$ and ΔT$_c$ are similar for both types of nanoparticles in 6% and 12% densities, while they differ in the case of higher molar percentages. Nonetheless, these differences are possibly attributed to variations in the random nucleation present in the samples. In the case of J$_c$ self-field, the values are very similar in all the studied range of nanoparticles densities.

Given the similarity observed in the nucleation behaviour and basic superconducting properties of BaZrO$_3$ and BaHfO$_3$ nanocomposites, there is a clear indication that nanoparticles of similar structure and size will behave equally during YBCO growth. This will allow us to consider these nanocomposites
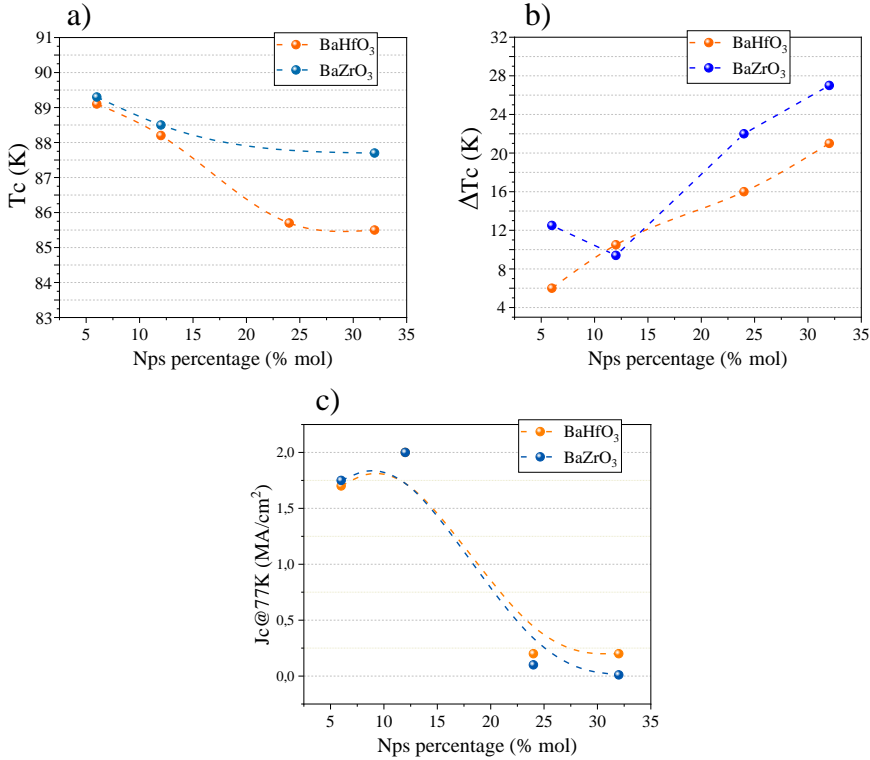
FIGURE 4.5: SQUID measurements of BaZrO$_3$ and BaHfO$_3$ nanocomposites of different percentages grown through PO$_2$ route. (a) T$_c$ (b) ΔT$_c$ (c) J$_c$-self field at 77K.

as equivalent in a first approximation, in order to analyse them together for statistical purposes.

We can see how increasing the percentage of nanoparticles, critical temperature decreases and ΔT$_c$ increases. While 6%mol. and 12%mol. nanoparticles maintain a T$_c$ above 88K and ΔT$_c$ below 13K, higher BaMO$_3$ percentages can decrease T$_c$ down to 85.5K and ΔT$_c$ up to 27K which indicates strong current percolation difficulties on the samples. This effect is similar to that observed in nanocomposites grown through temperature route in Chapter 3. The reason of this decrease is different depending on the percentage. The 6% and 12% nanocomposites measured with SQUID have virtually no a/b or random nucleation, and therefore the nanoparticles themselves might have an effect on diminishing the percolation of current, specially if aggregation or agglomeration exists. Above 12% molar, we have measured samples containing randomly oriented YBCO grains, which can also cause current blocking in addition to the high percentage of nanoparticles. These two factors affecting

current percolation could account for the steep decrease in J$_c$ self-field in the case of 24% and 32% nanocomposites. A more detailed analysis of the microstructure is needed to understand the detrimental effect of a high density of nanoparticles.
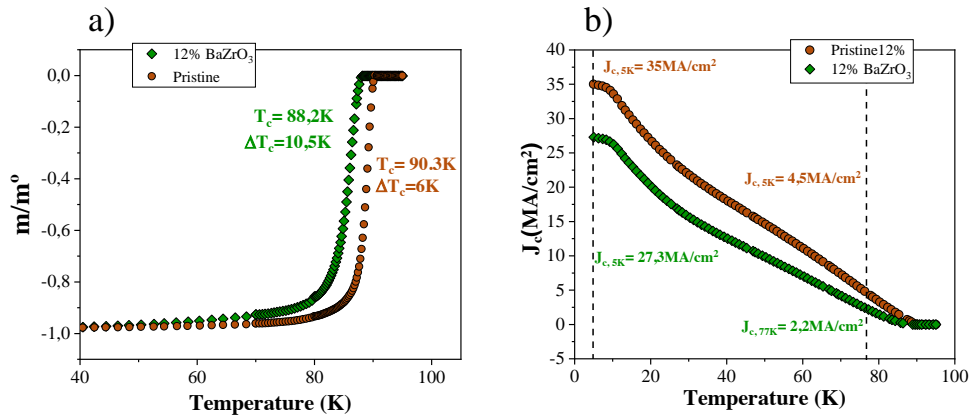

FIGURE 4.6: SQUID measurements of a pristine and a 12%BaZrO$_3$ film (a) Critical temperature. (b) J$_c$ vs temperature.

However, the nanocomposites with a lower density of nanoparticles of 6% and 12% present good J$_c$ self-field values in a range between 1.7 and 2.2MA/cm^2 at 77K. These films have good current percolation and are interesting candidates to investigate the vortex pinning under applied magnetic fields. In order to compare these samples with the best SQUID values reached for pristine films, Fig.4.6 shows the T$_c$ and J$_c$ versus temperature of a 12%BaZrO$_3$ nanocomposite and a typical pristine film grown through PO$_2$ route. We can see how T$_c$ is slightly lowered for the nanocomposite with respect to the pristine film, and J$_c$ self-field is also decreased; there's a factor 2 at 77K while at 5K the difference is a factor of only 1.3, with the 12%BaZrO$_3$ film reaching 27.3MA/cm^2 with respect to 35MA/cm^2 for the pristine film. The reason for this decrease will need to be investigated with detailed microstructure analysis, such as STEM shown later in this section, in order to design strategies for nanocomposite films to reach the high J$_c$ values available through PO$_2$ route. Nonetheless, we need to take into account that both type of films present good current percolation and that these nanocomposite films were grown with the optimized conditions for pristine samples. Thus, further investigations in fine-tuning the processing conditions for nanocomposites could still render an increase in properties.
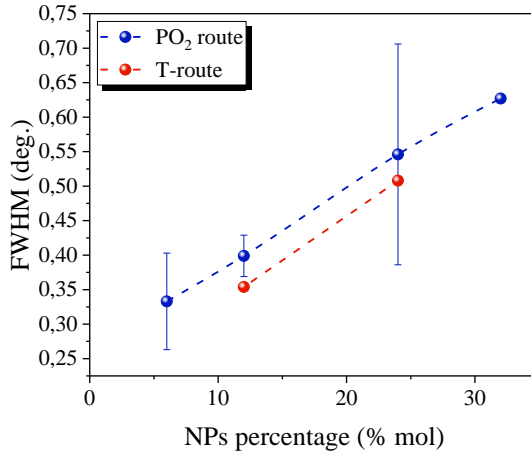
FIGURE 4.7: FWHM values obtained from rocking curves of nanocomposites with different percentages of nanoparticles.

Fig.4.7 shows the full width at half maximum of rocking curves measurements. We can observe a linear increase of FWHM with the density of nanoparticles in the films. This is similar to what was observed in Chapter 3, indicating that nanoparticles are affecting the uniaxial texture of the films. High rocking curve values as those detected for 24% and 32% molar percentage indicate some misalignment of the c-axis oriented YBCO grains, which would be in agreement with a decrease in properties. Nonetheless, the FWHM values all fall below 1°, and thus their values are not high enough to conclude that the bad current percolation comes solely from this YBCO misorientation.
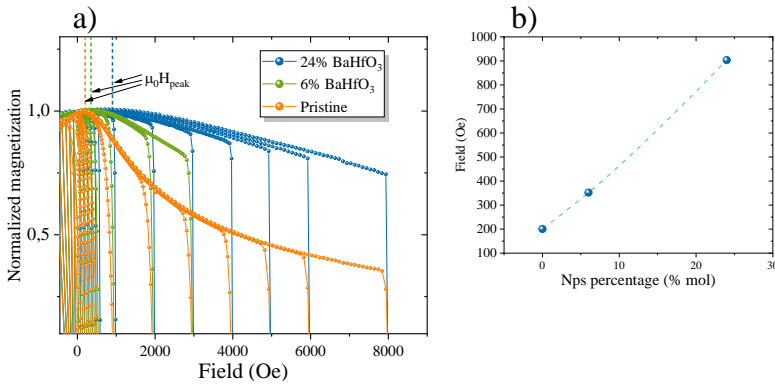
FIGURE 4.8: a) Applied magnetic field versus magnetic moment of a pristine sample, a 6% and a 24% BaHfO₃ nanocomposites. b) The granularity peak position versus nanoparticles density.

In order to detect current percolation properties, measurements of magnetic moment minor loops versus applied field were performed in SQUID. Fig.4.8 shows the positive branch of the magnetization loops of a pristine YBCO film and two different nanocomposites. When a magnetic field is applied and then decreased, current loops are generated through grain boundaries and currents are created around the grains. Therefore when the applied field is reduced, we will see a peak in magnetization when the reverse flux through grain boundaries is minimized [124]. This peak is an indication of magnetic granularity and can be compared for samples with the same thickness and grain size. Only when no grain boundaries exist within the sample, a peak in the magnetization at H=0 is observed. Several loops are performed with increasing maximum applied field until saturation of the magnetization peak is achieved. As shown in Fig.4.8 a), increasing nanoparticles percentage increases the peak's field as plotted in Fig.4.8 b). Thus, it is possible that introducing nanoparticles to the YBCO matrix increases the magnetic granularity of the films, which is detrimental to the percolation of current [125, 126].
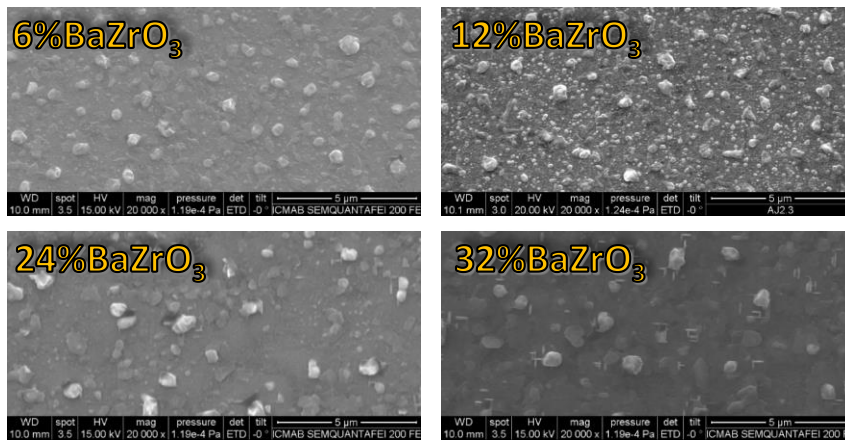
FIGURE 4.9: SEM images of nanocomposite films with different nanoparticles percentages.

To elucidate any possible relationship between the magnetic granularity (or in general the decrease in properties) and morphology of the films in nanocomposites with different nanoparticles percentages, SEM images were taken as shown in Fig.4.9. The surface of the films remains non-porous and homogeneous, with no indication of reactivity or agglomeration of secondary phases. The small particles observed in the surface belong to CuO, a by-product of YBCO growth when the 3:7 liquid composition is used, which contains an excess in Cu. In this case we observe how the density of CuO in

the surface slightly decreases with increasing nanoparticles percentage, which could indicate that the remaining copper might be trapped inside of the film's matrix.
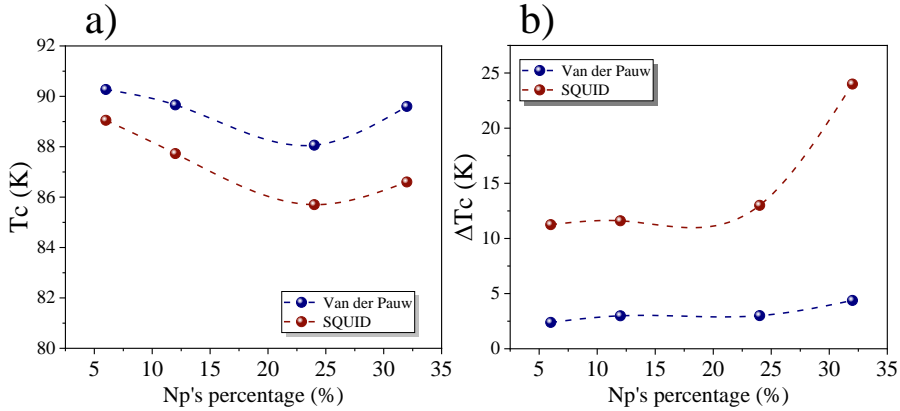

FIGURE 4.10: SQUID and Van der Pauw measurements of nanocomposites with different molar percentages. (a)T$_c$ (b)ΔT$_c$.

Fig.4.10 compares the T$_c$ and ΔT$_c$ values obtained by SQUID and Van der Pauw transport techniques. It has already been introduced how Van der Pauw measurements are sensitive to the material's properties and defects such as atomic substitution and strain, while SQUID T$_c$ decreases depending on the current loop percolation of the film. In this case, it is clear that the tendency is the same in both types of measurement, with T$_c$ decreasing and ΔT$_c$ increasing with nanoparticles percentages. Therefore, we must investigate factors beyond current percolation difficulties such as magnetic granularity. The effects that can play a role in lowering T$_c$ as measured by Van der Pauw are atomic substitution in the YBCO matrix, strain on the lattice or oxygen content. From this options, the one that seems more likely to be linked to the density of nanoparticles is strain between the nanoparticles and the YBCO matrix. A decrease in T$_c$ due to nanoparticles-generated strain was observed in PLD nanocomposites where the BaMO$_3$ nanoparticles where found to be epitaxially aligned with the YBCO crystalline lattice [127–129].

The strain created in the YBCO can be evaluated through the value of the c-axis parameter. High resolution XRD scans were used to calculate the c parameter of several nanocomposite samples and pristine films. Fig.4.11 shows the different values against nanoparticles density. It is clearly observed how introducing nanoparticles in the film increases the lattice parameter due to strain. The mismatch between BaZrO$_3$ and YBCO is ∼8%, a very high value that in nanocomposites with nanorods is shown to create dislocations in the
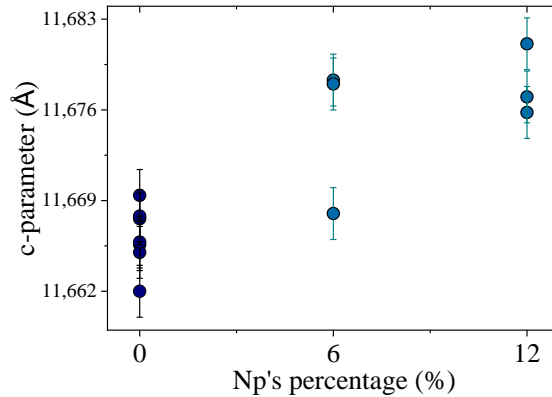
FIGURE 4.11: Calculated YBCO c-parameter for pristine and nanocomposite films grown through PO$_2$ route. Error bars correspond to the standard deviation in the linear regression determination.

epitaxial interface between YBCO and BZO, as well as oxygen vacancies [130]. In our case the high mismatch is also creating strain, which can lead to suppression of T$_c$, and a more detailed analysis of the orientation of nanoparticles inside the YBCO matrix will be performed in following sections.

To observe the microstructure of the films and further investigate the reason behind the decrease of T$_c$ and J$_c$ self-field with nanoparticles density, STEM images and EELS scans were performed. Fig.4.12 shows images of a 12%BaZrO$_3$ film. Small nanoparticles in the range of 5-15nm in diameter can be observed in the whole thickness of the sample. We observe that even when the nanoparticles are near the substrate interface, there's always at least one unit cell of YBCO that has nucleated on the substrate. This indicates the characteristic of the liquid of being able to wet the full substrate and impede for the nanoparticles to directly attach to the substrate interface. Some of the particles have coarsened increasing in size from the original 4nm until 10-20nm, but still keep a good distribution within the sample. Furthermore, the observed nanoparticles are epitaxially aligned with YBCO, supporting our theory that the decrease in T$_c$ could be related to strain effects. A quantitative analysis of the nanoparticles orientation will be performed in section 4.2.

If we observe a 24%BaHfO$_3$ film, shown in Fig.4.13, EELS scans clearly detect big aggregation of nanoparticles which can be observed in the signal from hafnium. Particles of tens of nanometers in width are dispersed in the YBCO matrix, sometimes occupying the whole thickness of the film. Therefore suggesting that coarsening and agglomeration of nanoparticles is promoted by the higher nanoparticles percentages.
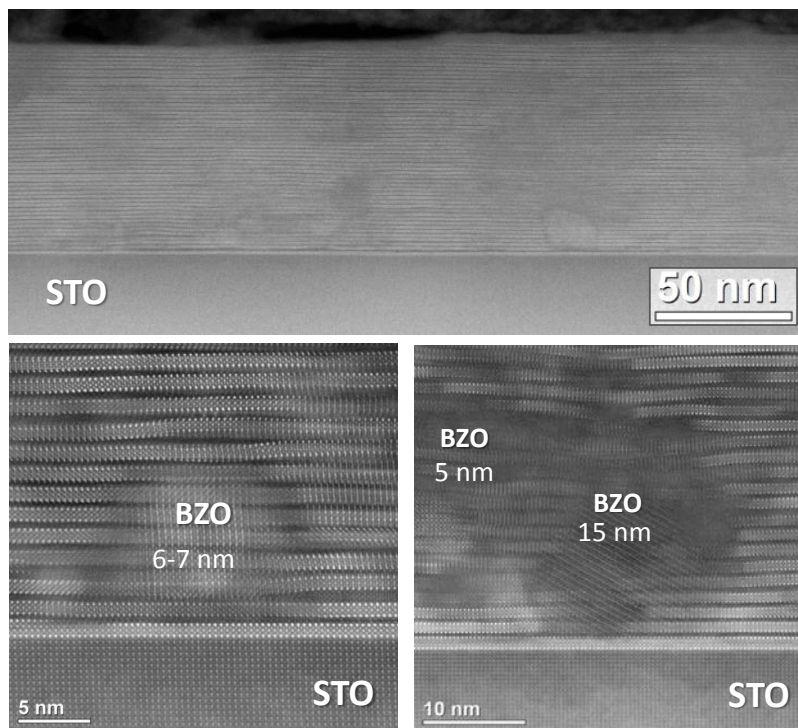
FIGURE 4.12: TEM images of a 12%BaZrO$_3$ film with different
magnifications showing nanoparticles of slightly different size
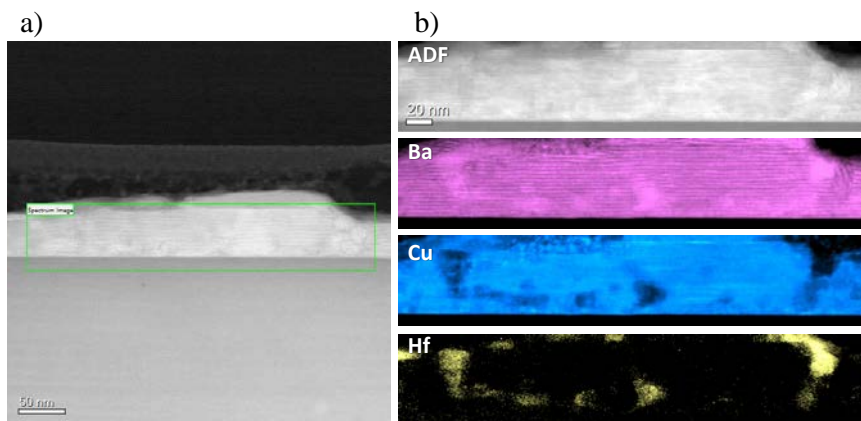

FIGURE 4.13: STEM images of a 24%BaHfO$_3$ film. (a) Low magnification image with
the green square marking the area for the EELS scan.(b) EELS analysis of several
elements present in the film.

It is remarkable that even with such a high density of big particles the nucleation of YBCO is not perturbed, as even surrounding the coarsened BaHfO$_3$ the YBCO matrix maintains its c-axis orientation. Nonetheless, the current percolation on these films will be very affected by the reduced superconducting cross-section that the particles create. Fig.4.14 shows a general view of the sample, where a high density of nanoparticles can be appreciated.
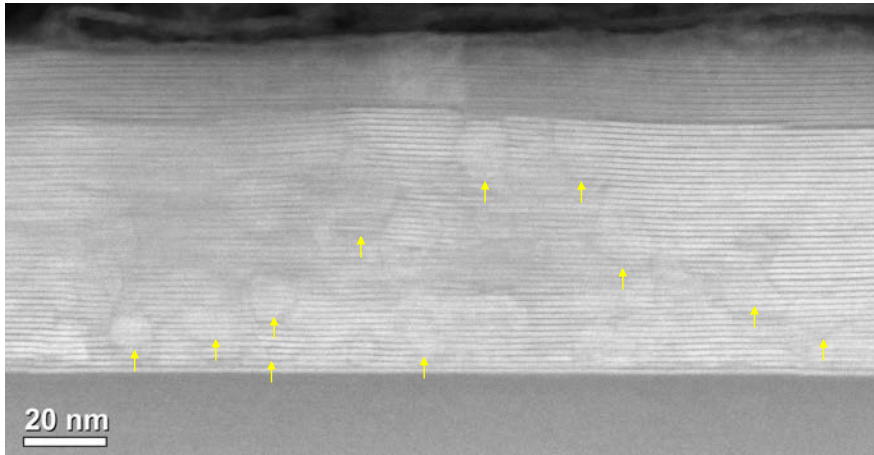
FIGURE 4.14: STEM image of a 24%BaHfO$_3$ film showing BaHfO$_3$ particles of different sizes as indicated by yellow arrows.

The size of the nanoparticles varies from their original 4nm up to 20nm. These findings correlate with the reduced J$_c$ of nanocomposites with densities higher than 12% molar, since the cross-section of YBCO will be reduced in these films. The difficulty in current percolation is worsened by the low thickness of the films. Increased thickness would provide more percolation paths and therefore improve J$_c$ self-field. Furthermore, if the coarsening and agglomeration of nanoparticles is avoided, the obtained films would have a big potential for vortex pinning, and therefore, further work should include investigating which step of the film processing leads to this behaviour.

4.1.2 Seed layer effect on nanocomposite films

For the PO$_2$ route, the final oxygen partial pressure and temperature have been optimized to low supersaturation conditions that promote c-axis aligned growth. Furthermore, by eliminating barium carbonate before YBCO growth and reaching the desired growing conditions in a fast manner, the c-axis growth is robust and reproducible in pristine films. Due to this robustness and optimized supersaturation conditions, introducing pre-formed nanoparticles to

the system does not impede the c-axis growth in the same conditions and epitaxial samples can be obtained for a wide range of nanoparticles densities. However, we face the problem of irreproducibility when increasing nanoparticles percentages above 6%, and approximately half of the samples with 12%BaMO$_3$ have a certain contribution of a/b nucleation, as shown in Fig.4.3. Thus, although some samples are fully epitaxial and show good superconducting properties, other samples grown under the same conditions show other crystalline orientations which is detrimental to the properties of the films. As we are studying a complex system with many entangled process variables, the origin of the observed irreproducibility could not be identified, and even when the same initial conditions are achieved, still some small inhomogeneities can lead to, in our case, different nucleations. One option to solve this irreproducibility would be to fine tune the supersaturation conditions to adapt to the nanoparticles presence.

In our case, we attempt reducing the possible presence of a/b or random nucleation while maintaining the same processing conditions, by tackling the interface with the substrate where c-axis nucleation occurs. To this end, a layer without nanoparticles in the first nanometers of the film was envisaged; this is, creating a seed layer by depositing a thin pyrolysed pristine YBCO layer and adding the pyrolysed nanocomposite film on top. Both layers will be grown at the same time, creating a final film with no interface between the two layers but avoiding the contact of the nanocomposite directly with the substrate. Several such films with nanoparticles percentages ranging from 6 to 24% BaMO$_3$ were grown under the standard PO$_2$ route conditions.
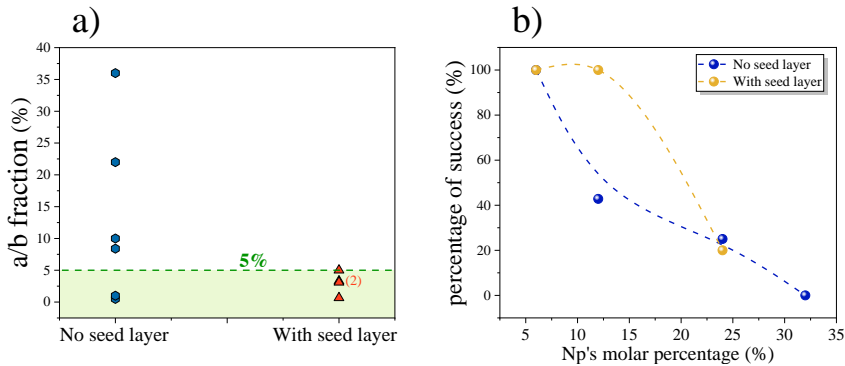

FIGURE 4.15: (a) Measured a/b fraction of 12%BaMO$_3$ films grown on top of seed layer and directly on the substrate. (b) Percentage of samples with a/b grains or random fraction below 5% for 12%BaMO$_3$ films with and without seed layer.

Fig.4.15 (a) shows the measured a/b fraction of 12%BaMO$_3$ nanocomposites grown with and without seed layer. The observed variability on a/b nucleation of these films when grown directly on the substrate disappears when the seed layer is introduced. All 12%BaMO$_3$ measured films on seed layer have an a/b fraction equal or lower to 5%, thus, using this additional layer is an effective way to ensure c-axis growth not being disturbed by the nanoparticles embedded in the liquid, and eliminating unsuccessful samples. Fig.4.15 (b) shows the percentage of samples with full c-axis orientation depending on the percentage of nanoparticles, with and without seed layer. Although the seed layer is useful in the case of 12%BaMO$_3$ films, when this percentage is increased up to 24%, the samples still show a relevant amount of random or a/b nucleation.
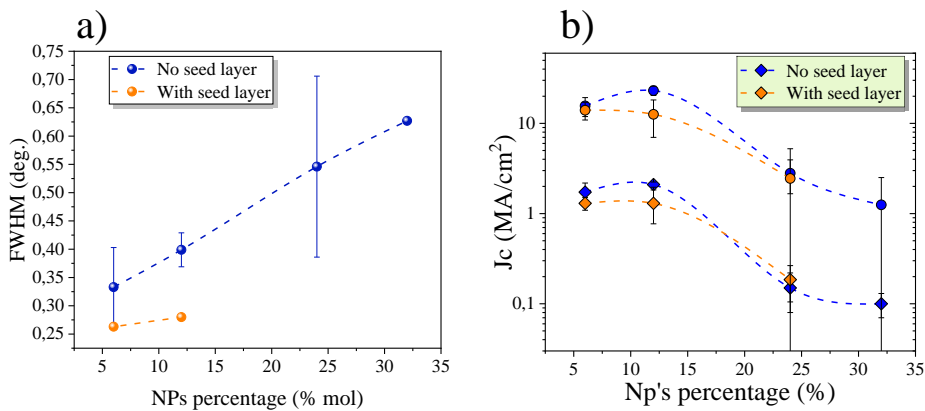
FIGURE 4.16: (a) FWHM from rocking curves of nanocomposites grown with and without seed layer. (b)J$_c$ self-field at 77K of the same samples as (a). Error bars in both graphs correspond to standard deviation between different samples.

To understand better the effect that a seed layer has on the films crystallization, rocking curve measurements were performed on samples with seed layer and compared to the values obtained for films grown directly on the substrate, as shown in Fig.4.16 (a). The use of seed layer decreases the values of FWHM, indicating that the crystallinity of YBCO increases when the YBCO grains nucleate at the bare substrate interface. Nonetheless, the rocking curve values are very low for both types of films, and therefore it is unlikely that this slightly better texture will have a strong effect on the superconducting properties.

J$_c$ self-field was measured by SQUID and compared to the films without seed layer that are 95% or more epitaxial, as shown in Fig.4.16 (b). We can see how the values of J$_c$ are very similar for the two type of films, and at 12%

molar percentage of nanoparticles the mean value of J_c is higher in the case of samples without seed layer. To conclude on the effect of a seed layer, we must separate the case of 12% of nanoparticles from the films with 24 or 32%. In nanocomposite films containing 12% of nanoparticles, there is a clear difference between samples with and without seed layer, since the seed layer avoids any unwanted a/b nucleation. Nonetheless, critical current density and T_c have very similar values regardless of the presence of the seed layer, indicating that the decrease of superconducting properties with respect to pristine films is still governed by strain and magnetic granularity. In the case of 24% or above percentages, the seed layer is not effective in preventing random nucleation, with the YBCO growth still being disturbed by the high volume fraction of nanoparticles. Further work should include the fine-tuning of growth conditions in order to tackle the issues that the seed layer has not improved.

4.2   Microstructural features of nanocomposite films
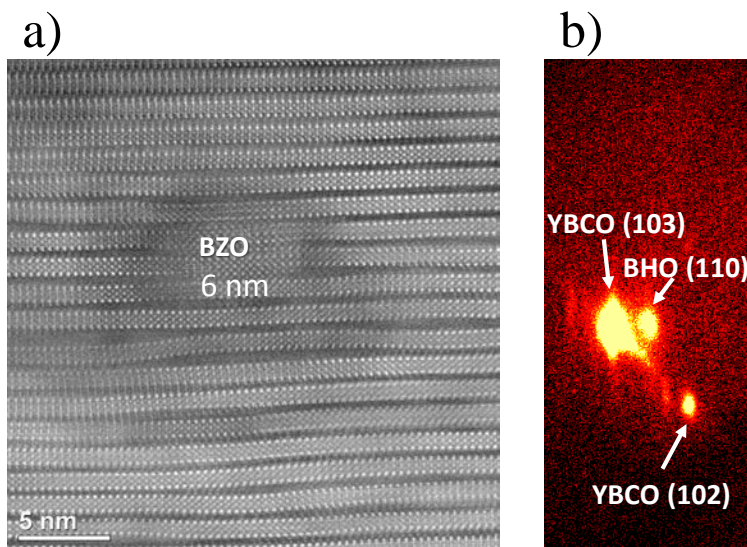
FIGURE 4.17: (a) TEM image of an epitaxial nanoparticle embedded in the YBCO matrix. (b) 2D frame of the BHO (110) reflection.

A YBCO nanocomposite film consists of particles of small nanometric diameter embedded in the YBCO crystalline matrix. Their potential effect as pinning centers will depend on their size and on the characteristics of the interface between the two materials, where lattice distortions or defects are created. By adding pre-formed nanoparticles we intend to pre-define the size

and shape of the pinning centers, but we need to take into account possible changes to the nanoparticles during the growth process as well as how they will be integrated in the YBCO crystalline matrix.
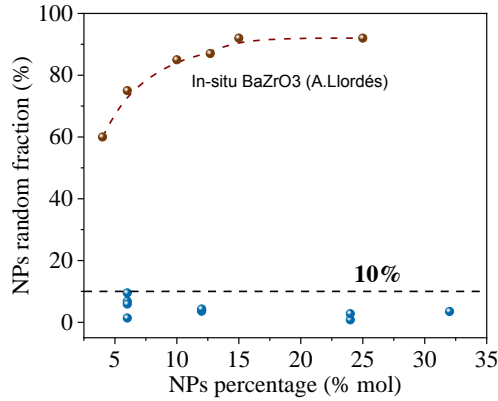

FIGURE 4.18: Nanoparticles random fraction measured for different molar percentage nanocomposites and compared to values reported in [131].

Fig.4.17 (a) shows a STEM image detail of a small nanoparticle embedded in the YBCO matrix. The YBCO structure presents one of the most common defects observed in CSD YBCO films: stacking faults or Y124 intergrowth, which consists of the addition of an extra CuO chains layer [114, 116]. The defects observed in our nanocomposite films will be studied in more detail in section 4.4. Moreover, we can observe that the YBCO planes are epitaxially matched to those of the nanoparticle, which probably is the cause of the additional CuO chains intercalated. To quantify the amount of nanoparticles that are epitaxially aligned, the 2D-XRD detector can be used to detect the most intense peak of BaZrO$_3$ phase, which is the (110) reflection. The epitaxial peak of this plane family appears at an angle of χ=45°, therefore a scan at this position was performed during 1 hour to accumulate enough intensity from the ring (polycrystalline fraction) and the pole (the epitaxial fraction). The results of one of such scans are shown in Fig.4.17. We can observe how all the intensity of the peak falls in the pole while no ring is detected. We can calculate the random fraction by the formula 4.2, explained in Appendix A.

$$\frac{I_{random}}{I_{pole}} = \frac{I_{ring}^{exp}\left(\frac{360}{\Delta}\right)4\pi}{8 I_{pole}^{exp}} \tag{4.2}$$

The random fraction of nanoparticles was calculated for films with different percentages of $BaZrO_3$ and $BaHfO_3$. As shown in Fig.4.18 all the measured samples had a random fraction equal or lower than 10% for all the studied range of nanoparticle density. This indicates that most of the nanoparticles are epitaxially oriented with the YBCO crystalline matrix. Such a behaviour of the nanoparticles is surprising since most CSD methodologies report a high $BaZrO_3$ random fraction as shown in Fig.4.18 by Llordés et al. [131, 132]. Under these processing conditions and film thickness, the growth of the YBCO film occurs in approximately one second, due to the high growth rates demonstrated in Chapter 2. It is therefore remarkable how the fast kinetics of the process still enable the nanoparticles to rotate during growth to become epitaxially aligned with the surrounding crystalline matrix. The reason behind this behaviour must lay behind the system trying to minimize its surface energy by avoiding incoherent interfaces, therefore favouring epitaxy. The liquid assisted process enables the rotation and the minimization of the surface energy. In other CSD methodologies such as TFA, the solid-gas reaction does not enable the rotation of the nanoparticles, which are embedded with random orientations, even though the growth process is much slower (~1nm/s). In these cases the incoherent interface of nanoparticles have been linked with strain and additional defects that can act as pinning centers [132], therefore the effect of this different behaviour of nanoparticles in TLAG films will need to be correlated with pinning properties of the films, in following sections.

4.2.1   In-situ XRD analysis of PO₂-route nanocomposites

During the time of this thesis our project had the opportunity to use Soleil Diffabs beamline for in-situ X-ray studies, as introduced in other chapters. An experiment to follow the behaviour of the nanoparticles during the PO_2 process was carried out with a 2 layers precursor film of 24%$BaHfO_3$. A thick film with high nanoparticles density was used to ensure a high enough intensity of the nanoparticles phase. To observe the diffraction coming from epitaxially aligned nanoparticles, the detector was placed at an angle of χ=45° similarly to the in-house X-ray scans shown in Fig.4.18. The film was heated under low PO_2 conditions and after the desired temperature of 850°C was reached, a jump in PO_2 was performed until PO_2=10^{-3}bar. The integrated scans were analysed and the main peaks are shown in Fig.4.19. The experimental conditions were different than those used to demonstrate 100nm/s growth rate in pristine films. Therefore the growth rate of YBCO in this experiment was estimated to be 30nm/s, which is significantly lower than the pristine films values but in the same range. Further experiments should include using the
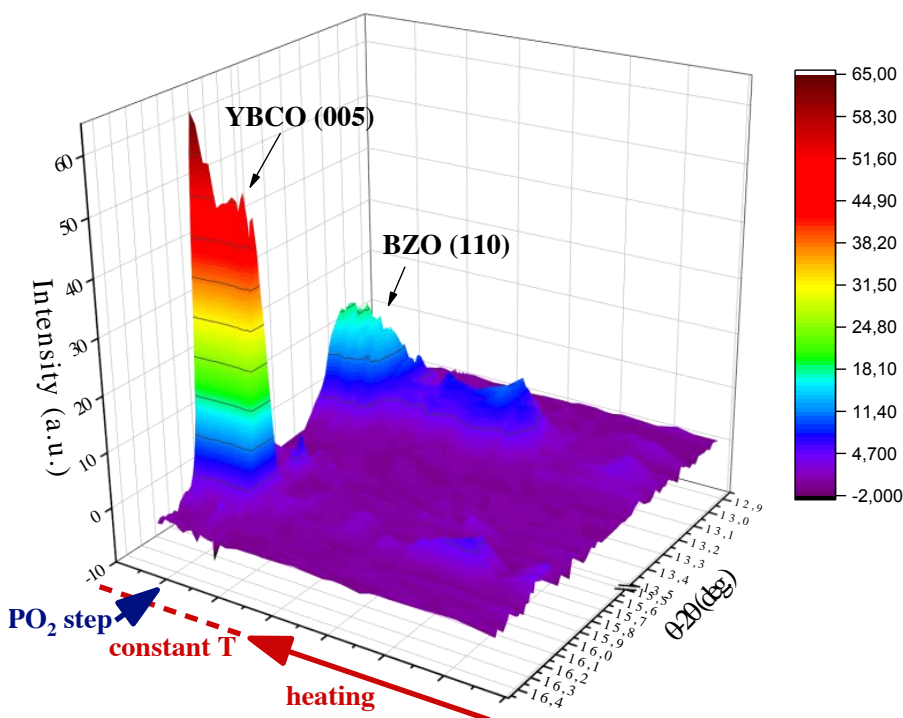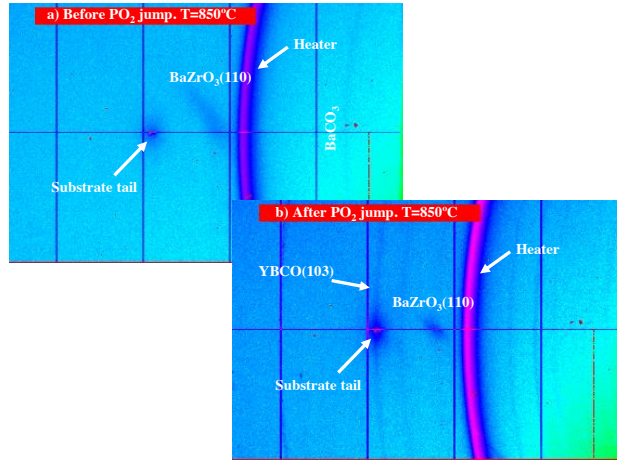
FIGURE 4.19: Synchrotron In-situ X-ray scans of a 24%BaHfO$_3$ nancomposite grown through the PO$_2$route with a jump between 10^{-6}bar and 10^{-3}bar done at 850ºC.

optimal conditions for high growth rate in order to demonstrate the maximum growth rate of nanocomposite films.

We can see that the peak of the nanoparticles is not visible during the heating stage, but appears before the pressure jump is performed, with a low intensity. When the pressure is changed, the growth of YBCO is very abrupt and the BaHfO$_3$ peak increases its intensity simultaneously. The initial increase in intensity could be attributed to some recrystallization of the randomly oriented nanoparticles. When YBCO is crystallized, the nanoparticles reorient themselves with the crystalline matrix giving the rise in intensity of the epitaxial part of the nanoparticles. Fig.4.20 shows the 2D frames of before and after the pressure jump, showing that the epitaxial peak of the nanoparticles as a pole in the X-ray frame only appears after the PO$_2$ jump. Thus, we can confirm that the crystallization of YBCO leads to the reorientation of BaHfO$_3$ to a coherent interface between both phases. The processing conditions of this experiment were different than the conditions used to demonstrate high

FIGURE 4.20: Synchrotron In-situ X-ray scans of a 24%BaHfO$_3$ nanocomposite grown through the PO$_2$route with a jump between 10^{-6}bar and 10^{-3}bar done at 850ºC.
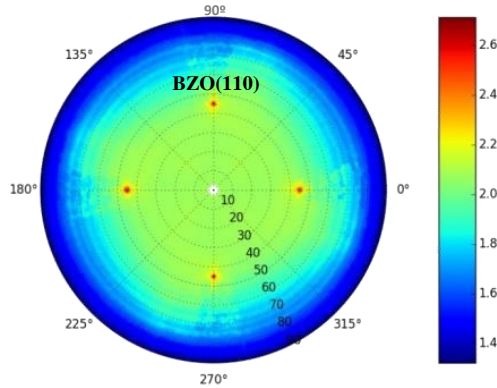

FIGURE 4.21: Pole figure obtained in Soleil synchrotron of BZO (110) reflection.

growth rates in pristine films shown in Chapter2. Therefore, we cannot compare growth rate values but we do not foresee a relevant difference between nanocomposite and pristine films values.

The epitaxy of the nanoparticles on the final film was confirmed by measuring a pole figure of the (110) peak of BaHfO$_3$ phase, as shown in Fig.4.21. We want to remark again this impressive result that emphasizes the fast kinetics of the liquid-assisted process.

4.3 YBCO growth with spontaneously segregated nanoparticles

Obtaining YBCO films with embedded nanoparticles can be attained through different methodologies. When YBCO is grown through physical deposition techniques such as PLD, the simultaneous deposition of YBCO and BZO by means of a mixed target allows the spontaneous segregation of $BaZrO_3$ aligned along the c-axis, forming nanoparticles or nanorods depending on the conditions, due to strain energy minimization [36, 133]. In the case of chemical solution deposition, the nanoparticles cannot be introduced during the growth process but need to be included in the precursor film. Depending on when the $BaMO_3$ phase is synthesized, we can distinguish between two type of nanocomposites. This chapter has been dedicated to ex-situ grown nanocomposites where pre-formed nanoparticles need to be stabilized in the YBCO precursor solution. The second option, extensively explored in literature, is to include the metal precursors of the nanoparticles phase in the precursor solution in order that the nanoparticles are spontaneously segregated (ss) during the growth process [53, 134–136]. This methodology has the drawback of having poor control of the size and composition of the nanoparticles, usually obtaining nanoparticles in the range of 20nm in diameter. Nonetheless, during the growth process it is possible to create defects induced by the nanoparticles, which have been shown to effectively increase vortex pinning. In this section we will show a preliminary study on how to grow TLAG nanocomposite films through spontaneous segregation techniques.
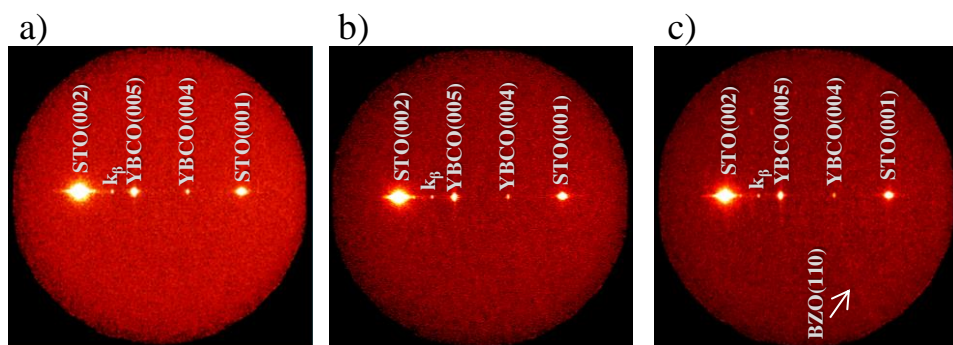

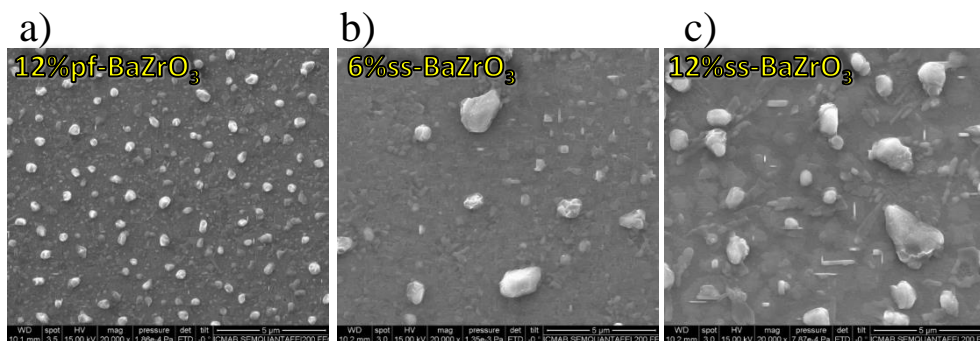FIGURE 4.22: GADDS 2D XRD of (a) preformed nps nanocomposite and (b) 6% in-situ nanocomposite (c) 12%$BaZrO_3$ in-situ nanocomposite grown through PO_2 route.

Zr(Ac)$_2$ was added to 3:7 YBCO precursor solution as well as the necessary amount of Ba(Ac)$_2$ to form $BaZrO_3$ and also keep the molar relationship

of YBCO between yttrium, barium and copper. The resulting solution was pyrolysed on top of SrTiO$_3$ and grown under the standard PO$_2$-route conditions. Two different molar percentages of BaZrO$_3$ were used, 6% and 12%. The 2D-XRD patterns of the resulting films are shown in Fig.4.22 (b) and (c) and compared to a nanocomposite grown with preformed nanoparticles in Fig.4.22 (a). The YBCO is fully c-textured for both 6% and 12% BaZrO$_3$. In the case of the 12% nanocomposite, a ring with 2θ: 30.1° is observed, which can be attributed to the BaZrO$_3$ (110) reflection, confirming that the desired phase has been grown during the process.

FIGURE 4.23: SEM images of (a) preformed nps nanocomposite and (b) 6% in-situ nanocomposite (c) 12% in-situ nanocomposite grown through PO$_2$ route.

Fig.4.23 shows SEM images for the same three films. The surface morphology shows some changes between pre-formed and spontaneously segregated nanocomposite films. The non-porous surface characteristic from liquid-mediated growth is present in both kind of nanocomposites. The pre-formed nanoparticles films show small CuO particles of approximately 0.5μm in diameter, while in the case of ss samples the particles on the surface are larger, reaching up to 2μm. The density of these big particles also increases with increasing BaZrO$_3$ percentage. EDX analysis was performed to try to detect the composition of these particles but the resolution is not high enough and no conclusive results were obtained.

Nanocomposites with spontaneous segregation methodology were grown also on top of seed layers. The SEM images of the resulting films are shown in Fig.4.24. The resulting morphology is very similar to those films without seed layer, with almost identical densities of big surface particles.

The properties of in-situ nanocomposites were studied by dc-SQUID. The T$_c$ and J$_c$ self-field of films with and without seed layer are shown in Fig.4.25. Although the texture and surface morphology of the films were very similar,
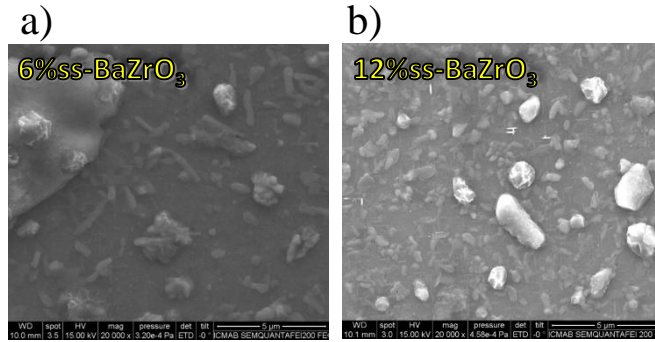
FIGURE 4.24: SEM images of in-situ nanocomposites grown
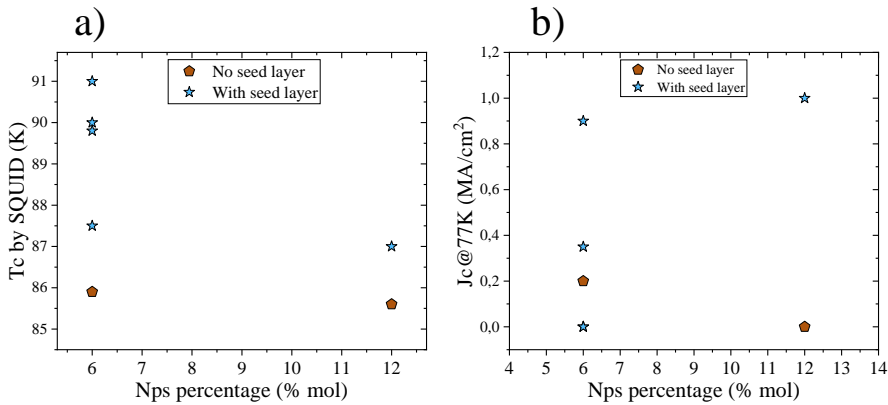on top of seed layers.

FIGURE 4.25: (a) T_c and (b)J_c self-field at 77K SQUID measurements of in-situ
nanocomposites of different %BaZrO$_3$ molar percentages.

the properties of the two types of films are very different. Films grown directly on the substrate showed very low T_c values and J_c self-field at 77K of
0.2MA/cm^2 or lower. On the other hand, seed-layered films showed critical
temperatures ranging from 87.5K up to 91K in the 6%BaZrO$_3$ samples and
a maximum of 87K T_c in the case of 12%BaZrO$_3$ films. J_c values were also
increased up to 1MA/cm^2 for both 6% and 12% films. The many factors influencing the superconducting properties of a film come into play, since these
films which have the same c-axis texture and surface morphology have very
different current percolation depending on the use of a seed layer.

STEM images of a 12%BaZrO$_3$ film grown on top of a seed layer are shown
in Fig.4.26. A layer of aggregated particles can be observed on top of the film.
Through the Fourier transformation of these particles they could be identified
as BaZrO$_3$. No nanoparticles were identified inside of the YBCO film, which
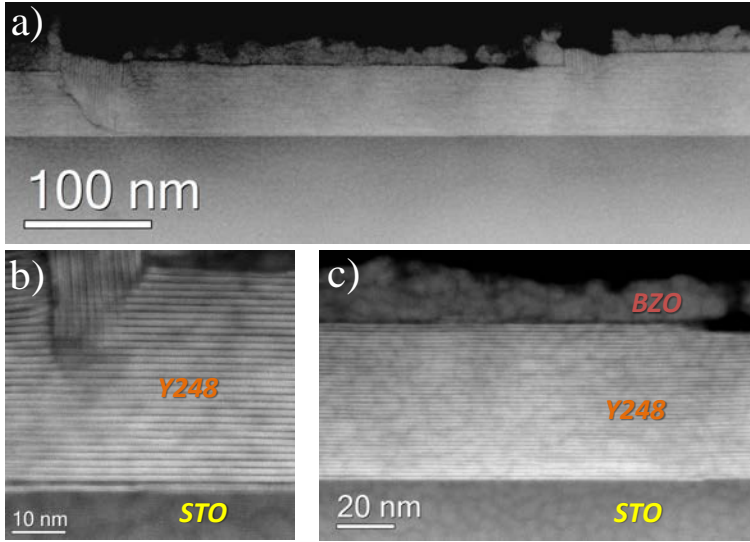
FIGURE 4.26: STEM images of an in-situ 12%BaZrO₃ film
grown on top of a pristine seed layer.

presents a full 248 stacking, this is, an extra layer of CuO chains in every unit
cell. All the images obtained from this film show an homogeneous sample of
c-axis oriented YBCO with few other defects besides the Y248 intergrowths.
The reason for a J_c self-field 4 times lower than a pristine sample grown un-
der the same conditions has to be related to the addition of spontaneous seg-
regation nanoparticles precursors, although the structural and microscopic
characterization techniques don't show a clear correlation to the measured
properties.

The presence of BaZrO₃ particles on the top of the film can be attributed
to the so-called pushing effect, observed for many kinds of materials when
small nanoparticles are inside of a melt where crystallization is occurring [137,
138]. According to theory, the melt is able to push small particles along with
the growing interface if the Van der Waals repulsive forces exceed the drag
viscosity. The critical radius r at which particles will become trapped in the
solid depends on the size of the particle and the growth rate of the solid (R).
Bigger particles will become trapped and high growth rates will tend towards
trapping particles as well, following the equation:

$$r \propto \frac{\Delta \sigma_0}{\eta R} \tag{4.3}$$

where $\Delta\sigma_0$ is the inter-facial energy and η the melt viscosity. Since high growth rates such as the ones found in TLAG should be able to trap very small particles, it is possible that the crystallization of the nanoparticles is occurring at a different stage than YBCO growth, which pushes the precursors to the surface where they are crystallized in $BaZrO_3$ of different particles sizes in a range of 5-20nm.This fact indicates the complexity of crystallizing two phases (BZO and YBCO) simultaneously at this ultrafast growth rates.

In this section we have analysed the potential of in-situ methodologies to grow nanocomposite films through TLAG. Although the nucleation of YBCO remains fully epitaxial when Zr and the corresponding Ba are added, and the $BaZrO_3$ phase is obtained, the nanoparticles are not trapped inside of the YBCO matrix but are pushed to the surface of the film. The reached J_c self-field of $1MA/cm^2$ entails the possibility of further work to improve these nanocomposites but a big effort should be carried out in order to tune the process so that nanoparticles would be embedded inside of the YBCO crystalline matrix. In this thesis we have focused the analysis presented in the following sections to the more successful nanocomposites prepared with pre-formed nanoparticles.

4.4 Defect structure and properties under magnetic fields

In the previous chapter we analysed the defect landscape of the nanocomposites grown through temperature route to understand the possible relationship between the observed microstructures and vortex pinning capabilities of the films. Nonetheless, the properties were governed by reactivity in the case of 2:3 stoichiometry and defects associated to poor liquid wettability such as big holes, in the case of 3:7. In the nanocomposites grown through PO_2-route we have achieved up to $2.2MA/cm^2$ of J_c self-field with no reactivity or porosity and therefore we want to correlate the observed microstructure of these films with critical current versus magnetic field measurements. To this end, Scanning Transmission Electron Microscopy images of several nanocomposite films were taken.

Fig.4.27 (a) shows a nanocomposite film as compared to a pristine film grown under the same conditions. We can observe the presence of small nanoparticles distributed along the film, indicated by the yellow arrows. Regarding the defects observed in the crystalline matrix, Fig.4.27 (b) shows a pristine film with c-axis oriented YBCO structure. The matrix presents a certain amount of long stacking faults distributed along the sample. In contrast,
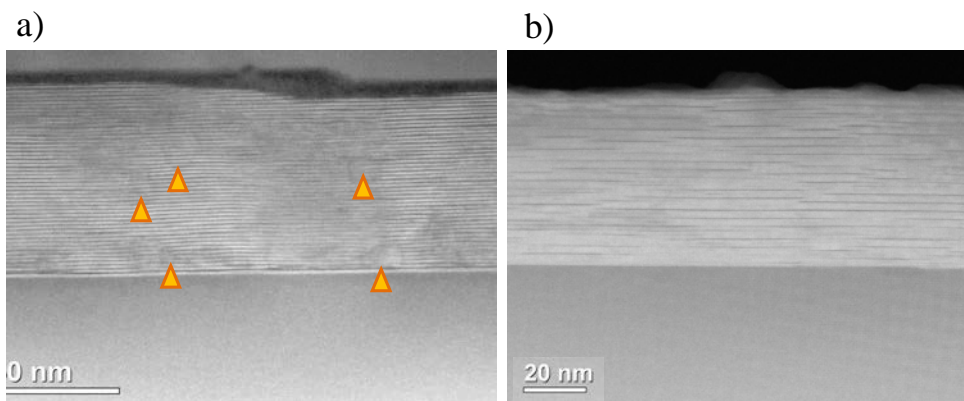
FIGURE 4.27: STEM images of two different films. (a)12%BaZrO$_3$ nanocomposite. Arrows indicate nanoparticles position. (b) Pristine TLAG films grown through the PO$_2$ route.

the nanocomposite film shows stacking faults in the whole thickness of the sample.

These defects can be better appreciated with higher resolution images shown in Fig.4.28. The size of the nanoparticles ranges between 6-10nm, which is slightly larger than the initial particles introduced in the YBCO precursor solution of 4±1nm but is indication of a very limited coarsening. The nanoparticles show no aggregation and the coherent interfaces of the particles can be appreciated in Fig.4.28 (a), as has been previously discussed in section 4.2.

It is noteworthy that the observed Y248 extend beyond the place where the nanoparticles are trapped and to the whole film thickness, evidenced in Fig.4.28 (b). The formation of stacking faults in TFA-CSD is usually attributed to the inter-facial energy accumulated in incoherent interfaces between YBCO and nanoparticles. In the case of TLAG nanocomposites grown through PO$_2$ route, the scenario is clearly different. The orientation of the nanoparticles is epitaxial with YBCO and therefore the coherent interfaces have a much lower energy which should correlate to a lower density of defects. However, the introduction of nanoparticles creates a film full of stacking faults as compared to pristine films which have a much lower density of defects. Moreover these defects are not limited to the vicinity of nanoparticles but are present through the whole sample, indicating that the particle's effect has a much larger range of influence, widening the possible scenarios or mechanisms through which nanoparticles are able to induce defects in the YBCO matrix. This long range effect could also be related to the ultrafast growth rates and how the growing matrix accommodates the nanoparticles. The presence of such a high density of Y248 intergrowths, which consist on an extra Cu-O chain, requires extra
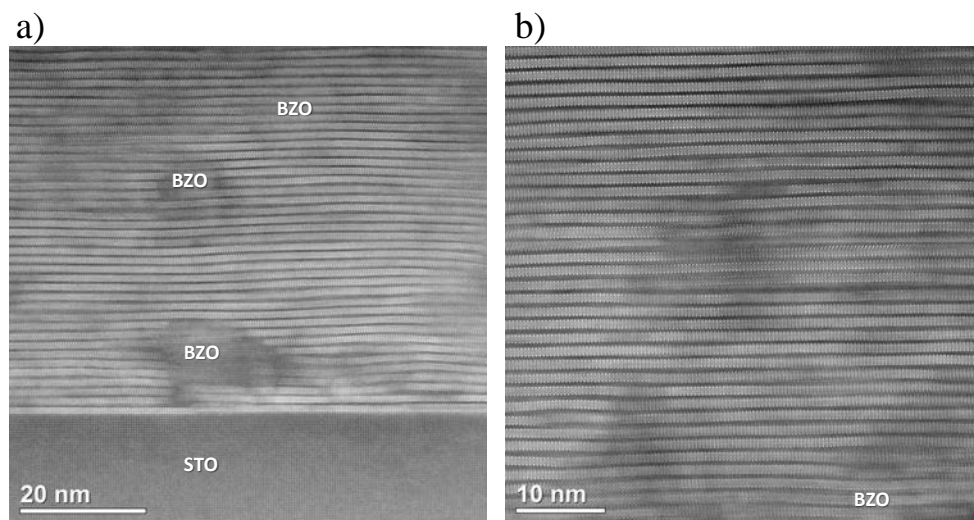
FIGURE 4.28: STEM images of a 12%molBaZrO$_3$ nanocomposite grown directly on top of the substrate through PO$_2$ route.

copper which would result in Cu off-stoichiometry on the Y123. Nonetheless, these films are grown with a 3:7 liquid which implies an excess of copper with respect to Y123. However, it has been shown how these extra Cu-O chains in CSD YBCO films contain a large amount of Cu vacancies, which allow the Y123 stoichiometry to be kept. It has been shown that these defects in the Cu-O chain are composed, in fact, of 2 Cu vacancies and 3 oxygen vacancies [119, 132]. The superconducting order parameter seems to be decreased in these cluster defects [139], thus acting as additional pinning centers. In addition, these defects have shown ferromagnetic behaviour [119], and to induce additional oxygen vacancies in the nearby Ba-O planes [140]. Thus, the overall effect of these clusters on the physical properties of the layers is still under investigation. Nevertheless, the overall pinning effect of the Y248 defects has been largely studied in our group, demonstrating that they are very effective pinning centers [132, 141, 142]. The T$_c$ of layers with a large amount of Y248 defects with cluster vacancies has been shown to be the same as that of Y123.

Fig.4.29 shows several STEM images from a 12% BaZrO$_3$ film grown on top of a seed layer. The nanoparticles are homogeneously distributed along the whole thickness of the sample, revealing that they are able to diffuse during the growth of YBCO. Therefore, these films should be treated as a full nanocomposite layer with reduced density of nanoparticles from the initial precursor solution instead of a system with one nanocomposite layer on top of a pristine film. In such a scenario, a 12% molar BaMO$_3$ film becomes a
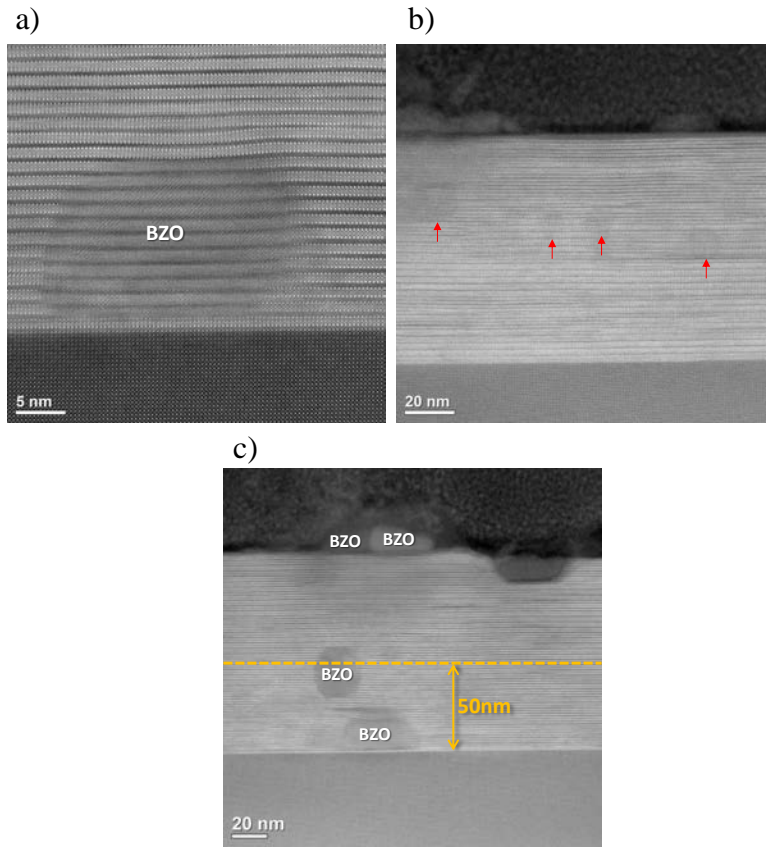
FIGURE 4.29: STEM images of a 12%BaZrO$_3$ nanocomposite grown on top of a seed layer. (a) Detail of a epitaxial nanoparticle near the substrate interface. (b) Homogeneous film with nanoparticles indicated by red arrows (c) Nanoparticles evenly distributed in the whole film thickness.

8%BaMO$_3$ nanocomposite. The film shows the same density of defects as those nanocomposites grown directly on top of the substrate, indicating that the nanoparticles have the same effect even if not homogeneously distributed on the initial pyrolysed film, confirming once more the long range repercussion to the presence of the nanoparticles.

To evaluate the density of local nanoscale distortions, XRD Williamson-Hall analysis can be used to calculate nanostrain. This method is able to quantify the statistical variations of distortions of the c-axis parameter in the YBCO matrix by measuring the broadening of the XRD epitaxial YBCO peaks [131, 132]. In particular, inhomogeneous strain (local and small distortions) will create a
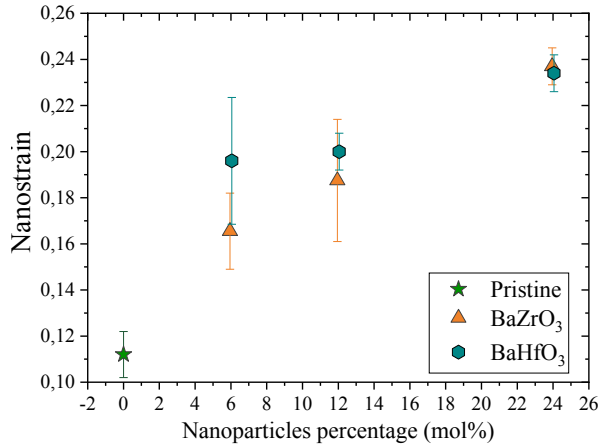
FIGURE 4.30: Nanostrain dependence with nanoparticles molar percentage of $BaZrO_3$ and $BaHfO_3$ nanocomposites and pristine films. Error bars correspond to standard deviation between different samples.

broadening of the peak instead of a shift in peak position created by homogeneous epitaxial strain. This type of broadening can be separated from the size broadening and therefore obtain a value of nanostrain which will be associated to the defect structure of the sample. More details on the Williamson-Hall analysis can be found in Appendix A. Fig.4.30 shows the mean nanostrain values as calculated in several samples for each density and type of nanoparticles, as well as pristine film values. There is a strong increase in nanostrain for nanocomposite films as compared to pristine samples, in agreement with the microstructural defects observed by STEM. The increase also follows the density of nanoparticles, as indicated by the higher values of nanostrain in the 24%$BaMO_3$ nanocomposites with respect to the 6% ones. Until this point we have considered $BaZrO_3$ and $BaHfO_3$ films to be equivalent, since no difference was observed in their nucleation or basic superconducting properties (T_c and J_c self-field). However, a certain shift is now detected if we look closely to nanostrain values. In both 6 and 12% nanocomposites, $BaHfO_3$ presents higher nanostrain than $BaZrO_3$. Although the difference is small if compared to the leap existing between pristine and nanocomposites in general, it could be related to the difference in melting point of the two nanoparticles phases. The aggregation and coarsening of nanoparticles is related to their melting point, in such a way that the tendency to coarsen will be higher when the processing temperature is closer to their melting temperature, due to increased atomic mobility [143]. The melting point increases with atomic number in the

BaMO$_3$ series, therefore it is slightly higher for BaHfO$_3$. Thus, if the coarsening is slightly smaller in the case of BaHfO$_3$ nanocomposites, a matrix with a higher number of smaller dispersed particles could account for higher nanostrain values than slightly bigger coarsened nanoparticles. Since TEM is a very local technique is difficult to confirm this scenario through direct observation but XRD Williamson-Hall analysis gives an account of the full sample volume.
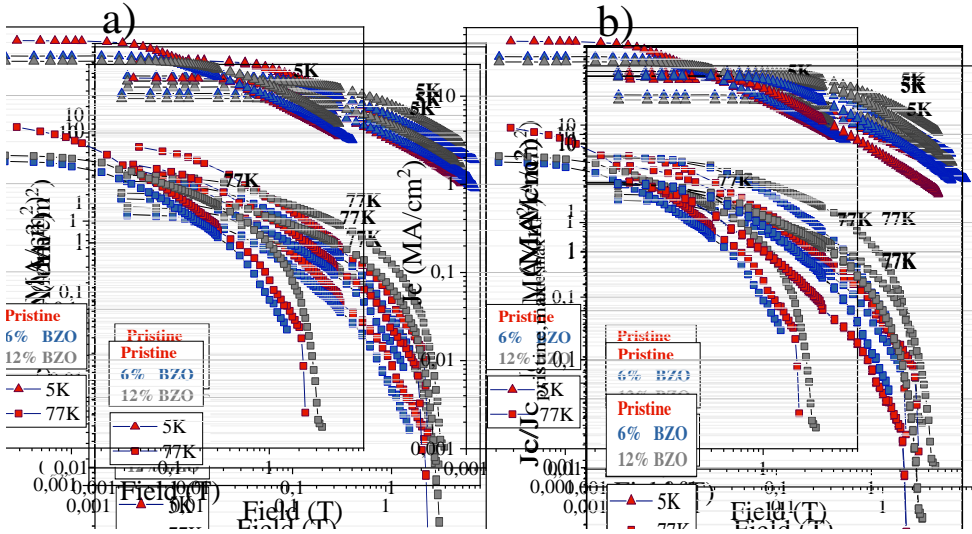

FIGURE 4.31: SQUID J$_c$ at different temperatures of BaZrO$_3$ nanocomposites. (a) Absolute values. (b) Values normalized to self-field J$_c$ of pristine films at each temperature.

As discussed in the introduction, one of the main challenges for YBCO applications is improving the critical current density at high applied magnetic fields. We can evaluate the J$_c$ behaviour with magnetic field through simple SQUID measurements of magnetization versus applied field. Fig.4.31 shows the calculated J$_c$ versus an applied field up to 5T parallel to c-axis using the Bean critical state. Even if J$_c$ self-field of nanocomposites is still not fully optimized to match pristine film values, the J$_c$ of 12% BaZrO$_3$ samples surpasses the pristine film beyond 0.1T at 77K and 0.15T at 5K. Therefore the nanocomposites have a marked smoother dependence of J$_c$ with magnetic field compared to pristine YBCO. Fig.4.31 (b) shows the normalized values to J$_c$ self-field, to better observe the different behaviour of the nanocomposite films. Notice too that the in-field plateau of J$_c$ is kept for higher magnetic fields when the nanoparticles density is higher. We are therefore improving vortex pinning by introducing nanoparticles.
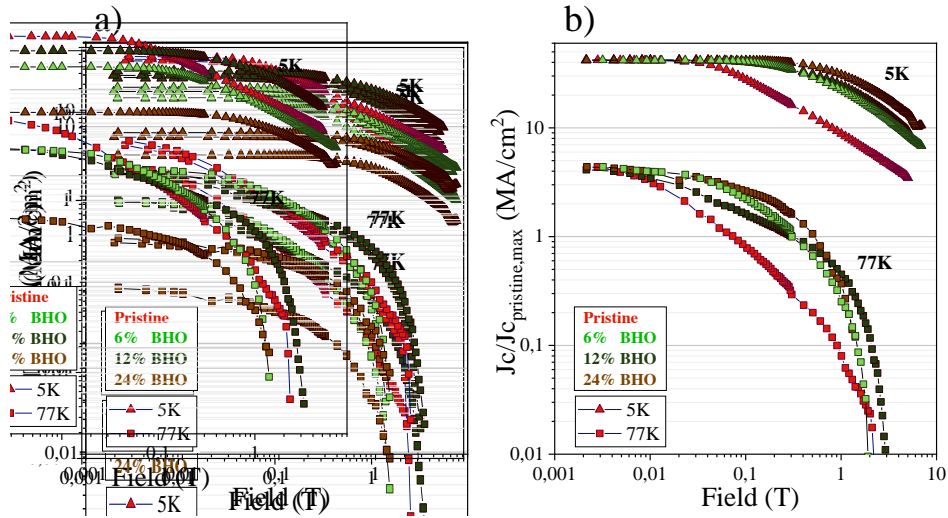
FIGURE 4.32: SQUID J_c at different temperatures of BaHfO$_3$ nanocomposites. (a) Absolute values. (b) Values normalized to self-field J_c of pristine films at each temperature.

Fig.4.32 shows the J_c versus applied magnetic field of BaHfO$_3$ films. The observed behaviour is similar to BaZrO$_3$ nanocomposites, such that 12% films overtake the pristine J_c at 0.1T and 0.15T for 5K and 77K, respectively. The measured 24% nanocomposite has very low critical current density values in all the applied fields, but in the normalized plot the potential of such film can be appreciated, since it has the largest plateau with magnetic field. Therefore if the self-field values could be optimized to match or at least resemble those of pristine samples, we would obtain remarkable nanocomposites. Nonetheless, the 6% and 12% films have also a smooth dependence with magnetic field.

Electrical transport measurements were performed in a 4-point bridge configuration, in order to evaluate the vortex pinning capabilities of the nanocomposite films, in collaboration with Juri Banchewski. Fig.4.33 (b) shows the critical current density versus orientation of magnetic field of a pristine film and a 6%BaZrO$_3$ film. The J_c of the nanocomposite film is higher than in the pristine film in all the position of magnetic field except in the 90° configuration, which corresponds to the a/b planes direction. The solid lines are the isotropic pinning contribution, calculated through the Blatter scaling approach [111]. The behaviour is similar for the three measured magnetic fields, although the difference in J_c is more pronounced for higher applied magnetic fields. The introduction of nanoparticles has created an enhancement of the isotropic pinning contribution due to the distorted YBCO matrix and Y248 intergrowths, which provide pinning centers in all the directions of applied
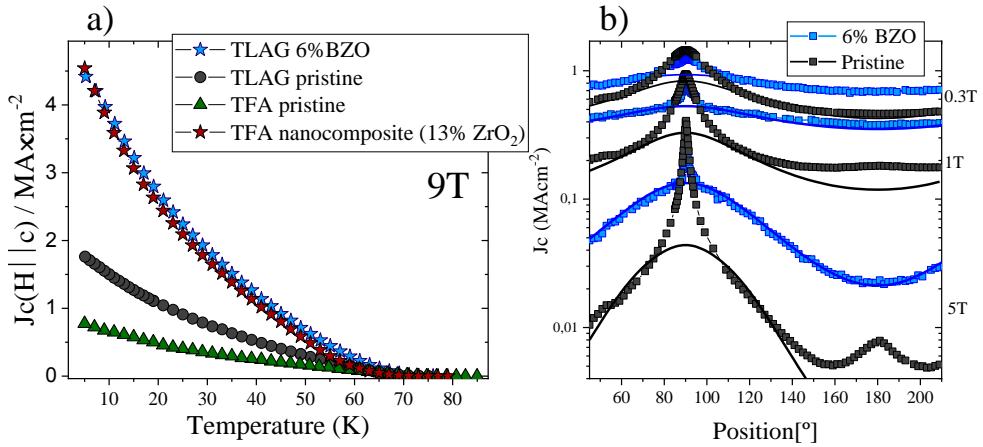
FIGURE 4.33: (a) J$_c$ versus temperature of different samples at an applied magnetic field of 9T parallel to c-axis. (b) J$_c$ of a pristine TLAG film and a 6%BaZrO$_3$ nanocomposite at 5K under different applied magnetic fields versus the angle of applied magnetic field vs the film surface: 180° is equivalent to H∥c-axis.

magnetic field. In the angle of 180°, there is a peak in the J$_c$ of the pristine film that has been suppressed in the case of the nanocomposite film. This position corresponds to magnetic field being parallel to c-axis, and therefore the peak observed in the pristine sample is attributed to vortex pinning by twin boundaries [144]. When nanoparticles are introduced, the vertical coherence of twin boundaries is broken, and therefore their effectiveness as vortex pinning centers is lost [145]. However, the contribution of isotropic defects described by the solid lines has increased considerably in the nanocomposites for all magnetic fields beyond 0.3T.

We also evaluated the critical current density versus temperature under high magnetic fields, as shown in Fig.4.33 (a). The measurement of a 6%BaZrO$_3$ was performed at 9T, and compared to a pristine TLAG sample and pristine and nanocomposite films grown through TFA-CSD methodologies. The TLAG pristine film shows a higher J$_c$ in all temperatures when compared to the TFA pristine sample, indicating that TLAG growth is able to create a good defect landscape and increase the irreversibility line of YBCO. The critical current density is further improved by the introduction of nanoparticles, with both TFA and TLAG reaching a J$_c$=4.5MA/cm^2 at 5K and 9T. Notice that the TFA nanocomposite shown in Fig.4.33 (a) is one of the nanocomposite with the best performance ever reached through this growth methodology. This plot also indicates the relevant contribution of the induced defects at low and medium temperatures, where the improvement in J$_c$ versus the pristine samples is much more relevant.

In order to quantify the vortex pinning efficiency of YBCO films, the value of H* was determined from the SQUID measurements for nanocomposite and pristine samples. H* is defined as the field at which J_c reaches the 90% of J_c self-field value. This arbitrary criteria is useful to compare films in terms of when their vortex pinning regime changes from single vortex pinning to collective pinning, this is, the point at which the density of vortices is starting to be higher than that of defects. Therefore a higher H* is an indirect indication of a higher density of pinning centers in the film.
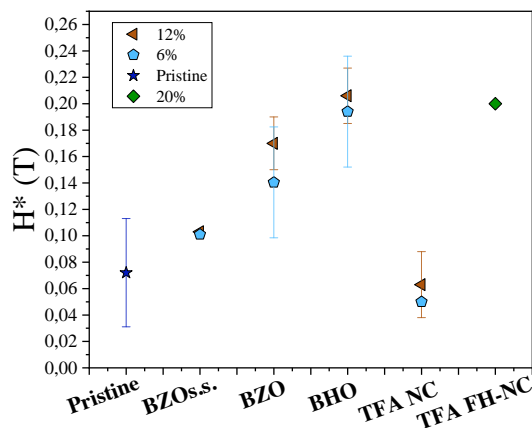
FIGURE 4.34: Values of H* at 5K for several types of TLAG nanocomposite films and TFA nanocomposites.

Fig.4.34 shows H* values for different TLAG films and other CSD methodologies. The difference between $BaZrO_3$ and $BaHfO_3$ is once more observed. The H* values are higher in the case of $BaHfO_3$ reaching up to 0.21mT at 5K. This is in the range of the highest reported values for CSD YBCO nanocomposites, exceeding by far the standard TFA nanocomposites and obtaining similar values to the newly reported method of flash heating, where the coarsening of nanoparticles has been limited [139].

The measurements for nanocomposites of spontaneous segregation are also included in the graph, which also show an improvement over pristine films. This shows that the structure of defects created by this methodology could be useful if the pushing effect could be controlled in order to trap the nanoparticles inside of the YBCO matrix.

We have previously analysed nanostrain values to quantify local distortions in the films. These values can be related to how effective is the vortex pinning of the samples, since more strain and distortions on the films also means

more density of pinning sites. Fig.4.35 shows nanostrain versus H* of pristine TLAG films, CSD-TFA nanocomposites and TLAG nanocomposites. The different values of nanostrain in the case of pristine films can be attributed to samples grown through different processing conditions which create different microstructures. The films with optimized J$_c$ self-field correspond to the lowest nanostrain values. The interesting feature is that while pristine films and CSD-TFA nanocomposites increase nanostrain with a limited increase in H*, TLAG nanocomposites show a large increase in H* that goes beyond the values expected from just nanostrain. We propose that using very small nanoparticles with diameter close to the coherence length of YBCO, we are able to create nanocomposites where the nanoparticles themselves are acting as pinning sites. This type of pinning has been demonstrated in nanocomposites grown by PLD or MOCVD where self-spontaneous nanorods of ∼5nm are segregated in the REBCO matrix [38, 146]. Also, it has just recently been proposed in CSD-TFA for again very small nanoparticles in in-situ and ex-situ nanocomposites [136, 147]. This type of pinning would not reflect on nanostrain measurements since the nanoparticles are not part of the YBCO crystalline structure. The synergistic effect between pinning by the nanoparticles and pinning due to local distortions and defects created by the introduction of nanoparticles can create a new landscape for vortex pinning in which multiple mechanisms are engineered in order to benefit from the full potential of nanocomposites.
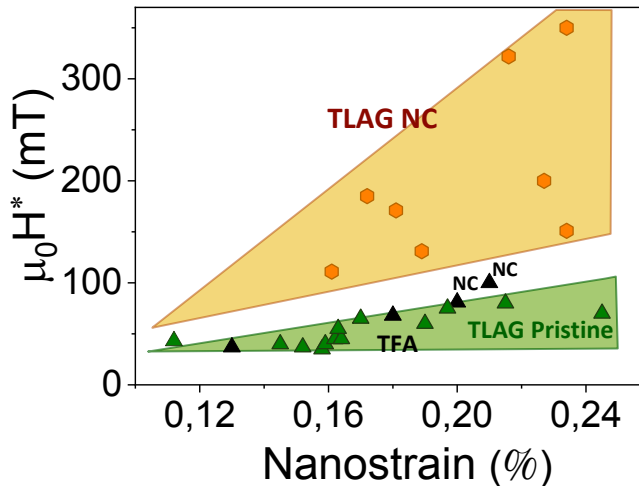

FIGURE 4.35: H* of pristine and nanocomposite TLAG films together with conventional TFA-CSD nanocomposites versus nanostrain.

We have demonstrated how TLAG process can benefit from the introduction of pre-formed nanoparticles creating a rich defect landscape and improving the pinning force of the films, obtaining higher critical current densities under applied magnetic fields and very high H* which give a promising avenue for TLAG nanocomposites. Further work should include a more in-depth analysis of the behaviour of these nanocomposites under magnetic field through transport measurements.

4.5 Conclusions

In this chapter we have analysed the growth and properties of nanocomposite films grown through the so-called PO_2 route. We have been successful in adding small pre-formed nanoparticles both of $BaZrO_3$ and $BaHfO_3$ inside the crystalline YBCO achieved by a PO_2 step at high temperatures. Fully c-axis textured films could be achieved with a nanoparticle density up to 12% although some irreproducibility exists in the 12% molar case, with a certain percentage of the samples presenting a/b nucleation. This irreproducibility could be overcome with the use of a seed layer which prevented any undesired crystalline orientations. Epitaxial films could also be obtained with 24% and 32% density of nanoparticles but a bigger tendency towards random nucleation was detected.

Nanocomposite films with 6% and 12% of $BaZrO_3$ and $BaHfO_3$ showed high J_c self-field values in the range of 1.7-2.2MA/cm^2 which proofs the compatibility of transient liquid assisted growth methodologies with high performance nanocomposites. The superconducting properties were decreased in the case of 24% and 32% densities due to aggregation and coarsening of the nanoparticles which reduced the cross section for current percolation.

The possibility to grow nanocomposite films through the technique of spontaneous segregation was tested, and although J_c's self-field up to 1MA/cm^2 were achieved for both 6% and 12% of $BaZrO_3$ when a seed layer was used, STEM images revealed that the nanoparticles are aggregated at the surface of the film due to pushing effect during growth.

Nanocomposites with pre-formed nanoparticles were investigated in-depth to understand their associated defect structure and its influence on super-conducting properties. STEM analysis and XRD revealed that the nanoparticles are epitaxially aligned with YBCO, a very uncommon feature for CSD nanocomposites. In-situ X-ray synchrotron studies evidenced how the nanoparticles are able to align with YBCO during growth. The grown films were observed by STEM which confirmed the epitaxy of nanoparticles and also showcased the full Y248 stacking of the films. We confirmed that the microstructure of nanocomposites is deeply affected by the introduction of small

pre-formed nanoparticles, as exemplified by the measured nanostrain which increases with the percentage of nanoparticles in the films.

Measuring the J$_c$ versus applied field revealed how nanocomposites have an improved pinning vortex performance, with the J$_c$ of nanocomposites being larger than in the pristine films above 0.1T at 5K. This confirms that introducing nanoparticles is increasing the number of pinning sites in the samples. Both BaHfO$_3$ and BaZrO$_3$ nanocomposites show very similar tendencies, but nanostrain and H* are slightly higher in the case of BaHfO$_3$, revealing that this phase has a more efficient vortex pinning than BaZrO$_3$, possibly due to its higher melting point which allows for less atomic mobility at high temperatures and therefore less aggregation. Nonetheless, H* of both nanocomposites are very high as compared with standard CSD nanocomposites. These good results are rendered in a publication in *Nature communications* [64], together with a general description of TLAG.

Electrical transport measurements revealed a strong isotropic pinning contribution for a 6%BaZrO$_3$ nanocomposite in all the directions of applied magnetic field, surpassing the critical current density of the pristine films. Furthermore, the J$_c$ at 9T for the nanocomposite is highly increased with respect to the pristine film. Therefore, we can conclude that by joining TLAG growth with nanocomposite technology we can achieve YBCO films taking advantage of the high growth rate associated to the use of transient liquids and improving vortex pinning, necessary for coated conductors used in applications under high magnetic fields.

Chapter 5

Towards coated conductors: thick films and buffer layers

The previous chapters of this thesis have focused on investigating the method of transient liquid assisted growth and its compatibility with growth of nanocomposite films. As such, we have mainly worked with thin films (in the range of 100nm) and deposited on single crystal substrates. Nonetheless, this novel growth methodology aims to become compatible with coated conductor technology, which would potentially benefit from the ultra-fast growth rates and high throughput of our technique. Thickness and substrates are the two main factors that need adapting on the road to coated conductors manufacturing. Thus, the knowledge obtained through the growth of thin films needs to be implemented to thick films, in the range of 1 micrometer. It is also necessary to prove the compatibility of the [Ba-Cu-O] liquid with buffer layers that will also be present in coated conductors. Moreover, the use of buffer layers is also interesting for the cases where we have encountered reactivity with single crystal substrates.

Therefore, this chapter will describe the efforts made to investigate the growth of YBCO thick films and thin films on top of buffer layers. This is still work in progress that requires further optimization, but in this thesis we aim to present preliminary results that prove the compatibility of TLAG with coated conductor requirements.

5.1   Thick films

In order to obtain YBCO films suitable for applications, many requirements need to be met. One of these requirements is carrying large critical currents, which is accomplished by large critical current densities but most importantly,

by increasing the thickness of the superconductor film. Thicknesses of 1 micrometer or higher while maintaining a good critical current density (J_c), will obtain the necessary high total critical current I_c(A), or critical current per centimerter-width, I_{c-w}(A/cm-w). In this section we separate the efforts of thick film growth aiming to 1 micrometer thick films in the two different processing routes of TLAG. The pyrolysed thick films were obtained by multi-deposition through spin-coating of the same solutions used in the case of thin films. Multi-deposition allows us to use the optimized pyrolysis parameters of thin layers. The thermal treatment was performed for each deposition until reaching the desired thickness of the films. Pyrolysis of thick layers suffer of large stresses during decomposition of the organic material, which tends to promote cracking of the layers. Usually, some additives need to be used in the precursor solution to avoid cracking in thick films of one single deposition [148]. Thus, multi-deposition is an easy way to scale-up the already optimized pyrolysis process, but other techniques such as ink-jet printing, able to deposit 1μm layer in one single deposition, should be investigated in order to simplify and shorten the pyrolysis process [149]. This goes beyond the scope of this thesis, but it is an active research interest in SUMAN group.

5.1.1 Thick films grown through the temperature route

As it has been explained in previous chapters, the temperature route consists of heating the films at a constant PO_2 until reaching the desired growth temperature at a certain heating ramp. This implies that YBCO growth will occur subsequently to barium carbonate elimination, which is the slowest reaction of the system. To eliminate $BaCO_3$, the following reaction must occur:

$$BaCO_3(s) + Cu_zO(s) \rightarrow BaCu_zO_2(s) + CO_2(g) \tag{5.1}$$
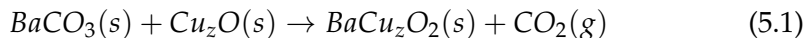
and since it requires the effective elimination of CO_2, it becomes more difficult when increasing the thickness of the film. Rasi's thesis [63] demonstrated how the temperature of barium carbonate decomposition increases with thickness through thermal analysis and evaluation of the volatile species, confirming the relevance of the gas transport. The presence of this phase can be very detrimental for the superconducting properties of YBCO. Therefore, we needed to confirm that complete elimination of $BaCO_3$ is possible in the growth process of thick films.

Fig.5.1 shows the integrated XRD pattern after different treatments performed on the same sample. In the pyrolysed film, a strong signal of orthorhombic barium carbonate is detected. After, the film was subjected to a
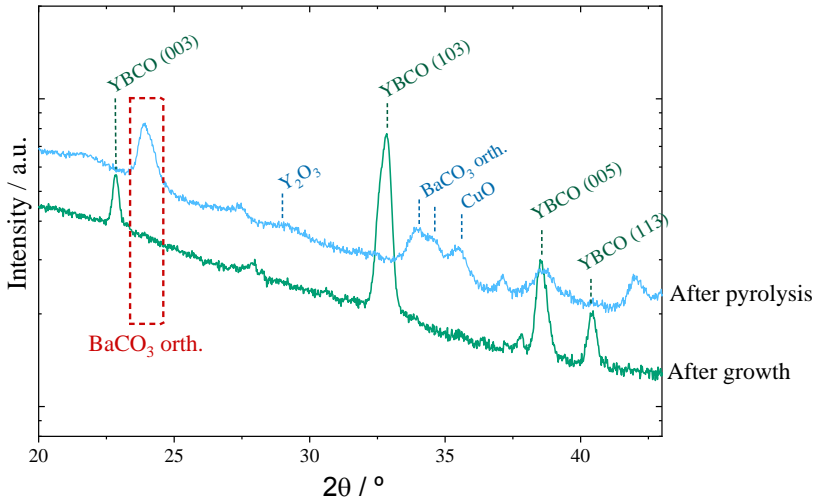
FIGURE 5.1: Grazing incidence XRD from the same $1\mu m$ thick film before and after growth. The complete disappearance of $BaCO_3$ is observed.

thermal treatment at 5ºC/s until 860ºC under PO_2=1·10^{-3}bar. Since the decomposition of barium carbonate and the growth of YBCO cannot be disentangled in these processing conditions, we analysed the spectra after the growth of YBCO. Most importantly, the barium carbonate has successfully been eliminated as no peaks belonging to this phase are observed in the XRD pattern after growth.

To perform the growth of thick YBCO films through temperature route, we must take into account the increased time necessary to eliminate barium carbonate, and therefore slower heating ramps and higher temperatures were chosen in relation to thin films.

Fig.5.2 presents the results of two thick films grown at different heating ramps both until 860ºC and PO_2=1·10^{-3}bar. The XRD scan of the sample grown at 5ºC/s shows mainly peaks corresponding to the YBCO phase. We can observe strong peaks of the c-axis oriented YBCO but we also detect peaks corresponding to random nucleation and a/b oriented grains. SEM in Fig.5.2 b) confirms the presence of randomly oriented grains. On the other hand, the sample grown at 10ºC/s presents a lot of unidentified peaks usually observed when reactivity occurs, while no peaks corresponding to YBCO could be identified. SEM shows many grains with different morphology and composition. The thickness of the films after growth was confirmed to be approximately $1\mu m$ by cross-section SEM . These results indicate that above 5ºC/s, the film suffers from strong reactivity with the STO single crystal. In the case

a)

b)
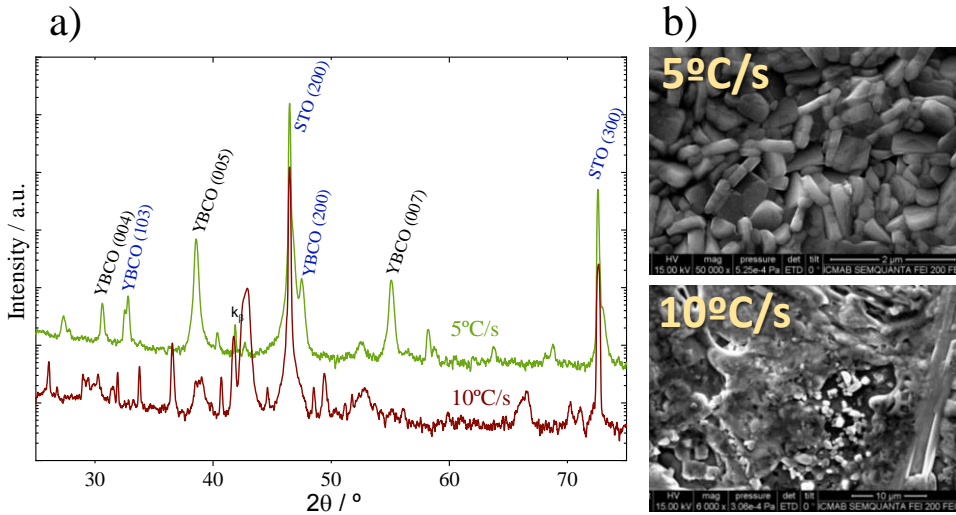
FIGURE 5.2: (a) High resolution θ-2θ XRD patterns of films grown at 5°C/s and 10°C/s. (b) SEM images of the surface of the same films.

of the thin films presented in Chapter 3, no reactivity was observed with heating ramps below 30°C/s, thus suggesting that the temperature at which the [Ba-Cu-O] liquid is formed depends on the thickness of the films, probably because the $BaCO_3$ decomposition depends on the thickness given a heating ramp. When the thickness of the film is larger, barium carbonate elimination occurs at higher temperatures and therefore the liquid formation and growth of YBCO will also occur at higher temperatures, in a region of the phase diagram where competitive phases (formed by reactivity with the single crystal) appear. Since the elimination of $BaCO_3$ and YBCO nucleation occur during the heating stage, the heating ramp is the most relevant processing parameter. In the case of thin films there exists a range of heating ramp in which the speed is high enough to obtain epitaxy but low enough to avoid reactivity. When the same conditions are applied to thick films, only varying the heating ramp, there is no window for epitaxy before the reactivity region. This implies that other processing conditions need to be optimized in order to disentangle the epitaxial growth from the reactivity region. Further work should include studying different PO_2 conditions, possible dwells at intermediate temperatures or including buffer layers non-reactive with the liquid, as will be discussed in the next section. At this stage, we can confirm the elimination of barium carbonate in thick films and the growth of YBCO with partly random nucleation.

5.1.2 Thick films grown through PO$_2$ route

In the PO$_2$ processing route, the experiments were performed in matgas furnace, introduced in the last section of Chapter 2. This furnace provides a higher flow of evacuation in the low PO$_2$ step, which is achieved by also lowering P_{tot}. The composition of the films corresponds to a 3:7 Ba:Cu relationship as it is the composition with best results in this route for thin films.
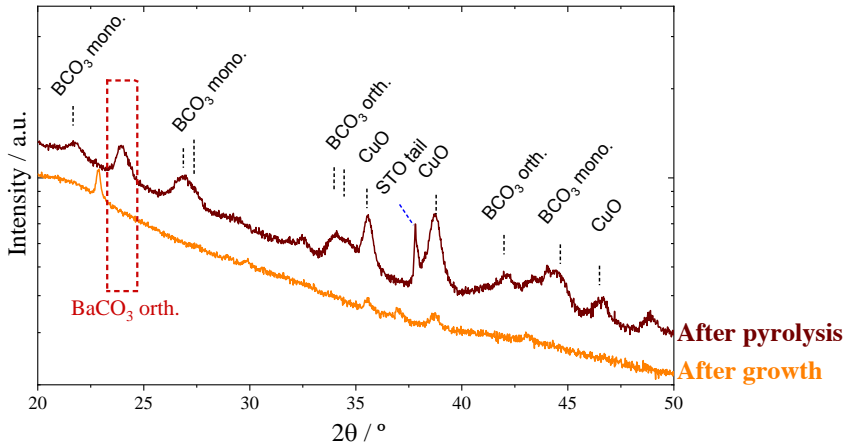

FIGURE 5.3: Grazing incidence XRD from a 1μm thick film before and after growth through PO$_2$ route. The complete disappearance of BaCO$_3$ is observed.

Fig.5.3 shows high resolution XRD patterns obtained in grazing incidence conditions of a film after the pyrolysis step and after it has been subjected to growth conditions. In this configuration, the epitaxial phases are not observed and we are probing a higher area of the sample, therefore maximizing the intensity of the polycrystalline phases present in the film. After growth, we observe the complete elimination of barium carbonate and all the pyrolysis phases except CuO, as expected since this compound is in excess with respect to the Y123 composition. Therefore we confirm the feasibility of effectively eliminating barium carbonate in ~1μm thick films under the PO$_2$ route processing conditions.

The processing conditions chosen to grow thick YBCO films through PO$_2$ route were to perform a dwell of 20min at 845ºC and P_{tot}=PO$_2$=1·10^{-6}bar, followed by a jump until P_{tot}=PO$_2$=1·10^{-3}bar and a dwell of 5 min at the final pressure conditions. Fig.5.4 shows the θ-2θ scan of the resulting film. The scan shows c-axis oriented peaks for YBCO, with no presence of randomly oriented grains or a/b nucleation, though some minor secondary phases are observed.
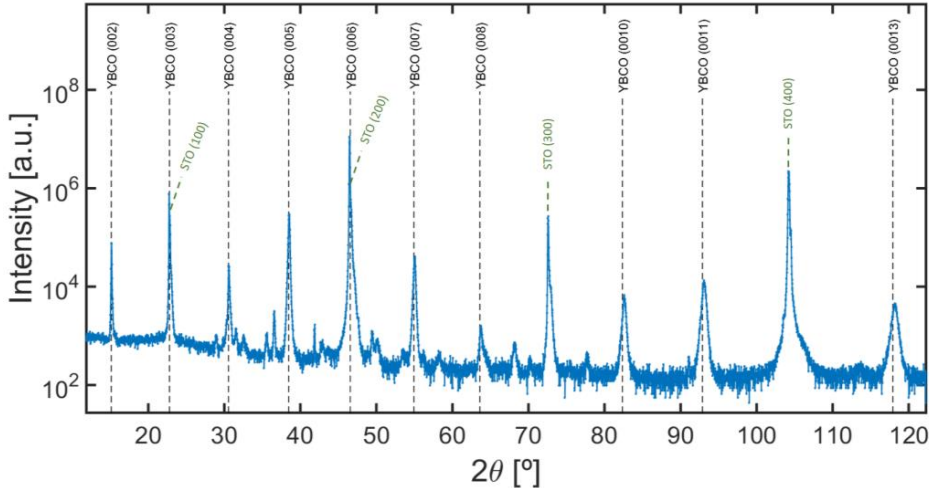
FIGURE 5.4: High resolution θ-2θ XRD pattern of a thick film grown through PO_2 route in Matgas furnace.

The texture of this film was further studied by XRD. Fig.5.5 a) shows the image of 2D-XRD, where the misalignment of the c-axis YBCO peaks can be observed. All the peaks belonging to the (00l) family have a broad peak width in the χ direction, with a FWHM$\approx$2-3°. The presence of some rings can also be appreciated, which together with the broad peaks can indicate grain misorientation in the sample. Phi scans and rocking curves were also measured as shown in Fig.5.5 b) and c), respectively. The calculated FWHM is higher than the values measured for thin films, but acceptable for the thickness range of our film. So, overall, we identify a rather good epitaxial fraction of YBCO material, though some misalignment is also present, which could induce less percolation currents.
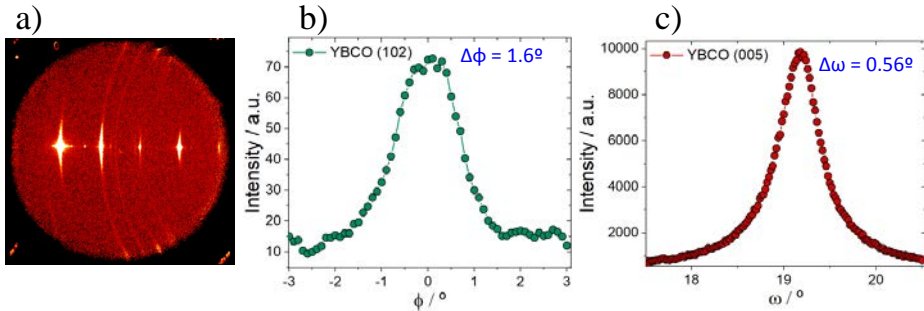
FIGURE 5.5: Further XRD studies of the thick film grown through PO_2 route: (a)2D XRD (b) Φ-scan (c) Rocking curve.

SEM top images and cross-section are shown in Fig.5.6 a) and b), respectively. From the top image we can appreciate the terraced surface, with flat steps and very low porosity, indicative of a liquid-based growth. By cutting the sample in half, we could perform cross-section SEM, which shows a homogeneous c-axis layer, very dense and with almost no pores except some at the substrate interface. The thickness shown by these SEM images is 800nm.

a)

b)
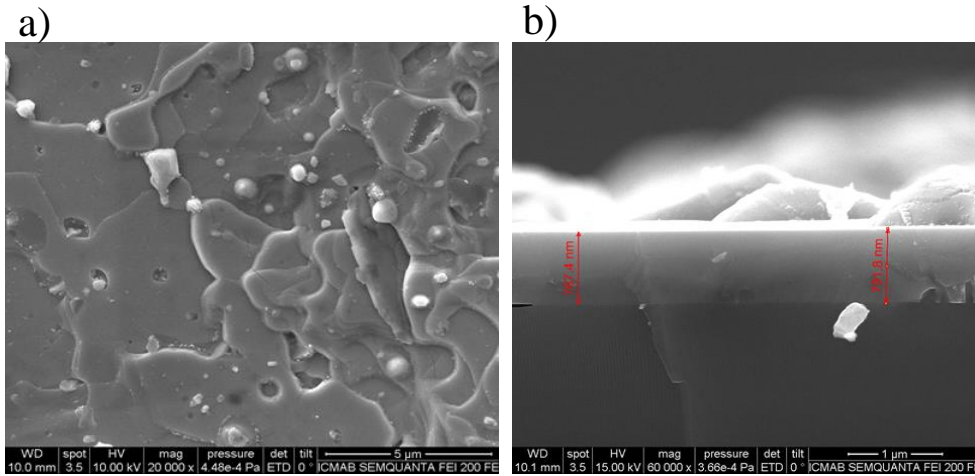
FIGURE 5.6: (a) Top-view SEM of a thick film grown through PO$_2$ route. (b) Cross-section SEM image of the same film as (a).

The physical properties of the film were evaluated: T$_c$ was measured by Van der Pauw methodology, giving a value of 92.2K, J$_c$ by SQUID at 77K was 0.4MA/cm^2 and 3.2MA/cm^2 at 5K. The high value of T$_c$ by Van der Pauw indicates that the material is not contaminated by reactivity products, and it is an indication that the low J$_c$ is due to bad percolation, possibly due to some grain misorientation or some secondary phases as evidenced in Fig.5.5 a). Further work should include an optimization of the YBCO texture and elimination of secondary phases in order to ensure good critical current densities. Nonetheless, it is remarkable that with small changes with respect to the growth of thin films we were able to obtain epitaxial films with no reactivity and good critical temperature. This is an indication of the robustness of YBCO growth through Ba-Cu transient liquid in the PO$_2$ processing conditions.
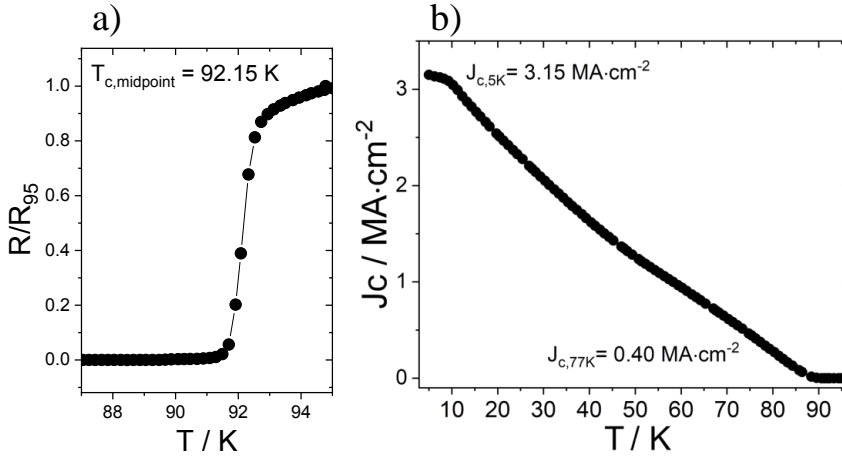
FIGURE 5.7: (a) T_c measured by Van der Pauw of a thick film grown through PO_2 route. (b) J_c self-field of the same film.

5.2   CSD buffer layers

In coated conductor technology, the metallic substrates require several buffer layers to serve various functions, such as preventing the oxidation of the substrate, providing texture templates, or preventing reactivity or cation diffusion of the REBCO layer with other materials of the layer [150]. Thus, it is important to investigate the compatibility of YBCO growth through TLAG with different buffer layers in an effort to go beyond single crystal substrates. Moreover, during the investigations performed for this thesis, we encountered reactivity with the single crystal substrates when processing conditions led to high reaction temperatures, and therefore a non-reactive buffer layer would widen the conditions suitable for growth. The reactivity of the [Ba-Cu-O] liquid is rather important with many surfaces and has been reported in various conditions and methods [105, 107, 151]. In this section, we present several buffer layers grown through CSD methodologies, considering that chemical solution deposition is also used in TLAG and it is a simple and inexpensive technology. Thus, in addition to a low reactivity with the melt, the chosen materials for these buffer layers must have a low mismatch with YBCO and must grow epitaxially through CSD growth. In this section we worked with thin YBCO films (~100nm), in order to use their optimized growth conditions.

5.2.1 Ba$_2$Cu$_3$O$_4$Cl$_2$ CSD layers

The material Ba$_2$Cu$_3$O$_4$Cl$_2$ is often referred as Ba2342. This oxychloride phase has a tetragonal structure and was first reported in single crystal form , which showed magnetic properties [152, 153]. More recently, it has been reported to grow epitaxially as small nanometric crystals inside of YBCO when chlorine is added to the YBCO precursor solution. Shimoyama et al. showed how these crystals grow epitaxially on STO single crystal substrates and how YBCO is c-axis aligned both on the sides and on top of Ba2342 [154, 155]. Since no cross-contamination of chlorine exists between both phases, it seems that Ba2342 is not reactive with YBCO, and therefore could be a suitable buffer layer. To explore this possibility, a short stay was performed in Professor Shimoyama's lab, using as well their fluorine-free methodology to grow YBCO in order to test the synthesized buffer layers.

Ba2342 precursor solution was prepared by mixing barium and copper commercial precursor solutions in the desired stoichiometry and adding a chlorinating agent, in this case chloro-pentane. The solution was deposited by spin-coating and pyrolysed at 500ºC. Afterwards, the growth profile shown in Fig.5.8 b) was followed, which corresponds to the conditions used by Shimoyama et al. to grow YBCO together with the Ba2342 phase.
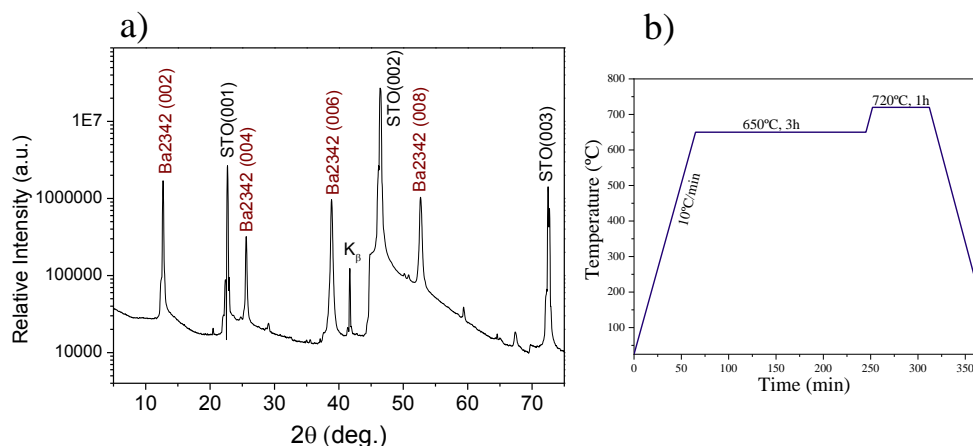
FIGURE 5.8: (a) θ-2θ XRD pattern of a Ba2342 film, obtained with Shimoyama's lab point-detector diffractometer.

Fig.5.8 a) shows the θ-2θ scan performed by a point detector of the resulting film. The epitaxial peaks of Ba2342 phase are detected, with a very small fraction of other unidentified secondary phases.

A scan in growth temperature between 720ºC and 780ºC was performed, giving always epitaxial films. The surface of the films grown at 720ºC, 750ºC
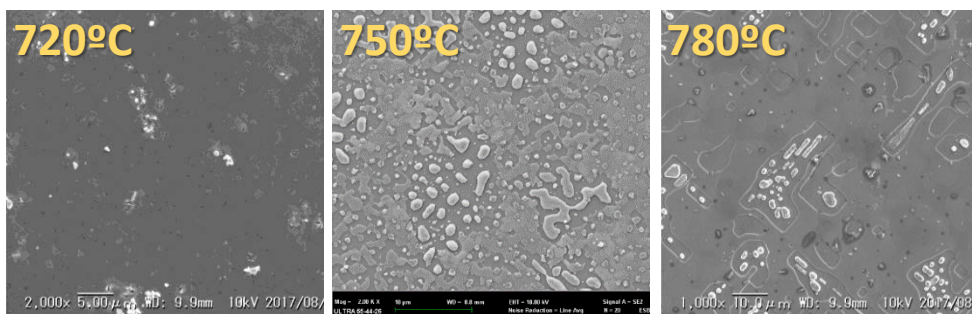
FIGURE 5.9: Top view SEM images of Ba2342 films grown at different temperatures.

and 780ºC was observed by SEM as shown in Fig.5.9. At 720ºC, the film is flat and homogeneous, but when increasing growth temperature, an increase of dewetting is observed, with large areas of the substrate not covered by the film. Hence, although the epitaxy of Ba2342 is maintained through a big range in temperature, the morphology of the films is only optimal below 750ºC, where no dewetting is observed. Therefore, to continue with the study of these films we chose the final temperature of 720ºC.
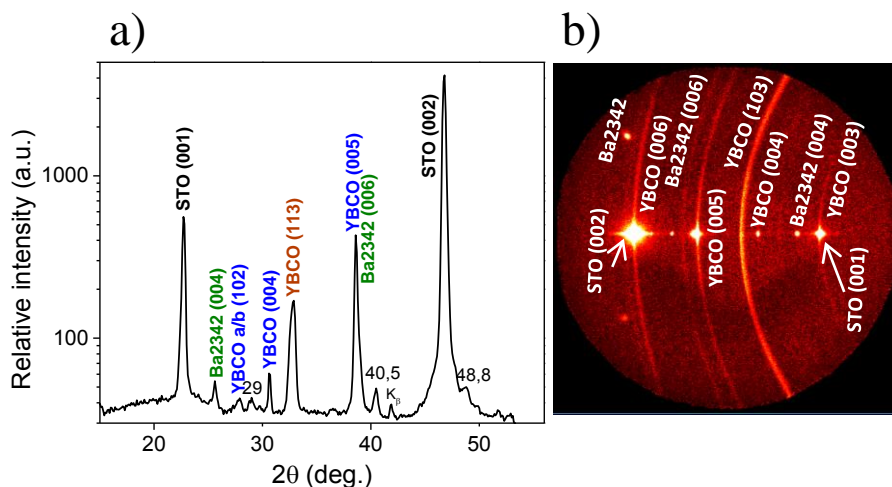
FIGURE 5.10: XRD patterns of a YBCO film grown on top of Ba2342. (a) Integrated θ-2θ scan of the GADDS image shown in (b).

YBCO precursor solution was deposited and pyrolysed on top of Ba2342 films. After an homogeneous pyrolysis was obtained, the films were subjected to YBCO growth conditions such as the ones shown in Fig.5.8 b). The step at

650° is designed to fully eliminate the barium carbonate before the growth of YBCO. The details and mechanisms of this growth process are different than TLAG and will not be discussed here [155], but it is useful to investigate the compatibility of Ba2342 buffer layer with YBCO nucleation. The X-ray diffraction pattern of the resulting film is shown in Fig.5.10. Fig.5.10 a) shows the integrated pattern of the 2D-XRD shown in Fig.5.10 b). The peaks corresponding to c-axis oriented Ba2342 are observed, although in the 2D-XRD image they show a very strong misorientation. Regarding YBCO, reflections corresponding to random nucleation and a/b grains are observed, as well as the epitaxial c-axis reflection which shows an epitaxial spot and a misoriented ring in the χ angle. We can conclude that the Ba2342 phase is compatible with YBCO since it has not reacted during YBCO growth. Achieving a fully epitaxially aligned YBCO film would require some further optimization.
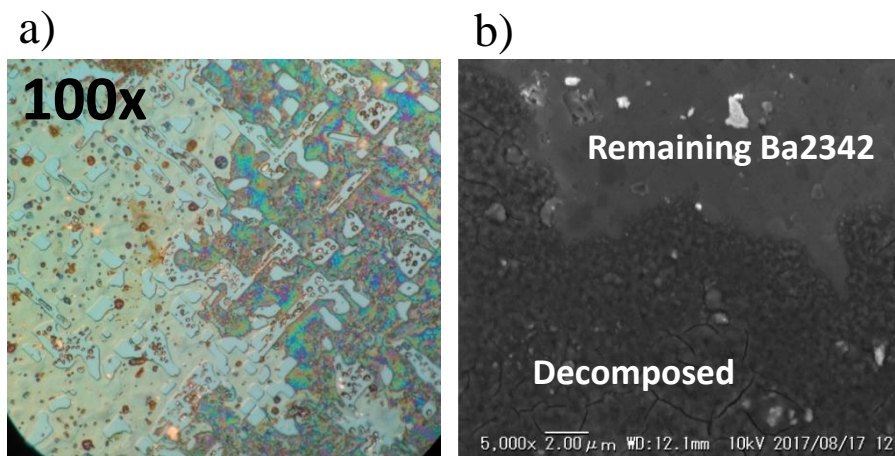
FIGURE 5.11: (a) Optical microscopy image with 100x augmentation of a partially decomposed Ba2342 sample. (b) Top-view SEM of a partially decomposed Ba2342 film.

While studying the Ba2342 films, it became apparent that the samples changed morphology several hours or days after their synthesis, with the changes being appreciated by the naked eye. To investigate these changes, we imaged the films through optical microscopy and SEM, which are presented in Fig.5.11. A clear change can be observed in the sample. In the optical microscopy image shown in Fig.5.11 a), on the left we observe a clear transparent phase corresponding to the remaining Ba2342, while on the right side the colored surface is consistent with the presence of an amorphous phase. This difference is also observed by SEM. The presence of an amorphous phase as a result of Ba2342 decomposition is also supported by XRD scans performed after the

change was observed in the samples, which only showed a slight decrease in the intensity of the Ba2342 peaks but didn't present any other crystalline phase. This decomposition poses a big difficulty for the use of Ba2342 as a buffer layer. The necessary storing conditions to avoid decomposition prior to YBCO deposition and growth should be investigated. Nonetheless, we succeeded in the growth of epitaxial Ba2342 films which opens the door to further studies and optimization.

5.2.2 Nd_2CuO_4 CSD layers

Several literature examples show Nd_2CuO_4 as a good material for YBCO buffer layers, a superconducting material with a tetragonal lattice which a-b lattice parameter has a low mismatch with YBCO [156]. In one of the examples, this perovskite has been tested by liquid phase epitaxy growth methodologies and on top of nickel oxide, a common substrate for coated conductors, showing no reactivity with REBCO or NiO [157]. Adapting the experimental details found in literature, a precursor solution for Nd_2CuO_4 was synthesized by mixing Cu acetate and Nd nitrate in methoxyethanol. The concentration of the solution was 0.2M. Homogeneous depositions were obtained by spin-coating the precursor solution on top of LAO and STO substrates, and a pyrolysis step was performed at 500ºC, following the same profile as the standard pyrolysis treatment for YBCO films introduced in Chapter 2.
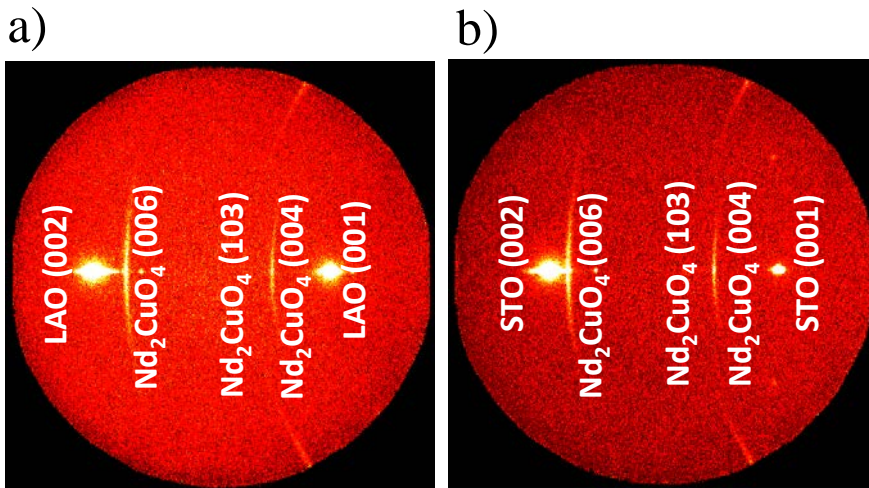
FIGURE 5.12: 2D XRD patterns for Nd_2CuO_4 films grown at 900ºC on top of (a) LAO and (b) STO.

To achieve the growth of epitaxial Nd_2CuO_4 films, we used a tubular furnace in atmospheric total pressure, a PO_2 of $2 \cdot 10^{-3}$bar and heating ramps of 20°C/min. Two different final temperatures were chosen, 850°C and 900°C, and samples on top of both LAO and STO were subjected to the treatment.
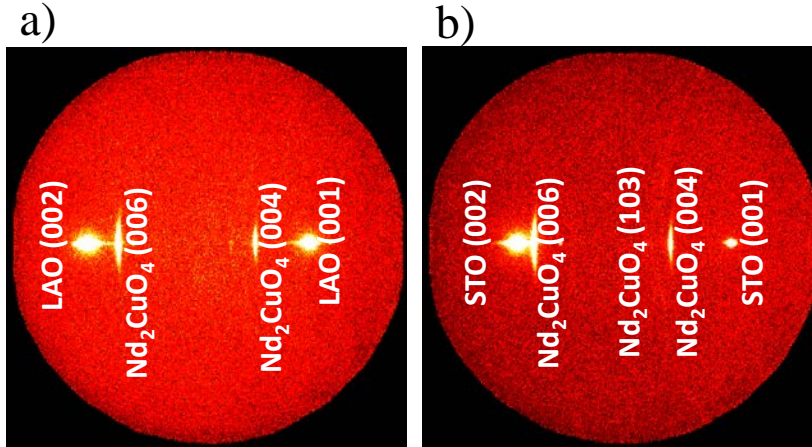
a)   b)

FIGURE 5.13: 2D XRD patterns for Nd_2CuO_4 films grown at 850°C on top of (a) LAO and (b) STO.

Fig.5.12 shows the 2D XRD patterns of samples grown at 900°C on top of LAO on a) and STO on b). Fig.5.13 shows the results for samples grown at 850°C. At 900°C, the films grown on both substrates show very similar behaviour. We detect the peaks corresponding to c-axis oriented Nd_2CuO_4 as well as some degree of random nucleation in the films, indicated by the presence of the (103) ring reflection. In the samples grown at 850°C in Fig.5.13, the orientation of the film is different depending on the substrate. The film grown on STO presents a lower misorientation of the c-axis aligned peaks and less amount of random nucleation, but the (103) ring can still be observed. On the other hand, random nucleation has completely disappeared in the film grown on LAO. Only peaks corresponding to epitaxial Nd_2CuO_4 are detected, which present a slight misorientation in the χ direction of $\sim 6^\circ$.

The Nd_2CuO_4 film grown at 850°C on LAO was chosen to test the compatibility with YBCO growth through TLAG temperature route.

YBCO precursor solution was deposited on top of a Nd_2CuO_4 film and subjected to the standard pyrolysis treatment. The film was grown in the RTA furnace at 835°C, $PO_2 = 1 \cdot 10^{-3}$ and a heating ramp of 40°C/s. This heating ramp was chosen due to the extensive reactivity with STO observed under these conditions on Chapter 3. Fig.5.14 shows the integrated XRD before and after the growth of YBCO on top of Nd_2CuO_4. After the treatment for YBCO
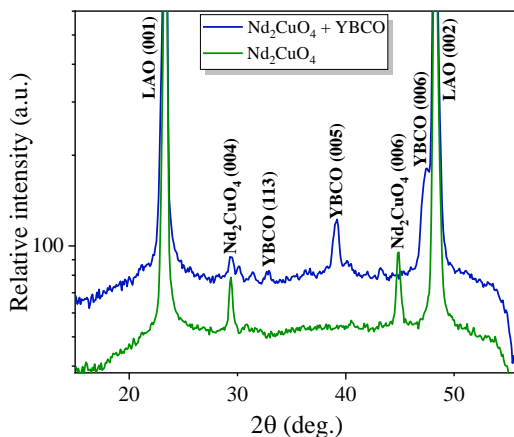
FIGURE 5.14: Integrated XRD pattern of a pristine
Nd_2CuO_4 film and with YBCO grown on top.

growth, we see how the peaks corresponding to Nd_2CuO_4 have mostly disappeared, which could indicate strong reactivity. Nonetheless, we observe the peaks corresponding to YBCO epitaxial orientation and a small fraction of random nucleation. No other phases which could be the product of reactivity of the buffer layer, such as Nd_2O_3, are detected.
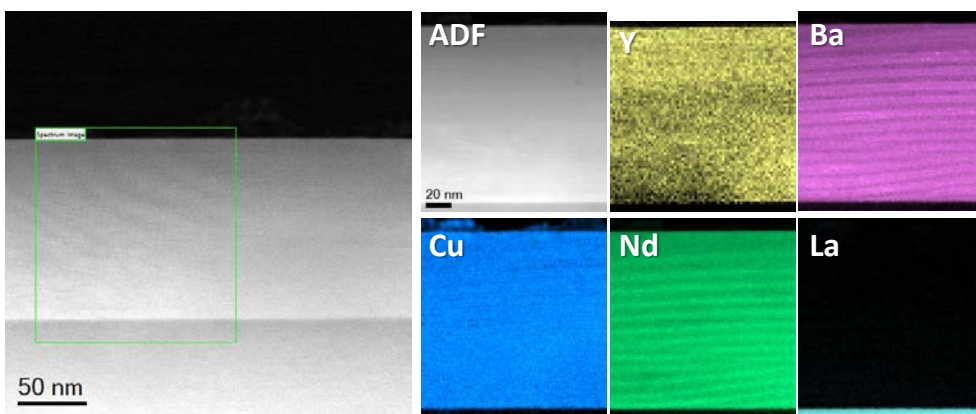

FIGURE 5.15: STEM image and corresponding EELS spectroscopy on the marked green frame of a YBCO film grown on top of a Nd_2CuO_4 buffer layer at 40ºC/s.

To investigate the behaviour of the Nd_2CuO_4 buffer layer when YBCO is grown on top at high heating ramps, we performed STEM analysis of the sample. Fig.5.15 shows an image of the whole thickness of the sample and EELS spectroscopy scans of several elements in the marked green frame. The film

is homogeneous and non-porous, and no points of reactivity with the substrate are detected. Nonetheless, the Nd_2CuO_4 buffer layer has completely dissolved, as evidenced by the presence of neodymium in the whole film. All the elements corresponding to YBCO are also homogeneously distributed in the whole film, which shows that Nd_2CuO_4 has diffused into the YBCO structure instead of forming other secondary phases. No trace of Nd_2CuO_4 phase was detected in any of the areas observed by STEM, but also no reactivity with the substrate, although with these processing conditions extended reactivity was found in films grown directly on top of single crystal substrates. It is possible that the dissolution of neodymium has changed supersaturation conditions and therefore the temperature at which YBCO growth is occurring, thus preventing reactivity with the substrate although the buffer itself is destroyed. This is not an ideal buffer, as it dissolves with the corrosive Ba-Cu melt in certain conditions, but it could be interesting to continue with its study either to understand the mechanism through which reactivity with the substrate has been avoided, or to find other conditions in which the buffer might not react with the liquid. Moreover, we know that 40ºC/s is on the extreme side and that epitaxy does not require such high heating ramps, thus opening the door to exploring other conditions where the Ba-Cu melt might be less reactive.

5.2.3   LaMnO$_3$ and La$_{0.8}$Sr$_{0.2}$MnO$_3$ CSD layers

The third crystalline material to be considered as a possible buffer layer is the perovskite $LaMnO_3$ (LMO) and its partially substituted counterpart, $La_{0.8}Sr_{0.2}MnO_3$ (LSMO). LMO has been used to grow REBCO materials on top through various methodologies [158]. SUMAN group in ICMAB has a wide experience in synthesizing LSMO thin films through CSD techniques, in an effort to achieve conducting buffer layers through CSD techniques. LSMO was successfully used as a buffer layer for YBCO grown through TFA-CSD methodology [159]. In this section we aim to investigate the compatibility of this previously developed buffer with YBCO grown through TLAG. A precursor solution was synthesized by dissolving lanthanum acetate and strontium acetate in a mixture of 80% of acetic acid and 20% of water in volume, with a final concentration of 0.3M [160]. $15\mu l$ of solution were deposited by spin coating. Afterwards the samples were placed in a tubular furnace and heated at 3ºC/min until 1000ºC, with a dwell of 30min. A flow of 0.6l/min of oxygen was started at 700ºC and shut down at the same temperature during cooling. This thermal treatment gives epitaxial LMO and LSMO films with 35nm in thickness [161].
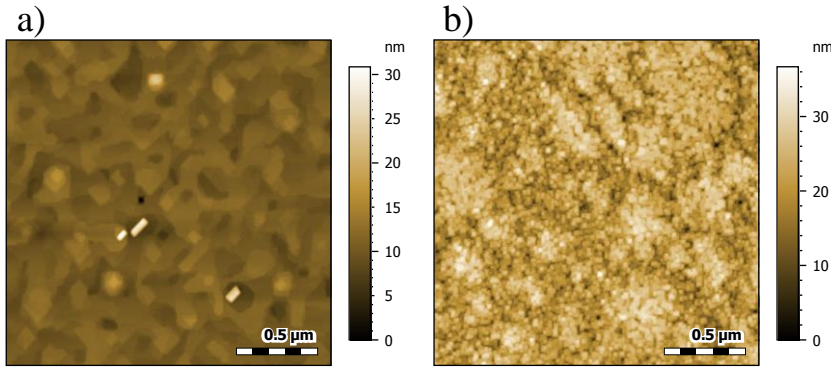
FIGURE 5.16: Topography AFM images of (a) LMO film and (b) LSMO film.

We investigated the surface of the films through atomic force microscopy in topography mode. Fig.5.16 shows the surface morphology of a) LMO and b) LSMO. The RMS factor, indication of the film's roughness, was measured as 1.3nm in LMO and 4.8nm in LSMO. It is important for the buffer layer to have a low roughness, in order to accommodate the growth of YBCO. Both RMS values are within an acceptable range, and therefore both compounds were used for the following step. Homogeneous pyrolysis of YBCO precursor solution were obtained on top of LMO and LSMO through the standard pyrolysis treatment. After, the films were grown in the RTA furnace at 835°C, $PO_2=1\cdot10^{-3}$bar, with two different heating ramps, 30°C/s and 60°C/s.
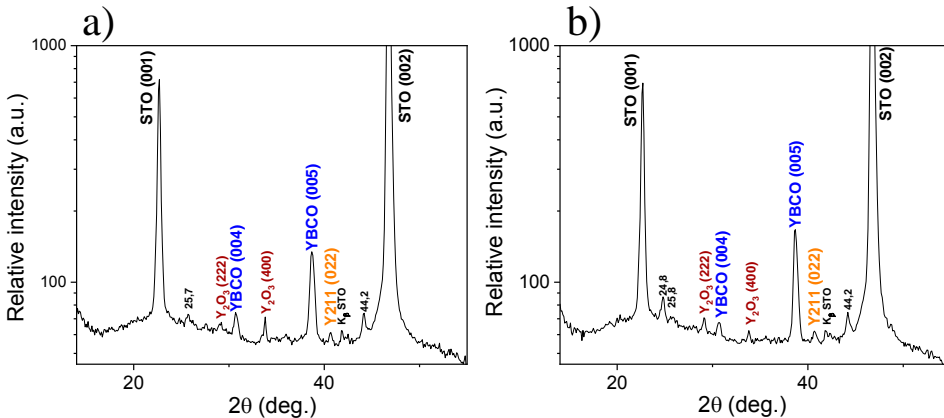
FIGURE 5.17: Integrated XRD patterns of YBCO films grown at 30°C/s on top of (a) LMO and (b) LSMO.

Fig.5.17 shows the integrated XRD pattern for samples grown at 30°C/s for LMO and LSMO. In both of them the growth of epitaxial YBCO can be

observed, as well as Y_2O_3 and a small fraction of Y211 phase. No peaks are detected for the LMO or LSMO layers, either due to the overlap with the STO peaks at this 2θ ranges or due to reactivity of the buffer layer.
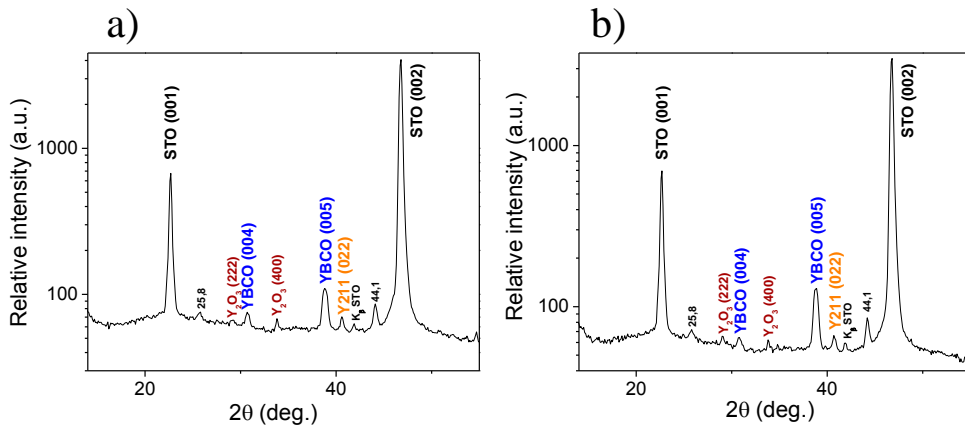
FIGURE 5.18: Integrated XRD patterns of YBCO films grown at 60ºC/s on top of (a) LMO and (b) LSMO.

The XRD patterns of YBCO grown on top of LMO and LSMO at 60ºC/s are shown in Fig.5.18. We also detected the growth of epitaxial YBCO and some Y_2O_3 and Y211 as secondary phases, similarly to the samples grown at 30ºC/s. The only observable difference is the increase of the peak found at 2θ=44.1, belonging to an unidentified phase which could indicate the presence of some reacted phases.

STEM analysis was performed on a sample with a LSMO buffer layer grown at 60ºC/s. Fig.5.19 shows two different spots of the same sample. In both of them, the LSMO epitaxial buffer layer can be appreciated, although the thickness varies greatly, being of 25nm in Fig.5.19 a) while in Fig.5.19 b) the buffer appears to be only 2-3nm thick. Furthermore, on top of the buffer there is Ba-Cu oxide with unknown stoichiometry in both cases. The epitaxial YBCO film starts on top of the Ba-Cu oxide. In other parts of the sample, the buffer has completely disappeared, as shown in Fig.5.20.

The image shown in Fig.5.20 a) shows an inhomogeneous film with a big particle of Ba-Cu oxide. To identify the presence of the different elements, EELS spectroscopy was performed on the marked green area, as shown in Fig.5.20 b). We can see how lanthanum and manganese from the LSMO layer have diffused into a big particle on top of the film, while barium and copper are forming a Ba-Cu oxide particle. Lanthanum is also present in the YBCO structure. The titanium spectra, present in STO substrate, shows how the substrate has remained unaffected by the [Ba-Cu-O] liquid.
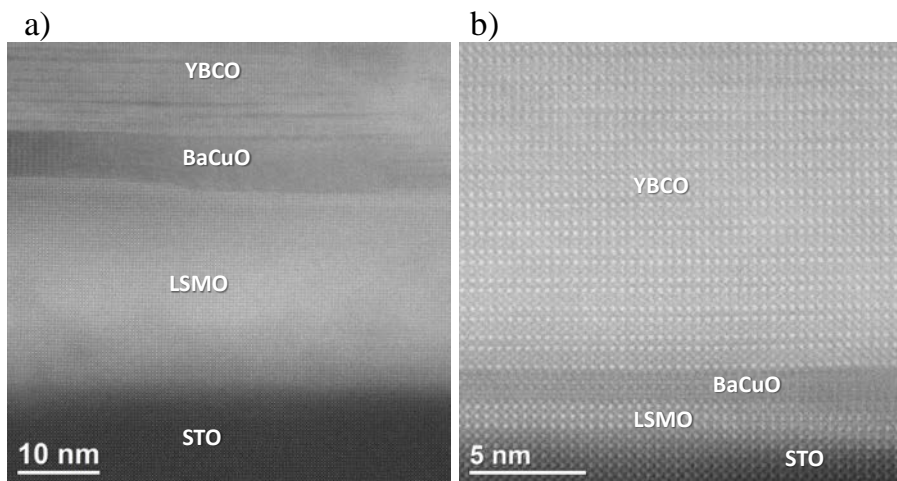
FIGURE 5.19: STEM images with different resolution of a YBCO film grown on top
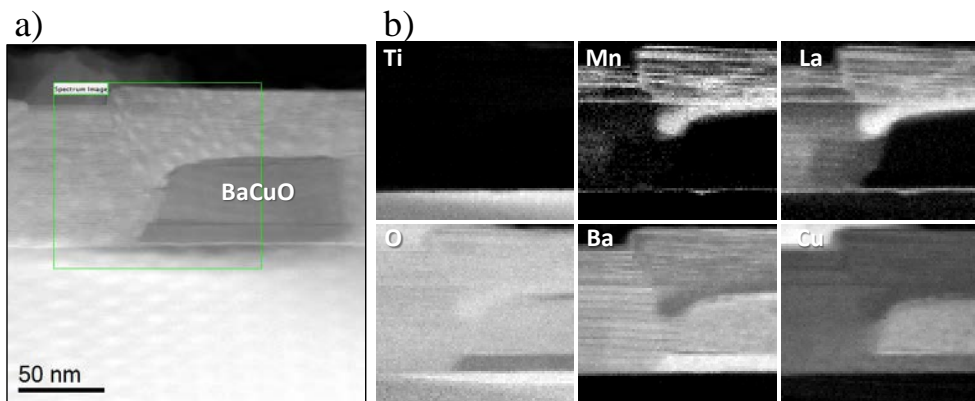of an LSMO buffer layer at 60ºC/s.

FIGURE 5.20: STEM image and corresponding EELS spectroscopy on the marked
green frame of a YBCO film grown on top of a Nd$_2$CuO$_4$ buffer layer at 40ºC/s.

It is difficult to assess the compatibility of LMO or LSMO with YBCO growth
through TLAG. On one hand, we have found reactivity with the buffer layer,
but on the other hand, we have achieved YBCO epitaxial growth and reactiv-
ity is local, with parts of the buffer layer still present. We can compare this to
the reactivity encountered in section 3.2.1, where at 60ºC/s, the most extreme
situation, the YBCO buffer layer had completely dissolved and the reactiv-
ity with the single crystal was extensive. LMO has been investigated in the
conditions where the highest reactivity occurs and has shown a lower interac-
tion with the [Ba-Cu-O] liquid, thus being an interesting candidate for further

studies. These experiments were performed with the intention of finding a CSD buffer completely unreactive with the growth of YBCO with 2:3 stoichiometry by T-route, Nonetheless, TLAG works also with other stoichiometry and processing conditions, which could modify the time and/or temperature during which the liquid is in contact with the buffer layer, which could lead to a lower reactivity. We must also consider how the same crystalline material can show different behaviour when synthesized in different ways, due to other factors that can affect the reactivity of the layer such as porosity or roughness of the surface. For example, LMO thin films synthesized by pulsed laser deposition could achieve buffer layers with different properties. Overall, we believe that LMO is a promising material since it has shown limited reactivity under the most extreme conditions, and therefore a bigger effort in optimizing both the growth of the LMO thin films and the YBCO growth conditions could lead to a useful buffer layer.

5.3 PLD buffer layers and commercial tapes

Pulsed laser deposition (PLD) is an effective method for synthesizing thin epitaxial films with good crystalline quality. Since it is an extensively studied technique, the optimal processing conditions to grow many materials are well known. From our investigations with CSD buffer layers we chose $LaMnO_3$ as a material with potential as a buffer layer and thus in this section we will show the results on LMO buffers grown through PLD. Furthermore, commercial tapes designed as coated conductors substrates with an outer LMO buffer will also be investigated in terms of compatibility with YBCO growth through TLAG.

5.3.1 PLD $LaMnO_3$ buffer layers

Thin PLD $LaMnO_3$ films were synthesized in collaboration with Dr. Max Sieger at the PLD service from ICMAB, on top of STO substrates with the following optimized conditions: the films were deposited at 650ºC and PO_2=5·10^{-3}mbar, with 3000 pulses and a frequency of 3Hz. The growth of LMO through PLD has been previously reported [162]. The AFM and XRD of the obtained $LaMnO_3$ films are shown in Fig.5.21. The roughness of the layers is 0.2nm, which is an indication of a very good planarity, and the XRD pattern shows the epitaxial peaks of $LaMnO_3$, making these films good candidates as buffer layers. YBCO precursor solution with 3:7 eutectic liquid composition was pyrolysed on top of the films following the standard pyrolysis treatment. In this case, we chose the 3:7 stoichiometry due to the lower growth temperature used to grow YBCO with this liquid composition, which could possibly
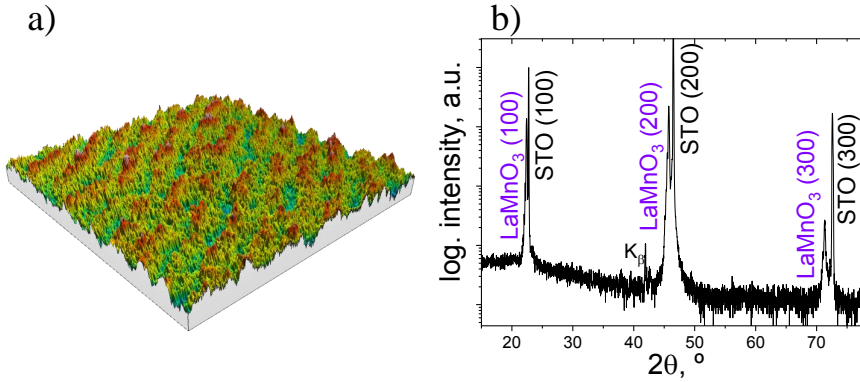
FIGURE 5.21: (a) AFM topography of a PLD LMO film (b) Integrated θ-2θ XRD pattern of a PLD-LMO film.

lead to a less extensive reactivity. We chose the best growth conditions found for both processing routes; T-route and PO_2-route.
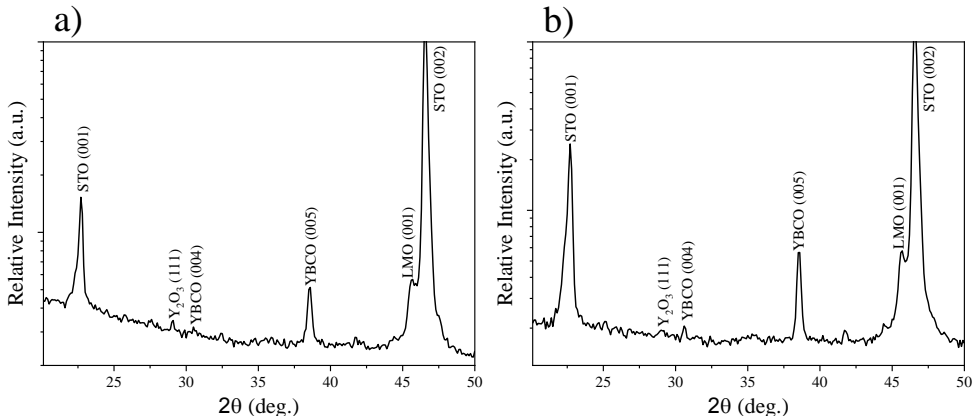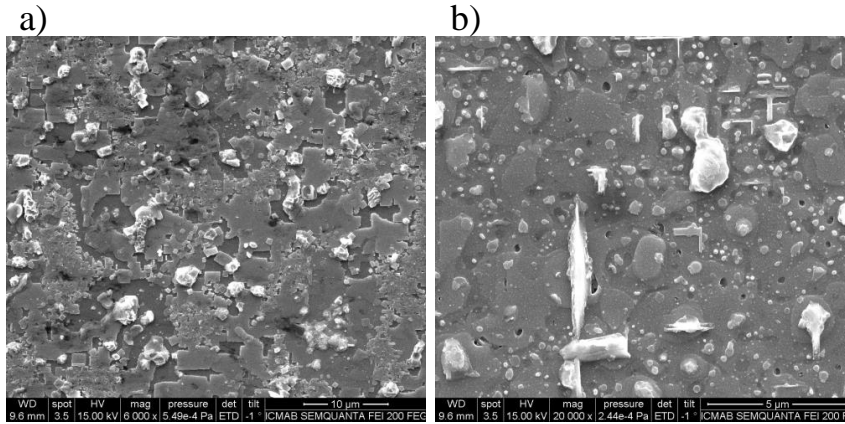

FIGURE 5.22: Integrated θ-2θ XRD pattern of YBCO films grown on top of PLD-LMO buffer layers through (a) Temperature route at 770ºC and 20ºC/s and (b) PO_2 route at 830ºC and a jump between $1 \cdot 10^{-5}$bar and $1 \cdot 10^{-3}$bar.

Fig.5.22 a) shows the integrated XRD pattern for a YBCO film grown on top of LMO buffer through the temperature route, at 20ºC/s until 770ºC and a PO_2 of $1 \cdot 10^{-3}$bar. In Fig.5.22 b) we show the XRD of a film grown through PO_2 route, with a jump between $1 \cdot 10^{-5}$bar and $1 \cdot 10^{-3}$bar performed at 830ºC after heating at 20ºC/s and performing a 5min dwell in the low PO_2 stage. Both films show the peaks corresponding to (00l) epitaxial YBCO, with a small presence of Y_2O_3, and also the epitaxial buffer layer of LMO is detected. These

XRD show a very promising result by confirming the presence of the epitaxial buffer layer after the growth of YBCO.

a)   b)

FIGURE 5.23: Top view SEM of YBCO films grown on top of PLD-LMO buffer layers through (a) Temperature route at 770°C and 20°C/s and (b) PO_2 route at 830°C and a jump between $1 \cdot 10^{-5}$ bar and $1 \cdot 10^{-3}$ bar.

To observe the microstructure of the film surface, SEM was performed on both films and is shown in Fig.5.23. The film grown through T-route shows a slightly inhomogeneous surface, with particles on top as well as some dewetting. The morphology of the film grown through PO_2 route is quite different, with a more homogeneous coverage and less porous surface, although some big particles can also be observed, and some terrace-like features are also present. The T_c of the film grown through PO_2 route was measured by SQUID, giving a value of 89.8K. A bad current percolation due to porosity or the presence of secondary phases result in very low J_c self-field values. In conclusion, the PLD-LMO thin films can successfully act as buffer layers for the growth of epitaxial YBCO films. Optimization of processing conditions is still necessary to improve the current percolation but is a good first result.

5.3.2   YBCO growth on SuNAM buffered metallic substrates

SuNAM company in Korea produces REBCO coated conductors with a carefully designed architecture, schematically shown in Fig.5.24 (a). They also commercialize this architecture without the REBCO layer, which consists of a polished hastelloy, layers of non-textured Al_2O_3 and Y_2O_3, followed by epitaxial MgO deposited through Ion-beam assisted deposition (IBAD) and a final layer of 20nm thick $LaMnO_3$, deposited by sputtering. AFM shown in Fig.5.24 (b) gives a roughness of 2nm for the final layer, and XRD in Fig.5.24 (c) shows
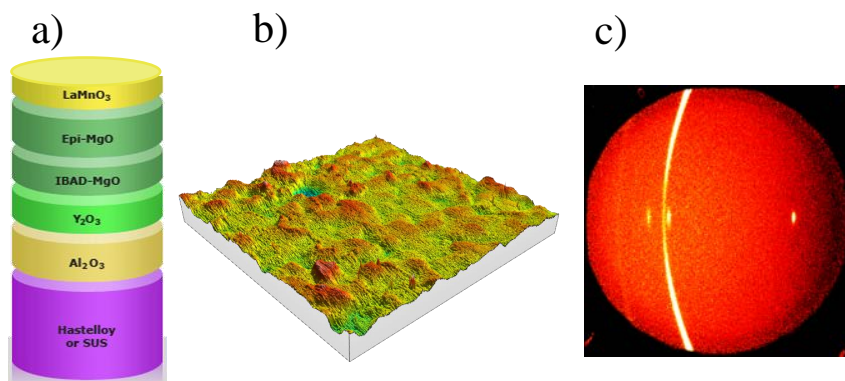
FIGURE 5.24: (a) SuNAM tape architecture (b) Topography image of the LMO layer in SuNAM tape (c) GADDS 2D-XRD of SuNAM tape.

the textured and non-textured phases of the tape. In this case, we studied both the TLAG temperature and PO_2 route compatibility with SuNAM tape.
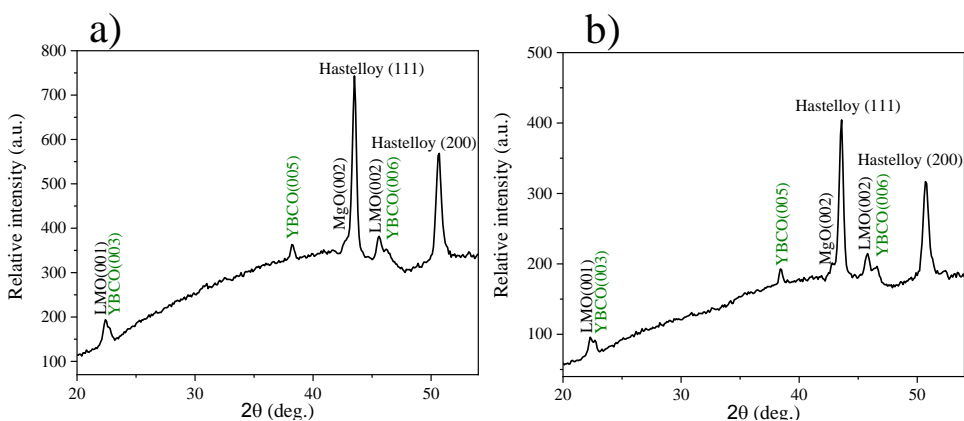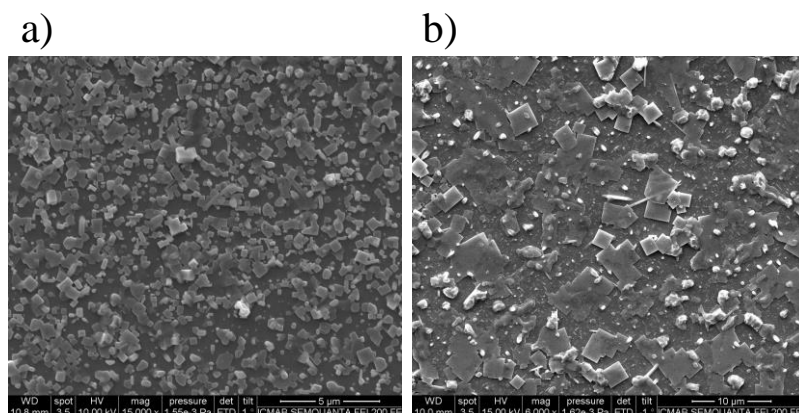

FIGURE 5.25: Integrated XRD pattern of YBCO films grown on top of SuNAM tapes through temperature route (a) with 1:2:3 stoichiometry and (b) 1:2:4.66 stoichiometry.

Two different liquid stoichiometry were used, the 2:3 and the 3:7, each with its different set of conditions. YBCO precursor solution was deposited by spin-coating and pyrolysed on top of the tape with the standard pyrolysis conditions, obtaining homogeneous precursor films. Through temperature route, the sample with 2:3 stoichiometry was grown at 835ºC with a heating ramp of 20ºC/s, and $PO_2 = 1 \cdot 10^{-3}$ bar. In the case of the sample with 3:7 liquid composition, the processing conditions were a growing temperature of 770ºC, a heating ramp of 20ºC/s, and $PO_2 = 1 \cdot 10^{-3}$ bar.

a) b)

FIGURE 5.26: Top view SEM of YBCO films grown on top of SuNAM tapes through temperature route (a) with 1:2:3 stoichiometry and (b) 1:2:4.66 stoichiometry.

Fig.5.25 shows the integrated XRD pattern for the YBCO films grown on top of the SuNAM tape with a) 2:3 and b) 3:7 stoichiometry. The presence of epitaxial YBCO can be observed in both films, as well as the epitaxial LMO buffer layer, MgO and hastelloy. This points towards a successful growth of YBCO without reactivity with the tape.
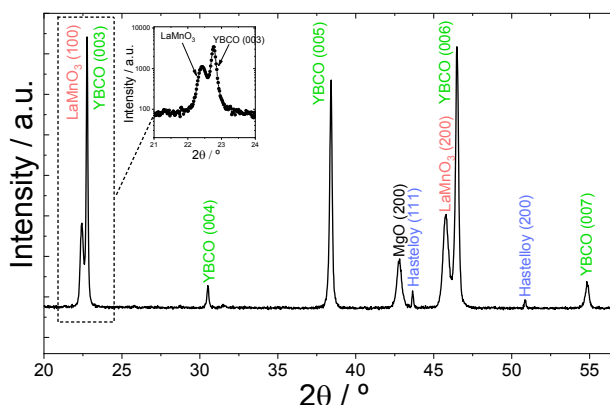

FIGURE 5.27: High resolution θ-2θ high resolution scan between 20-57° of a YBCO film grown on SuNAM tape through the PO$_2$ route.

SEM shown in Fig.5.26 a) for 2:3 stoichiometry film displays an inhomogeneous surface with the presence of small crystals with some dewetting. In the case of the 3:7 film, shown in Fig.5.26 b), some larger square crystals are also present in the surface. Although this kind of morphology will probably hinder good percolation of current, there are no signs of reactivity which usually
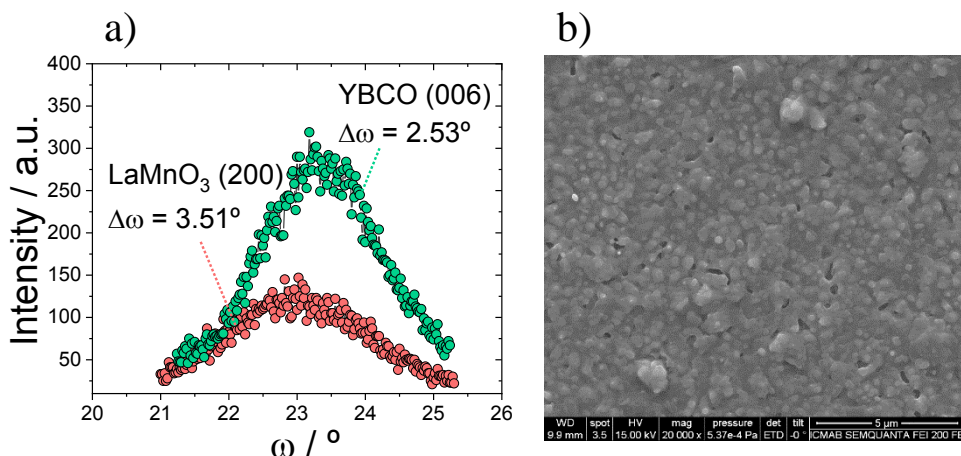
FIGURE 5.28: (a) Rocking curve scans for YBCO and LMO layers of the YBCO film grown on top of SuNAM tape (b) Top-view SEM of the same sample.

appear in the shape of long needles observable by SEM. Preliminary analysis of T_c and J_c shows that tuning process parameters should be further studied. We must take into account that the processing conditions were optimized for single crystals, and should be adapted now to the buffer layer.
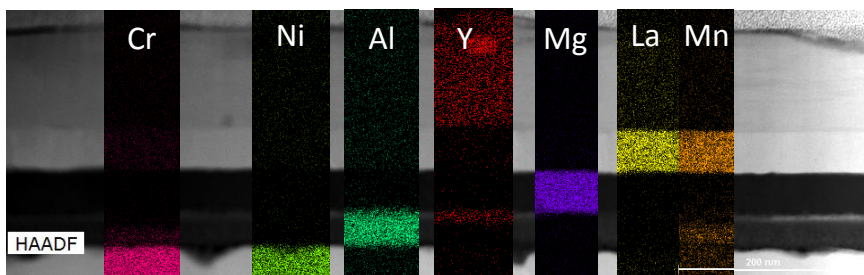

FIGURE 5.29: TEM image and EELS scans of different elements of a SuNAM tape with YBCO grown on top.

Regarding the PO_2-route, a pyrolysed film with 3:7 stoichiometry was grown in Matgas furnace at 830°C with a PO_2 jump between 10^{-5} and 10^{-3}bars after a heating stage at 20°C/min. A high resolution θ-2θ scan is shown in Fig.5.27. The epitaxial (00l) YBCO peaks can be appreciated, as well as the $LaMnO_3$, hastelloy and epitaxial MgO. YBCO is closely matched to the lanthanum manganite, as can be observed by their almost superposing peaks. The texture of the film can be further evaluated by the rocking curve in Fig.5.28 a) where the scans for both YBCO and LMO are shown. The FWHM of YBCO is 2.5°, a very

good value for a film grown on top of a commercial tape. Notice that the rocking curve of YBCO is even smaller than that of the LMO layer underneath. Fig.5.28 b) shows the SEM of the same sample, a percolative homogeneous layer with some small porosity. EELS STEM spectroscopy was used in order to observe the stability of the different layers, as shown in Fig.5.29. The elements corresponding to the hastelloy, Al_2O_3, MgO, $LaMnO_3$ and YBCO have not diffused during the growth, showing abrupt interfaces and completely stable films. This behaviour was observed in all the imaged parts of the sample.
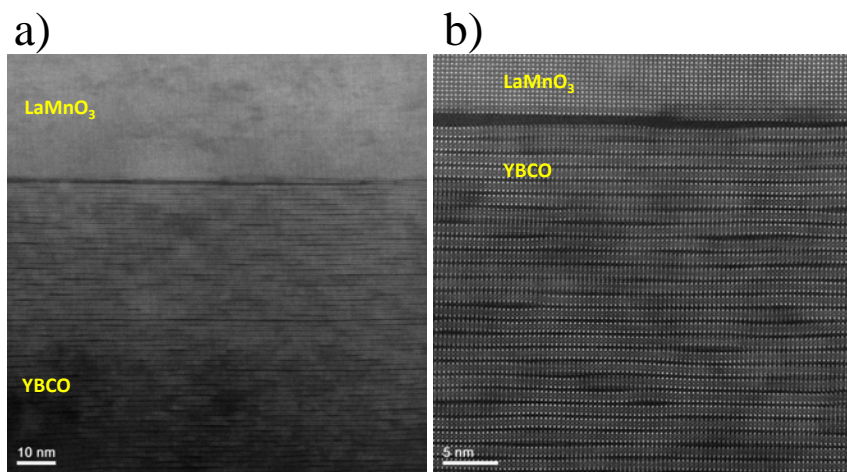
FIGURE 5.30: STEM images with different resolutions of a YBCO film grown on top of SuNAM tape through PO_2 route.

To further study the crystallinity and morphology of the $LaMnO_3$ buffer layer after YBCO growth, STEM images of the PO_2 sample were obtained. Fig.5.30 shows two different spots of the sample, where the c-axis aligned YBCO has grown on top of the LMO buffer layer. The manganite does not show any sign of reactivity and maintains a good crystallinity and flat surface in all the observed areas. The total absence of reactivity under these processing conditions shows the potential of TLAG and in particular of PO_2 route for being scaled up to coated conductor technologies. The superconducting properties of this film are shown in Fig.5.31. T_c was measured by Van der Pauw, giving a T_c=90.5K. J_c self-field at 77K measured by SQUID is 0.4MA/cm^2, and 4.9MA/cm^2 at 5K. Although there is still room for optimization of the properties, the growth process has succeeded already in obtaining epitaxial films without reactivity with the tape, which are two of the main challenges when facing growth on commercial buffered metallic substrates.
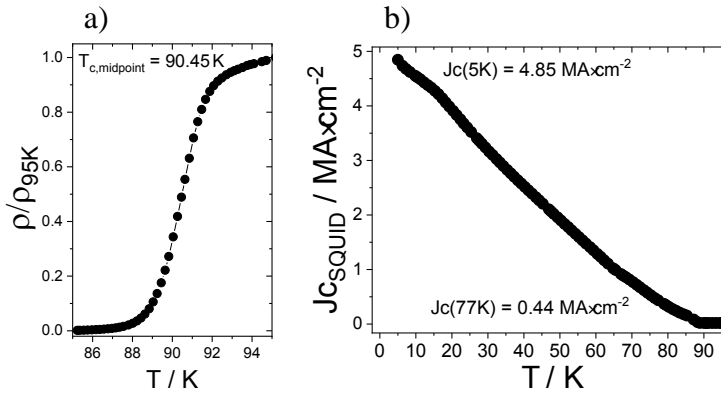
FIGURE 5.31: (a) T_c measured by Van der Pauw and (b) J_c vs T measured by SQUID of a film grown on SuNAM tape grown by PO_2-route.

5.4 Conclusions

This chapter has described the first efforts dedicated to study the compatibility of TLAG methodologies with the necessary requirements for coated conductor implementation. One of the goals of this viability study is to be able to grow YBCO films of at least 1 micromater in thickness. Only with such thickness the total current transported through the film might be adequate for real applications. Therefore, we have tackled the issues that can arise due to increased thickness of the films. We have demonstrated how TLAG is capable of eliminating $BaCO_3$ in 1μm thick films both through the temperature route and PO_2 route processes. The effective elimination of this precursor is necessary for a good orientation of the films and a good percolation of current.

Regarding the YBCO growth of thick films, we have shown how PO_2 route achieves epitaxial growth of up to 1 micrometer films, with a compact non-porous structure, and a rocking curve of 0.5°. Van der Pauw gives a T_c of 90.3K, although some optimization of the process is necessary to increase J_c, limited at this time to $0.4MA/cm^2$. Regarding the processing conditions of the temperature route, random nucleation prevails in the growth of thick films, and when heating ramp is increased in order to grow the films in a region where c-axis nucleation is promoted, we encounter reactivity with the single crystal substrates. Therefore we need other strategies to achieve epitaxial thick films through T-route, such as developing a buffer layer that blocks reactivity with the substrate.

The second part of this chapter has been devoted to investigate different buffer layers compatible with the Ba-Cu-O liquid in order to avoid reactivity in different conditions. We have investigated different materials and different growth methods for the buffer layers. Although no buffer has been studied extensively, we have aimed at performing experiments that could assess the potential of the different materials as unreactive buffer layers. We have used CSD methodologies to successfully grow thin epitaxial films of $Ba_2Cu_3O_4Cl_2$(Ba2342), Nd_2CuO_4, $LaMnO_3$ and $La_{0.8}Sr_{0.2}MnO_3$. In the case of Ba2342, to our knowledge it is the first time that such films have been reported. Ba2342 showed a strong instability in atmospheric conditions and YBCO films grown on top contained an important fraction of random nucleation. When YBCO was grown on top of Nd_2CuO_4, c-axis orientation was achieved but STEM analysis showed that the buffer layer had dissolved and Nd atoms diffused into the YBCO structure. In the case of LMO and LSMO we obtained promising results, since even when using $60^{\circ}C/s$ heating ramp, the buffer layer was not completely destroyed and reactivity with the substrate was strongly decreased in comparison with films grown without buffer layer under the same conditions. Since LMO showed the lower reactivity with the Ba-Cu-O melt, we synthesized LMO films through PLD to test layers of the same material but with different roughness and morphology. The growth of YBCO on top of these buffers was epitaxial both through the temperature route and PO_2 route, and the LMO peaks were also detected after growth. Nonetheless, SEM shows some dewetting and inhomogeneity of the films, and thus further optimization is needed in order to reach films with good current percolation. Finally, we also attempted the growth of YBCO on top of commercial SuNAM tapes, which have a film of LMO as the last layer of their architecture. Through temperature route conditions, the YBCO grown on top is epitaxially aligned but shows some dewetting through SEM. In the case of PO_2 route, the film was epitaxial and its surface was very homogeneous, with a T_c of 89.3K and a J_c=0.4MA/cm^2, which are very promising results. In conclusion, we have shown preliminary results that prove the compatibility of TLAG methodologies with the growth of thick films, different buffer layers and coated conductors. Although there is still a lot of optimization to be done, we have shown the potential of these method to be scaled-up towards long length coated conductors. Further work should also include the implementation of the knowledge gathered in the growth of nanocomposites into the step of growing thick films and films on top of buffered metallic substrates.

Final conclusions

This thesis has presented the research on the growth of YBCO nanocomposite films through transient liquid assisted growth, a new methodology which combines the presence of a transient liquid that provides ultrafast growth rates with the inexpensive methods of chemical solution deposition. We have also performed a brief screening on possible buffer layers and thick films growth.

It is the first time that the successful growth of epitaxial nanocomposites grown through an ultrafast CSD methodology has been reported. Growth rates of up to 100nm/s in both processing routes have been demonstrated in pristine films by in-situ synchrotron X-ray diffraction. In the case of nanocomposite films we could demonstrate 90nm/s growth rate in T-route and through PO_2 we envisage a similar result, although it could not be confirmed since the experimental conditions than that used in high growth rate pristine films.

Pre-formed nanoparticles of $BaZrO_3$, LaF_3 and $BaHfO_3$ obtained in colloidal solutions were stabilized in the YBCO precursor solution, achieving the necessary final solutions for the growth of nanocomposites.

Different results were obtained depending on the processing route used for the growth of the films, showing how the reactions and kinetics of YBCO crystallization are of furthermost importance for the incorporation of artificial pinning centers. In particular, supersaturation of Y in the Ba-Cu liquid governs the nucleation of YBCO in TLAG both for pristine and nanocomposite films.

Through the temperature route, two Ba-Cu liquid stoichiometry were tested. When the eutectic composition 3:7 was used, epitaxial nanocomposites with 12%$BaZrO_3$ and 12%$BaHfO_3$ were easily obtained with the same growth conditions used for pristine films. On the other hand, films with 2:3 liquid composition required optimization in order to eliminate the random nucleation created by the presence of nanoparticles. We proved how very small changes in heating ramp had a big influence in controlling epitaxial nucleation, since $BaCO_3$ elimination is occurring during heating and therefore, changing heating ramp we change the temperature at which YBCO nucleation occurs. We also demonstrated the benefits of using a PLD YBCO buffer layer. In this

route we achieved a self-field critical current density at 77K of $J_c=0.6MA/cm^2$ with 2:3 stoichiometry, due to the presence of reactivity with the substrate, and $1MA/cm^2$ with 3:7 stoichiometry, due to liquid wetting problems also present in pristine films. Further work is necessary to optimize these values but they are a good starting point together with the success on growing epitaxial nanocomposites with both liquid stoichiometry.

In the PO_2 route, working with 3:7 liquid, allowed epitaxial growth of nanocomposites with 6% and 12% molar of $BaZrO_3$ and $BaHfO_3$ with good superconducting properties. A certain irreproducibility in the nucleation was observed, with half of the $12\%BaMO_3$ films presenting a/b nucleation, which was fixed by using a seed layer. These nanocomposites have J_c up to $2.2MA/cm^2$ at 77K and self-field, and a $T_c=90K$ as measured by Van der Pauw, which proves that we can grow films with embedded small nanoparticles and very good superconducting properties. The final goal of increasing critical current densities at high magnetic fields, requires an understanding of the microstructure of the nanocomposites, in order to nanoengineer the defects that will most enhance vortex pinning. For that reason, STEM was performed in several films to investigate the effect that nanoparticles have on the growth process. We discovered a high density of 248 stacking, occupying the whole film thickness. Furthermore, the nanoparticles revealed to be epitaxially oriented with the YBCO matrix, a surprising result due to the fast kinetics of the process.

In-situ synchrotron X-ray studies both for the temperature and PO_2 route showcased the phase evolution for YBCO and the nanoparticles during growth. The diffraction peak of BZO appeared simultaneously to the growth of YBCO, indicating that nanoparticles recrystallize during the growth process. In the PO_2-route, the peak belongs to epitaxial nanoparticles.

The superconducting properties under magnetic field of nanocomposites grown through the PO_2-route were further investigated due to their promising results. The critical current density exceeded that of pristine films above 0.1T at 5K, demonstrating their effective pinning capabilities. Furthermore, evaluation of the J_c vs H reveals that TLAG nanocomposites have an outstanding H* as compared to standard CSD nanocomposites. Electric transport measurements at 9T showed the enhanced J_c as compared to pristine films, specially at low temperatures. Therefore, all together we could demonstrate the benefits of fabricating TLAG nanocomposites.

The scaling of any methodology developed in a laboratory requires many steps to reach a final product, i.e. coated conductors. Transient liquid assisted growth and its nanocomposite films aspire to be scaled up to final applications, and with this in mind, during this thesis we also performed experiments devoted to bring TLAG closer to a final coated conductor, testing the growth

of thick films up to 1μm and several buffer layers. We demonstrated the complete barium carbonate elimination of 1μm thick films through the PO$_2$-route and T-route. Epitaxial thick films were obtained through the PO$_2$-route with high T$_c$, while T-route requires further optimization of the processing conditions. So far, the thick films of this work showed J$_c$=0.4MA/cm^2 at 77K and self-field.

We were able to grow four different buffer layers through CSD methodologies: Ba$_2$Cu$_3$O$_4$Cl$_2$, Nd$_2$CuO$_4$, LaMnO$_3$ and La$_{0.8}$Sr$_{0.2}$MnO$_3$. The material with the most promising behaviour was LaMnO$_3$ (LMO), since it presented only local reactivity at very high heating ramps. Thus, we also used PLD techniques to grow LMO thin films, which showed no reactivity with YBCO-TLAG both through the PO$_2$-route and T-route. Finally, we used SuNAM commercial tape which contains LMO as their final buffer layer, and we demonstrated the epitaxial growth of YBCO with very good texture, shown by a rocking curve of 2.5°. STEM showed no reactivity during the growth process, and we obtained a T$_c$=89.3K as measured by Van der Pauw and critical current density of J$_c$=0.4MA/cm^2 at 77K and self-field. The J$_c$ values can still be optimized by fine-tuning the growth conditions, but this is already an important step forward towards demonstrating the usefulness of TLAG for coated conductor industries.

In conclusion, we have investigated YBCO nanocomposites grown through the novel TLAG method, gaining insight in the nucleation of these films through two distinct processing paths, achieving epitaxial nanocomposites. The properties of these nanocomposites have been evaluated, showing potential for vortex pinning, making TLAG films compatible with applications at high magnetic fields. This effort together with general aspects of TLAG is described in a publication in *Nature communications* [64]. We have also presented preliminary studies on the growth of thick films and buffer layers, overall contributing to the understanding and applicability of transient liquid assisted growth.

This work opens the door to further research on the compatibility of TLAG with applications at high magnetic fields. Further work should include the optimization of superconducting properties of T-route nanocomposites, both by fine-tuning the buffer layers introduced in this thesis and through improving liquid wettability in the case of 3:7 stoichiometry. Optimizing the growth conditions of PO$_2$-route nanocomposites could also render even higher critical current densities for these films. Most importantly, the work on thick films and growth on commercial tapes should be carried on. Deposition methods such as ink-jet printing which obtain thick films in one single deposition should be studied, as well the optimization of the growth process both

for pristine thick films and nanocomposites. All of this work will be continued in ICMAB by different members of the SUMAN group, working towards demonstrating the feasibility of the growth of thick YBCO nanocomposite films on top of commercial buffered substrates by TLAG.

Appendix A

Characterization techniques

A.1 X-ray Diffraction techniques

X-ray diffraction (XRD) is one of the most common techniques for structural characterization of crystalline materials. It is non destructive and probes a very big sample volume. Depending on the configuration and equipment used, multiple information of the samples can be obtained, such as phase composition, degree of epitaxy, etc.
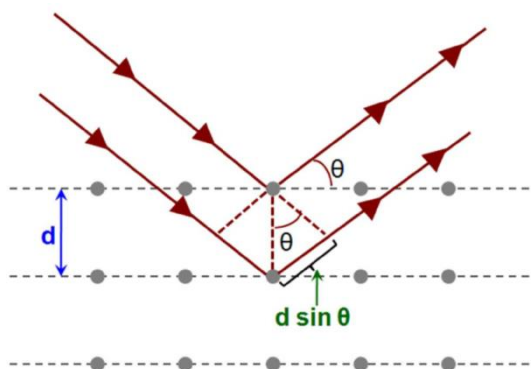
FIGURE A.1: Depiction of Bragg's law.

XRD techniques rely on the fact that the wavelength of X-rays is of the same order of magnitude as the spacing between planes of crystalline materials. According to Bragg's law, depicted in Fig.A.1, when a monochromatic X-ray beam irradiates a crystalline matrix, the beam will be scattered with the same wavelength as the incident beam, and for certain incident angles the diffracted beam will interfere constructively [163]. The intensity of this

diffracted wave will be detected an related to a certain inter-planar distance following the equation:

$$2d_{hkl}sin\theta = n\lambda \tag{A.1}$$

where d_{hkl} is the distance between crystalline planes of the same family, θ is the incident angle and n a positive integer of the wavelength, λ. Therefore, each family of crystalline planes, which has a characteristic spacing, will only diffract at a specific incident angle, through which they can be identified. Moreover, when the sample is polycrystalline, each plane family will diffract in a ring in their specific diffraction angle when moving in χ or ω angles, in the typical Bragg-Brentano configuration used in X-ray diffraction systems and shown in Fig.A.2 [164]. On the other hand, if a sample is epitaxial the constructive interference will only occur at certain positions of χ and ω, since the planes oriented in only one direction will only fulfil Bragg's law in specific positions of the reciprocal space.
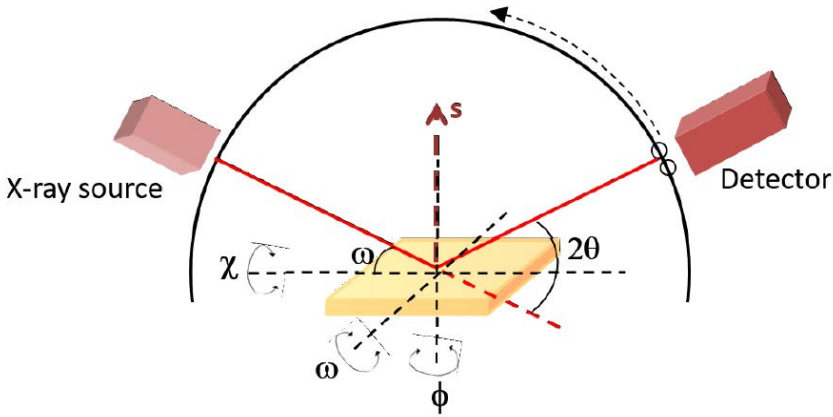
FIGURE A.2: Depiction of Bragg-Brentano configuration for XRD.

In this thesis two diffractometers were used and operated by ICMAB's technicians. The first equipment is a Discover D8 Bruker diffractometer equipped with a Lynxeye XE energy dispersive 1D detector and a CuK$_\alpha$ X-ray source of 8.049keV. The second diffractometer is a Bruker-AXS D8 Advance equipped with a two-dimensional detector, a General Area Detector Diffraction system.

A.1.1 θ-2θ Scans

The most common measurement to identify the phases and grain orientations present in a crystalline film is a θ-2θ scan, in which the peak positions can be

matched to their corresponding phase through comparison with data sheets. The two available detectors were used to measure these kind of scans. The Discover D8 diffractometer measured between 5° and 120° with a step of 0.02°. The high resolution of this diffractometer is useful to identify small secondary phases, but in order to observe the texture of the films, the 2D detector of GADDS system was used. Scans were performed with one frame of the 2D detector which encloses a range of 2θ of 30°, which we fix between 15° and 55°. The χ angle has an opening of 70°. But in order to detect all the epitaxial peaks we need to perform a scan in ω in order to fulfil the bragg-brentano configuration of all the different peaks. The measurement scans ω between 5° and 25° at the fixed χ and 2θ frame during 30 minutes.

A.1.2 Grazing incidence scans

In order to detect a higher intensity from polycrystalline components of the samples, we can eliminate the high intensity bragg epitaxial peaks by performing a θ-2θ scan with a very low omega angle, $\omega \approx 1°$. In this way we will not detect the substrate peaks or other epitaxial phases, but is a useful technique to evaluate the phases present in films such as pyrolysed samples which contain polycrystalline phases, detected in all the ω range.

A.1.3 a/b fraction determination

GADDS diffractometer was used in order to quantify the amount of a/b grains. We choose the reflection (104) and perform a ϕ scan with the 2D detector in the 2θ and χ positions where the epitaxial c-axis grains show this reflection. Another frame is taken of the pole of a/b oriented grains of the same reflection, to be able to compare the intensities of both peaks following the equation:

$$v_{ab} = \frac{2I_{ab}sin(34\frac{\pi}{180})}{2I_{ab}sin(34\frac{\pi}{180}) + I_{c}sin(56\frac{\pi}{180})} \tag{A.2}$$

as shown by Granozio et al.

A.1.4 Nanoparticles random fraction

In order to determine the fraction of randomly oriented nanoparticles versus epitaxial ones, GADDS diffractometer was used to take a frame, during 30 min, of the pole of the most intense peak of the nanoparticles phase. This is the (110) reflection of $BaZrO_3$ and $BaHfO_3$ and its epitaxial peak appears at χ=45°. From the obtained scan we can separate the epitaxial contribution

from the ring by calculating the intensities and following the formula:

$$\frac{I_{random}}{I_{epitaxial}} = \frac{I_{ring}^{exp} \cdot \left(\frac{360}{\Delta\chi}\right) \cdot 4\pi}{8 \cdot I_{pole}^{exp}} \tag{A.3}$$

The intensity of the random fraction is calculated by integrating the intensity in a specific $\Delta2\theta$ of 1.5° and a $\Delta\chi$ of 30°. We then consider this intensity as homogeneous for the full 360° χ ring and solid ring of 4π. The intensity of the epitaxial fraction is calculated by integrating the pole with the same boundaries for all the samples and multiplied by the 8 poles present by symmetry [131].

A.1.5 In-situ synchrotron radiation XRD

The ERC Advanced grant in which this thesis is included, obtained the opportunity to use beamline time in Soleil synchrotron. The Diffabs beamline is equipped with several XRD detectors and is able to use ultrafast acquisition while heating the sample to the desired temperature.

Two different stays of 6 days were performed. The heating stage used the first week was a DHS900 which allows a heating ramp up to 0.8°C/s. In the second stay a new heater Anton Paar DHS1100 allowed up to 5°C/s. The heating ramp used during the experiments is important due to the fast kinetics of TLAG process. The heaters are equipped with different domes mainly transparent to X-rays which allow a closed system in which a gas flow can be introduced to obtain the desired PO_2 conditions. The gas flow was ensured by not fully tying the connection between the heating stage and the dome. Therefore, the gas flow conditions could not be controlled. In order to perform experiments through the PO_2 route, a set-up designed in ICMAB needed to be attached to the provided heating system. A turbo pump (attached to a rotary pump) was used for the lower PO_2 step, which could reach down to 10^{-6}bar. In the case of the higher PO_2 step, a rotary pump is attached to a massflow system through a needle valve to set up the desired PO_2. Both pumps are connected to electrovalves which can be switched on and off from outside the experimental hutch. The upper pressure is set before starting the experiment. Then the lowest pressure circuit is open and the adquisition starts while heating the sample. Once the desired temperature is reached, the pressure is changed by closing the low pressure circuit and opening the high pressure one. The PO_2-meter located near the sample stage detected a pressure jump in less than one second.

The detector used for in-situ experiments is an area detector X-ray hybrid pixel area detector (XPAD) which for the used energy obtains an wide range

in 2θ and χ angles, with acquisition times per data point of 500 ms (for phase evolution before YBCO growth) and 100 ms (for YBCO growth), respectively. To follow random phases, grazing XRD scans were recorded, whereas to follow YBCO growth the Bragg conditions with the (005) peak were met (θ-2θ geometry).

A.1.6 Nanostrain determination

The determination of nanoscale local distortions in a crystalline matrix can be done through Williamson-Hall plot. A full θ-2θ spectra is obtained with the Discover D8 Bruker diffractometer with a high resolution of 0.02° per step. Each (00l) YBCO peak is fitted through gaussian or lorentzian functions to obtain the value of full width at half maximum. Peak broadening can be described in general through Scherrer equation as:

$$\beta = \frac{k\lambda}{Lcos\theta} \tag{A.4}$$

where k is a constant with value close to 1, λ is the used wavelength, L is the crystallite size and θ the bragg angle of the peak. β is related to FWHM with a different factor for each peak fitting function. This formula gives us the relationship between peak broadening and crystallite size, but inhomogeneous strain in the matrix is another source of broadening of XRD peaks. Therefore the observed peak width is a convolution of broadening by the crystallite size and nanostrain, which according to Williamson-Hall analysis can be separated thanks to the different contributions when going to higher (00l) reflections, in our case. The broadening due to strain is given by:

$$\beta_e = C\epsilon tan\theta \tag{A.5}$$

and the deconvolution can be done, in the case of gaussian fitting, as a sum of squares as:

$$\beta_{total}^2 = \beta_L^2 + \beta_e^2 + (\frac{k\lambda}{Lcos\theta})^2 + (C\epsilon tan\theta)^2 \tag{A.6}$$

which can be reorganized to obtain the equation of a straight line, as:

$$\beta_{total}^2 cos\theta = (\frac{k\lambda}{L})^2 + (C\epsilon sin\theta)^2 \tag{A.7}$$

By calculating the broadening of each peak through fitting and substracting the instrumental broadening, and plotting $(sin\theta)^2$ as x and $\beta_{total}^2 cos\theta$ as y, the nanostrain value can be extracted from the slope of the linear fit.

A.2   SQUID dc-magnetometry

Dc-magnetometry was used to evaluate sample properties such as critical temperature, T_c, and critical current versus temperature, $J_c(T)$ or versus magnetic field, $J_c(\mu_0 H)$. The measurements were conducted by Dr. Bozzo in a Quantum Design Superconducting Quantum Interference device (SQUID) equipped with a vacuum pump, a superconducting solenoid magnet of 7T and temperature control between 1.8K and 400K. The detection set-up has three pick up coils in which the sample is moved perpendicular to the applied magnetic field. A current proportional to the magnetic flux variation is induced on the pick-up coils, and through a second derivative SQUID detector system, it is amplified and transformed into current that varies linearly with small changes of the magnetic flux. Inductive SQUID measurements are fast and non-destructive, besides allowing a broad range of temperature and magnetic field variations. Therefore, they have been extensively used in this thesis for evaluating the superconducting properties of the samples.

A.2.1 T_c measurements

The measurement of the critical temperature of the samples relies on measuring magnetization while heating. First of all, the sample is cooled until 10K or 50K under zero field. Once the sample is at the starting temperature, a magnetic field of 0.2mT is applied to magnetize the sample. Then the magnetization is measured while the sample is heated at 0.5K/min. While heating, magnetic flux enters the sample through the surface, decreasing the magnetization. Thus one can evaluate the disappearance of the superconducting state while heating. The value of T_c is defined as the onset temperature at which the magnetization signal is distinguished from zero. The width of the transition temperature, ΔT_c, is defined as the temperature difference between the 10% and 90% of the maximum magnetization.

A.2.2 J_c vs T measurement

To calculate critical current density one needs to measure the irreversible magnetization of the sample. To measure J_c at zero applied field, the sample is cooled to 5K, while magnetized with a magnetic field of 3T. Subsequently, the magnetic field is decreased to zero and the magnetization is measured while heating. The critical current density is determined using the Bean critical state model, according to the expression for a thin film with a squared shape. J_c is calculated according to Beam model equations:

$$J_c = \frac{3m}{a^3 t} A_{corr} \tag{A.8}$$

where m is magnetic moment, a is the lateral dimension of the sample and t the thickness. A correction factor is also introduced to use the real area of the sample . The calculation of this factor can be found in Palau's thesis.

A.2.3 J_c vs H measurement

Calculating critical currents when a magnetic field is applied requires cooling the sample until the desired temperature, typically 5K or 77K, and measure the magnetization pursuing a magnetic field loop. A magnetic field parallel to the c-axis is applied from 0T to 5T and then reversed until -5T measuring all four quadrants of the magnetization loop. The measurement is finished after repeating the first quadrant up to 0.3T. Critical current density is calculated by the Bean critical state model:

$$J_c = \frac{3(m_1 - m_2)}{2a^3 t} A_{corr} \tag{A.9}$$

A.3 Electrical transport measurements

In order to carry out electrical transport measurements we used a Physical properties measurement system (PPMS) of Quantum design located at ICMAB. The measurements and data treatment were performed by Juri Banchewski during his thesis, which is being developed during the same period as this work.

A.3.1 T_c by Van der Pauw

Critical temperature was measured following the so-called Van der Pauw method in which 4 silver contacts are placed on top of the sample in order to measure the R(T) curves. T_c is determined by the temperature at which 50% of the transition between the normal and superconducting state is achieved [165]. The width of the transition, ΔT_c, is determined by the 10%-90% criterion.

A.3.2 Transport measurements

The critical current is measured in low cross-section bridges obtained through a photolithography process and 4 silver contacts deposited on top by sputtering [166]. Bridges of 40μm in width were usually used for the analysis of the

samples in this thesis. An electrical current is applied to the contacted track, and the voltage drop is measured. The critical current is calculated as the necessary current to create a $10\mu V/cm$ electric field in the superconductor. This setup was used to measure critical current at different temperatures, at different applied magnetic fields up to 9T and different orientation of magnetic field.

A.4 Electron microscopy techniques

A.4.1 Transmission Electron Microscopy

Transmission Electron Microscopy (TEM) is a very powerful technique able to obtain information down to the atomic level. The principle relies on using an electron beam to interact with a very thin sample. The information that we can acquire from the transmission of a beam is of the same scale as the wavelength of that beam, and electrons have a wavelength of the order of magnitude of atomic distances, opening the door to such a high resolution. The microscope consists of a column under vacuum where a series of electromagnetic lenses collimate the beam originated from an electron source, focusing it on the sample. After interacting with the specimen, the transmitted beam is again passed through objective lenses until finally reaching the detector. To be able to work with the transmission mode, the width of the specimen cannot be much larger than the mean free path of the electrons, and therefore sample preparation is crucial to be able to obtain high resolution images of the films. The lamellae are typically 15-30nm in width. TEM studies were performed by Dr. Roger Guzmán, a post-doctoral researcher in our group (SUMAN). Specimen preparation was done through conventional methods, by grinding, dimpling and low voltage Ar ion milling, as well as Focused ion beam (FIB) in some cases, achieving the final width of the sample. Two different TEM microscopes were used depending on the required resolution. For low magnification images a FEI Tecnai G2 F20 working at 200kV was used, located at "Institut Català de Nanociència i Nanotecnologia" (ICN2). A FEI Titan 60-300 microscope equipped with a Gatan TRIDIEM 866 ERS energy filter, an X-FEG gun, and a CETCOR probe corrector was operated in STEM mode at 300 kV to obtain high resolution images in the Advanced Microscopy Laboratory (AML) in Zaragoza. This microscope also has an Electron Energy Loss Spectrometer (EELS) able to detect the scatter electrons and determine atomic composition of the samples.

A.4.2   Scanning Electron Microscopy

Scanning Electron Microscopy also relies on the use of a focused electron beam to obtain information of the sample. In this case, the beam is focused on the surface of the sample, which will interact with the atoms in the first tens of nanometers of the film. Two different kind of electrons will be scattered and received by the SEM detectors. The secondary electrons are produced due to inelastic interaction with ionized surface atoms, and the contrast will be created depending on the depth at which these atoms are found. Therefore the SE detector will create a topography image of high resolution, useful to investigate the morphology of the surface of our films. The SEM is also equipped with a backscattered electrons detector which are electrons with higher energy that have interacted with atomic nuclei and therefore the contrast will depend on the composition of the film. The obtained images are a good added information to the topography images, since it can identify which features of the film are not of the same composition, such as CuO particles.

The SEM microscope located at ICMAB is a FEI Quanta 200 FEG operated under high vacuum and 15keV. The microscope was operated by myself.

A.5   Dynamic light scattering measurements

DLS is a technique that is able to calculate the size of nanoparticles in a colloidal solution by determining the speed of Brownian motion. This is evaluated through the translational diffusion coefficient, which depends not only on the size of the nanoparticle's core but also on any component attached to the surface in solution. The colloidal solution is illuminated with light of a specific wavelength, and the rate fluctuations of the scattered light are measured in the detector. The measurements were performed in a Zetasizer Nano ZS from Malvern Instruments.

Bibliography

[1] H. Kamerlingh Onnes. "The liquefaction of helium". In: *Koninklijke Nederlandse Akademie von Wetenschappen, Proceedings* 11 (1908), pp. 1908–1909. DOI: 10.1007/978-94-009-2079-8_7.

[2] H. Kamerlingh Onnes. "Further experiments with Liquid Helium G. On the electrical resistance of Pure Metals etc. VI. On the Sudden Change in the Rate at which the Resistance of Mercury Disappears". In: *KNAW, Proceedings* 14 (1911), pp. 1911–1912. DOI: 10.1007/978-94-009-2079-8_17.

[3] Walther Meissner and Robert Ochsenfeld. "Ein neuer effekt bei eintritt der supraleitfähigkeit". In: *Naturwissenschaften* 21.44 (1933), pp. 787–788.

[4] Fritz London and Heinz London. "The electromagnetic equations of the supraconductor". In: *Proceedings of the Royal Society of London. Series A-Mathematical and Physical Sciences* 149.866 (1935), pp. 71–88. DOI: 10.1098/rspa.1935.0048.

[5] John Bardeen, Leon N. Cooper, and John Robert Schrieffer. "Theory of superconductivity". In: *Physical review* 108.5 (1957), p. 1175. DOI: 10.1103/PhysRev.108.1175.

[6] J.N. Rjabinin and L.W. Shubnikow. "Magnetic properties and critical currents of supra-conducting alloys". In: *Nature* 135.3415 (1935), pp. 581–582. DOI: 10.1038/135581a0.

[7] Lev Davidovich Landau. *Collected papers of L.D. Landau.* 1965. ISBN: 9780080105864.

[8] J. George Bednorz and K. Alex Müller. "Possible high T_c superconductivity in the Ba-La-Cu-O system". In: *Zeitschrift für Physik B Condensed Matter* 64.2 (1986), pp. 189–193. DOI: 10.1007/bf01303701.

[9] Maw-Kuen Wu et al. "Superconductivity at 93 K in a new mixed-phase Y-Ba-Cu-O compound system at ambient pressure". In: *Physical review letters* 58.9 (1987), p. 908. DOI: 10.1103/PhysRevLett.58.908.

[10] A.P. Drozdov et al. "Superconductivity at 250K in lanthanum hydride under high pressures". In: *Nature* 569.7757 (2019), pp. 528–531. DOI: 10.1038/s41586-019-1201-8.

[11] Jagdish Kumar et al. "Enhanced superconducting performance of melt quenched $Bi_2Sr_2CaCu_2O_8$ (Bi-2212) superconductor". In: *Materials Chemistry and Physics* 139.2-3 (2013), pp. 681–688. DOI: 10.1016/j.matchemphys.2013.02.016.

[12] Kazuyuki Isawa et al. "Irreversibility line for a Pb-doped Hg-Ba-Ca-Cu-O superconductor". In: *Applied physics letters* 64.10 (1994), pp. 1301–1303. DOI: 10.1063/1.111941.

[13] Alex Gurevich. "To use or not to use cool superconductors?" In: *Nature materials* 10.4 (2011), pp. 255–259. DOI: 10.1038/nmat2991.

[14] David Larbalestier et al. "High-T$_c$ superconducting materials for electric power applications". In: *Materials For Sustainable Energy: A Collection of Peer-Reviewed Research and Review Articles from Nature Publishing Group*. World Scientific, 2011, pp. 311–320. DOI: 10.1142/9789814317665_0046.

[15] Alexei A. Abrikosov. "On the magnetic properties of superconductors of the second group". In: *Sov. Phys. JETP* 5 (1957), pp. 1174–1182.

[16] Charles P. Bean. "Magnetization of hard superconductors". In: *Physical review letters* 8.6 (1962), p. 250. DOI: 10.1103/PhysRevLett.8.250.

[17] Charles P. Bean. "Magnetization of high-field superconductors". In: *Reviews of modern physics* 36.1 (1964), p. 31. DOI: 10.1103/RevModPhys.36.31.

[18] Siegfried Graser et al. "How grain boundaries limit supercurrents in high-temperature superconductors". In: *Nature Physics* 6.8 (2010), pp. 609–614. DOI: 10.1038/nphys1687.

[19] Yasuhiro Iijima et al. "Biaxially aligned YBa$_2Cu_3O_{7-x}$ thin film tapes". In: *Physica C: Superconductivity* 185 (1991), pp. 1959–1960. DOI: 10.1016/0921-4534(91)91104-C.

[20] Seok Ju Lee et al. "Recent status and progress on HTS cables for AC and DC power transmission in Korea". In: *IEEE Transactions on Applied Superconductivity* 28.4 (2018), pp. 1–5. DOI: 10.1109/TASC.2018.2820721.

[21] Kideok Sim et al. "Design and current transporting characteristics of 80 kV direct current high temperature superconducting cable core". In: *IEEE transactions on applied superconductivity* 23.3 (2013), pp. 5401804–5401804. DOI: 10.1109/TASC.2012.2237001.

[22] Byeongmo Yang et al. "Qualification test of a 80 kV 500 MW HTS DC cable for applying into real grid". In: *IEEE Transactions on Applied Superconductivity* 25.3 (2015), pp. 1–5. DOI: 10.1109/TASC.2015.2396683.

[23] Hae-Jin Sung et al. "Design, fabrication, and analysis of HTS coils for a 10-kW wind power generator employing a brushless exciter". In: *IEEE Transactions on Applied Superconductivity* 27.4 (2017), pp. 1–5. DOI: 10.1109/TASC.2017.2651118.

[24] T. Winkler, EcoSwing Consortium, et al. "The EcoSwing Project". In: *IOP Conference Series: Materials Science and Engineering*. Vol. 502. 1. IOP Publishing. 2019, p. 012004. DOI: 10.1088/1757-899X/502/1/012004.

[25] Xavier Obradors and Teresa Puig. "Coated conductors for power applications: materials challenges". In: *Superconductor Science and Technology* 27.4 (2014), p. 044003. DOI: 10.1088/0953-2048/27/4/044003.

[26] Richard P Feynman. "There's plenty of room at the bottom: An invitation to enter a new field of physics". In: *Handbook of Nanoscience, Engineering, and Technology*. CRC Press, 2018, pp. 26–35. DOI: 10.1201/9781315217178-6.

[27] Timothy J Haugan et al. "Artificial Pinning Centers in (Y, RE)-Ba-Cu-O Superconductors: Recent Progress and Future Perspective". In: *Superconductor Science and Technology* (2019). DOI: 10.1088/1361-6668/ab4ccd.

[28] T. Matsushita. "Flux pinning in superconducting 123 materials". In: *Superconductor Science and Technology* 13.6 (2000), p. 730. DOI: 10.1088/0953-2048/13/6/320.

[29] Takayuki Terai, Kazuyuki Kusagaya, and Yoichi Takahashi. "Modification of the high-Tc superconductor $YBa_2Cu_3O_{7-x}$ by particle-beam irradiation". In: *Physica C: Superconductivity* 190.1-2 (1991), pp. 116–118. DOI: 10.1016/S0921-4534(05)80219-9.

[30] J.C. Barbour et al. "Irradiation effects in high temperature superconductors". In: *Nuclear Instruments and Methods in Physics Research Section B: Beam Interactions with Materials and Atoms* 65.1-4 (1992), IN9–538. DOI: 10.1016/0168-583X(92)95100-6.

[31] M. Sparing et al. "Artificial pinning centres in YBCO thin films induced by substrate decoration with gas-phase-prepared Y_2O_3 nanoparticles". In: *Superconductor Science and Technology* 20.9 (2007), S239. DOI: 10.1088/0953-2048/20/9/S19.

[32] Tolga Aytug et al. "Analysis of flux pinning in $YBa_2Cu_3O_{7-\delta}$ films by nanoparticle-modified substrate surfaces". In: *Physical Review B* 74.18 (2006), p. 184505. DOI: 10.1103/PhysRevB.74.184505.

[33] David Andrews, Thomas Nann, and Robert H Lipson. *Comprehensive nanoscience and nanotechnology*. Vol. 3. Academic Press, 2019. ISBN: 0123743966.

[34] T. Haugan et al. "Island growth of Y_2BaCuO_5 nanoparticles in (211 1.5nm/123 10nm)$\times$ N composite multilayer structures to enhance flux pinning of $YBa_2Cu_3O_{7-\delta}$ films". In: *Journal of materials research* 18.11 (2003), pp. 2618–2623. DOI: 10.1557/JMR.2003.0366.

[35] T. Haugan et al. "Addition of nanoparticle dispersions to enhance flux pinning of the $YBa_2Cu_3O_{7-x}$ superconductor". In: *Nature* 430.7002 (2004), pp. 867–870. DOI: 10.1038/nature02792.

[36] J.L. MacManus-Driscoll et al. "Strongly enhanced current densities in superconducting coated conductors of $YBa_2Cu_3O_{7-x}$ + $BaZrO_3$". In: *Nature materials* 3.7 (2004), pp. 439–443. DOI: 10.1038/nmat1156.

[37] B Maiorov et al. "Synergetic combination of different types of defect to optimize pinning landscape using $BaZrO_3$-doped $YBa_2Cu_3O_7$". In: *Nature materials* 8.5 (2009), pp. 398–404. DOI: 10.1038/nmat2408.

[38] Sukill Kang et al. "High-performance high-Tc superconducting wires". In: *Science* 311.5769 (2006), pp. 1911–1914. DOI: 10.1126/science.1124872.

[39] Y. Yamada et al. "Epitaxial nanostructure and defects effective for pinning in $Y(RE)Ba_2Cu_3O_{7-x}$ coated conductors". In: *Applied Physics Letters* 87.13 (2005), p. 132502. DOI: 10.1063/1.2061874.

[40] Theodor Schneller et al. *Chemical solution deposition of functional oxide thin films*. Springer, 2013. DOI: 10.1007/978-3-211-99311-8.

[41] Robert W. Schwartz. "Chemical solution deposition of perovskite thin films". In: *Chemistry of materials* 9.11 (1997), pp. 2325–2340. DOI: 10.1021/cm970286f.

[42] Helmut Dislich. "Sol-gel: science, processes and products". In: *Journal of non-crystalline solids* 80.1-3 (1986), pp. 115–121. DOI: 10.1016/0022-3093(86)90384-4.

[43] DC Williams. "Properties and applications of oxide layers deposited on glass from organic solutions". In: *Journal of Modern Optics* 9 (1962), pp. 249–254.

[44] W Geffcken and E Berger. "Verfahren zur änderung des reflexionsvermögens optischer gläser". In: *Deutsches Reichspatent, assigned to Jenaer Glaswerk Schott & Gen., Jena* 736 (1939), p. 411.

[45] K.D. Budd, Sandwip Dey, and DA Payne. "Sol-gel processing of $PbTiO_3$, $PbZrO_3$, PZT, and PLZT thin films." In: *British Ceramic Proceedings*. Inst of Ceramics. 1985, pp. 107–121.

[46] S.K. Dey, K.D. Budd, and D.A. Payne. "Thin-film ferroelectrics of PZT of sol-gel processing". In: *IEEE transactions on ultrasonics, ferroelectrics, and frequency control* 35.1 (1988), pp. 80–81. DOI: 10.1109/58.4153.

[47] Rainer Waser et al. "Chemical deposition methods for ferroelectric thin films". In: *Ferroelectrics* 259.1 (2001), pp. 205–214. DOI: 10.1080/00150190108008740.

[48] Theodor Schneller and Rainer Waser. "Chemical solution deposition of ferroelectric thin films. State of the art and recent trends". In: *Ferroelectrics* 267.1 (2002), pp. 293–301. DOI: 10.1080/00150190210989.

[49] Rainer Waser et al. "Advanced chemical deposition techniques-from research to production". In: *Integrated Ferroelectrics* 36.1-4 (2001), pp. 3–20. DOI: 10.1080/10584580108015524.

[50] Arunava Gupta et al. "Superconducting oxide films with high transition temperature prepared from metal trifluoroacetate precursors". In: *Applied Physics Letters* 52.24 (1988), pp. 2077–2079. DOI: 10.1063/1.99752.

[51] T. Araki and I. Hirabayashi. "Review of a chemical approach to $YBa_2Cu_3O_{7-x}$ coated superconductors metalorganic deposition using trifluoroacetates". In: *Superconductor science and technology* 16.11 (2003), pp. 91–94. ISSN: 14764660. DOI: 10.1088/0953-2048/16/11/R01.

[52] Xavier Obradors et al. "Growth, nanostructure and vortex pinning in superconducting $YBa_2Cu_3O_7$ thin films based on trifluoroacetate solutions". In: *Superconductor Science and Technology* 25.12 (2012), p. 123001. DOI: 10.1088/0953-2048/25/12/123001.

[53] J. Gutiérrez et al. "Strong isotropic flux pinning in solution-derived $YBa_2Cu_3O_{7-x}$ nanocomposite superconductor films". In: *Nature Materials* 6.5 (2007), pp. 367–373. ISSN: 14764660. DOI: 10.1038/nmat1893.

[54] Vyacheslav Solovyov, Ivo K. Dimitrov, and Qiang Li. "Growth of thick $YBa_2Cu_3O_7$ layers via a barium fluoride process". In: *Superconductor Science and Technology* 26.1 (2012), p. 013001. DOI: 10.1088/0953-2048/26/1/013001.

[55] Yue Zhao et al. "Structural and superconducting characteristics of $YBa_2Cu_3O_{7-x}$ films grown by fluorine-free metal-organic deposition route". In: *Acta Materialia* 144 (2018), pp. 844–852. DOI: 10.1016/j.actamat.2017.11.050.

[56] Xiang Xue Xu et al. "High Performance of YBCO Films Prepared by Fluorine-Free MOD Method and a Direct Annealing Process". In: *Key Engineering Materials*. Vol. 537. Trans Tech Publ. 2013, pp. 243–246. DOI: 10.4028/www.scientific.net/KEM.537.243.

[57] Kenichi Tsukada et al. "Preparation of high-Jc $YBa_2Cu_3O_{7-y}$ films on CeO$_2$-buffered yttria-stabilized zirconia substrates by fluorine-free metalorganic deposition". In: *Japanese journal of applied physics* 44.7R (2005), p. 4914. DOI: 10.1143/JJAP.44.4914.

[58] C. Apetrii et al. "YBCO thin films prepared by fluorine-free polymer-based chemical solution deposition". In: *IEEE transactions on applied superconductivity* 15.2 (2005), pp. 2642–2644. DOI: 10.1109/TASC.2005.847756.

[59] Y.R. Patta, D.E. Wesolowski, and M.J. Cima. "Aqueous polymer-nitrate solution deposition of YBCO films". In: *Physica C: Superconductivity* 469.4 (2009), pp. 129–134. DOI: 10.1016/j.physc.2008.12.006.

[60] Peir Yung Chu and Relva C. Buchanan. "Reactive liquid phase sintering of solution-derived YBa$_2$Cu$_3$O$_{7-x}$ superconducting thin films: Part I. Ambient and precursor effects on BaO-CuO liquid phase formation". In: *Journal of Materials Research* 8.9 (1993), pp. 2134–2142. ISSN: 20445326. DOI: 10.1557/JMR.1993.2134.

[61] A.H. Hamdi et al. "Formation of thin-film high T$_c$ superconductors by metalorganic deposition". In: *Applied physics letters* 51.25 (1987), pp. 2152–2154. DOI: 10.1063/1.98978.

[62] L. Soler. "Liquid-assisted ultrafast growth of superconducting films derived from chemical solutions". Universitat Autonoma de Barcelona, 2019. ISBN: 9788449087059. URL: https://ddd.uab.cat/record/213642.

[63] S. Rasi. "Advanced thermal analysis of ReBCO superconductor precursor films and functional oxides". Universitat de Girona, 2018.

[64] L. Soler et al. "Ultrafast transient liquid assisted growth of high current density superconducting films". In: *Nature communications* 11.1 (2020), pp. 1–8. DOI: 10.1038/s41467-019-13791-1.

[65] Katrien De Keukeleere et al. "Solution-based synthesis of BaZrO$_3$ nanoparticles: Conventional versus microwave synthesis". In: *Journal of Nanoparticle Research* 15.11 (2013). ISSN: 13880764. DOI: 10.1007/s11051-013-2074-7.

[66] Kouichi Nakashima et al. "Preparation of $BaZrO_3$ nanoparticles using a solvothermal reaction". In: *IOP Conference Series: Materials Science and Engineering* 18.SYMPOSIUM 6 (2011). ISSN: 1757899X. DOI: 10.1088/1757-899X/18/9/092049.

[67] Jordi Martínez-Esaín et al. "Tailoring the Synthesis of LnF_3 (Ln = La-Lu and Y) Nanocrystals via Mechanistic Study of the Coprecipitation Method". In: *Langmuir* 34.22 (2018), pp. 6443–6453. ISSN: 15205827. DOI: 10.1021/acs.langmuir.7b03454.

[68] Jordi Martínez-Esaín et al. "Faceted-Charge Patchy LnF_3 Nanocrystals with a Selective Solvent Interaction". In: *Angewandte Chemie - International Edition* 57.45 (2018), pp. 14747–14751. ISSN: 15213773. DOI: 10.1002/anie.201806273.

[69] Niranjan Sahu, B. Parija, and S. Panigrahi. "Fundamental understanding and modeling of spin coating process: A review". In: *Indian Journal of Physics* 83.4 (2009), pp. 493–502. ISSN: 09731458. DOI: 10.1007/s12648-009-0009-z.

[70] Theodor Schneller et al. *Chemical solution deposition of functional oxide thin films*. 2013, pp. 1–796. ISBN: 9783211993118. DOI: 10.1007/978-3-211-99311-8.

[71] R. Bachelet et al. "Self-assembly of $SrTiO_3$(001) chemical-terminations: A route for oxide-nanostructure fabrication by selective growth". In: *Chemistry of Materials* 21.12 (2009), pp. 2494–2498. ISSN: 08974756. DOI: 10.1021/cm900540z.

[72] Byung Hyo Kim et al. "Critical differences in 3D atomic structure of individual ligand-protected nanocrystals in solution". In: *Science* 368.6486 (2020), pp. 60–67. DOI: 10.1126/science.aax3233.

[73] Fermín Otálora and Juanma García-Ruiz. "Nucleation and growth of the Naica giant gypsum crystals". In: *Chemical Society Reviews* 43.7 (2014), pp. 2013–2026. ISSN: 03060012. DOI: 10.1039/c3cs60320b.

[74] F. Miletto Granozio and U. Scotti Di Uccio. "Gibbs energy and growth habits of YBCO". In: *Journal of Alloys and Compounds* 251.1-2 (1997), pp. 56–64. ISSN: 09258388. DOI: 10.1016/S0925-8388(96)02769-7.

[75] K. Kelton and A.L. Greer. *Nucleation in condensed matter: applications in materials and biology*. Vol. 15. 2010, Elsevier, pp. 1–796. ISBN: 978-0-08-042147-6. DOI: 10.1007/978-3-211-99311-8.

[76] X. Obradors et al. "Chemical solution route to self-assembled epitaxial oxide nanostructures". In: *Chemical Society Reviews* 43.7 (2014), pp. 2200–2225. DOI: 10.1039/C3CS60365B.

[77] Y. A. Jee et al. "Top-seeded melt growth of Y-Ba-Cu-O superconductor with multiseeding". In: *Superconductor Science and Technology* 13.2 (2000), pp. 195–201. ISSN: 09532048. DOI: 10.1088/0953-2048/13/2/314.

[78] Y. Shiohara and A. Endo. "Crystal growth of bulk high-Tc superconducting oxide materials". In: *Materials Science and Engineering R: Reports* 19.1-2 (1997), pp. 1–86. ISSN: 0927796X. DOI: 10.1016/S0927-796X(96)00198-2.

[79] Katsumi Nomura et al. "Initial growth mechanism of $YBa_2Cu_3O_y$ crystal on MgO substrate by liquid-phase epitaxy". In: *Journal of Materials Research* 16.10 (2001), pp. 2947–2958. DOI: 10.1557/JMR.2001.0405.

[80] C Klemenz and H J Scheel. "Liquid phase epitaxy of high-Tc superconductors". In: *Journal of Crystal Growth* 129.3-4 (1993), pp. 421–429. DOI: 10.1016/0022-0248(93)90476-D.

[81] A. Kursumovic et al. "Hybrid liquid phase epitaxy processes for $YBa_2Cu_3O_7$ film growth". In: *Superconductor Science and Technology* 17.10 (2004), pp. 1215–1223. ISSN: 09532048. DOI: 10.1088/0953-2048/17/10/024.

[82] Jae Hun Lee et al. "RCE-DR, a novel process for coated conductor fabrication with high performance". In: *Superconductor Science and Technology* 27.4 (2014). ISSN: 13616668. DOI: 10.1088/0953-2048/27/4/044018.

[83] T. Itoh. "Role of CuO for the decarbonation of $BaCO_3$ and $CaCO_3$ in the solid-state reaction of CuO with $BaCO_3$ and that of CuO with $CaCO_3$". In: *Journal of Materials Science Letters* 22 (2003), pp. 185–189. ISSN: 1573-4811. DOI: 10.1023/A:1022293724698.

[84] F. Parmigiani et al. "Observation of carboxylic groups in the lattice of sintered $YBa_2Cu_3O_{7-y}$ high-Tc superconductors". In: *Physical Review B* 36.13 (1987), pp. 7148–7150. ISSN: 0163-1829. DOI: 10.1103/PhysRevB.36.7148.

[85] T. Puig et al. "The influence of growth conditions on the microstructure and critical currents of TFA-MOD $YBa_2Cu_3O_7$ films". In: *Superconductor Science and Technology* 18.8 (2005), pp. 1141–1150. ISSN: 09532048. DOI: 10.1088/0953-2048/18/8/020.

[86] J. Gázquez et al. "Nucleation mechanism of $YBa_2Cu_3O_7$ by CSD using TFA precursors". In: *Journal of Physics: Conference Series* 43.1 (2006), pp. 321–324. ISSN: 17426596. DOI: 10.1088/1742-6596/43/1/080.

[87] M. Nevřiva et al. "On the determination of the CuO-BaCuO$_2$ and CuO-YCuO$_{2.5}$ binary phase diagrams". In: *Journal of Crystal Growth* 91.3 (1988), pp. 434–438. ISSN: 00220248. DOI: 10.1016/0022-0248(88)90265-5.

[88] Wei Zhang, Kozo Osamura, and Shojiro Ochiai. "Phase Diagram of the BaO-CuO Binary System". In: *Journal of the American Ceramic Society* 73.7 (1990), pp. 1958–1964. ISSN: 15512916. DOI: 10.1111/j.1151-2916.1990.tb05252.x.

[89] G. F. Voronin and S. A. Degterov. "Solid state equilibria in the Ba-Cu-O system". In: *Journal of Solid State Chemistry* 110.1 (1994), pp. 50–57. ISSN: 1095726X. DOI: 10.1006/jssc.1994.1134.

[90] P et al. Roura. "Melting of CuO-BaO films prepared by chemical solution deposition (CSD)". In: (to be published).

[91] T.B. Lindemer and E.D. Specht. "The BaO-CuO system. Solid-liquid equilibria and thermodynamics of BaCuO$_2$ and BaCu$_2$O$_2$". In: *Physica C: Superconductivity* 255.1-2 (1995), pp. 81–94. ISSN: 0921-4534. DOI: 10.1016/0921-4534(95)00460-2.

[92] Fadila Taïr et al. "Melting temperature of YBa$_2$Cu$_3$O$_{7-x}$ and GdBa$_2$Cu$_3$O$_{7-x}$ at subatmospheric partial pressure". In: *Journal of Alloys and Compounds* 692 (2017), pp. 787–792. ISSN: 09258388. DOI: 10.1016/j.jallcom.2016.08.072.

[93] C. S. Macdougall, F.A. Washburn, and T.B. Lindemer. "Study of phase behavior in the YBa$_2$Cu$_3$O$_7$-BaCuO$_{2+y}$-CuO-Ag system". In: *Physica C: Superconductivity* 196.3-4 (1992), pp. 390–398. ISSN: 0921-4534. DOI: 10.1016/0921-4534(92)90462-L.

[94] J.L. MacManus-Driscoll, J.C. Bravman, and R.B. Beyers. "Phase equilibria in the YBaCuO system and melt processing of Ag clad Y$_1$Ba$_2$Cu$_3$O$_{7-x}$ tapes at reduced oxygen partial pressures". In: *Physica C: Superconductivity* 241.3-4 (1995), pp. 401–413. ISSN: 0921-4534. DOI: 10.1016/0921-4534(94)02369-7.

[95] Byeong-Joo -J Lee and Dong Nyung Lee. "Thermodynamic Evaluation for the Y$_2$O$_3$-BaO-CuO$_x$ System". In: *Journal of the American Ceramic Society* 74.1 (1991), pp. 78–84. ISSN: 15512916. DOI: 10.1111/j.1151-2916.1991.tb07300.x.

[96] A. Kuršumović et al. "Study of the rate-limiting processes in liquid-phase epitaxy of thick YBaCuO films". In: *Journal of Crystal Growth* 218.1 (2000), pp. 45–56. ISSN: 00220248. DOI: 10.1016/S0022-0248(00)00519-4.

[97]   Yusuke Ichino et al. "Orientation mechanism of $REBa_2Cu_3O_y$ (RE = Nd, Sm, Gd, Y, Yb) thin films prepared by pulsed laser deposition". In: *IEEE Transactions on Applied Superconductivity* 13.2 III (2003), pp. 2735–2738. ISSN: 10518223. DOI: 10.1109/TASC.2003.811972.

[98]   M. Murakami et al. "Melt-processed light rare earth element-Ba-Cu-O". In: *Superconductor Science and Technology* 9.12 (1996), pp. 1015–1032. DOI: 10.1088/0953-2048/9/12/001.

[99]   Toshihiro Iguchi et al. "Fabrication of Gd-Ba-Cu-O films by the metal-organic deposition method using trifluoroacetates". In: *Superconductor Science and Technology* 15.10 (2002), pp. 1415–1420. ISSN: 09532048. DOI: 10.1088/0953-2048/15/10/309.

[100] Jung Woo Lee et al. "Stability phase diagram of $GdBa_2Cu_3O_{7-\delta}$ in low oxygen pressures". In: *Journal of Alloys and Compounds* 602 (2014), pp. 78–86. ISSN: 09258388. DOI: 10.1016/j.jallcom.2014.02.170.

[101] V. Breit et al. "Evidence for chain superconductivity in near-stoichiometric $YBa_2Cu_3O_x$ single crystals". In: *Physical Review B* 52.22 (1995), pp. 4–7. ISSN: 01631829. DOI: 10.1103/PhysRevB.52.R15727.

[102] A. Stangl. "Oxygen kinetics and charge doping for high critical current YBCO films". Universitat Autonoma de Barcelona, 2019. ISBN: 9788449087103. URL: https://ddd.uab.cat/record/213664.

[103] P. Cayado et al. "Epitaxial $YBa_2Cu_3O_{7-x}$ nanocomposite thin films from colloidal solutions". In: *Superconductor Science and Technology* 28.12 (2015), p. 124007. ISSN: 13616668. DOI: 10.1088/0953-2048/28/12/124007.

[104] F. Lu, F. Kametani, and E. E. Hellstrom. "Optimization of a fluorine-free metal-organic deposition to fabricate $BaZrO_3$-doped $YBa_2Cu_3O_{7-x}$ film on RABITS substrates". In: *Superconductor Science and Technology* 26.4 (2013). ISSN: 09532048. DOI: 10.1088/0953-2048/26/4/045016.

[105] H. J. Scheel, W. Sadowski, and L. Schellenberg. "Crucible corrosion in crystal growth of $YBa_2Cu_3O_{7-x}$". In: *Superconductor Science and Technology* 2.1 (1989), pp. 17–21. ISSN: 09532048. DOI: 10.1088/0953-2048/2/1/004.

[106] Kunihiko Oka and Hiromi Unoki. " Phase Diagram of the La_2O_3-CuO System and Crystal Growth of $(La,Ba)_2 CuO_4$ ". In: *Japanese Journal of Applied Physics* 26.Part 2, No. 10 (2005), pp. L1590–L1592. ISSN: 0021-4922. DOI: 10.1143/jjap.26.l1590.

[107] A. Erb, E. Walker, and R. Flükiger. "BaZrO$_3$: the solution for the crucible corrosion problem during the single crystal growth of high-Tc superconductors REBa$_2$Cu$_3$O$_{7-\delta}$; RE = Y, Pr". In: *Physica C: Superconductivity and its Applications* 245.3-4 (1995), pp. 245–251. ISSN: 09214534. DOI: 10.1016/0921-4534(95)00123-9.

[108] Y. A. Jee et al. "Comparison of texture development and superconducting properties of YBCO thin films prepared by TFA and PLD processes". In: *Physica C: Superconductivity and its Applications* 356.4 (2001), pp. 297–303. ISSN: 09214534. DOI: 10.1016/S0921-4534(01)00281-7.

[109] D. Dimos et al. "Orientation Dependence of Grain-Boundary Critical Currents in i". In: *Physical Review Letters* 61.2 (1988), pp. 219–222. ISSN: 0031-9007. DOI: 10.1103/PhysRevLett.61.219.

[110] K. Matsumoto et al. "Critical Current Control in Y$Ba_2Cu_3O_{7-x}$ Films Using Artificial Pinning Centers". In: *Japanese Journal of Applied Physics* 44.7 (2005), pp. 246–248. DOI: 10.1143/JJAP.44.L246.

[111] T. Puig and J. Guti. "Vortex pinning in chemical solution nanostructured YBCO films". In: *Superconducting Science and Technology* 21.3 (2008), pp. 1–12. DOI: 10.1088/0953-2048/21/3/034008.

[112] F. Sandiumenge et al. "Optimization of Flux Pinning in Bulk Melt Textured 1-2-3 Superconductors: Bringing Dislocations under Control". In: *Applied Materials* 12.5 (2000), pp. 375–381. DOI: 10.1002/(SICI)1521-4095(200003)12:5<375::AID-ADMA375>3.0.CO;2-9.

[113] West Lafayette. "Atomic Structures of High-Tc Superconductors". In: 129 (1993), pp. 165–176. DOI: 10.4028/www.scientific.net/MSF.129.165.

[114] J. Gazquez et al. "Structural defects in trifluoroacetate derived Y$Ba_2Cu_3O_{7-x}$ thin films". In: *Superconductor Science and Technology* 25.6 (2012), pp. 1–8. DOI: 10.1088/0953-2048/25/6/065009.

[115] Ch. Jooss, R. Warthmann, and H. Kronmüller. "Pinning mechanism of vortices at antiphase boundaries in Y$Ba_2Cu_3O_{7-x}$". In: *Physical Review B* 61.18 (2000), pp. 12433–12446. ISSN: 0163-1829. DOI: 10.1103/PhysRevB.61.12433. URL: https://link.aps.org/doi/10.1103/PhysRevB.61.12433.

[116] Roger Guzman et al. "Probing localized strain in solution-derived Y$Ba_2Cu_3O_{7-x}$ nanocomposite thin films". In: *Physical Review Materials* 1.2 (2017), p. 024801. ISSN: 2475-9953. DOI: 10.1103/PhysRevMaterials.1.024801.

[117]   M. Coll et al. "Size-controlled spontaneously segregated Ba_2YTaO_6 nanoparticles in $YBa_2Cu_3O_{7-x}$ nanocomposites obtained by chemical solution deposition." In: *Superconductor Science and Technology* 27.4 (2014), p. 044008. ISSN: 0953-2048. DOI: 10.1088/0953-2048/27/4/044008.

[118]   A. Palau et al. "Disentangling vortex pinning landscape in chemical solution deposited superconducting $YBa_2Cu_3O_{7-x}$ films and nanocomposites". In: *Superconductor Science and Technology* 31.3 (2018), p. 034004. ISSN: 0953-2048. DOI: 10.1088/1361-6668/aaa65e.

[119]   Jaume Gazquez et al. "Emerging Diluted Ferromagnetism in High-Tc Superconductors Driven by Point Defect Clusters". In: *Advanced Science* 3.6 (2016), p. 1500295. DOI: 10.1002/advs.201500295.

[120]   Jung Woo Lee et al. "Enhanced flux pinning properties of MOD-processed $YBa_2Cu_3O_{7-x}$ thin films with $BaZrO_3$ nanoparticles using a Ba-deficient coating solution". In: *IEEE Transactions on Applied Superconductivity* 23.3 (2013), pp. 7–10. ISSN: 10518223. DOI: 10.1109/TASC.2013.2244155.

[121]   O. Castano et al. "Influence of porosity on the critical currents of trifluoroacetate-MOD $YBa_2Cu_3O_7$ films". In: *IEEE transactions on applied superconductivity* 13.2 (2003), pp. 2504–2507. DOI: 10.1109/TASC.2003.811832.

[122]   Alberto Pomar et al. "Enhanced vortex pinning in YBCO coated conductors with BZO nanoparticles from chemical solution deposition". In: *IEEE transactions on applied superconductivity* 19.3 (2009), pp. 3258–3261. DOI: 10.1109/TASC.2009.2018422.

[123]   X. Obradors et al. "Nucleation and mesostrain influence on percolating critical currents of solution derived $YBa_2Cu_3O_7$ superconducting thin films". In: *Physica C: Superconductivity and its applications* 482 (2012), pp. 58–67. DOI: 10.1016/j.physc.2012.04.020.

[124]   A. Palau. "Critical currents and dissipation of grain and grain boundary networks in coated conductors". Universitat Autonoma de Barcelona, 2005. ISBN: 8468946389. URL: https://ddd.uab.cat/record/38161.

[125]   MF Chisholm and SJ Pennycook. "Structural origin of reduced critical currents at $YBa_2Cu_3O_{7-\delta}$ grain boundaries". In: *Nature* 351.6321 (1991), pp. 47–49. DOI: 10.1038/351047a0.

[126]   D. Dimos, P. Chaudhari, and J. Mannhart. "Superconducting transport properties of grain boundaries in $YBa_2Cu_3O_{7-x}$ bicrystals". In: *Physical Review B* 41.7 (1990), p. 4038. DOI: 10.1103/PhysRevB.41.4038.

[127] Paolo Mele et al. "Insertion of nanoparticulate artificial pinning centres in $YBa_2Cu_3O_{7-x}$ films by laser ablation of a Y_2O_3-surface modified target". In: *Superconductor Science and Technology* 20.7 (2007), p. 616. DOI: 10.1088/0953-2048/20/7/006.

[128] Paolo Mele et al. "High pinning performance of $YBa_2Cu_3O_{7-x}$ films added with Y_2O_3 nanoparticulate defects". In: *Superconductor Science and Technology* 28.2 (2014), p. 024002. DOI: 10.1088/0953-2048/28/2/024002.

[129] Max Sieger et al. "Tailoring microstructure and superconducting properties in thick $BaHfO_3$ and $Ba_2Y(Nb/Ta)O_6$ doped YBCO films on technical templates". In: *IEEE Transactions on Applied Superconductivity* 27.4 (2016), pp. 1–7. DOI: 10.1109/TASC.2016.2644858.

[130] Claudia Cantoni et al. "Strain-driven oxygen deficiency in self-assembled, nanostructured, composite oxide films". In: *Acs Nano* 5.6 (2011), pp. 4783–4789. DOI: 10.1021/nn2007628.

[131] A. Llordes. "Superconducting nanocomposite films grown by chemical soultion deposition: synthesis, microstructure and properties." Universitat Autonoma de Barcelona, 2010.

[132] A. Llordés et al. "Nanoscale strain-induced pair suppression as a vortex-pinning mechanism in high-temperature superconductors". In: *Nature Materials* 11.4 (2012), pp. 329–336. ISSN: 14764660. DOI: 10.1038/nmat3247.

[133] Sung Hun Wee et al. "Engineering nanocolumnar defect configurations for optimized vortex pinning in high temperature superconducting nanocomposite wires". In: *Scientific reports* 3 (2013), p. 2310. DOI: doi.org/10.1038/srep02310.

[134] Katrien De Keukeleere et al. "Superconducting $YBa_2Cu_3O_{7-\delta}$ Nanocomposites Using Preformed ZrO_2 Nanocrystals: Growth Mechanisms and Vortex Pinning Properties". In: *Advanced Electronic Materials* 2.10 (2016), pp. 1–9. ISSN: 2199160X. DOI: 10.1002/aelm.201600161.

[135] M. Coll et al. "Solution-derived $YBa_2Cu_3O_7$ nanocomposite films with a Ba_2YTaO_6 secondary phase for improved superconducting properties". In: *Superconductor Science and Technology* 26.1 (2012), p. 015001. DOI: 10.1088/0953-2048/26/1/015001.

[136] Ziliang Li et al. "Control of nanostructure and pinning properties in solution deposited $YBa_2Cu_3O_{7-x}$ nanocomposites with preformed perovskite nanoparticles". In: *Scientific reports* 9.1 (2019), pp. 1–14. DOI: 10.1038/s41598-019-42291-x.

[137] Jürgen Pötschke and Volker Rogge. "On the behaviour of foreign particles at an advancing solid-liquid interface". In: *Journal of Crystal Growth* 94.3 (1989), pp. 726–738. ISSN: 00220248. DOI: 10.1016/0022-0248(89)90097-3.

[138] D. R. Uhlmann, B. Chalmers, and K. A. Jackson. "Interaction between particles and a solid-liquid interface". In: *Journal of Applied Physics* 35.10 (1964), pp. 2986–2993. ISSN: 00218979. DOI: 10.1063/1.1713142.

[139] Z. Li. "Growth and characterization of nanocomposite YBaCuO-BaMO$_3$ (M = Zr, Hf) thin films from colloidal solutions". Universitat Autonoma de Barcelona, 2018. ISBN: 9788449081521. URL: https://ddd.uab.cat/record/201515.

[140] Bernat Mundet et al. "Local strain-driven migration of oxygen vacancies to apical sites in $YBa_2Cu_3O_{7-x}$". In: *Nanoscale* 12.10 (2020), pp. 5922–5931. DOI: 10.1039/D0NR00666A.

[141] A. Palau et al. "Disentangling vortex pinning landscape in chemical solution deposited superconducting $YBa_2Cu_3O_{7-x}$ films and nanocomposites". In: *Superconductor Science and Technology* 31.3 (2018), p. 034004. DOI: 10.1088/1361-6668/aaa65e.

[142] F. Valles. "Vortex pinning and creep in YBCO nanocomposite films grown by chemical solution deposition". Universitat Autònoma de Barcelona, 2019. ISBN: 9788449087189. URL: https://ddd.uab.cat/record/213601.

[143] J.P.F. Feighan, A. Kursumovic, and J.L. MacManus-Driscoll. "Materials design for artificial pinning centres in superconductor PLD coated conductors". In: *Superconductor Science and Technology* 30.12 (2017), p. 123001. DOI: 10.1088/1361-6668/aa90d1.

[144] Victor Rouco et al. "Role of twin boundaries on vortex pinning of CSD YBCO nanocomposites". In: *Superconductor Science and Technology* 27.12 (2014), p. 125009. DOI: 10.1088/0953-2048/27/12/125009.

[145] Roger Guzman et al. "Strain-driven broken twin boundary coherence in YBa$_2$Cu$_3$O$_7$-δ nanocomposite thin films". In: *Applied Physics Letters* 102.8 (2013), p. 081906. DOI: 10.1063/1.4793749.

[146] Judy Z. Wu et al. "The effect of lattice strain on the diameter of $BaZrO_3$ nanorods in epitaxial YBa$_2$Cu$_3$O$_{7-\delta}$ films". In: *Superconductor Science and Technology* 27.4 (2014), p. 044010. DOI: 10.1088/0953-2048/27/4/044010.

[147] Masashi Miura et al. "Tuning nanoparticle size for enhanced functionality in perovskite thin films deposited by metal-organic deposition". In: *NPG Asia Materials* 9.11 (2017), e447–e447. DOI: 10.1038/am.2017.197.

[148] B. Villarejo. "Synthesis of defect free $YBa_2Cu_3O_{7-x}$ films over 1μm by CSD using inkjet printing". Universitat Autonoma de Barcelona, 2018. ISBN: 9788449081897. URL: https://ddd.uab.cat/record/202186.

[149] Cornelia Pop et al. "Growth of all-chemical high critical current $YBa_2Cu_3O_{7-\delta}$ thick films and coated conductors". In: *Superconductor Science and Technology* 32.1 (2018), p. 015004. DOI: 10.1088/1361-6668/aaea4e.

[150] S.R. Foltyn et al. "Materials science challenges for high-temperature superconducting wire". In: *Nature materials* 6.9 (2007), pp. 631–642. DOI: 10.1038/nmat1989.

[151] Yasuji Yamada et al. "Liquid phase epitaxy for the production of $YBa_2Cu_3O_{7-\delta}$ coated conductor". In: *Applied superconductivity* 4.10-11 (1996), pp. 497–506. DOI: 10.1016/S0964-1807(97)00036-7.

[152] S. Noro et al. "Magnetic properties of $Ba_2Cu_3O_4Cl_2$ single crystals". In: *Materials Science and Engineering: B* 25.2-3 (1994), pp. 167–170. DOI: 10.1016/0921-5107(94)90219-4.

[153] K. Ruck et al. "Phase Diagram Investigations in the System Ba-Cu-O-Cl and Magnetic Properties of $Ba_3Cu_2O_4Cl_2$ and $Ba_2Cu_3O_4Cl_2$". In: *Journal of Solid State Chemistry* 141.2 (1998), pp. 378–384. DOI: 10.1006/jssc.1998.7956.

[154] Takanori Motoki et al. "Microstructures and improved J_c-H characteristics of Cl-containing YBCO thin films prepared by the fluorine-free MOD method". In: *Superconductor Science and Technology* 29.1 (2015), p. 015006. DOI: 10.1088/0953-2048/29/1/015006.

[155] Takanori Motoki et al. "Dramatic effects of chlorine addition on expanding synthesis conditions for fluorine-free metal-organic decomposition $YBa_2Cu_3O_y$ films". In: *Applied Physics Express* 10.2 (2017), p. 023102. DOI: 10.7567/APEX.10.023102.

[156] O. Matsumoto et al. "Material characterization of superconducting T-Nd_2CuO_4 films synthesized by metal organic decomposition". In: *Physica C: Superconductivity and its applications* 470.20 (2010), pp. 1029–1032. DOI: 10.1016/j.physc.2010.05.027.

[157]   X. Qi et al. "YBCO/Nd_2CuO_4/NiO/Ni coated conductors fabricated by liquid phase epitaxy based techniques". In: *Superconductor Science and Technology* 17.10 (2004), p. 1144. DOI: 10.1088/0953-2048/17/10/010.

[158]   Soon-Mi Choi et al. "Characteristics of high-J_c GdBCO coated conductors fabricated by the RCE-DR process". In: *IEEE transactions on applied superconductivity* 23.3 (2012), pp. 8001004–8001004. DOI: 10.1109/TASC.2012.2234814.

[159]   A. Hassini et al. "Atomically flat MOD $La_{0.7}Sr_{0.3}MnO_3$ buffer layers for high critical current $YBa_2Cu_3O_7$ TFA films". In: *Superconductor Science and Technology* 20.9 (2007), S230. DOI: 10.1088/0953-2048/20/9/S18.

[160]   R. Ortega. "Resistive memory devices based on complex oxides". Universitat Autònoma de Barcelona, 2015. ISBN: 9788449062360. URL: https://ddd.uab.cat/record/165692.

[161]   J.C. Gonzalez-Rosillo. "Volume resistive switching in metallic perovskite oxides driven by the metal-insulator transition". Universitat Autonoma de Barcelona, 2018. ISBN: 9788449071508. URL: https://ddd.uab.cat/record/185722.

[162]   S.F. Wang et al. "Pulsed Laser Deposition of a Single Buffer Layer of $LaMnO_3$ for $YBa_2Cu_3O_{7-x}$ Coated Conductors". In: *Journal of superconductivity and novel magnetism* 19.6 (2006), pp. 485–488. DOI: 10.1007/s10948-006-0139-x.

[163]   William Henry Bragg and William Lawrence Bragg. "The reflection of X-rays by crystals". In: *Proceedings of the Royal Society of London. Series A, Containing Papers of a Mathematical and Physical Character* 88.605 (1913), pp. 428–438. DOI: 10.1098/rspa.1913.0040.

[164]   Mario Birkholz. *Thin film analysis by X-ray scattering*. John Wiley & Sons, 2006. ISBN: 3527607048.

[165]   L.J. Van der Pauw. "A method of measuring the resistivity and hall coefficient on lamellae of arbitrary shape". In: *Philips Technical review* 20 (1958), pp. 220–224.

[166]   V. Rouco. "Controlling Vortex Pinning and Dynamics of Nanostructured YBCO Thin Films Grown by Chemical Solution Deposition." Universitat Autonoma de Barcelona, 2014. ISBN: 9788449043543. URL: https://ddd.uab.cat/record/127057.